U.PORTO
FACULDADE DE CIÊNCIAS
UNIVERSIDADE DO PORTO

Lattice location of transition metals in silicon by means of emission channeling

Daniel José da Silva

Thesis submitted to the Faculty of Science of the University of Porto in partial fulfillment of the requirements for the degree of Doctor in Physics

2014

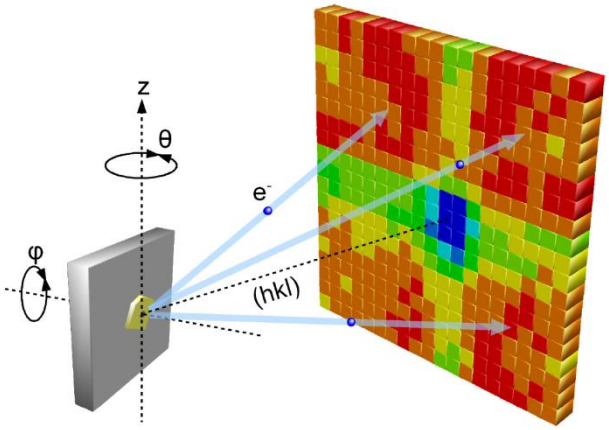

Lattice location of transition metals in silicon by means of emission channeling

Daniel José da Silva
MAP-fis Doctoral Program
Department of Physics and Astronomy
2014

Supervisor
Dr. João Pedro Esteves de Araújo, Assistant Professor, Faculty of Science of the University of Porto
co-Supervisor
Dr. Ulrich Wahl, Principal Researcher, Center of Nuclear Sciences and Technologies of the University of Lisbon

To my parents
To my sister
To Inês

Acknowledgments

Besides having widen my horizons, these last four years allowed me to meet new nice people and to build stronger relationships with those I knew before. The following paragraphs list all the people that in one way or another have turned this work possible. I will never forget your support. *"Gratitude is the heart's memory"*, French proverb.

The first persons I want to thank are my supervisors. Thank you João Pedro. A good PhD program needs novel and innovative ideas in the context of a promising topic. The fact is that we need to know the right people, not only to understand how we can contribute but also to be supported when exotic techniques are required. You were the person who established that bridge. Uli, your expertize on the subjects treated in this PhD is unquestionable, both from the emission channeling technique and on the topic of impurities in semiconductors. Thank you very much for the discussions of the results, your pertinent comments and questions risen after each data analysis. If there is one person which I could say that without him things would be incomparably much more difficult is you. And you Guilherme, thank you for your support on handling emission channeling experiments, for keeping measuring ^{59}Fe offline, for your friendship.

I would like to thank Fundação para a Ciência e Tecnologia (FCT), for my PhD grant (SFRH/BD/69435/2010) and project (CERN-FP-123585-2011) that financed the beam times, needed to collect data for this work, and the conferences that I attended. I also acknowledge the European Commission 7th Framework through ENSAR (European Nuclear Science and Applications Research, Contract No. 262010) that supported my participation in ISOLDE workshops. The ISOLDE collaboration is also acknowledged for providing pure radioactive beams. I am lucky to say that the success of the collections made for the present work was 100%. A special thank to the organizing committee of the international conference on defects in semiconductors (ICDS) 2013 for the Corbett award.

I also would like to thank the president of the jury Dr. Orfeu Bertolami, and the members of the jury Dr. André Vantomme, Dr. Katharina Lorenz, Dr. Vítor Torres and Dr. Mikhail Vasilevskiy, for their availability and for spending time to read this thesis.

Thank you Eric, Valérie, Lígia and Angelo, for your support during the beam times. A special thank to Lino for your availability to discuss results and ideas, but above all, for your friendship, you are definitely someone we can rely on. While the experimental

work was performed at ISOLDE, the whole analysis was carried out in Portugal, at IFIMUP. Thank you João Azevedo, José Diogo, Ana Pires, Arlete, Célia, Catarina, Rui, Bernardo, Zé Miguel, Paz, Mariana, Dina, Isabel, Aurelio, Alberto, David Navas, Vanji, Suellen Moraes, Paula Quitério, Sara, Miguel Rosmaninho and João Amaral for the friendly environment that you bring everyday to the student's office. Thank you Maria Armanda Sá and Isabel Alves for the bureaucracy. A special thank to João Horta, Gonçalo, Luís Guerra, Marcelo, Joel and Pedro Machado, especially for the discussions during lunch time, when speaking about different subjects, including the recent World Cup 2014. Also, a special thank to João Ventura and André Pereira, both examples of dedication to work.

I would like to thank my friends Vasco Gonçalves and João Caetano. I learned a lot discussing physics with you during our undergraduation, which also contributed, to a minor but still, to some extent to this PhD. A very special thank to Daniel, Mário, Marta and Marisa, my eternal friends.

Mas o meu maior agradecimento vai para o meu pai, que me mostrou e continua a mostrar todos os dias que o esforço e dedicação são acompanhados de momentos inesquecíveis, e para a minha mãe, pela sua disponibilidade incondicional para com os seus filhos. Sem eles nunca poderia chegar a este dia e verificar que estou preparado para enfrentar qualquer eventualidade na minha vida. Obrigado Andreia por teres sido uma irmã amiga. O meu agradecimento final vai para ti, Inês, que tens sido ao longo de todo este processo a minha maior companhia. Contigo todos os objetivos tornam-se possíveis de alcançar.

Daniel, November 2014

Resumo

O comportamento dos metais de transição (MT) em silício tem sido alvo de investigação intensiva nas últimas seis décadas. A sua introdução durante a produção de silício, crescimento do cristal e fabrico dos dispositivos tem feito deles contaminantes difíceis de evitar. Uma vez no silício, formam facilmente níveis de energia no hiato de energia do silício, quando isolados ou depois de precipitarem. Um importante efeito é a redução de eficiência dos dispositivos feitos em silício, sendo dramático, em particular, nas aplicações fotovoltaicas. Uma maneira de evitar estes efeitos passa por manipular a localização dos MT: alguns complexos formados pelos MT ou posições da forma isolada não introduzem qualquer nível de energia. Os defeitos que levam a este tipo de passivação estão ainda em debate. Outra maneira de mitigar a redução de eficiência baseia-se na redução das ligações pendentes dos MT com o hidrogénio. O mais importante e usado procedimento na redução dos efeitos indesejados dos níveis de energia introduzidos baseiam-se, no entanto, nas técnicas chamadas de "gettering", onde os MT são forçados a moverem-se para zonas inativas dos dispositivos. Apesar dos efeitos macroscópicos destas técnicas serem conhecidos, os mecanismos microscópicos são ainda escassamente compreendidos, nomeadamente os complexos formados pelos MT envolvidos no efeito "gettering" de regiões defeituosas, de camadas de silício dopado do tipo p e através da difusão de fósforo.

Os MT também podem ser usados como dopantes magnéticos em semicondutores. Até agora, apenas semicondutores binários têm sido investigados com alguma intensidade, depois da descoberta do ferromagnetismo diluído de (Ga,Mn)As. No entanto, a temperatura máxima de Curie encontrada chega apenas a 185 K, que é bastante baixa para aplicações práticas. Outros semicondutores têm sido, por isso, sugeridos recentemente, como o silício. Uma característica importante prende-se com a localização dos MT, e respetivas frações. É sabido que a incorporação dos MT em posições substitucionais resulta em defeitos com momento magnético diferente de zero e estáveis termicamente. A implantação iónica é uma das maneiras capazes de obter MT nas posições substitucionais. As frações incorporadas nestas posições são, no entanto, ainda desconhecidas.

Estas questões podem ser exploradas através do estudo das posições dos MT da série 3d depois de serem implantados. Em particular, a existência de diferentes complexos provocará a observação de diferentes posições. Neste trabalho investigamos as posições, e respetiva estabilidade térmica, dos isótopos radioativos ^{56}Mn, ^{59}Fe, ^{61}Co e ^{65}Ni, em silício ligeiramente e altamente dopado dos dois tipos n e p, com

a técnica "emission channeling". Em todos os casos identificamos posições substitucionais ("ideal S"), posições deslocadas relativamente à posição "bond-centered" ("near-BC"), e posições deslocadas relativamente à posição intersticial tetraédrica ("near-T").

A dependência das posições "near-BC" com a temperatura de recozimento foi análoga para todos os MT estudados, por isso os respetivos complexos devem ter sido formados independentemente da natureza do metal de transição. São sugeridas duas origens: envolvendo duas lacunas com o metal de transição em posições "bond-centered", e envolvendo aglomerados de lacunas com o metal de transição em posições deslocadas relativamente a posições "bond-centered". Enquanto que o primeiro caso não explica o deslocamento observado, o segundo fá-lo definitivamente. As posições "near-BC" devem, por isso, corresponder a uma combinação de diferentes complexos onde estes dois tipos de complexos devem participar. Uma vez que a estabilidade térmica das posições "near-BC" aumenta do silício do tipo n para o silício do tipo n^+, é sugerido que os respetivos aglomerados de lacunas devem participar na técnica de "gettering" que envolve a difusão de fósforo.

Os complexos envolvidos nas posições "near-T" devem ser mais diversificados uma vez que as respetivas frações e deslocamentos variam significativamente com a temperatura de recozimento. Descobriu-se que os MT implantados ocupam posições "near-T" no pico de concentração do metal de transição em questão (a uma distância R_p relativamente à superfície) quando o recozimento é feito a baixas temperaturas, enquanto que para altas temperaturas de recozimento os MT tendem a ocupar posições "near-T" a uma distância $R_p/2$ relativamente à superfície, rica em lacunas. Além do mais, a fração "near-T" do Mn, Fe e Co aumenta com a dopagem, de n para p^+, que provavelmente se deve à união com o dopante elétrico boro. Este facto está de acordo com a natureza da carga do Mn, Fe e Co, positiva, em silíco do tipo p, enquanto que, por exemplo, a neutralidade do Ni deve ter prevenido o aumento da fração "near-T". Este trabalho confirma, por isso, que o mecanismo de união é ditado pelas interações de "Coulomb". Os deslocamentos observados também estão de acordo com previsões teóricas. Alguns resultados obtidos nesta tese foram também comparados com investigações de espectroscopia de Mössbauer da literatura. Em particular, verificamos que a fração "near-T" do ^{61}Co aumenta na mesma gama de temperaturas de recozimento em que uma componente de Mössbauer, dupleto atribuído a dímeros de Co, aparece. Uma comparação com investigações de "emission channeling" sobre Fe está, no entanto, em contradição com tal conclusão. A atribuição das posições "near-T" ao começo do fenómeno de agrupamento é, por isso, provavelmente incorreto.

A observação de posições "ideal S" deveu-se provavelmente à captura dos MT por parte de lacunas individuais. Os casos particulares do Mn e Co são importantes uma vez que são os principais candidatos a dopantes magnéticos. Enquanto $\sim$ 60 % do Co pode ocupar posições "ideal S", menos de $\sim$ 30 % do Mn foi encontrado na forma substitutional. Por isso, apesar do momento magnético do Co ser menor do que o do Mn, Co é mais facilmente incorporado em posições "ideal S", para doses $\sim 10^{12}$ cm^{-2}. A questão levantada neste trabalho prende-se com a origem das posições "ideal S" do Co: serão todas originadas pela forma isolada do cobalto?

Abstract

The behavior of transition metals (TMs) in silicon is a subject that has been studied extensively during the last six decades. Their unintentional introduction during the Si production, crystal growth and device manufacturing have made them difficult contaminants to avoid. Once in silicon they easily form deep levels, either when in the isolated form or when forming precipitates. One important effect is the reduction of efficiency of silicon-based devices, being dramatic, in particular, in photovoltaic applications. One way to avoid such effects is by engineering the location of the TM: some TM complexes or lattice sites of the isolated form do not introduce any level in the silicon bandgap. Which point defects lead to such passivation is still under debate. Another way is to mitigate the reduction of efficiency by reducing the dangling bonds of TMs with hydrogen. The most important and commonly used procedures to diminish the unwanted effects of the introduced deep levels are, nevertheless, based on the so-called gettering techniques, where TMs are forced to move away from the active area of devices. Although the macroscopic effects of all the gettering techniques are well known, the related microscopic mechanisms are still poorly understood, namely the TM complexes involved in gettering into defective regions, into *p*-type layers and by phosphorus diffusion.

TMs can also be used as magnetic dopants in semiconductors. So far, only binary semiconductors have been intensively addressed, after the discovery of dilute ferromagnetism of (Ga,Mn)As. However, the maximum found Curie temperature was only 185 K, which is too low for practical applications. Other semiconductors have hence been recently suggested, such as silicon. One important feature is the lattice sites occupied by TMs, and related fractions. It is currently well established that the incorporation of TMs on substitutional sites leads to thermally stable point defects with none-zero magnetic moment. One way to obtain substitutional TMs is by ion implantation. Which fraction is incorporated on S sites is, however, still unknown.

All these issues can be explored by investigating the lattice sites of implanted 3d TMs. In particular, different complexes will correspond to different lattice sites. Here, we have investigated the lattice location and thermal stability of the implanted 3d TM probes ^{56}Mn, ^{59}Fe, ^{61}Co and ^{65}Ni in both lightly and heavily doped *n*- and *p*-type Si by means of emission channeling experiments. In all cases we identified ideal substitutional (S) sites, displaced bond-centered (near-BC) sites and displaced tetrahedral interstitial (near-T) sites.

The dependence of the near-BC sites on annealing temperature was similar for all investigated TMs, hence the related complexes may be formed irrespective of the TM nature. Two main origins are suggested: involving divacancies where the TM occupies BC sites (between two vacant sites) and involving fourfold coordinated vacancy clusters with the TM occupying a position near the ideal BC site. While the first case cannot explain the observed displacement, the second case definitely does. The observed near-BC sites may hence correspond to a combination of different complexes where these two types of complexes may participate. Since the thermal stability of near-BC sites increases from n- to n^+-type Si, it is suggested that the related multivacancy complexes may participate in P-diffusion gettering.

The complexes involved in the observed near-T sites seem to be more diversified, as the related fraction and displacement change significantly with annealing temperature. One has found that implanted TMs occupy near-T sites around the related peak concentration (at R_p from the surface), after low temperature anneals, while for high annealing temperatures TMs tend to occupy near-T sites at midway between the peak concentration and the surface (at $R_p/2$ from the surface), rich in vacancies. Moreover, the near-T fraction of Mn, Fe and Co increases from n- to p^+-type silicon, which might be due to the TM pairing with the electric dopant boron. This fact agrees with the positive charge nature of interstitial Mn, Fe and Co, while, for instance, the charge state of Ni is neutral in p-type Si which might have prevented the increase of its near-T fraction. It is therefore confirmed that the related pairing mechanism is driven by Coulomb interactions. The observed displacement also matches with theoretical predictions. Some of the results obtained in this thesis were also compared to Mössbauer spectroscopy investigations from literature. In particular, it was found that, in n-type Si, the near-T fraction of ^{61}Co increases in the annealing temperature range where a Mössbauer doublet component appears, attributed to Co-dimers. A comparison to emission channeling investigations on iron is, however, at variance with such a conclusion. The attribution of near-T sites to the beginning of clustering is hence most likely incorrect.

The observation of ideal S sites might be due to the trapping of TMs into single vacancies produced during implantation. The particular cases of Mn and Co are important as they are the main TM candidates for magnetic dopants. While $\sim$ 60% of Co can occupy ideal S sites, no more than $\sim$ 30% of Mn is in the S form. Hence, although the magnetic moment of Co is smaller than that of Mn, Co is easier incorporated on S sites, for fluences of $\sim 10^{12}$ cm^{-2}. The question that this work raises is whether the S sites actually originate from the substitutional form of Co.

Preface

Silicon is the most commonly used material in todays semiconductor industry. Impurity atoms, whether they are inherently present or intentionally introduced, play a decisive role in the performance of semiconductor applications. More specifically, the local structural configuration of the impurity atoms in the single-crystalline lattice of the semiconductor (i.e. the exact lattice location of the impurity and the configuration of the surrounding atoms) has a major influence on the electronic energy levels and the spin state of the impurities, hence determining the electronic, magnetic and optical properties of the doped semiconductor. This PhD thesis unravels the structural configuration of 3d transition metals in Si by investigating the lattice location and thermal stability of the radioactive probes ^{56}Mn, ^{59}Fe, ^{61}Co and ^{65}Ni with the emission channeling technique, focusing on the following five goals:

- to study the geometry and thermal stability of the complexes resulting from the interaction of 3d transition metals with implantation-induced defects, that might be responsible for some of the electrical activity reported in the literature and for the gettering centers provoked by electron irradiation or ion implantation,

- to investigate the microscopic mechanism of Fe, Co and Mn trapping by the electric dopant B^- in p-type silicon, i.e. to determine which geometry FeB may present and to study the kinetics of the related formation and dissociation,

- to determine whether complexes resulting from the interaction of transition metals with defects, such as those vacancy-related, are involved in P-diffusion gettering by studying the influence of heavy electronic n^+ doping on the observed lattice sites,

- to explore the microscopic mechanism of clustering by comparing the influence of annealing on the lattice sites of Co to Mössbauer spectroscopy investigations that have claimed to observe Co-dimers,

- to determine the substitutional fraction of implanted Mn and Co, thought to be the source of possible dilute ferromagnetism, and to study which additional fractions, and related geometries, may be present.

The work performed in this PhD thesis resulted from experimental research at the IFIMUP unit of the IN-Institute of Nanoscience and Nanotechnology located at the "Universidade do Porto", Portugal, at the "Centro de Ciências e Tecnologias Nucleares" (C2TN) of the "Instituto Superior Técnico" located at the "Universidade de Lisboa", Portugal, and at the ISOLDE facility located at the "Organisation Européenne pour la Recherche Nucléaire" (CERN), Switzerland. This thesis is organized as follows: chapter 1 discusses the technological relevance of transition metals in silicon, chapter 2 describes in detail the current understanding of the related microscopic mechanisms and chapter 3 describes the emission channeling technique. Finally chapter 4 compiles the six manuscripts concerning the lattice location of Fe, Ni, Co and Mn listed below:

I **Influence of n^+- and p^+ doping on the lattice sites of implanted Fe in silicon**

D. J. Silva, U. Wahl, J. G. Correia and J. P. Araújo.

Journal of Applied Physics **114**, 103503 (2013)

II **Influence of the doping on the lattice sites of Fe in Si**

D. J. Silva, U. Wahl, J. G. Correia and J. P. Araújo.

AIP Conference Proceedings **1583**, 24 (2014)

III **Lattice location and thermal stability of implanted nickel in silicon studied by on-line Emission Channeling**

D. J. Silva, U. Wahl, J. G. Correia, L. M. C. Pereira, L. M. Amorim, E. Bosne, M. R. da Silva and J. P. Araújo.

Journal of Applied Physics **115**, 023504 (2014)

IV **Origin of the lattice sites occupied by implanted Co in Si**

D. J. Silva, U. Wahl, J. G. Correia, L. M. C. Pereira, L. M. Amorim, M. R. da Silva and J. P. Araújo.

Semiconductor Science and Technology **29**, 125006 (2014)

V **Lattice sites of implanted Co in heavily doped silicon**

D. J. Silva, U. Wahl, J. G. Correia, L. M. C. Pereira, L. M. Amorim, A. Costa, V. Augustyns, M. R. da Silva and J. P. Araújo.

in preparation for *Semiconductor Science and Technology*

VI **Direct observation of the lattice sites of implanted manganese in silicon**

D. J. Silva, U. Wahl, J. G. Correia, L. M. C. Pereira, L. M. Amorim, S. Decoster, M. R. da Silva and J. P. Araújo.

in preparation for *Physical Review B*

Contents

Chapter 1

Characteristics of transition metals in silicon

This chapter describes the three roles where transition metals are of importance in Si technology: as unintentionally introduced electrically active impurities that provoke the malfunctioning of Si-based devices; as magnetic dopants in the pursuit for dilute magnetic semiconductors; and as electric contacts in the form of silicide. Though these three technological roles are relevant, the unwanted electrical activity of transition metals has been a serious concern for the semiconductor industry. A further section dedicated to the source of contamination is hence given: during the silicon production, crystal growth and device processing. Finally, ways are described to mitigate the harmful electrical effects with, e.g., hydrogen passivation and gettering techniques. This description will be helpful for understanding how the unveiling of the microscopic behavior of transition metals can be advantageous in the resolution of fundamental adversities faced by the semiconductor industry.

1.1 Silicon - the ubiquitous semiconductor

Technological breakthroughs have marked Mankind History. The stone age, bronze age and iron age brought new tools and techniques which made possible the saving of time for social life. Part of this time was used to generate more knowledge in such a way that the invention of writing was inevitable. With the industrial revolution the writing became ineffective and on the 20^{th} century the information age, with the spread of personal computers and other related technologies, made possible by

the invention of semiconductor components, e.g. transistors, changed the way people live their everyday life. In fact, the semiconductor industry has been a major force driving world economy and led to the appearance of highly innovative and increasingly small and efficient portable gadgets. The Moore's law, which states that the number of transistors in integrated circuits doubles every eighteen months, has hence been followed.

It is curious to find silicon as a second choice in the first semiconductor components. The fact is that germanium was the basis of the first invented transistor. Three reasons had justified its use. First, germanium can be easily processed at low temperatures. Second, germanium-based devices can function at high frequencies, due to the high mobilities of the charge carriers. Third, single crystal growth of germanium was early developed. It turns out that the disadvantages overcome these benefits. At least for most applications, which accelerated the rising of silicon-based devices. Germanium has a small bandgap (0.66 eV [1]). It may appear very interesting and useful at first sight when handling with long electromagnetic wavelengths, but very inappropriate for the majority of devices. One example can be found in the inability for germanium-based devices to function at high temperatures, due to thermal runaway. This functioning failure has been a very prominent barrier for its industrial commercialization. In contrast, silicon has a bandgap of 1.12 eV [1], which handles with overheat. Moreover, silicon shows a stable oxide, which provides a low density of interface states. Nevertheless, these features would never be relevant without its abundance on Earth. Silicon, as a material, is not available in nature (at least in Earth's nature), but in the form of silica (silicon dioxide), e.g. in sand. By making use of a simple process, one can easily separate silicon from oxygen [2]. No other semiconductor with such characteristics is present in the Earth's crust in such quantities. All these features of silicon are responsible for the rise of the information age. Of course that there are still some obstacles for its full usability, mostly concerning its purity as will be described in the following sections.

1.2 Technological relevance of transition metals

1.2.1 Transition metals as electrically active impurities

After proving the functioning concept of several Si-based devices during the first steps of the semiconductor research, it was realized that their efficiencies were being under-

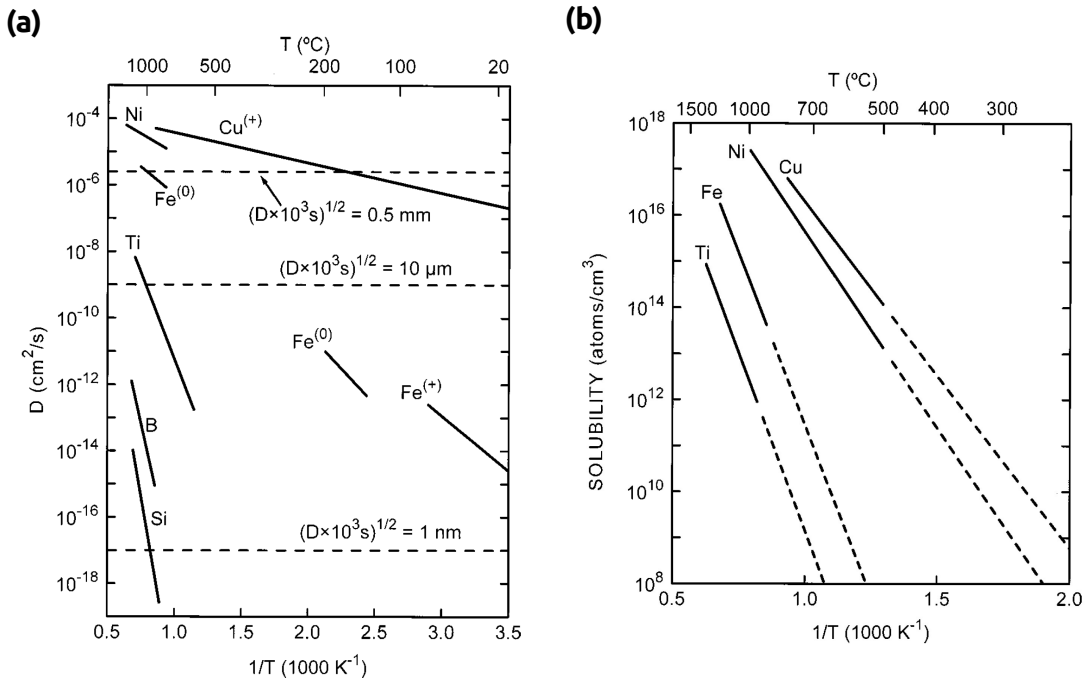

Figure 1.1: Temperature dependence of the (**a**) diffusion coefficient and (**b**) solubility of several elements, including the transition metals Ti, Fe, Ni and Cu [6].

mined by the quality of the silicon material. Several studies, based first on electron paramagnetic resonance (EPR) and afterwards on deep level transient spectroscopy (DLTS), observed several deep levels within the silicon bandgap, which would not exist in pure Si [3]. We currently know of several contributions for the presence of deep levels. However, the most harmful contribution comes from the presence of transition metal (TM) impurities. TMs exhibit a high diffusivity, already substantial at low temperatures, and a low solubility at room temperature, which becomes significant at elevated temperatures (see Fig. 1.1) [4, 5]. These two physical properties provoke the precipitation of TMs into silicides during cool down, in particular near the silicon wafer surface which is commonly the active region of the devices. These precipitates usually introduce deep levels. Another source of unwanted electrical activity comes from the presence of TMs as point defects.

There has been some controversy about the exact deep levels that each TM introduces. Some of them are now well accepted while others are still object of current research. One parameter which turns such understanding even more complex is the influence of the occupied lattice site of the isolated form of TMs. Figure 1.2 exemplifies such impact for 3d TMs. Depending on the two lattice sites, substitutional or interstitial

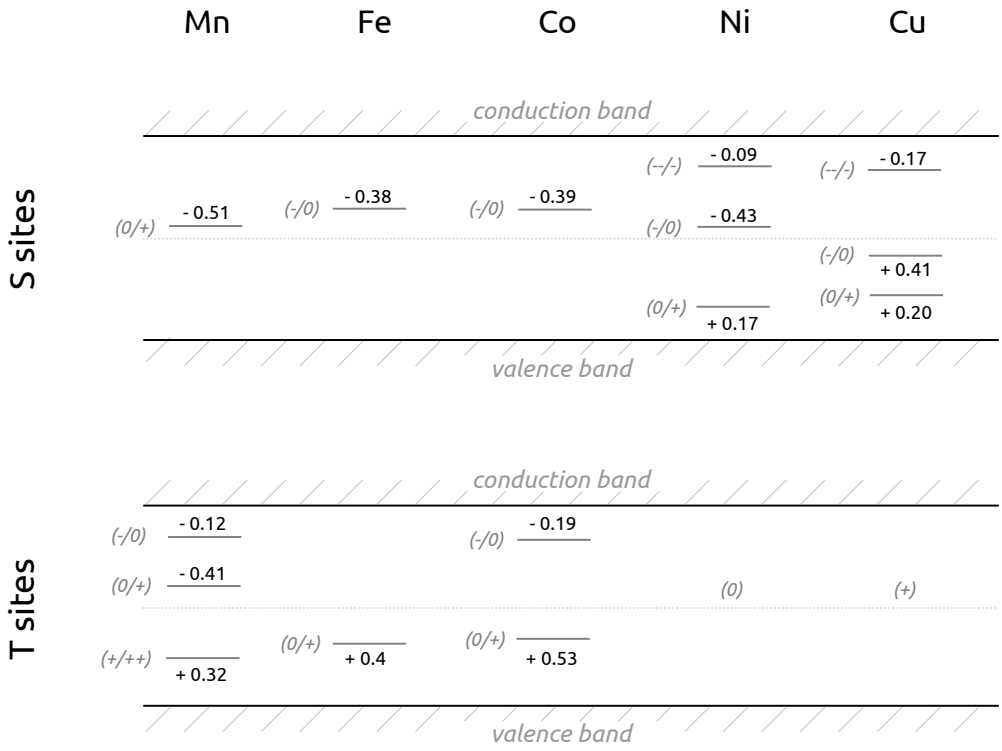

Figure 1.2: Deep levels for the 3d transition metals Mn, Fe, Co, Ni and Cu, when in the substitutional and interstitial tetrahedral forms. The sign in brackets represents the charge state transitions. The values of the energy levels are shown with respect to the conduction band (if negative) or to the valence band (if positive). Detailed information about the electronic structure of these transition metals can be found in the references of appendix A.

tetrahedral sites, different deep levels are formed. The change of the lattice site can sometimes reduce the number of deep levels. One extreme case occurs for Ni, which has three deep levels when occupying substitutional sites and none when sitting on interstitial tetrahedral sites. This example shows clearly that the manipulation of the occupied lattice site may reduce the electrical activity of 3d TMs. Such defect engineering has been nevertheless difficult to attain. In addition, the pairing with other point defects, such as with other impurities or with native defects, turns the related complexes, in the majority of cases, still electrically active, by introducing other deep levels [7]. One such example arises when the positively charged Fe^{+}, in its interstitial form, forms pairs with the electric acceptors B^{-} through Coulomb interactions. FeB

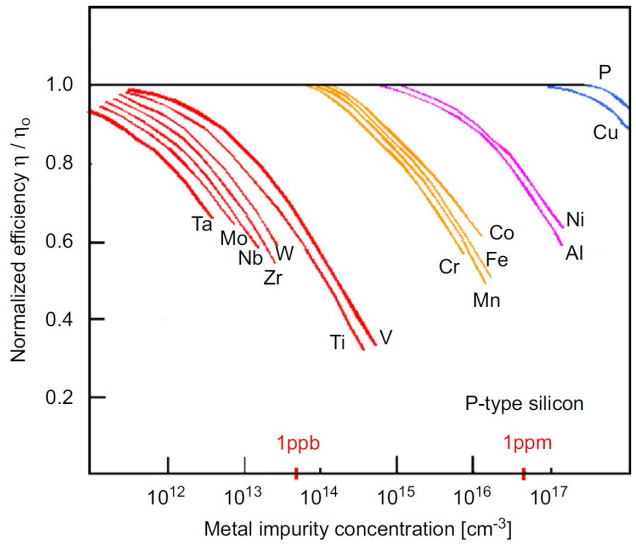

Figure 1.3: Normalized efficiency of PV silicon cells as a function of concentration for several transition metal impurities [8].

pairs introduce one deep acceptor level in the silicon bandgap (see appendix A). A similar behavior can occur when 3d TMs form pairs with hydrogen, oxygen, carbon, clusters of vacancies, etc. The complexity is therefore boundless. In particular, one can have processes which reduce one specific deep level, but form others. The clarification of the microscopic mechanisms underlying the behavior of TMs is therefore crucial.

The majority of the current Si-based devices requires purities of $\sim$ 99.9999% (often referred purities of 6N) [9]. So far, only the Siemens process has successfully allowed to attain such pure silicon [10]. However, the price of the resulting silicon material has faced a considerable market volatility in the last six years, ranging from $\sim$ 12 to $\sim$ 383 €kg^{-1}, which is, in any case, unaffordable for some technologies. One example comes from the photovoltaic (PV) industry, in which the minority carrier lifetime is currently the limiting factor of efficiency [11, 12]. Figure 1.3 shows clearly that the presence of TMs affects the normalized efficiency of solar cells, which becomes significant when the concentration of 3d TMs approaches values close to 1 ppm [8]. S. Pizzini has examined the competitiveness of silicon solar cells with the current available PV plants [8]:

"*... In order to make PV appealing for the energy market and competitive with conventional sources and nuclear energy, PV plants should get hundreds of GW yearly, so that the amount of silicon needed will exceed one million tons/year. As the investment cost for a conventional Siemens-type of plant of 1000 tons/year could be estimated*

around 100 million €, the financial means needed to build those plants are above any reasonable economic limit. ..."

The research has been focused on finding a new way to produce silicon with less stringent purity than that allowed by the Siemens processes, but still good enough for the PV technology. One appealing way relies on modifying the metallurgical grade silicon production (raw silicon) [9]. Such modifications are discussed in more details in the next section.

Summarizing, the introduction of deep levels by TM contaminants within the silicon bandgap has been hampering the effective functioning of silicon-based devices. The complexes that are responsible for those levels have been under debate. Although the identification of some deep levels and their assignments to specific complexes are currently well established, there are other deep levels that are still on the top research level, e.g. regarding the structural forms of the complexes that include TMs.

1.2.2 Transition metals as magnetic dopants

In the last subsection it was shown how the unwanted electrical activity of the related complexes (or silicides) of TMs can affect the proper functioning of Si-based devices. There are, however, other physical properties that may be introduced if controlling the incorporation of 3d TMs in the silicon material. One example involves the use of the magnetic moment in spintronic devices.

Before entering into more details on the magnetic properties of 3d TMs in Si one should first say a few words about applications that may take advantage of the magnetic moment in semiconductors in general. Datta and Das proposed in 1990 the concept of a new transistor that makes use of two ferromagnets as drain and source, and in which the voltage base could control the spin of the charge carriers [13]. It was shown, however, that such device could not be practicable since the polarized spin carriers have only a limited coherence length before flipping [14], but, as it happens recurrently in science, the simple idea of developing a new generation of devices with both magnetic and semiconducting properties, even with significant obstacles, was in the air which intensified the research dedicated on the pursuit of those materials.

The first materials that combined both semiconductor and magnetic properties were investigated back in the 60s, such as europium chalcogenides (e.g. EuO) and chromium spinels ($CdCr_2S_4, CdCr_2Se_4$). However, it turned out that the hard reproducibility,

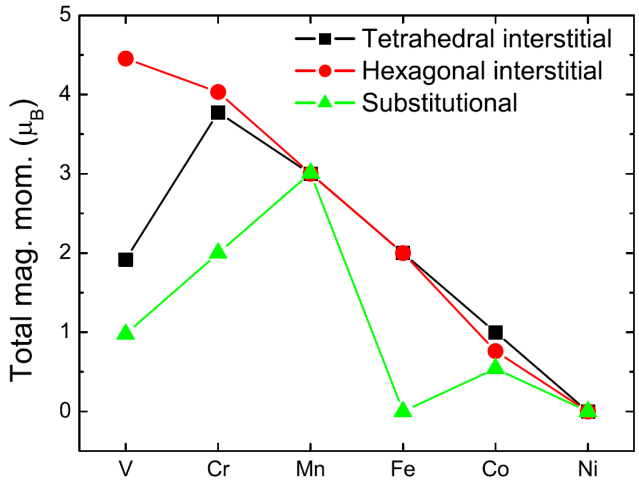

Figure 1.4: Magnetic moment of V, Cr, Mn, Fe, Co and Ni when occupying substitutional, interstitial tetrahedral and interstitial hexagonal lattice sites, obtained with *ab initio* calculations [16].

difficult integration into current semiconductors (due to the different structures) and low Curie temperatures made them only interesting for academic purposes and thus were readily discarded. The idea of having a semiconductor with magnetic properties which could be effectively integrated with nowadays semiconductors was finally made possible with the discovery of dilute ferromagnetism of Mn-doped GaAs [15]: it was found that the ferromagnetism was carrier-mediated by the holes created by the substitutional Mn itself.

At first sight, one may think that the story of the main discoveries that would lead to a final magnetic semiconductor ends here. It is not, however, the case due to the still low Curie temperatures ($\sim$ 185 K at most for (Ga,Mn)As [17]). On one hand the problem of reproducibility and integration into semiconductor-devices was solved, but on the other hand the need of functioning below room temperature was hampering their applicability. Research is presently trying to find ways to synthesize DMSs with Curie temperatures above room temperature. In that respect, several TM-doped semiconductor systems have been investigated. In particular, one semiconductor which scientists are considering is Si. The physical properties of TM-doped Si have not, however, been investigated with the intensity of, e.g., GaAs systems due to the aforementioned ease of TMs to precipitate in silicon [14].

The ferromagnetism of TM-doped Si systems will obviously be influenced by the magnetic moment of the TM species and by their occupied lattice sites. Figure 1.4

shows the magnetic moment of several TMs, obtained from first principle calculations, when occupying three different lattice sites [16]. The lattice site where TMs show the largest values is the interstitial site with hexagonal symmetry. It turns out that TMs are not stable on this site. The lattice site with the second largest magnetic moment is the interstitial site with tetrahedral symmetry, which is of little use due to the high diffusivity of TMs when occupying T sites, and hence due to precipitation for the reasons pointed out above. The only left possible site is thus the substitutional site.

A major obstacle has still to be overcome on how to incorporate the TMs on substitutional sites. One way is by creating single vacancies through irradiation, or by implanting the TM itself. A first study on a Mn-implanted Si system was found to be very promising. Ferromagnetism was indeed present [18]. However, further investigations concluded that the ferromagnetism was originated by secondary phases, such as silicides. The main example of detected secondary phases was $MnSi_{1.7}$ nanoparticles [19]. Moreover, a recent investigation based on extended X-ray absorption fine structure (EXAFS) has concluded that the local environment of Mn is too complex in order to only form silicide precipitates plus substitutional Mn [20], giving rise to the hypothesis that more complicated complexes may participate.

The complexes formed by implanted TMs in Si are hence still under debate. In particular, the incorporation of the Mn and Co magnetic dopants into substitutional sites are controversial and are currently the main question which has still to be answered. The other complex structures formed by implanted Mn and Co have also to be investigated in terms of structural, electric and magnetic characterization, to understand whether they can interfere with possible dilute ferromagnetism of the substitutional form.

1.2.3 Transition metals as metal contacts

When trying to create metal contacts by depositing TMs on Si-device structures one verifies the formation of silicides. This is again due to the high diffusivity of TMs and thus due to the ease of forming well defined structures with Si atoms. These silicides may create beneficial or harmful effects depending on whether the goal is the formation of Schottky or Ohmic contacts [21]. It has been shown that the Schottky or Ohmic behaviors depend on the silicide formed and on the doping of the silicon material. For example, if one uses heavily n-type doped Si, a Schottky diode is usually formed. If using lightly n- or p-type Si, one usually obtains ohmic contacts [22]. Both

approaches can be advantageous since they can be used on one hand in high speed electronics (Schottky contacts) and on the other hand in MOS technology (e.g. in interconnects as ohmic contacts) [23, 24].

One particular advantage of silicide contacts comes from the fact that the interface between silicon and the silicide is free of contamination. Also, the lattice mismatch between the silicon lattice and the silicide structures is usually insignificant, allowing to obtain interfaces free of imperfections [22]. While the structural forms of the silicides are nowadays quite well known, the dynamics of formation is still unclear, e.g. if the formation of some silicides start with dimers and if so which lattice sites the involved TMs may occupy.

1.3 Source of unintentional contamination

This section describes the unintentional contamination processes that occur during the chain of treatments of Si-based devices, from the Si production and crystal growth to the final device processing.

1.3.1 Silicon production

As aforementioned, Si is only present in nature in the silica form (SiO_2). The first challenge is hence to separate silicon from oxygen. This process can be easily performed by reacting highly pure silica with wood, charcoal or coal in an electric arc furnace at temperatures over 1900°C: $SiO_2 + 2C \rightarrow Si + 2CO$ [2]. The resulting Si material is called metallurgical grade (MG) silicon and has a purity of $\sim$ 98%. To achieve purities of $\sim$ 99.9999%, several procedures were adopted in what is currently known as the Siemens process, that generally consists on decomposing trichlorosilane from the reaction $Si(s) + 3HCl(g) \rightarrow HSiCl_3(g)$ by chemical vapor deposition on a hot filament: $2HSiCl_3(g)(+H_2(g)) \rightarrow Si(s) + SiCl_4(g) + 2HCl(g)$ [25]. The silicon material resulting from the Siemens process is known as electronic grade (EG) silicon (sometimes referred as semiconductor grade silicon).

EG silicon has been used on PV cells. However, for the reasons pointed out in the last section, such high purities are not needed for this particular technology [11]. To reduce the production cost, new routes have been suggested, either by modifying the Siemens process or by using a different purifying procedure in MG silicon. This last

Table 1.1: Typical concentrations (cm^{-3}) of 3d transition metal impurities in metallurgical and electronic grade silicon [26, 27].

	Ti	V	Cr	Mn	Fe	Co	Ni	Cu
EG	$\lesssim 10^{13}$	$\lesssim 10^{13}$	$\sim 10^{13}$	$\lesssim 10^{13}$	$\sim 5 \times 10^{14}$	$\lesssim 10^{13}$	$\sim 5 \times 10^{14}$	$\sim 5 \times 10^{14}$
MG	$\sim 10^{19}$	$\sim 10^{18}$	$\sim 10^{18}$	$\sim 5 \times 10^{18}$	$\sim 5 \times 10^{19}$	-	$\sim 5 \times 10^{18}$	$\sim 10^{18}$

route is the most popular. How the purity can be improved is still under debate and will not be treated here. One should, however, emphasize the starting point and where to go. In that respect, we know the TM content of MG and EG silicon. The so-called solar grade (SoG) silicon specifications must lie between them [8]. Both specifications are shown in table 1.1.

1.3.2 Crystal growth

The silicon product, either involving the Siemens process or new routes from MG silicon, is polycrystalline. In order to obtain single crystals two methods are usually used: the Czochralski and the floating zone methods. While the first method may reduce the purity of silicon, due to contaminations from, e.g., impure crucibles made of quartz, the second was developed to avoid such contaminations [2, 28].

The **Czochralski method** is usually performed in an inert atmosphere, such as argon, and inert chamber, such as quartz. It begins with the melting of silicon when the chamber is heated to $\sim 1500°C$. When Si is fully melted, a small seed crystal mounted at the end of a rotating shaft is slowly lowered until it dips below the surface of the molten Si. Afterwards the shaft rotates counterclockwise and the crucible rotates clockwise. The rotating rod is then drawn upwards very slowly, allowing an ingot to be formed. The width is regulated by the precise control of the temperature, speed of rotation and speed of the seed holder withdraw.

The **floating zone method** consists of the melting of a narrow region of the silicon ingot. This molten zone is moved along the ingot (or the ingot is pulled through the heater). This procedure avoids the use of contaminated quartz. Moreover, the molten region melts impure solid at its forward edge and leaves a wake of pure material solidified behind it as it moves through the ingot. This is achieved due to the so called segregation phenomenon. The principle is that the segregation coefficient $k = C_s/C_l$ (C_s and C_l being the impurity concentrations in the solid and liquid phases) is usually less than one for TMs. The impurity atoms will diffuse to the liquid region at the

solid-liquid boundary. Therefore, by passing a crystal ingot through a thin section of the furnace very slowly, such that only a small region of the ingot is molten at any time, the impurities will be segregated at the end of the crystal. When high purity is required the process is repeated. The ingot can grow as a perfect single crystal due to a seed crystal that is placed at the base.

In both methods, electric dopant impurities can be added to the molten Si during the process. Due to its higher complexity, the floating zone method is more expensive than the Czochralski one. After the crystal growth, one still has to cut the ingot into slices to produce the final silicon wafer. This is currently done by sawing the ingot with SiC wires. It is worthwhile to remark that it has recently been suggested the use of diamond wires, which avoids more effectively the cracking, important for the final cost since the thickness of wafers may reduce [29].

1.3.3 Device processing

Silicon wafers are not free of further contamination. In fact, several processes can, to some extent, contaminate the wafer during the device processing. One particular example is that of iron which is present in stainless steel, usually used in wafer processing setups [30]. Though a list of possible contamination mechanisms would be long, there are five which are worthwhile to point out [31]. The first is known as **backside contamination** and relies on the diffusion of TM impurities from alloys, which are usually part of handling materials. The second contamination process occurs during **wet etching**. It seems contradictory at first sight, since liquid etchants are supposed to remove imperfections and impurities, but they also present a degree of purity. Even in low concentrations, we have seen that TMs can be destructive to some applications. Some etchants have purities which do not fulfill these requirements. Contamination from **thermal treatments** can also occur through the out-diffusion of TMs from the chamber materials, and further absorption in the silicon wafer.

So far, the three processes described above involve contamination by some kind of diffusion mechanism. The following two will have in common implantation mechanisms. One of them occurs during **dry etching**. Here, the main source is located in the electrodes, which may contain TMs, that are sputtered with the ions from a plasma, e.g. argon. The resulting etched TMs may be further implanted in the silicon wafer. Last but not least, contamination can take place during **ion implantation** of, e.g., electric dopants. The cause is the sputtering of TMs present in the sample holder, or

materials near the silicon wafer, and their further implantation.

1.4 Mitigation of the unwanted electrical effects

It is clear from the examination of the last subsection that there will always be a significant amount of TM contaminants influencing the good operation of devices. One way to reduce the related harmful effects is by purifying the silicon material. Another way is by engineering TM defects in such a way that the harmful effects are reduced. This section describes two processes that mitigate the harmful effects of TMs.

1.4.1 H passivation

The electrical activity of TMs comes from the fact that their electronic structures are completely different from that of silicon. For instance, TMs will have, in most cases, more valence electrons than silicon. One implication of these different electronic structures is the creation of dangling bonds, which is followed by their electrical activity in silicon. One way to reduce them is by using other impurities that could saturate these dangling bonds. Hydrogen seems to be the most feasible impurity for this purpose [32]: hydrogen only has one valence electron. In fact, it has been shown that hydrogen passivates several deep levels introduced by other impurities, including 3d TMs. The precise microscopic mechanisms are, however, still under debate but seem to be different depending on the impurity. In particular, it is still under debate which TM electric deep levels are effectively passivated when the efficiency of PV cells is increased during the hydrogen exposure of the silicon material [33–35]. Furthermore, hydrogen can also passivate the electrical activity of defective bonds, unreconstructed surface dangling bonds and dangling bonds from interfaces. The introduction of hydrogen in Si can be performed already during the silicon production (or during its crystal growth), by implantation or by chemical reaction on the surface of the wafer. It has been, nevertheless, shown that the exposure to a hydrogen-contaminated plasma is the most effective mechanism to increase the efficiency of devices [36].

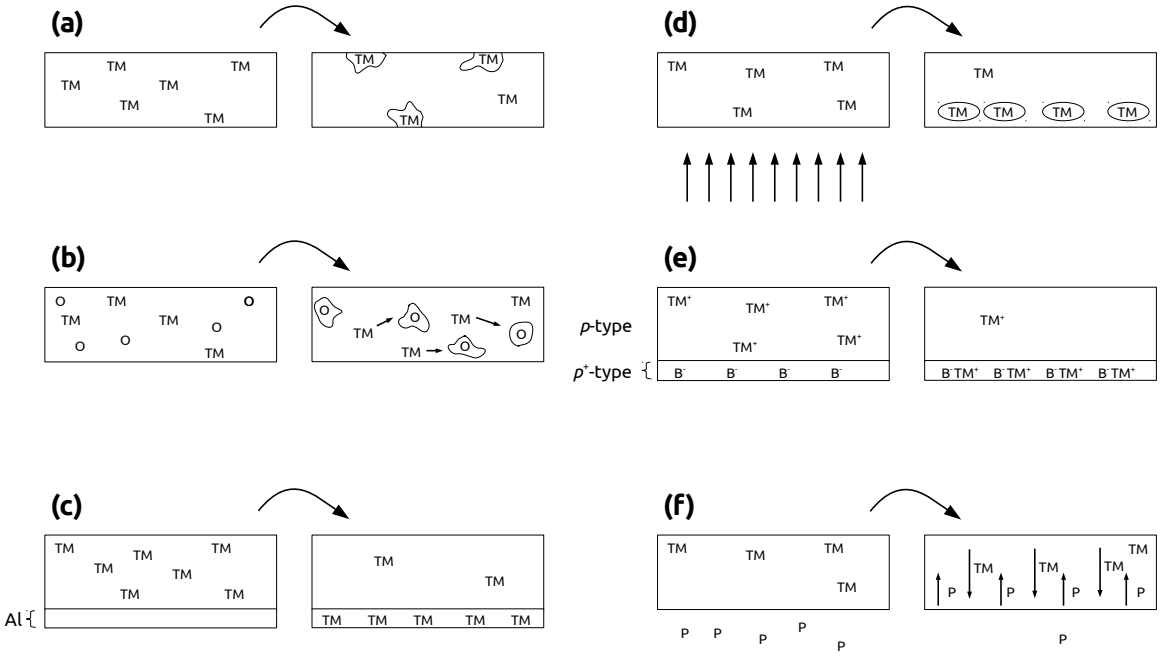

Figure 1.5: Scheme of the procedures of five gettering techniques. TM represents transition metals, P phosphorus, B boron and O oxygen. (a) depicts the normal precipitation of TMs upon cooling down. (b) shows the usual internal gettering. (c) represents aluminum gettering. (d) displays gettering by defects provoked by irradiation or ion implantation. (e) illustrates gettering through the formation of transition metal-acceptor pairs. Finally, (f) depicts phosphorus diffusion gettering.

1.4.2 Gettering techniques

Transition metals precipitate easily near the surface during cool down (see Fig. 1.5 (**a**)). This fact occurs because the barrier to metal-silicide nucleation is lower at those regions, which is problematic since the surface of the silicon wafer is very often the active region of devices. One way to mitigate these harmful effects is by passivating the deep levels with H, but such process is not very efficient for all the TMs as they do not deactivate all deep levels. To increase the effectiveness of mitigation, industry has relied on a group of procedures known as gettering. Gettering consists of moving the TM impurities to inactive regions of devices [6].

Gettering procedures can be divided into two categories [6]. The first relies on homogeneous precipitation, rather than preferential precipitation at the surface, by introducing nucleation sites uniformly in the sample. It turns out that oxygen, also highly present following Czochralski crystal growth, shows a very low mobility

but precipitates when cooling down, which results in the formation of homogeneous precipitates [37]. These oxygen precipitates have been used as nucleation sites for TMs, as seen in Fig. 1.5 (**b**), where their involvement resulted in the most popular gettering technique in the semiconductor industry [38]. This gettering category, also known as **internal gettering**, has still some drawbacks, mainly due to the dependence on the oxygen concentration profile that may change with the device processing step. Another way to getter TMs is by introducing gettering centers at the backside of the silicon wafer, by either forcing the TM to be trapped or form precipitates. The procedures that rely on backside gettering are known as **external gettering**.

One possible way to perform external gettering is by segregating the TMs into aluminum (Fig. 1.5 (**c**)) [6]. Damaging the backside of the silicon wafer, as seen Fig. 1.5 (**d**), have also been seen to trap effectively TM impurities. The introduction of sinks of vacancies, has been very efficient when irradiating the silicon wafer with electrons or when implanting light impurities, such as He [39]. If using a p^+-type layer at the backside of a p-type silicon wafer, it has been observed an external gettering effect for TMs mostly positively charged when diffusing interstitially. This gettering effect is due to the trapping of the positive TM ions by the negative and immobile electric acceptors (Fig. 1.5 (**e**)) [30]. Last but not least, the in-diffusion of phosphorus from a specific source, e.g. $POCl_3$ gas at temperature above 850°C, has been seen to produce a strong gettering effect on TMs, as seen in Fig. 1.5 (**f**). Though the microscopic mechanism underlying this gettering effect is still under debate, P-diffusion has been the most popular external gettering procedure for Fe [40] and Ni [41].

The macroscopic behavior of TMs is well established for the five gettering procedures pointed out above. However, the related microscopic mechanisms are still not completely clear. We still do not know which complexes are formed during the trapping of TMs into damaged regions, the complete picture of TM trapping by B^- (e.g. if TMs actually occupy tetrahedral interstitial sites when forming the pair), or the general microscopic mechanism of P-diffusion gettering.

Bibliography

[1] S. M. Sze, Physics of semiconductor devices, Wiley-Interscience, 1969.

[2] J. Orton, The Story of Semiconductors, Oxford University Press, 2004.

[3] H. J. Queisser, E. Haller, Defects in semiconductors: Some fatal, some vital, Science 281 (1998) 945.

[4] K. Graff, Metal Impurities in Silicon-Device Fabrication, 2nd Edition, Springer, 2000.

[5] E. R. Weber, Transition metals in silicon, Appl. Phys. A 30 (1983) 1.

[6] S. M. Myers, M. Seibt, W. Schröter, Mechanisms of transition-metal gettering in silicon, J. Appl. Phys. 88 (2000) 3795.

[7] E. R. Weber, Understanding defects in semiconductors as key to advancing device technology, Physica B 340 (2003) 1.

[8] S. Pizzini, Towards solar grade silicon: Challenges and benefits for low cost photovoltaics, Sol. Energy Mater. Sol. Cells 94 (2010) 1528.

[9] D. Sarti, R. Einhaus, Silicon feedstock for the multi-crystalline photovoltaic industry, Sol. Energy Mater. Sol. Cells 72 (2002) 27.

[10] A. A. Istratov, T. Buonassisi, R. J. McDonald, A. Smith, R. Schindler, J. A. Rand, J. P. Kalejs, E. R. Weber, Metal content of multicrystalline silicon for solar cells and its impact on minority carrier diffusion length, J. Appl. Phys. 94 (2003) 6552.

[11] A. F. Braga, S. P. Moreira, P. R. Zampieri, J. M. Bacchin, P. R. Mei, New processes for the production of solar-grade polycrystalline silicon: A review, Sol. Energy Mater. Sol. Cells 92 (2008) 418.

[12] T. M. Razykov, C. S. Ferekides, D. Morel, E. Stefanakos, H. S. Ullal, H. M. Upadhyaya, Solar photovoltaic electricity: Current status and future prospects, Solar Energy 85 (2011) 1580.

[13] S. Datta, B. Das, Electronic analog of the electrooptic modulator, Appl. Phys. Lett. 56 (1990) 665.

[14] S. Zhou, H. Schmidt, Mn-doped Ge and Si: A review of the experimental status, Materials 3 (2010) 5054.

[15] T. Dietl, A ten-year perspective on dilute magnetic semiconductors and oxides, Nature Mater. 9 (2010) 965.

[16] Z. Z. Zhang, B. Partoens, K. Chang, F. M. Peeters, First-principles study of transition metal impurities in Si, Phys. Rev. B 77 (2008) 155201.

[17] T. Jungwirth, K. Y. Wang, J. Maek, K. W. Edmonds, J. König, J. Sinova, M. Polini, N. A. Goncharuk, A. H. MacDonald, M. Sawicki, A. W. Rushforth, R. P. Campion, L. X. Zhao, C. T. Foxon, B. L. Gallagher, Prospects for high temperature ferromagnetism in (Ga, Mn)As semiconductors, Phys. Rev. B 72 (2005) 165204.

[18] M. Bolduc, C. Awo-Affouda, A. Stollenwerk, M. B. Huang, F. G. Ramos, G. Agnello, V. P. LaBella, Above room temperature ferromagnetism in Mn-ion implanted Si, Phys. Rev. B 71 (2005) 033302.

[19] S. Zhou, K. Potzger, G. Zhang, A. Mücklich, F. Eichhorn, N. Schell, R. Grötzschel, B. Schmidt, W. Skorupa, M. Helm, J. Fassbender, D. Geiger, Structural and magnetic properties of Mn-implanted Si, Phys. Rev. B 75 (2007) 085203.

[20] A. Wolska, K. Lawniczak-Jablonska, M. Klepka, M. S. Walczak, A. Misiuk, Local structure around Mn atoms in Si crystals implanted with Mn^+ studied using X-ray absorption spectroscopy techniques, Phys. Rev. B 75 (2007) 113201.

[21] F. M. D'Heurle, Silicide interfaces in silicon technology, J. Electron. Mater. 27 (1998) 1138.

[22] S. P. Murarka, Refractory silicides for integrated circuits, J. Vac. Sci. Technol. 17 (1980) 775.

[23] J. P. Gambino, E. G. Colgan, Silicides and ohmic contacts, Mater. Chem. Phys. 52 (1998) 99.

[24] S.-L. Zhang, M. Östling, Metal silicides in CMOS technology: Past, present, and future trends, Crit. Rev. Solid State Mater. Sci. 28 (2003) 1.

[25] P. Woditsch, W. Koch, Solar grade silicon feedstock supply for PV industry, Sol. Energy Mater. Sol. Cells 72 (2002) 11.

[26] A. A. Istratov, T. Buonassisi, M. D. Pickett, M. Heuer, E. R. Weber, Control of metal impurities in "dirty" multicrystalline silicon for solar cells, Mater. Sci. Eng. B 134 (2006) 282.

[27] S. Pizzini, Bulk solar grade silicon: How chemistry and physics play to get a benevolent microstructured material, Appl. Phys. A 96 (2009) 171.

[28] R. C. Newman, Defects in silicon, Rep. Prog. Phys. 45 (1982) 1163.

[29] X. Yu, P. Wang, X. Li, D. Yang, Thin Czochralski silicon solar cells based on diamond wire sawing technology, Sol. Energy Mater. Sol. Cells 98 (2012) 337.

[30] A. A. Istratov, H. Hieslmair, E. R. Weber, Iron contamination in silicon technology, Appl. Phys. A 70 (2000) 489.

[31] J.-P. Joly, Metallic contamination assessment of silicon wafers, Microelectron. Eng. 40 (1998) 285.

[32] S. J. Pearton, J. W. Corbett, T. S. Shi, Hydrogen in crystalline semiconductors, Appl. Phys. A 43 (1987) 153.

[33] P. Karzel, A. Frey, S. Fritz, G. Hahn, Influence of hydrogen on interstitial iron concentration in multicrystalline silicon during annealing steps, J. Appl. Phys. 113 (2013) 114903.

[34] D. J. Backlund, S. K. Estreicher, Structural, electrical, and vibrational properties of $\mathrm{Ti}-\mathrm{H}$ and $\mathrm{Ni}-\mathrm{H}$ complexes in Si, Phys. Rev. B 82 (2010) 155208.

[35] L. Scheffler, V. Kolkovsky, J. Weber, A re-examination of cobalt-related defects in n- and p-type silicon, Phys. Status Solidi A 209 (2012) 1913.

[36] R. Lüdemann, Hydrogen passivation of multicrystalline silicon solar cells, Mater. Sci. Eng. B 58 (1999) 86.

[37] R. C. Newman, Oxygen diffusion and precipitation in Czochralski silicon, J. Phys. Condens. Matter 12 (2000) 335.

[38] D. Gilles, E. R. Weber, S. Hahn, Mechanism of internal gettering of interstitial impurities in Czochralski-grown silicon, Phys. Rev. Lett. 64 (1990) 196.

[39] V. Raineri, M. Saggio, E. Rimini, Voids in silicon by he implantation: From basic to applications, J. Mater. Res. 15 (2000) 1449.

[40] A. Haarahiltunen, H. Savin, M. Yli-Koski, H. Talvitie, J. Sinkkonen, Modeling phosphorus diffusion gettering of iron in single crystal silicon, J. Appl. Phys. 105 (2009) 023510.

[41] A. Ourmazd, W. Schröter, Phosphorus gettering and intrinsic gettering of nickel in silicon, Appl. Phys. Lett. 45 (1984) 781.

Chapter 2

Complexes in silicon involving transition metals

In this chapter it is described in detail the current understanding about the microscopic behavior of transition metals (TMs) when located in their most stable interstitial position, their diffusion and interaction with point defects (such as vacancy-related defects, electric dopants or light impurities), with line and planar defects, and with volume defects. Clustering and precipitation are also treated, as well as the microscopic mechanisms of gettering. Finally, the microscopic picture of implanted TMs in silicon and the resulting magnetism introduced by them, will be focused on the last two sections.

2.1 Introduction

The intensive research on the microscopic behavior of various TMs in the last six decades has developed a good level of understanding of the basic mechanisms underlying their influence on the performance of silicon-based devices. Nevertheless, there are still questions to be answered and even some quantitative models to be confirmed or to be obtained with more accuracy. In 1999, Istratov *et al.* analyzed the particular case of iron, the most studied 3d TM in Si [1]:

"Iron is one of most ubiquitous and detrimental metal impurities in silicon technology, and has been intensively studied over the past 45 years. Recently, we have undertaken an extensive critical analysis of the current state of understanding of properties of

iron in silicon. This analysis revealed that some of the fundamental properties of iron, such as its diffusivity or interaction with shallow acceptors, which were thought to be fully understood, are actually uncertain or inaccurate. Additionally, a number of other important defect reactions of iron, such as interaction of iron with oxygen, are hardly studied at all. ..."

Fifteen years later the majority of the questions concerning Fe is still under investigation, mainly its microscopic behavior when interacting with vacancy-related defects. These issues become even less understood for other TMs such as Mn, Co and Ni [2].

The physical properties diffusivity and solubility of TMs were first studied in 1956 by J. D. Struthers [3], by making use of the radiotracer impurities ^{59}Fe and ^{64}Cu. Radiotracer methods rely on the detection of radioactive probe atoms in different layers of the sample by measuring the related radioactivity. The model described by the two Ficks laws was found to be in agreement with the obtained data points, in which the diffusion coefficient follows the Arrhenius formula:

$$D = D_0 exp[-E_m/(K_B T)], \tag{2.1}$$

where D_0 is the pre factor and E_m is the activation energy for migration. It was shown that the TMs could, e.g., diffuse some micrometers during 1 hour at temperatures $\gtrsim$ 100°C. This extraordinary discovery led to the conclusion that the microscopic diffusion mechanism would have to incorporate a very fast process. At that time two diffusion mechanisms were generally accepted: the interstitial and substitutional. While in the interstitial mechanism the impurity wanders freely on interstitial sites, in the substitutional mechanism the impurity diffuses through vacant sites. Because each diffusion step in the substitutional mechanism is also influenced by the diffusion of vacancies, one is able to deduce that impurities might be fast diffusers if diffusing interstitially. In addition, in the interstitial mechanism, the impurity can follow several paths, while in the substitutional mechanism the impurity have only one possibility if only one vacancy is present in its neighborhood. The first microscopic model for diffusion of TMs in Si was hence based on the interstitial mechanism. The interstitial sites involved in the mechanism were further investigated. Experimental results were leading to the conclusion that the involved sites of Mn, Fe, Co, Ni and Cu, present tetrahedral symmetry [4], which was further confirmed with first principle studies [5, 6]. One should note that the values concerning the activation energy for diffusion of these 3d TMs are actually smaller that thought before. The observation of higher values was a consequence of the unwanted inclusion of other defects that hampers the diffusion. The diffusivity of Cu and Ni has hence been updated [7, 8].

The data concerning the solubility of 3d TMs, based on electron paramagnetic resonance (EPR) and neutron activation analysis (NAA), were first compiled by E. R. Weber [4]. While NAA relies on the selective detection of radiation produced by activating the species of the material with neutrons, the EPR measurements provide a way to investigate impurities that form paramagnetic point defects. In his review he found with good precision the matching of the solubility, in the temperature range $\sim 800°C$ and $\sim 1200°C$, with the predicted formula:

$$S = S_0 exp(\Delta H/k_B T), \tag{2.2}$$

where S_0 is the solubility at 0 K and ΔH is the relative partial excess enthalpy in the silicon lattice with respect to the most stable silicide phase. His review [4] is still, in a great level of accuracy.

TMs react easily with other defects in silicon due to their fast diffusing nature. What dictates their stable location will be related to the properties of the additional defects. One has hence to know which defects, other than TMs, are present, their abundance and the mechanisms that may lead to pairing. Defects are usually divided into point defects (very simple structures with 0-dimensions), line defects (1-dimensional), planar defects (2-dimensional) and volume defects (3-dimensional) [9]. Examples of defects can be seen in Fig. 2.1. The two most important point defects are the vacancy (absence of one Si host atom) and the self-interstitial (Si atom on interstitial positions). Normally, these point defects are produced at the same time: a Si host atom dissociates from its natural position provoking the appearance of a vacancy and a self-interstitial. This pair is usually known as Frenkel defect. If the self-interstitial, produced by the Frenkel mechanism, is deposited at the surface we have a Schottky defect. In the absence of additional defects, Frenkel defects usually convert into Schottky defects by means of out-diffusion of the self-interstitial. Single vacancies also show some mobility and hence can aggregate. An example is the formation of divacancies, but also the thermal stability of trivacancies, tetravacancies, pentavacancies and hexavacancies has been predicted. If several point defects, such as vacancies and impurities, aggregate into simple structures a complex is formed. If the complex becomes large the defect can be further identified as being extended. While dislocations are the main example for both line and planar defects, volume defects include precipitates and voids.

The charge state of point defects can dramatically change their geometry, and consequently their thermal stability. One example that occurs in crystals is the Jahn-Teller distortion, which shows how both structures, electronic and geometric, are coupled. For point defects, the pairing mechanism can sometimes be dictated by the Coulomb

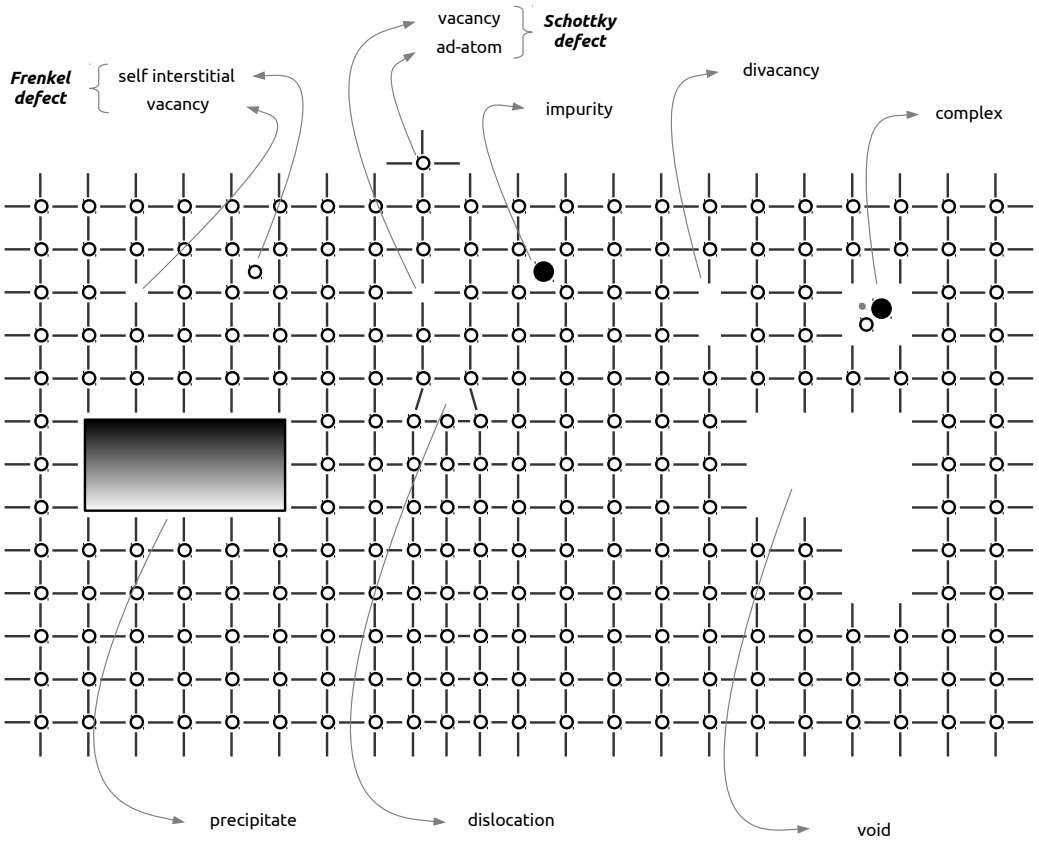

Figure 2.1: Classification of several defects present in a perfect lattice. At the top point defects are represented while at the bottom one line defect (the dislocation) and two volume defects (precipitate and void) are depicted.

attraction of its various components. In these cases, if, e.g., a fast diffuser has the opposite charge of immobile point defects, they will combine easier. Such pairing mechanisms can hence be controlled by changing the charge state of the several single point defects. The electronic doping plays therefore an important role. By doping the semiconductor with donors one will add additional electrons to the conduction band which can, e.g., be trapped by the point defects and hence cause the defect to become negatively charged. From an electronic point of view such point defects are known to have deep acceptor levels in the bandgap. On the contrary, if doping the semiconductor with acceptors, electrons from the valence band will be captured by the acceptors producing holes. These holes can in turn capture electrons from other point defects, making them, e.g., to become positively charged. In this case they are known to present deep donor levels in the bandgap. One can hence know which charge state a

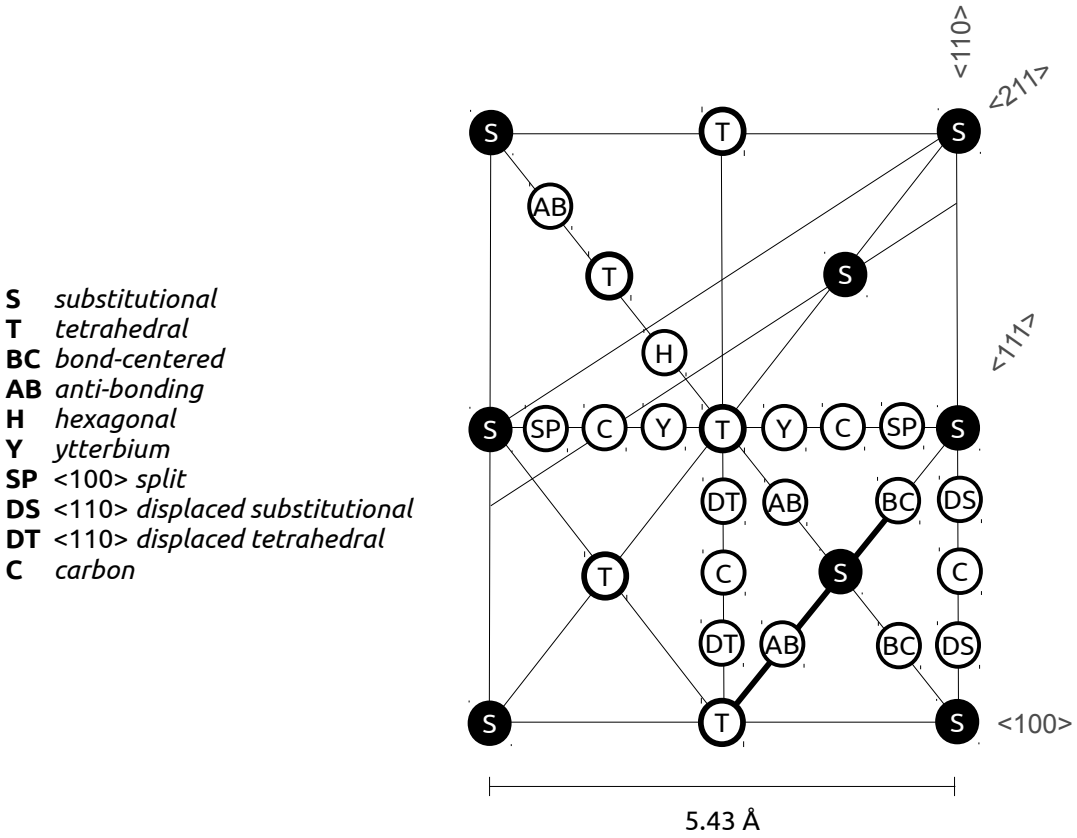

Figure 2.2: High-symmetry sites of the diamond lattice in the {110} plane.

point defect will likely have if knowing where the Fermi level is. Of course that the deep levels of the several point defects have to be known previously. One very effective direct technique that identifies the several deep levels of point defects is deep level transient spectroscopy (DLTS), developed by D. V. Lang and described in Ref. [10]. Another important phenomenon is the increase of thermal stability of a specific point defect by counter doping with another point defect. For instance, because substitutional iron, which we will denote from now on as Fe_S, captures conduction electrons provided mainly by the donor dopants, since it becomes negatively charged in n-type silicon (see Fig. 1.2), its solubility might be increased.

Now we have a brief, but necessary, general information about the type of defects that might pair with TMs. We still nevertheless need to use a nomenclature for the matematical sites of the silicon crystal lattice, which is a diamond-like structure, in order to explore in detail the structure of several TM complexes. In that respect, Fig. 2.2 shows the location of regular lattice sites in a {110} silicon plane.

2.2 Pairing with point defects

This section discusses three of the main groups of point defects which can pair with TMs: vacancy-related defects, electric dopants and light impurities. In all these cases the structural form of the related TM-complexes is discussed based on both experimental and theoretical works from literature. No section is dedicated to self-interstitial (I) defects since the complexes formed by TMs and I have not been investigated intensively as those formed by TMs and the three aforementioned defects. One should, however, note that most of the self-interstitials which are not out-diffused or captured by vacancies, tend to be trapped by substitutional carbon (C_S). For environments rich in implanted transition metals (in concentrations > [C]), I could form a significant number of complexes with TMs. However, the interactions between TMs and I are not as energetic as, e.g., those involving vacancies. For instance, the activation energy for dissociation, calculated from first principles, of Fe_S is $\sim$ 2.92 eV, while that of the Fe_iI pair is $\sim$ 1.7 eV [11]. A different situation occurs when self-interstitials interact with immobile complexes constituted by TMs and, e.g., by immobile impurities or vacancy-related defects. The information of such interactions is, however, scarce.

2.2.1 Vacancy-type defects

The formation of vacancy-related defects may have three origins. First, the quality of the silicon material dictates how perfect and pure the material might be, which ultimately determines the vacancy content: while a bad crystal growth will obviously induce the creation of more single vacancies, some impurities will certainly easier kick-out Si host atoms. Second, Si host atoms can dissociate from their position in the lattice by thermal activation, creating Frenkel defects. Last but not least, the creation of vacancy-related defects can be induced by irradiating the Si material with electrons or by implanting impurities, such as electric dopants. From the three described situations, irradiation and ion implantation are the most effective and controlled ways to introduce single vacancies.

Single vacancies are extremely mobile. In fact, it is the Si host atoms that are actually diffusing. The activation energy for single vacancy migration was first obtained experimentally, with EPR, in 1963 [12]. The obtained value of 0.3 eV is still in good agreement with current experiments.

The high mobility of single vacancies makes them interact easily with other defects,

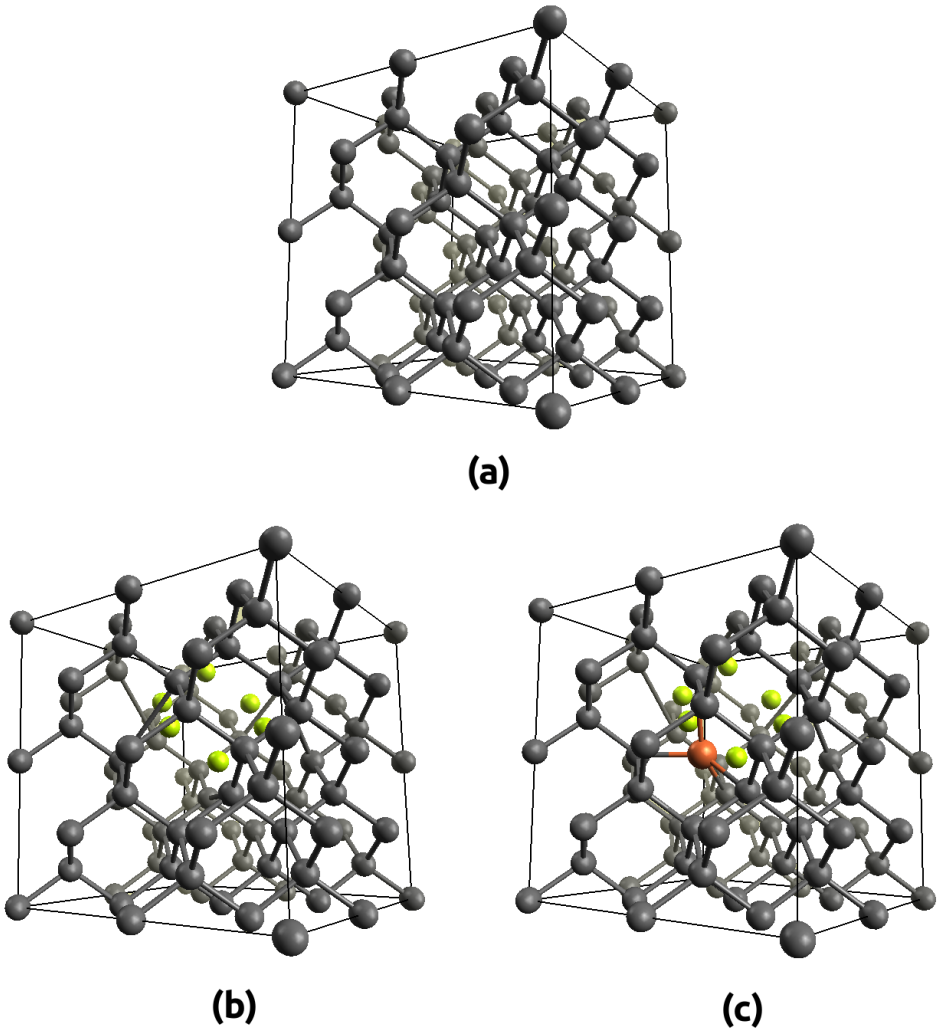

Figure 2.3: Most stable structure of a (a) perfect diamond lattice (b) with a fourfold coordinated hexavacancy, in green, and (c) an extra Si atom or Cu, in orange.

such as with other single vacancies. This interaction may lead to the formation of multivacancies, from which the most well-known is the double vacancy, also known as divacancy. Divacancies were first investigated systematically with EPR in 1965 [12]. The diffusion mechanism, inferred at that time, consisted of two diffusion steps made by each of the two vacancies. This model was in agreement with the obtained experimental activation energy for migration of 1.3 eV. It has recently been inferred a different diffusion mechanism by *ab initio* calculations, in which only one diffusion step takes place, with both vacancies diffusing at the same time [13]. The predicted activation energy for migration was, nevertheless, very similar to the previous model ($\sim$ 1.35 eV). The calculated activation energy for dissociation was 2.05 eV.

As one may expect, more complex multivacancies can arise, however they are less studied experimentally due to their complexity. The scientific community has hence relied on first principle calculations. Estreicher *et al.* has investigated the kinetics of multivacancies that follows the removal of Si host atoms in hexagonal rings (see Fig. 2.3 (a-b)) [14–16]. Note that all Si host atoms are fourfold coordinated. Recently, it has been shown by Makhov *et al.* [17] that additional fourfold coordinated Si atoms can be added inside the hexavacancy ring, resulting into a relative minimum of the total energy. These fourfold coordinated vacancy clusters include the existence of trivacancies, tetravacancies and pentavacancies, as illustrated in Fig. 2.3 (c).

The interaction between TMs and vacancy-related defects was first studied by Ludwig *et al.* with the observation of EPR lines associated to substitutional neutral chromium, and both positively and negatively charged manganese, resulting from the TM trapping into single vacancies (see Fig 2.4 (a)) [18, 19]. Mössbauer spectroscopy (MS) has further confirmed the existence of components where Co and Fe present cubic symmetry [20–26], most likely due to their substitutional forms. The experimental conditions were, however, different as on one hand EPR investigations relied mostly on the contamination of the Si material by diffusion processes, while on the other hand MS studies were based on Si samples where TMs were introduced by ion implantation. One immediately can state that the substitutional fraction found in MS studies might be larger than that found in EPR investigations, which was indeed experimentally observed. Electrical characterization methods, such as DLTS, have also suggested that several observed energy levels were due to the substitutional form of the TMs, e.g. those of Co [27]. So far, all these methods have only allowed to identify the occupied lattice sites indirectly by, e.g., obtaining local information of the point defects. The first work that proved unambiguously the presence of 3d TMs on substitutional sites was based on the emission channeling (EC) technique applied to implanted Cu in Si [28–30]. Afterwards, a similar study found that some of the implanted Fe also occupies substitutional sites [31, 32]. One should, however, note that the fact that substitutional Cu or Fe were observed does not necessarily mean that these sites were related to isolated TMs without involving other point defects in the neighborhood. Nevertheless, it is not likely that such involvement would result in the observation of substitutional sites from three different sample orientations. Additionally, the activation energy for dissociation of Fe was found very close to that obtained from *ab initio* calculations (2.6-3.5 eV compared to the theoretical prediction 2.92 eV [11]). The trapping of TMs by single vacancies is not only confined to the substitutional site. TMs can also occupy lattice sites displaced from the tetrahedral interstitial (T)

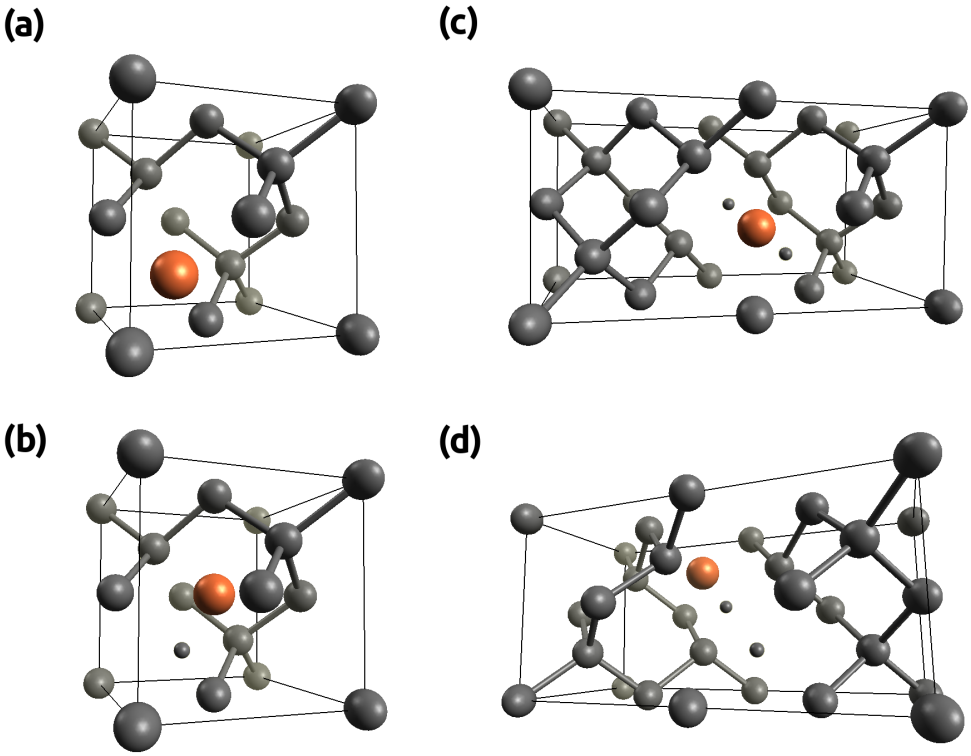

Figure 2.4: Possible positions of transition metals (orange) inside single vacancies and divacancies. In (a) the transition metal occupies an ideal substitutional site after being trapped by a single vacancy. In (b) the single vacancy forms a complex with a transition metal that occupies a site displaced from the ideal tetrahedral interstitial position. (c) depicts a transition metal occupying a site in between two vacant atoms (bond-centered site). Finally, in (d) the transition metal occupies a site displaced from the tetrahedral interstitial site inside a divacancy.

site near the vacancy, as suggested by a theoretical investigation of Estreicher *et al.* [11] (see Fig. 2.4 (b)). This predicted structure was suggested after observing a MS doublet line of ^{57m}Fe [22, 23, 33, 34], and EC displaced T sites from ^{59}Fe [31].

One should finally examine the literature about the interaction between TMs and small clusters of vacancies, still considered point defects. It has been shown from first principle studies that the most stable position of, e.g., Fe inside divacancies is the ideal bond-centered (BC) site (see Fig. 2.4 (c)) [11]. Several deep levels assigned to this iron-divacancy complex have been found [35]. Furthermore, Fe may also present some stability near T sites within divacancies, as illustrated in Fig. 2.4 (d), which could also explain the component and lattice sites from MS and EC studies pointed out in the last paragraph [31, 34]. Multivacancies associated to more than two vacancies

may also play a role. In that respect, the only available information about complexes resulting from the interaction between TMs and fourfold coordinated vacancy clusters comes from theory, in which the predicted most stable position of Cu was found to be a position near the BC site (see Fig. 2.3 (c)) [36]. The results of the Makhov *et al.* work were, however, not yet available at that time. Therefore, trivacancies, tetravacancies and pentavacancies, which may also be very stable, were not investigated theoretically. These structures have never been experimentally identified.

2.2.2 Electric dopants

Electric dopants donate electrons to the conduction band or accept electrons from the valence band of the semiconductor. Therefore, they may be electrically charged on their natural substitutional position. If the TM contaminant diffuses in the semiconductor with a charge state different from neutral it may easily interact with ionized electric dopants through the Coulomb force. For example, the electric dopant boron accepts electrons from the valence band of the semiconductor, becoming negatively charged. If a specific TM gains a positive charge in *p*-type Si, it will be attracted by B^- and, hence, perhaps will be paired to B^-. If a TM becomes negatively charged, both boron and the TM will repel, avoiding the formation of pairs. If a TM is neutral, no Coulomb interaction will occur and the pair, if found, will be driven by another type of interaction. The same analysis can be made for pairs of aluminum with TMs. For the case of *n*-type dopants, e.g. phosphorus and arsenic, a similar approach can be performed but with the opposite charge states.

The most investigated pairs in silicon is FeB [37]. Its influence on the carrier lifetime of minority carriers has, for instance, been used to quantify the Fe content of samples [38, 39]. Iron is known to introduce a deep donor level close to the valence band, being hence most likely positively charged in *p*-type silicon, and therefore might easily interact with B^-. FeB pairs were first suggested by Collins and Carlson in 1957 [40], being then experimentally confirmed by Ludwig and Woodbury in 1962 with EPR measurements [41]. Pairs of Fe with the *p*-type dopant aluminum have also been observed [37]. Most of Mn and Co are also positively charged in *p*-type Si [42–44]. Their related pairs with acceptors have been tentatively ascribed to observed Mössbauer components and DLTS lines [45, 46]. On the contrary, reports of evidence of TM pairing with *n*-type dopants have not been clear, even for TMs which are negatively charged in *n*-type Si, e.g. Co and Mn.

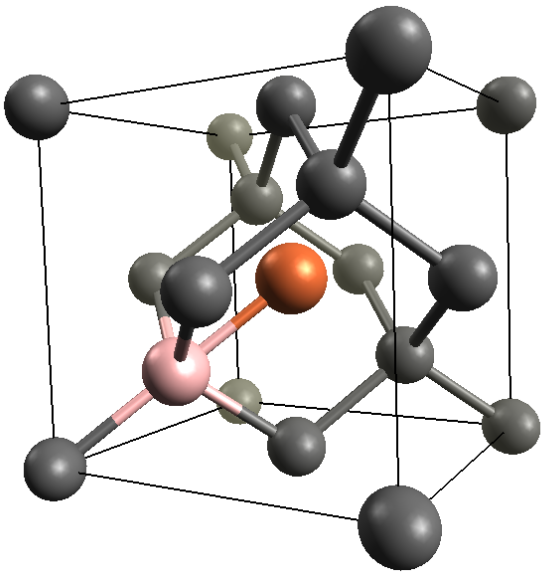

Figure 2.5: Representation of a FeB pair within a silicon unit cell, with Fe in orange and B in pink.

One question that may arise is which position the TM is more stable when establishing the pair with the immobile substitutional acceptor ion. For the case of Fe, it has been shown by EPR [47] and MS [48] that its local environment has a trigonal <111> symmetry, within FeB pairs. This symmetry may correspond to the closest T site of the substitutional B^- (see Fig. 2.5). Density functional theory calculations have also predicted a similar structure with, however, an inwards breathing mode relaxation around the B^- ion [49]. MnB and CoB pairs are likely to have a similar structure.

2.2.3 Light impurities

Several light elements are also frequently encountered as impurities in silicon. Some of them are beneficial while others are harmful [50]. One of the main impurities that can be found in silicon is oxygen. Oxygen is introduced mainly by the silica crucibles used in the Czochralski (CZ) crystal growth method [51]. The content of O in Floating Zone (FZ) silicon is, hence, much less than in CZ silicon, $> 10^{18}$ cm^{-3} for CZ and $\lesssim 10^{16}$ cm^{-3} for FZ silicon [51]. It is currently well established that isolated O sits on slightly puckered BC sites [52]. The mobility of O atoms is low (activation energy for migration of 2.56 eV [52]). In fact, as aforementioned, the precipitation of oxygen, when cooling down from high temperatures, is homogeneous. When creating vacancies in a Si sample, e.g. through ion implantation or electron radiation, the

interstitial oxygen easily traps mobile single vacancies V forming OV pairs, so-called A-centers after its identification in 1961 [53, 54]. The mobility of A-centers is still low, making likely the formation of immobile complexes with TMs. One such example is the formation of Fe_SO_{BC} pairs [11]. It has also been predicted, from *ab initio* calculations, that the trapping of Cu by A-centers produces two distinct point defects: Cu_S and O_i [55, 56]. The unambiguous experimental identification of such interaction mechanisms is, however, still missing.

Carbon is also abundant in silicon mainly due to the use of graphite components during crystal growth [51, 57]. Since C is a group 4 element, like Si, it can easily be incorporated on S sites [58]. It has been shown that when damaging C-rich samples the mobile self-interstitials easily kick-out C_S atoms, generating the fast diffuser interstitial C_i, that occupies a particular lattice site so-called C site (see Fig. 2.2) [59]. C_i interacts easily with other immobile impurities, such as immobile C_S or O_{BC} [60]. What is, nevertheless, less likely is its pairing with other mobile impurities, such as TMs. Estreicher *et al.* have shown that the binding energy of $Fe_i - C_i$ pairs may range only from 0.52 to 0.73 eV [11]. Such pairs are therefore easily dissociated if formed at room temperature. Interactions of TMs with more complicated complexes made of carbon, e.g. C_iO_i, C_iC_S and IC_iO_i [60, 61], have not yet been investigated.

As mentioned in the last chapter, hydrogen may be used to passivate deep levels. It has been seen that the efficiency enhancement provoked by introducing hydrogen is in fact the mixture of two phenomena: the removal of some deep levels and the introduction of others. The identification of complexes that are passivated and those that are activated electrically are still under debate [62–66]. The most stable position of isolated H is the ideal BC site when positively charged, and the ideal T site when in the negative charge state. Neutral H can occupy both positions [67]. In all cases H is a fast diffuser at room temperature (activation energy for migration of ~ 0.3 eV [68]), facilitating its interactions with electrically active complexes. H_iFe_i pairs and related kinetics have been investigated with *ab initio* calculations [49]. The binding energy of the most stable structure of H_iFe_i ranges from 0.4 to 0.82 eV. These energies are relatively low and thus the pairs may dissociate easily. Fe may sit on interstitial sites with hexagonal symmetry while H may sit on T sites. In this case, Fe is not passivated as H_iFe_i introduces one donor and one acceptor levels, in contrast to the presence of only one donor level by interstitial Fe [49, 69–71]. It has also been predicted that Cu might occupy substitutional sites when pairing with H [55]. The pair formation between Ni and H is still ambiguous [65].

The pairing of H with immobile defects is much more likely than with other fast

diffusing impurities [72]. Such more complex structures may in turn interact easier with TMs. Although the investigation of such structures is missing in literature, it is worthwhile to list possible immobile H complexes which may interact with TMs. Single vacancies are an important example where H is captured on BC sites to remove the dangling bond of one of the four neighbor silicon atoms [67, 73–76]. H may also pair with donor dopants, such as As, satisfying the dangling bond of the fifth unpaired electron of As, also on a BC site [67, 77]. The same can be applied to acceptors, such as B, but with H removing the dangling bond of one Si neighbor atom of the acceptor on an anti-bonding (AB) site [67, 77]. Finally, one has to note that the H contamination was also shown to enhance the diffusion of O_i [78]. In that respect, it was concluded that H may form a complex with O_i, again on BC sites, in such a way that the thermal stability of immobile isolated O_i is reduced.

2.3 Planar and line defects

Planar and line defects may occur with external stress, e.g. during crystal growth, or internal stress, e.g. due to the stress provoked by precipitates or extended defects. Line defects include the edge and screw dislocations. While in the first case the defect is raised by an additional or absent row of atoms, in the second case the dislocation is induced by the opposite tendency of changing the direction of the rows, e.g., between two planes, behaving like a screw. The dislocation usually ends at the surface of the semiconductor. If the dislocation only lies inside the semiconductor we have a dislocation loop. Planar defects usually involve elements other than those of the semiconductor (extrinsic defects). However, they can also involve the semiconductor elements, but to a minor extent. Planar defects include stacking faults, twins and grain boundaries. Stacking faults and twins are related to the modification of the stacking sequence. In silicon the stacking sequence of the (111) planes is ...ABCAB... . The missing of one, e.g. C, creates a stacking fault (...ABAB...) while the opposite rearrangement creates a twin (...ABCBA...). Finally, the grain boundary defect includes the frontier between the silicon material with volume defects. Reference [79] covers a more exhaustive analysis of line and planar defects. Finally, one should mention that planar and line defects have also been used as gettering centers, such as to trap Fe into stacking faults [80] or to precipitate Cu or Ni on interfaces of silicon bicrystals [81–86].

2.4 Clustering

Our understanding about the structures and physical properties of TM precipitates has currently reached a high level of accuracy. However, the available information about clustering, i.e. the knowledge of the first steps of precipitation, is still scarce, mainly due to the need of observing the microscopic behavior of TMs in a very small time window or need to immobilize the TMs immediately after the beginning of precipitation. In this section, the information under debate about the formation of TM-dimers, which might be involved in the first stage of clustering, is examined. The most stable silicide precipitates which 3d TMs form, are also described.

2.4.1 Dimers

What we know so far about TM-dimer structures is essentially based on theoretical investigations. Experiments that have claimed to observe physical properties of TM-dimers have been limited. It is nevertheless curious that one of the first substantial work on the subject was experimental: in 1982, Muller *et al.* published results on EPR that included several resonances assigned to Fe-dimers, involving nevertheless the extra point defects single and double vacancies, and the electric dopants B and Al [87]. The list of EPR resonances can be consulted in Ref. [37] and in appendix A. Such assignments were, however, rather speculative. Sanati *et al.* investigated, with *ab initio* calculations, such dimers and predicted the stability of the Fe_TFe_T and Fe_TFe_S dimers [88], yet with the Fe_TFe_S being the most stable dimer.

In 1984 Langouche *et al.* used the MS technique to investigate the local environment of implanted ^{57}Co and discovered a peculiar doublet component in a narrow annealing temperature range [21, 89]. They suggested that such doublet could be due to the formation of Co-dimers. The structure of those dimers was, however, unknown. Fourteen years later an *ab initio* work concluded that the two Co atoms would have to occupy substitutional sites, but one extra self-interstitial would have to participate [90].

Copper is an interesting example where an experimental photoluminescence line (1024 meV) has been assigned to a Cu-dimer by comparing to *ab initio* calculations, in which one Cu atom may occupy an S site while the other a T site [56]. It was, however, predicted that Cu-dimers made of two Cu on T sites with an extra Si atom could also be stable.

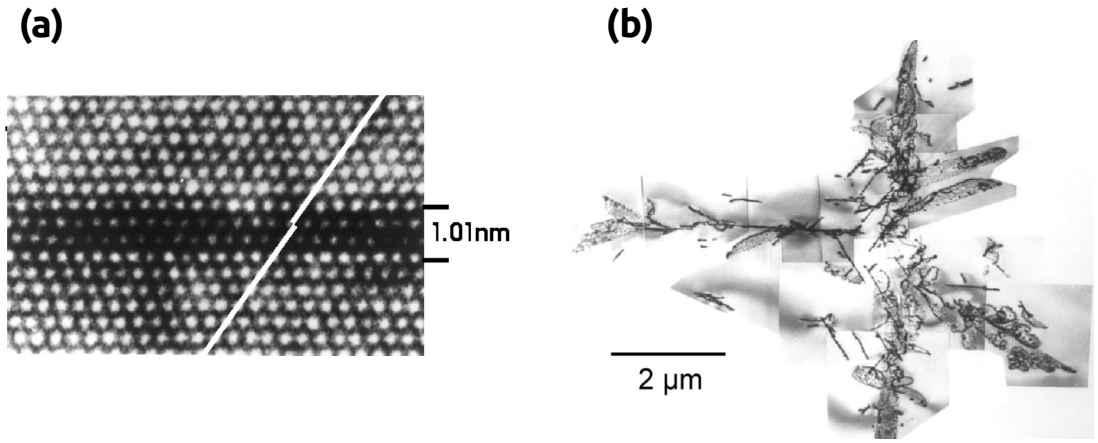

Figure 2.6: Transmission electron microscopy images from a (a) platelet-like precipitate of $NiSi_2$, and from (b) precipitate-dislocation colonies of Cu_3Si [42].

Experimental works on Mn- and Ni-dimers are inexistent. The most stable structure of Mn dimers was, however, predicted by Bernardini *et al.* to be Mn_TMn_S in *n*-type Si and Mn_SMn_S in *p*-type Si [91]. It was shown that both structures might be more energetically favorable than the isolated interstitial Mn. Zhang *et al.* performed similar *ab initio* calculations in intrinsic silicon, but included the study of Fe- and Co-dimers, and their magnetic properties [92]. For the cases of Mn, Fe and Co the most stable structures were Fe_TFe_S, Mn_TMn_S and Co_TCo_S. For Ni the most stable structure was, however, Ni_TNi_T. In both investigations there were no extra defects involved.

2.4.2 Formation of silicide precipitates

Once the activation barrier to nucleation is overcome, e.g. by forming dimers in a defective area, precipitation is followed by the formation of silicides. Silicide precipitates tend to acquire the morphology of the perfect silicide lattice structures, which have been investigated extensively for decades by virtue of their use as electric contacts [93]. For instance, Co silicides have been synthesized in 3 different morphologies: Co_2Si [94], CoSi [95] and $CoSi_2$ [96, 97]. Co_2Si presents a so-called Ni_2In structure, CoSi a cesium chloride structure and $CoSi_2$ a calcium fluoride structure. Only $CoSi_2$ has been seen to precipitate [98]. The lattice mismatch compared to Si of $CoSi_2$ is just $\sim$ -1.2%, resulting in the formation of platelet-like precipitates lying on {111} planes with a diameter ranging from 100 to 600 nm and thickness of approximately 3 nm [98–100]. A similar precipitate is formed by Ni, with a lattice mismatch of $\sim$ -0.46% [98]. The

observed $NiSi_2$ platelet-like precipitates have a diameter ranging from 20 nm to 900 nm (see Fig. 2.6 (a)) [81, 98]. A slightly different case has been observed for Fe. Fe forms $FeSi_2$ silicides, again with the calcium fluoride structure but with a distortion [101]. The lattice mismatch between $FeSi_2$ and Si is, however, much larger ($\sim$-11%) [42], making Fe precipitating usually at Si-silicon oxide interfaces [102]. The case of Cu is different from those described above. The most stable silicide of Cu is Cu_3Si, which is polymorph at room temperature [103]. Its lattice mismatch compared to the Si lattice is $\sim$ 50% [42]. Cu_3Si precipitates in, e.g., platelet-like structures is accompanied by the formation of strain-relieving dislocations, constituting the so-called precipitate-dislocation colonies [104]. Last but not least, Mn precipitates in $MnSi_{1.7}$ compounds [105–108]. $MnSi_{1.7}$ nanoparticles have been observed in Mn-implanted silicon samples [105, 109–111].

2.5 Implantation-induced defects

Ion implantation has been extensively used to dope semiconductors in a controlled manner. The main drawback of this process is the significant creation of defects that usually keep the dopants inactive. Only annealing, that recovers the damage, can sometimes activate the dopants. The general mechanisms of defect formation by implanted TMs is examined in this section.

The defects provoked by ion implantation are induced by the kinetic energy transfer of the incoming ion exceeding the displacement threshold energy of host atoms, which is $\sim$ 36 eV for the case of Si [112, 113]. The so-called primary knock-on atom will in turn kick-out a second knock-on atom and so on, creating a collision cascade. Note that the implanted TM ion will pursue with its kick-out sequence. At the end of the collision cascade the TM ion will be surrounded by defective regions. The profile of the implanted TM can be predicted by Monte Carlo simulations, such as those obtained with the SRIM code [114]. The amount of induced defects will depend on several parameters, such as the mass and energy of implanted ion, the material and its temperature, the flux density of the implanted TM ion and its total implantation fluence.

The most likely defect that an implanted impurity can produce is the Frenkel pair. It has been shown that two regions of defects are induced [115]. One around the peak concentration of the implanted impurity (at R_p from the surface), and another midway between the peak concentration of the implanted impurity and the surface (at

$R_p/2$ from the surface). While the first region is rich in vacancies, the second region is rich in self-interstitials in addition to the implanted impurity. One way to reduce the number of defects is by annealing the sample at temperatures above the activation energy for migration of self-interstitials or vacancy-related defects. This may provoke their reunion. Such annealing may also cause the formation of bigger multivacancies such as the fourfold coordinated vacancy clusters discussed above. A limit case is the formation of voids [116–118]. The annealing of multivacancies and clusters of self-interstitials have extensively been investigated [113, 119] with, e.g., transmission electron microscopy (TEM), Rutherford backscattering spectrometry (RBS), Raman spectroscopy (RS), electron paramagnetic resonance (EPR) and infrared spectroscopy (IS). It has been shown that divacancies anneal at 100-250°C [120]. Clusters of vacancies [121] and self-interstitials [122] have been shown to anneal at 800-1000°C. If, e.g., the implantation fluence is too high, one can provoke so many defects that the sample will end up amorphized in the defective regions [113, 123–126]. As aforementioned, light impurities may interact with implantation-induced defects. For instance, oxygen may form A-centers (OV), while substitutional carbon might be converted to the fast interstitial carbon. Hydrogen can also interact with single or multivacancies by reducing the dangling bonds on BC sites.

2.6 Microscopic description of gettering centers

From the five gettering techniques described in chapter 1, the microscopic mechanisms of the atomic trapping by defects, trapping by electric dopants and P-diffusion gettering, are the less understood, being addressed in detail in this section.

2.6.1 Atomic trapping by defects

Two types of defective gettering centers may arise from implanted impurities, depending on the implantation energy and fluence [42, 127]: while voids are usually produced close to the surface following implanting from tens to hundreds of keV with implantation fluences of $\sim 10^{16}$ cm^{-2}, dislocations plus point defects deep in the sample usually result from high implantation energies (in the order of MeVs) and lower implantation fluences ($\lesssim 10^{16}$ cm^{-2}). The trapping of TMs into defective regions induced by ion implantation usually does not involve secondary phase formation [42]. In the following both types of atomic trapping by defects are described.

Chemisorption: It has been observed that TMs tend to bond with the Si host atoms present in the surface of voids, at R_p [116, 128–133]. These sinks of voids are usually formed after annealing the implanted sample at temperatures between 700°C and 1200°C [134, 135]. The size of the induced voids is approximately 10 nm in diameter. Chemisorption has been observed for the 3d TMs Fe [130, 136], Co [136], Ni [129, 137, 138] and Cu [116, 128–132, 136]. The binding mechanism of TMs with the Si atoms from the void surface is still under debate. Deweerd *et al.* observed the existence of two Mössbauer quadrupole doublets from ^{57}Co, which they linked to chemisorption [139]. Azevedo *et al.* performed an extended X-ray absorption fine structure (EXAFS) investigation on Cu that suggested the existence of two types of Cu bonds, Cu-Si and Cu-Cu [140]. They suggested that these two types of Cu bonds may result from similar structures as those responsible for the two different Mössbauer components of ^{57}Co.

Binding to dislocations and point (or extended) defects: The trapping of TMs in Si samples implanted with MeV H or He ions has been observed to occur in both "R_p" and "$R_p/2$" regions [115]. While in the former region the involvement of dislocations is currently well accepted, the origin of gettering centers at $R_p/2$ has been a topic of controversy. It is well established that they might be vacancy-related, however, while some works have concluded that small vacancy clusters are originated at $R_p/2$ [133, 141–145], others claim to have observed nanocavities [146–148]. One should finally note that it has been seen that the presence of oxygen in significant quantity hampers the trapping of Fe, Ni and Cu in the "$R_p/2$" defects [42].

2.6.2 Interaction with electric dopants

The microscopic behavior of TMs when pairing with electric dopants has been investigated by exploring the kinetics of their formation, through the Coulomb attraction. Here, the model currently accepted is exposed and exemplified for FeB pairs, in which the most stable structure has been described in section 2.2.2. [37, 42, 149, 150]. The rms width of diffusion d of an interstitial Fe during time τ in the absence of traps is given by [151]

$$d = [6D\tau]^{1/2}, \tag{2.3}$$

where D is the microscopic diffusion coefficient, that can be obtained from Eq. 2.1. If B^- is present, some of the Fe^+ atoms will pair with B^-. The quantity of the paired

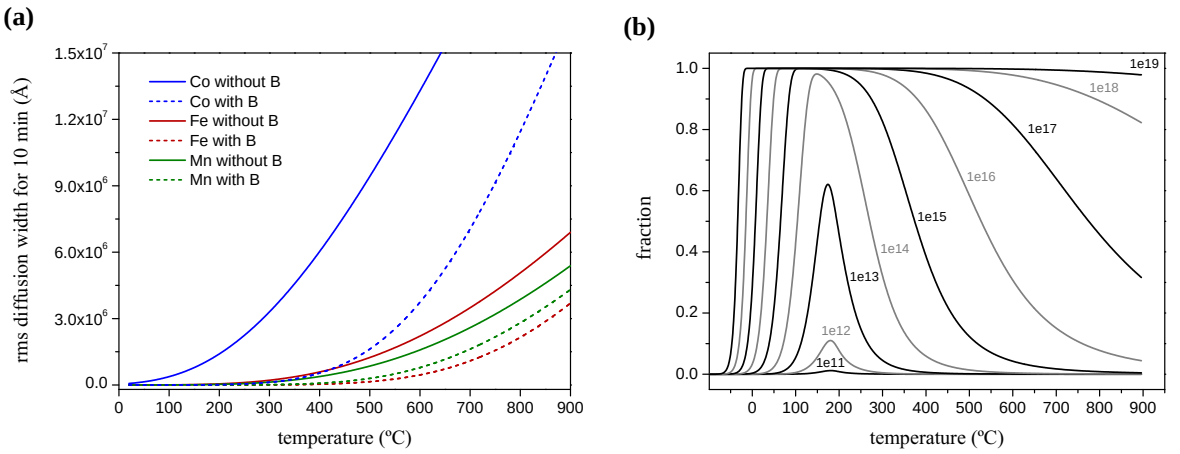

Figure 2.7: (a) rms diffusion width of interstitial Fe, Mn and Co in Si for 10 min with and without the presence of 5×10^{19} cm^{-3} boron. (b) Fraction of Fe paired with boron, according to the model described in the text. $1 \times 10^{11} - 1 \times 10^{19}$ stand for different boron concentrations, in cm^{-3}.

Fe can be obtained from [149]

$$\frac{[\mathrm{FeB}]}{[\mathrm{Fe}^+][\mathrm{B}^-]} = \frac{Z}{N} exp(E_b/(k_B T)), \tag{2.4}$$

where N is the density of interstitial sites in Si (5×10^{22} cm^{-3}), Z is the number of pair configurations (4 if Fe sits on T sites and B on substitutional sites), E_b is the electrostatic pair binding energy and [B$^-$] is the concentration of ionized B$^-$. For simplicity we will consider [B$^-$]=[B], even though for high concentrations of B, the concentration of ionized B becomes smaller. From this equation one can deduce the following result for the fraction of isolated interstitial Fe:

$$f_i = \frac{[\mathrm{Fe}^+]}{[\mathrm{Fe}^+] + [\mathrm{FeB}]} = \frac{1}{1 + [\mathrm{B}^-]\frac{Z}{N} exp(E_b/(k_B T))}. \tag{2.5}$$

The rms width of diffusion for Fe$^+$ in a system that includes B$^-$ can now be obtained by $d = [6 f_i D \tau]^{1/2}$. Figure 2.7 (a) shows that the presence of B does not stop the diffusion of Fe but slows it down. The same applies, e.g., to Co and Mn.

The fraction f_i obtained above assumes that the system is already in equilibrium. To compare to experimental works involving annealing, one has hence to use a dynamic equation. But before, it is necessary to know the rate of Fe$^+$ capture by B$^-$, and related breakup rate. The capture rate is given by (Ham's law, see Refs. [37, 151]):

$$\nu = 4\pi R [\mathrm{B}^-] D, \tag{2.6}$$

where R is the capture radius. To obtain this radius one can assume that R is as large as several nm, so that the Coulomb attraction can be used. Fe^+ is considered to be captured when the electrostatic attraction potential energy $U(r)$ between Fe^+ and B^- exceeds the average thermal energy, k_BT [37]. Considering

$$U(r) = \frac{e^2}{4\pi\epsilon_0\epsilon r} exp(-r/\lambda_D), \tag{2.7}$$

where $\lambda_D = \sqrt{\frac{\epsilon\epsilon_0 k_B T}{e^2 p}}$ and p is the concentration of holes, one obtains

$$k_BT = \frac{e^2}{4\pi\epsilon_0\epsilon R} exp(-R/\lambda_D). \tag{2.8}$$

For simplicity one can neglect the exponential factor for $p \lesssim 10^{17}$ cm^{-3}, which finally gives

$$R = \frac{e^2}{4\pi\epsilon_0\epsilon k_B T}. \tag{2.9}$$

At room temperature R is hence $\sim$ 47 Å, but if considering the exponential factor, when the above condition for p cannot be satisfied, the value of R can range from 5 to 50 Å. The breakup rate is simply given by [37]

$$\Lambda = \nu_0 exp(-E_d/(k_BT)), \tag{2.10}$$

where ν_0 is the attempt frequency and E_d is the activation energy for dissociation $E_d = E_m + E_b$ (E_b is the binding energy and E_m is the activation energy for migration). The dynamic equation to obtain f_i as a function of time is [151]

$$\frac{d\mathrm{N_i}}{dt}(t) = -(4\pi RD[\mathrm{B^-}])\mathrm{N_i}(t) + \Lambda \mathrm{P}(t), \tag{2.11}$$

where $\mathrm{N_i}$(t) is the time evolution of the isolated interstitial Fe concentration and $\mathrm{P}(t)$ is the time evolution of the FeB pair concentration. Since

$$[\mathrm{Fe}] = \mathrm{N_i}(t) + \mathrm{P}(t) \tag{2.12}$$

we have finally

$$\frac{d\mathrm{N_i}}{dt} = -(4\pi R[\mathrm{B^-}]D + \Lambda)\mathrm{N_i}(t) + \Lambda[\mathrm{Fe}]. \tag{2.13}$$

By using the Euler method to solve first order differential equations and by using t=10 min, which will be useful in the interpretation of the involvement of FeB pairs in this work, we can finally obtain the curves of f_i as a function of temperature, shown in Fig. 2.7 (b) for the case of Fe. The same approach can be used for other positively charged TMs in p-type Si:B, e.g., Mn and Co.

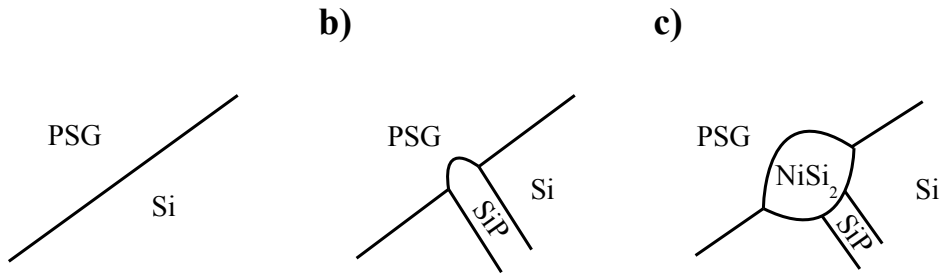

Figure 2.8: Model currently accepted for P-diffusion gettering of Ni [152]. The process starts with the diffusion of P from a phosphorus-silicate glass (PSG) to the Si material (a). SiP precipitates are formed (b), leaving free self-interstitials to react with Ni, forming finally the respective silicide (c).

This model states that TM-electric dopant pairs can be easily reformed after annealing. This is in fact observed experimentally for the case of the FeB pairs. It has been seen that Fe paired with B can be dissociated in low doped p-type samples (with [B] around 10^{15} cm^{-3}) by annealing up to 200°C, and reformed again when cooling down back to room temperature [37, 102]. Annealing above 200°C causes the dissociated interstitial Fe to be trapped in more effective traps, such as surface defects or dislocations. The maximum annealing temperature for which Fe can reform FeB pairs is, however, increased with the doping level of the silicon material.

2.6.3 P-diffusion gettering

The microscopic understanding of P-diffusion gettering of substitutional metal impurities is nowadays well established. However, for the TM impurities that diffuse interstitially, such as those of the 3d series, the microscopic models are very scarce [153]. In the following two paragraphs, it is described the current understanding of P-diffusion gettering of substitutional metal impurities and the model tried so far to explain the microscopic mechanism of P-diffusion gettering of interstitial 3d TMs.

When P diffuses into Si, the concentration of self-interstitials I may increase due to the preference of substitutional sites by P [154]: self-interstitials tend usually to form mobile P-I pairs near the surface, dissociating easier in the bulk than near the surface. The high concentration [I] in the bulk will hence tend to kick-out the TMs that have a substantial substitutional fraction, e.g. Au, Pt and Zn. Because near the surface the

kick-out rate may be smaller, the TM will tend to segregate in the opposite direction of P-I pair diffusion.

The aforementioned mechanism cannot explain the gettering effect of P-diffusion on 3d TMs, observed for Fe [155–158], Co [159, 160], Ni [152] and Cu [155], in which their isolated form is interstitial. It was hence suggested another mechanism by considering the involvement of SiP precipitates (see Fig. 2.8 (a-b)) [152]. Because SiP has a higher volume than Si, self-interstitials are injected near the SiP volume and further react with TM atoms, forming silicides (Fig. 2.8 (c)). It was recently suggested that the generation of oxygen precipitates, promoted by vacancies produced during Pdiffusion, might also behave as gettering centers [153].

2.7 Ferromagnetism of implanted silicon samples

This section analyzes in more detail the current understanding about the origin of ferromagnetism found after implanting 3d TM impurities in silicon, namely in Mn-doped Si systems for the reasons pointed out in chapter 1.

The first experimental investigation about the magnetism of implanted Mn was performed by Bolduc *et al.* in 2005 [161]. They found that the silicon system, implanted with $\sim 10^{16}$ cm^{-2} Mn at 300 keV and 350 °C, was modified in such a way that the material was ferromagnetic up to 400°C. Their work was very promising at that time, however, they did not confirm whether secondary phases could contribute to the observed magnetism. Based on superconducting quantum interference device (SQUID) measurements and secondary ion mass spectroscopy (SIMS), the same authors published a new work on the influence of annealing on the ferromagnetism of implanted Mn [162, 163], observing that the saturation magnetization was reducing while the Mn concentration at $R_p/2$ was decreasing. This information led to the conclusion that the ferromagnetism was rising in a very defective region (plenty of vacancies). Complex structures, such as vacancy clusters or even already silicides, could be responsible for the observed ferromagnetism. The authors hence started to question the effective contribution of the dilute Mn for the ferromagnetism, however excluding $MnSi_{1.7}$ precipitates arguing that such silicide would be paramagnetic at room temperature [164, 165]. Meanwhile, Zhou *et al.* attributed the observed ferromagnetism to nanoparticles of $MnSi_{1.7}$ precipitates in the vacancy-rich "$R_p/2$" region, by making use of high resolution structural characterization techniques such as X-ray diffraction [105, 109]. Other experimental investigations have shared this interpretation [166],

being in particular confirmed by *ab initio* calculations the influence of stoichiometry, strain, accumulated charge and interface between $MnSi_{1.7}$ and Si on the magnetic properties of $MnSi_{1.7}$ nanoparticles [111]. Investigations based on EXAFS and X-ray absorption near edge structure (XANES) also tried to observe $MnSi_{1.7}$ nanoparticles, but without success [167]. One has to note that in this case the used implantation energy was 160 keV, which could have played a role in preventing the formation of $MnSi_{1.7}$ nanoparticles [167]. However, more recently it has been observed Mn inclusions of several nm when implanting Mn at 160 keV [168–170]. In summary, the investigation of the geometrical structures that implanted Mn forms, at fluences of $\sim 10^{16}$ cm^{-2}, seems to be well established. Whether $MnSi_{1.7}$ nanoparticles or extended defects formed by Mn are responsible, partially or totally, for the observed ferromagnetism is, however, still under debate.

Investigations on the magnetism of other dilute TMs in silicon have been scarce. Banduru *et al.* also claimed to have observed ferromagnetism of Co-implanted silicon samples at room temperature. Whether second phases are involved is still unknown [171]. The ferromagnetism of Fe has been recently addressed by Yilgin *et al.* [172]. They observed Fe oxides near the surface which they suggested to be responsible for the observed ferromagnetism. The magnetism of implanted Cu and Ni has not been addressed so far.

2.8 Preferred lattice sites of implanted Cu, Fe and Ag

One way to explore the complexes formed by implanted TMs with defects, either produced during ion implantation or already present in the silicon material, is by investigating their lattice sites. For the case of low concentrations of impurities, only the emission channeling (EC) technique has been used for this purpose. This technique will be addressed in detail in the next chapter. For now only the results achieved so far will be focused. Only the 3d TMs ^{67}Cu [28–30, 32] and ^{59}Fe [31, 32], and the 4d TM ^{111}Ag [173] have been investigated. In all cases the implantation was performed at room temperature at 60 keV. The fluence ranged between 10^{12} and 10^{14} cm^{-2}. ^{59}Fe and ^{111}Ag were only investigated in low doped Si (0.03-10^4 Ωcm), while ^{67}Cu was also investigated in highly doped n^+- and p^+-type Si (0.001-1.3$10^3$ Ωcm).

^{67}Cu was found on ideal S sites and sites displaced from S sites towards bond-centered

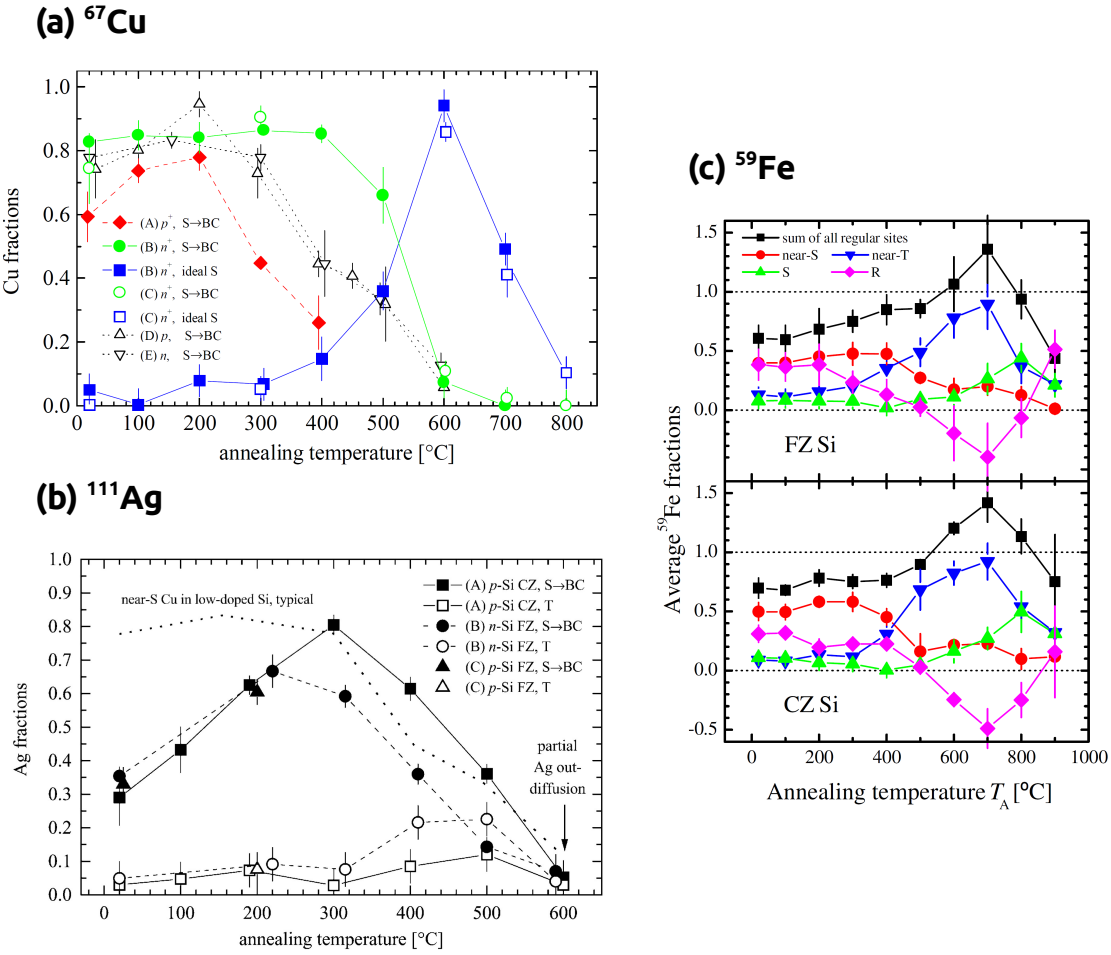

Figure 2.9: Fraction of the several emission channeling lattice sites as a function of annealing temperature for (a) ^{67}Cu [29], (b) ^{111}Ag [173] and (c) ^{59}Fe in CZ and FZ Si [32].

sites (near-S sites) [28–30, 32]. While the ideal S sites were assigned to the substitutional form of ^{67}Cu, the observed near-S sites were associated to multivacancies. The structure of the complexes involving near-S ^{67}Cu could not, however, be inferred. The near-S fraction prevailed up to annealing temperatures T_A around 500°C, while ideal S sites were only found in highly doped n^+-type Si between T_A = 500°C and T_A = 800°C (see Fig. 2.9 (a)). The thermal stability of near-S sites increased with the doping from p^+ to n^+.

^{111}Ag was observed on near-S sites and sites near the ideal tetrahedral interstitial site (near-T sites) [173]. Near-T sites were also suggested to be due to complexes

involving multivacancies, but with a different structure compared to those related to near-S sites. Again, the structure could not be inferred. While near-S sites started to be annealed already at 400°C, the near-T fraction increased after annealing 400°C and disappeared for $T_A = 600$°C, with the long-range diffusion of ^{111}Ag (see Fig. 2.9 (b)).

^{59}Fe was incorporated on all the three types of sites found for ^{67}Cu and ^{111}Ag: ideal S, near-S and near-T sites [31, 32]. While near-S sites prevailed up to the annealing temperature of 400°C, near-T sites were preferred following annealing between 500°C and 700°C (see Fig. 2.9 (c)). Ideal S sites dominated, along with near-T sites, between the annealing temperatures of 800°C and 900°C. This picture did not change from CZ to FZ silicon. Oxygen may hence not be involved on the complexes where Fe occupies the three identified lattice sites. Moreover, it was seen that the use of different fluences, from 10^{12} to 10^{14} cm^{-2}, ended up on the observation of the same lattice sites of ^{59}Fe. Clustering was therefore ruled out. One interesting observation was the increase of the sum of the three regular fractions to values above 100%, which will be discussed in detail in chapter 4.

Finally, one should mention that the investigation of all the three TMs in lightly doped silicon was performed for both doping types, n and p. The similar results between the two doping types might have been due to the high concentration of produced defects during implantation, which may have shifted the Fermi level to the midgap of the silicon bandgap.

Bibliography

[1] A. A. Istratov, H. Hieslmair, E. R. Weber, What do we know about iron in silicon after 45 yr of research, Physica B 273 (1999) 412.

[2] E. R. Weber, Understanding defects in semiconductors as key to advancing device technology, Physica B 340 (2003) 1.

[3] J. D. Struthers, Solubility and diffusivity of gold, iron, and copper in silicon, J. Appl. Phys. 27 (1956) 1560.

[4] E. R. Weber, Transition metals in silicon, Appl. Phys. A 30 (1983) 1.

[5] G. G. Deleo, G. D. Watkins, W. B. Fowler, Theory of interstitial transition-metal impurities in silicon, Phys. Rev. B 23 (1981) 1851.

[6] G. G. Deleo, G. D. Watkins, W. B. Fowler, Level positions of interstitial transition-metal impurities in silicon, Phys. Rev. B 25 (1982) 4972.

[7] J. Lindroos, D. P. Fenning, D. J. Backlund, E. Verlage, A. Gorgulla, S. K. Estreicher, H. Savin, T. Buonassisi, Nickel: A very fast diffuser in silicon, J. Appl. Phys. 113 (2013) 204906.

[8] A. A. Istratov, C. Flink, H. Hieslmair, E. R. Weber, T. Heiser, Intrinsic diffusion coefficient of interstitial copper in silicon, Phys. Rev. Lett. 81 (1998) 1243.

[9] P. M. Fahey, P. B. Griffin, J. D. Plummer, Point defects and dopant diffusion in silicon, Rev. Mod. Phys. 61 (1989) 289.

[10] D. V. Lang, Deep-level transient spectroscopy: A new method to characterize traps in semiconductors, J. Appl. Phys. 45 (1974) 3023.

[11] S. K. Estreicher, M. Sanati, N. G. Szwacki, Iron in silicon: Interactions with radiation defects, carbon, and oxygen, Phys. Rev. B 77 (2008) 125214.

[12] G. D. Watkins, J. W. Corbett, Defects in irradiated silicon: Electron paramagnetic resonance of the divacancy, Phys. Rev. 138 (1965) 543.

[13] G. S. Hwang, W. A. Goddard, Diffusion and dissociation of neutral divacancies in crystalline silicon, Phys. Rev. B 65 (2002) 2332051.

[14] S. K. Estreicher, J. L. Hastings, P. A. Fedders, The ring-hexavacany in silicon: A stable and inactive defect, Appl. Phys. Lett. 70 (1997) 432.

[15] J. L. Hastings, S. K. Estreicher, P. A. Fedders, Vacancy aggregates in silicon, Phys. Rev. B 56 (1997) 10215.

[16] T. M. E. Staab, A. Sieck, M. Haugk, M. J. Puska, T. Frauenheim, H. S. Leipner, Stability of large vacancy clusters in silicon, Phys. Rev. B 65 (2002) 1152101.

[17] D. V. Makhov, L. J. Lewis, Stable fourfold configurations for small vacancy clusters in silicon from *ab initio* calculations, Phys. Rev. Lett. 92 (2004) 255504.

[18] H. H. Woodbury, G. W. Ludwig, Spin resonance of transition metals in silicon, Phys. Rev. 117 (1960) 102.

[19] G. W. Ludwig, H. H. Woodbury, Electronic structure of transition metal ions in a tetrahedral lattice, Phys. Rev. Lett. 5 (1960) 98.

[20] G. Langouche, M. D. Potter, Identification of substitutional and interstitial Co implanted in Si, Nucl. Instrum. Methods Phys. Res. B 19 (1987) 322.

[21] G. Langouche, M. D. Potter, I. Dézsi, M. F. Wu, A. Vantomme, Mössbauer spectroscopy study of the thermal annealing behavior of very low and very high dose Co-implanted Si, Nucl. Instrum. Methods Phys. Res. B 37 (1989) 438.

[22] G. Weyer, H. P. Gunnlaugsson, M. Dietrich, M. Fanciulli, K. Bharuth-Ram, R. Sielemann, Creation and annealing of defect structures in silicon-based semiconductors during and after implantations at 77-500 K, Nucl. Instrum. Methods Phys. Res. B 206 (2003) 90.

[23] G. Weyer, Defects in semiconductors - results from Mössbauer spectroscopy, Hyperfine Interact. 177 (2007) 1.

[24] G. Weyer, A. Burchard, M. Fanciulli, V. N. Fedoseyev, H. P. Gunnlaugsson, V. I. Mishin, R. Sielemann, The electronic configuration of substitutional Fe in silicon, Physica B 273 (1999) 363.

[25] H. P. Gunnlaugsson, M. Dietrich, M. Fanciulli, K. Bharuth-Ram, R. Sielemann, G. Weyer, Detection of substitutional and interstitial Fe in silicon by Mössbauer spectrocopy, Phys. Scr. 101 (2002) 82.

[26] H. P. Gunnlaugsson, M. Fanciulli, M. Dietrich, K. Bharuth-Ram, R. Sielemann, G. Weyer, I. Collaboration, ^{57}Fe Mössbauer study of radiation damage in ion-implanted Si, SiGe and SiSn, Nucl. Instrum. Methods Phys. Res. B 186 (2002) 55.

[27] L. Scheffler, V. Kolkovsky, J. Weber, Isolated substitutional cobalt and Co-related complexes in silicon, J. Appl. Phys. 113 (2013) 183714.

[28] U. Wahl, J. G. Correia, A. Vantomme, G. Langouche, Lattice location of implanted Cu in Si, Physica B 273 (1999) 367.

[29] U. Wahl, A. Vantomme, G. Langouche, J. P. Araújo, L. Peralta, J. G. Correia, Lattice location of implanted Cu in highly doped Si, Appl. Phys. Lett. 77 (2000) 2142.

[30] U. Wahl, A. Vantomme, G. Langouche, J. G. Correia, Lattice location and stability of ion implanted Cu in Si, Phys. Rev. Lett. 84 (2000) 1495.

[31] U. Wahl, J. G. Correia, E. Rita, J. P. Araújo, J. C. Soares, Lattice sites of implanted Fe in Si, Phys. Rev. B 72 (2005) 1.

[32] U. Wahl, J. G. Correia, E. Rita, J. P. Araújo, J. C. Soares, Fe and Cu in Si: Lattice sites and trapping at implantation-related defects, Nucl. Instrum. Methods Phys. Res. B 253 (2006) 167.

[33] H. P. Gunnlaugsson, M. Dietrich, M. Fanciulli, K. Bharuth-Ram, R. Sielemann, G. Weyer, Detection of diffusional jumps of interstitial Fe in silicon by Mössbauer spectroscopy, Physica B 308 (2001) 418.

[34] H. P. Gunnlaugsson, G. Weyer, N. E. Christensen, M. Dietrich, M. Fanciulli, K. Bharuth-Ram, R. Sielemann, A. Svane, On the kinetics of the formation of interstitial Fe-vacancy pairs in silicon at high temperatures, Physica B 340 (2003) 532.

[35] C. K. Tang, L. Vines, V. P. Markevich, B. G. Svensson, E. V. Monakhov, Divacancy-iron complexes in silicon, J. Appl. Phys. 113 (2013) 044503.

[36] S. K. Estreicher, Rich chemistry of copper in crystalline silicon, Phys. Rev. B 60 (1999) 5375.

[37] A. A. Istratov, H. Hieslmair, E. R. Weber, Iron and its complexes in silicon, Appl. Phys. A 69 (1999) 13.

[38] G. Zoth, W. Bergholz, A fast, preparation-free method to detect iron in silicon, J. Appl. Phys. 67 (1990) 6764.

[39] L. J. Geerligs, D. Macdonald, Dynamics of light-induced FeB pair dissociation in crystalline silicon, Appl. Phys. Lett. 85 (2004) 5227.

[40] C. B. Collins, R. O. Carlson, Properties of silicon doped with iron or copper, Phys. Rev. 108 (1957) 1409.

[41] G. W. Ludwig, H. H. Woodbury, Electron spin resonance in semiconductors, Solid State Phys. 13 (1962) 223.

[42] S. M. Myers, M. Seibt, W. Schröter, Mechanisms of transition-metal gettering in silicon, J. Appl. Phys. 88 (2000) 3795.

[43] D. Gilles, W. Schröter, W. Bergholz, Impact of the electronic structure on the solubility and diffusion of 3d transition elements in silicon, Phys. Rev. B 41 (1990) 5770.

[44] H. Lemke, K. Irmscher, Proof of interstitial cobalt defects in silicon float zone crystals doped during crystal growth, ECS Trans. 3 (2006) 299.

[45] A.-M. V. Bavel, M. Bennebroek, D. Neerinck, G. Langouche, Mössbauer search for Co-acceptor pairs in Si, Nucl. Instrum. Methods Phys. Res. B 76 (1993) 434.

[46] T. Roth, P. Rosenits, S. Diez, S. W. Glunz, D. MacDonald, S. Beljakowa, G. Pensl, Electronic properties and dopant pairing behavior of manganese in boron-doped silicon, J. Appl. Phys. 102 (2007) 103716.

[47] W. Gehlhoff, K. Irmscher, EPR identification of the different charge states of the iron-acceptor pairs in silicon, Solid State Phen. 32 (1993) 219.

[48] H. P. Gunnlaugsson, K. Bharuth-Ram, M. Dietrich, M. Fanciulli, H. O. U. Fynbo, G. Weyer, Formation of $Fe_i - B$ pairs in silicon at high temperatures, Hyperfine Interact. 169 (2006) 1315.

[49] M. Sanati, N. G. Szwacki, S. K. Estreicher, Interstitial Fe in Si and its interactions with hydrogen and shallow dopants, Phys. Rev. B 76 (2007) 125204.

[50] R. C. Newman, Light impurities and their interactions in silicon, Mater. Sci. Eng. B 36 (1996) 1.

[51] R. C. Newman, Defects in silicon, Rep. Prog. Phys. 45 (1982) 1163.

[52] J. W. Corbett, R. S. McDonald, G. D. Watkins, The configuration and diffusion of isolated oxygen in silicon and germanium, J. Phys. Chem. Solids 25 (1964) 873.

[53] G. D. Watkins, J. W. Corbett, Defects in irradiated silicon. i. electron spin resonance of the Si − A center, Phys. Rev. 121 (1961) 1001.

[54] J. W. Corbett, G. D. Watkins, R. M. Chrenko, R. S. McDonald, Defects in irradiated silicon. ii. infrared absorption of the Si − A center, Phys. Rev. 121 (1961) 1015.

[55] D. West, S. K. Estreicher, S. Knack, J. Weber, Copper interactions with H, O, and the self-interstitial in silicon, Phys. Rev. B 68 (2003) 352101.

[56] S. K. Estreicher, First-principles theory of copper in silicon, Mater. Sci. Semicond. Process 7 (2004) 101.

[57] S. Pizzini, Towards solar grade silicon: Challenges and benefits for low cost photovoltaics, Sol. Energy Mater. Sol. Cells 94 (2010) 1528.

[58] G. D. Watkins, K. L. Brower, EPR observation of the isolated interstitial carbon atom in silicon, Phys. Rev. Lett. 36 (1976) 1329.

[59] L. W. Song, X. D. Zhan, B. W. Benson, G. D. Watkins, Bistable interstitial-carbon substitutional-carbon pair in silicon, Phys. Rev. B 42 (1990) 5765.

[60] D. J. Backlund, S. K. Estreicher, C4 defect and its precursors in Si: First-principles theory, Phys. Rev. B 77 (2008) 205205.

[61] A. Docaj, S. K. Estreicher, Three carbon pairs in Si, Physica B 407 (2012) 2981.

[62] B. L. Sopori, X. Deng, J. P. Benner, A. Rohatgi, P. Sana, S. K. Estreicher, Y. K. Park, M. A. Roberson, Hydrogen in silicon: A discussion of diffusion and passivation mechanisms, Sol. Energy Mater. Sol. Cells 41 (1996) 159.

[63] P. Karzel, A. Frey, S. Fritz, G. Hahn, Influence of hydrogen on interstitial iron concentration in multicrystalline silicon during annealing steps, J. Appl. Phys. 113 (2013) 114903.

[64] P. Santos, J. Coutinho, V. J. B. Torres, Rayson, P. R. Briddon, Hydrogen passivation of titanium impurities in silicon: Effect of doping conditions, Appl. Phys. Lett. 105 (2014) 032108.

[65] D. J. Backlund, S. K. Estreicher, Structural, electrical, and vibrational properties of Ti − H and Ni − H complexes in Si, Phys. Rev. B 82 (2010) 155208.

[66] L. Scheffler, V. Kolkovsky, J. Weber, A re-examination of cobalt-related defects in n- and p-type silicon, Phys. Status Solidi A 209 (2012) 1913.

[67] S. K. Estreicher, Hydrogen-related defects in crystalline semiconductors: A theorist's perspective, Mater. Sci. Eng. R 14 (1995) 319.

[68] J. W. Corbett, S. N. Sahu, T. S. Shi, L. C. Snyder, Atomic and molecular hydrogen in the Si lattice, Phys. Lett. A 93 (1983) 303.

[69] T. Sadoh, K. Tsukamoto, A. Baba, D. Bai, A. Kenjo, T. Tsurushima, H. Mori, H. Nakashima, Deep level of iron-hydrogen complex in silicon, J. Appl. Phys. 82 (1997) 3828.

[70] N. G. Szwacki, S. K. Estreicher, First-principles investigations of $\mathrm{Fe}-\mathrm{H}$ interactions in silicon, Physica B 401 (2007) 171.

[71] N. G. Szwacki, M. Sanati, S. K. Estreicher, Two FeH pairs in n-type Si and their implications: A theoretical study, Phys. Rev. B 78 (2008) 113202.

[72] S. M. Myers, M. I. Baskes, H. K. Birnbaum, J. W. Corbett, G. G. DeLeo, S. K. Estreicher, E. E. Haller, P. Jena, N. M. Johnson, R. Kirchheim, S. J. Pearton, M. J. Stavola, Hydrogen interactions with defects in crystalline solids, Rev. Mod. Phys. 64 (1992) 559.

[73] S. J. Pearton, J. W. Corbett, T. S. Shi, Hydrogen in crystalline semiconductors, Appl. Phys. A 43 (1987) 153.

[74] S. K. Estreicher, J. L. Hastings, P. A. Feeders, Hydrogen-defect interactions in Si, Mater. Sci. Eng. B 58 (1999) 31.

[75] S. K. Estreicher, A. Docaj, M. B. Bebek, D. J. Backlund, M. Stavola, Hydrogen in C-rich Si and the diffusion of vacancy-H complexes, Phys. Status Solidi A 209 (2012) 1872.

[76] M. A. Roberson, S. K. Estreicher, Vacancy and vacancy-hydrogen complexes in silicon, Phys. Rev. B 49 (1994) 17040.

[77] S. K. Estreicher, L. Throckmorton, D. S. Marynick, Hydrogen passivation of shallow acceptors and donors in C-Si: Comparisons and trends, Phys. Rev. B 39 (1989) 13241.

[78] S. K. Estreicher, Interstitial O in Si and its interactions with H, Phys. Rev. B 41 (1990) 9886.

[79] F. Shimura, Semiconductor silicon crystal technology, Academic press limited, 1989.

[80] B. Shen, X. Y. Zhang, K. Yang, P. Chen, R. Zhang, Y. Shi, Y. D. Zheng, T. Sekiguchi, K. Sumino, Gettering of Fe impurities by bulk stacking faults in Czochralski-grown silicon, Appl. Phys. Lett. 70 (1997) 1876.

[81] M. Seibt, W. Schröter, Precipitation behaviour of nickel in silicon, Philos. Mag. A 59 (1989) 337.

[82] A. Ihlal, R. Rizk, O. B. M. H. Duparc, Correlation between the gettering efficiencies and the energies of interfaces in silicon bicrystals, J. Appl. Phys. 80 (1996) 2665.

[83] M. Seibt, H. Hedemann, A. A. Istratov, F. Riedel, A. Sattler, W. Schröter, Structural and electrical properties of metal suicide precipitates in silicon, Phys. Status Solidi A 171 (1999) 301.

[84] M. Seibt, V. Kveder, W. Schrter, O. Vob, Structural and electrical properties of metal impurities at dislocations in silicon, Phys. Status Solidi A 202 (2005) 911.

[85] T. Buonassisi, A. A. Istratov, M. D. Pickett, M. A. Marcus, T. F. Ciszek, E. R. Weber, Metal precipitation at grain boundaries in silicon: Dependence on grain boundary character and dislocation decoration, Appl. Phys. Lett. 89 (2006) 042102.

[86] K. Hoummada, D. Mangelinck, B. Gault, M. Cabié, Nickel segregation on dislocation loops in implanted silicon, Scripta Mater. 64 (2011) 378.

[87] S. H. Muller, G. M. Tuynman, E. G. Sieverts, C. A. J. Ammerlaan, Electron paramagnetic resonance on iron-related centers in silicon, Phys. Rev. B 25 (1982) 25.

[88] M. Sanati, S. K. Estreicher, First-principles study of iron and iron pairs in Si, Physica B 401 (2007) 105.

[89] G. Langouche, M. D. Potter, D. Schroyen, Observation of Co-dimer formation during thermal annealing of Co-implanted Si, Phys. Rev. Lett. 53 (1984) 1364.

[90] A.-M. V. Bavel, G. Langouche, H. Overhof, The atomic structure of Co dimers in silicon, Semicond. Sci. Technol. 13 (1998) 108.

[91] F. Bernardini, S. Picozzi, A. Continenza, Energetic stability and magnetic properties of Mn dimers in silicon, Appl. Phys. Lett. 84 (2004) 2289.

[92] Z. Z. Zhang, B. Partoens, K. Chang, F. M. Peeters, First-principles study of transition metal impurities in Si, Phys. Rev. B 77 (2008) 155201.

[93] S.-L. Zhang, M. stling, Metal silicides in cmos technology: Past, present, and future trends, Crit. Rev. Solid State Mater. Sci. 28 (2003) 1.

[94] S. Geller, V. M. Wolontis, The crystal structure of Co_2Si, Acta Cryst. 8 (1955) 83.

[95] D. Walter, I. W. Karyasa, Synthesis and characterization of cobalt monosilicide (CoSi) with CsCl structure stabilized by a β-SiC matrix, Z. Anorg. Allg. Chem. 631 (2005) 1285.

[96] I. Dézsi, H. Engelmann, U. Gonser, G. Langouche, Cobalt-silicide structures studied by Mössbauer spectroscopy, Hyperfine Interact. 33 (1987) 161.

[97] M. Falke, U. Falke, A. Bleloch, S. Teichert, G. Beddies, H.-J. Hinneberg, Real structure of the $CoSi_2$ Si (001) interface studied by dedicated aberration-corrected scanning transmission electron microscopy, Appl. Phys. Lett. 86 (2005) 1.

[98] A. A. Istratov, E. R. Weber, Electrical properties and recombination activity of copper, nickel and cobalt in silicon, Appl. Phys. A 66 (1998) 123.

[99] M. Seibt, K. Graff, Characterization of haze-forming precipitates in silicon, J. Appl. Phys. 63 (1988) 4444.

[100] D. P. Adams, S. M. Yalisov, D. J. Eaglesham, Interfacial and surface energetics of $CoSi_2$, J. Appl. Phys. 76 (1994) 5190.

[101] S. J. Clark, H. M. Al-Allak, S. Brand, R. A. Abram, Structure and electronic properties of $FeSi_2$, Phys. Rev. B 58 (1998) 10389.

[102] A. A. Istratov, H. Hieslmair, E. R. Weber, Iron contamination in silicon technology, Appl. Phys. A 70 (2000) 489.

[103] J. K. Solberg, The crystal structure of η-Cu_3Si precipitates in silicon, Acta Cryst. A 34 (1978) 684.

[104] M. Seibt, M. Griess, A. A. Istratov, H. Hedemann, A. Sattler, W. Schröter, Formation and properties of copper silicide precipitates in silicon, Phys. Status Solidi A 166 (1998) 171.

[105] S. Zhou, K. Potzger, G. Zhang, A. Mücklich, F. Eichhorn, N. Schell, R. Grötzschel, B. Schmidt, W. Skorupa, M. Helm, J. Fassbender, D. Geiger, Structural and magnetic properties of Mn-implanted Si, Phys. Rev. B 75 (2007) 085203.

[106] H. W. Knott, M. H. Mueller, L. Hearton, The crystal structure of $Mn_{15}Si_{26}$, Acta Cryst. 23 (1967) 549.

[107] Z.-Q. Zou, W.-C. Li, J.-M. Liang, D. Wang, Self-organized growth of higher manganese silicide nanowires on Si(1 1 1), (1 1 0) and (0 0 1) surfaces, Acta Mater. 59 (2011) 7473.

[108] D. Wang, Z.-Q. Zou, Formation of manganese silicide nanowires on Si(111) surfaces by the reactive epitaxy method, Nanotechnology 20 (2009) 275607.

[109] S. Zhou, A. Shalimov, K. Potzger, M. Helm, J. Fassbender, H. Schmidt, $MnSi_{1.7}$ nanoparticles embedded in Si: Superparamagnetism with collective behavior, Phys. Rev. B 80 (2009) 174423.

[110] V. Ko, K. L. Teo, T. Liew, T. C. Chong, M. MacKenzie, I. MacLaren, J. N. Chapman, Origins of ferromagnetism in transition-metal doped Si, J. Appl. Phys. 104 (2008) 033912.

[111] S. Yabuuchi, H. Kageshima, Y. Ono, M. Nagase, A. Fujiwara, E. Ohta, Origin of ferromagnetism of $MnSi_{1.7}$si1.7 nanoparticles in Si: First-principles calculations, Phys. Rev. B 78 (2008) 045307.

[112] E. Holmström, A. Kuronen, K. Nordlund, Threshold defect production in silicon determined by density functional theory molecular dynamics simulations, Phys. Rev. B 78 (2008) 045202.

[113] L. Pelaz, L. A. Marqués, J. Barbolla, Ion-beam-induced amorphization and recrystallization in silicon, J. Appl. Phys. 96 (2004) 5947.

[114] J. F. Ziegler, Srim-2003, Nucl. Instrum. Methods Phys. Res. B 219 (2004) 1027.

[115] R. A. Brown, O. Kononchuk, G. A. Rozgonyi, S. Koveshnikov, A. P. Knights, P. Simpson, F. Gonzlez, Impurity gettering to secondary defects created by MeV ion implantation in silicon, J. Appl. Phys. 84 (1998) 2459.

[116] V. Raineri, P. G. Fallica, G. Percolla, A. Battaglia, M. Barbagallo, S. U. Campisano, Gettering of metals by voids in silicon, J. Appl. Phys. 78 (1995) 3727.

[117] V. Raineri, M. Saggio, E. Rimini, Voids in silicon by He implantation: From basic to applications, J. Mater. Res. 15 (2000) 1449.

[118] A. H. M. Smets, W. M. M. Kessels, M. C. M. V. de Sanden, Vacancies and voids in hydrogenated amorphous silicon, Appl. Phys. Lett. 82 (2003) 1547.

[119] G. Hobler, G. Otto, Status and open problems in modeling of as-implanted damage in silicon, Mater. Sci. Semicond. Process. 6 (2003) 1.

[120] H. J. Stein, F. L. Vook, J. A. Borders, Direct evidence of divacancy formation in silicon by ion implantation, Appl. Phys. Lett. 14 (1969) 328.

[121] A. P. Knights, F. Malik, P. G. Coleman, The equivalence of vacancy-type damage in ion-implanted Si seen by positron annihilation spectroscopy, Appl. Phys. Lett. 75 (1999) 466.

[122] N. E. B. Cowern, G. Mannino, P. A. Stolk, F. Roozeboom, H. G. A. Huizing, J. G. M. V. Berkum, F. Cristiano, A. Claverie, M. Jaraz, Energetics of self-interstitial clusters in Si, Phys. Rev. Lett. 82 (1999) 4460.

[123] L. Pelaz, L. A. Marqués, M. Aboy, J. Barbolla, G. H. Gilmer, Atomistic modeling of amorphization and recrystallization in silicon, Appl. Phys. Lett. 82 (2003) 2038.

[124] L. A. Marqués, L. Pelaz, M. Aboy, L. Enrquez, J. Barbolla, Microscopic description of the irradiation-induced amorphization in silicon, Phys. Rev. Lett. 91 (2003) 1355041.

[125] K. R. C. Mok, M. Jaraiz, I. Martin-Bragado, J. E. Rubio, P. Castrillo, R. Pinacho, J. Barbolla, M. P. Srinivasan, Ion-beam amorphization of semiconductors: A physical model based on the amorphous pocket population, J. Appl. Phys. 98 (2005) 046104.

[126] K. R. C. Mok, F. Benistant, M. Jaraiz, J. E. Rubio, P. Castrillo, R. Pinacho, M. P. Srinivasan, Comprehensive model of damage accumulation in silicon, J. Appl. Phys. 103 (2008) 014911.

[127] G. F. Cerofolini, F. Corni, S. Frabboni, C. Nobili, G. Ottaviani, R. Tonini, Hydrogen and helium bubbles in silicon, Mater. Sci. Eng. R 27 (2000) 1.

[128] A. Kinomura, Y. Horino, Y. Nakano, J. S. Williams, Gettering of copper to hydrogen-induced cavities in multicrystalline silicon, J. Appl. Phys. 98 (2005) 066102.

[129] S. M. Myers, D. M. Follstaedt, D. M. Bishop, Binding of copper and nickel to cavities in silicon formed by helium ion implantation, Mater. Res. Soc. Symp. Proc. 316 (1994) 33.

[130] M. H. F. Overwijk, J. Politiek, R. C. M. de Kruif, P. C. Zalm, Proximity gettering of transition metals in silicon by ion implantation, Nucl. Instrum. Methods Phys. Res. B 96 (1995) 257.

[131] S. A. McHugo, E. R. Weber, S. M. Myers, G. A. Petersen, Competitive gettering of copper in Czochralski silicon by implantation-induced cavities and internal gettering sites, Appl. Phys. Lett. 69 (1996) 3060.

[132] S. M. Myers, D. M. Follstaedt, Interaction of copper with cavities in silicon, J. Appl. Phys. 79 (1996) 1337.

[133] G. A. Rozgonyi, J. M. Glasko, K. L. Beaman, S. V. Koveshnikov, Gettering issues using MeV ion implantation, Mater. Sci. Eng. B 72 (2000) 87.

[134] S. Ruffell, P. J. Simpson, A. P. Knights, The effect of the annealing ramp rate on the formation of voids in silicon, J. Phys. Condens. Matter 19 (2007) 466202.

[135] S. Frabboni, F. Corni, C. Nobili, R. Tonini, G. Ottaviani, Nanovoid formation in helium-implanted single-crystal silicon studied by *in situ* techniques, Phys. Rev. B 69 (2004) 165209.

[136] S. M. Myers, G. A. Petersen, C. H. Seager, Binding of cobalt and iron to cavities in silicon, J. Appl. Phys. 80 (1996) 3717.

[137] B. Mohadjeri, J. S. Williams, J. Wong-Leung, Gettering of nickel to cavities in silicon introduced by hydrogen implantation, Appl. Phys. Lett. (1995) 1889.

[138] M. Zhang, X. Zeng, P. K. Chu, R. Scholz, C. Lin, Nickel precipitation at nanocavities in separation by implantation of oxygen, J. Vac. Sci. Technol. A 18 (2000) 2249.

[139] W. Deweerd, T. Barancira, S. Bukshpan, S. Demuynck, G. Langouche, K. Milants, R. Moons, J. Verheyden, H. Pattyn, Mössbauer study of the proximity gettering of cobalt atoms to He-induced nanosized voids in C-si, Phys. Rev. B 53 (1996) 16637.

[140] G. D. M. Azevedo, M. C. Ridgway, J. Betlehem, K. M. Yu, C. J. Glover, G. J. Foran, EXAFS measurements of metal-decorated nanocavities in Si, Nucl. Instrum. Methods Phys. Res. B 199 (2003) 179.

[141] S. V. Koveshnikov, G. A. Rozgonyi, Mechanism of iron gettering in MeV Si ion implanted epitaxial silicon, J. Appl. Phys. 84 (1998) 3078.

[142] M. Tamura, T. Ando, K. Ohyu, MeV-ion-induced damage in Si and its annealing, Nucl. Instrum. Methods Phys. Res. B 59 (1991) 572.

[143] J. S. Williams, M. J. Conway, B. C. Williams, J. Wong-Leung, Direct observation of voids in the vacancy excess region of ion bombarded silicon, Appl. Phys. Lett. 78 (2001) 2867.

[144] R. Krause-Rehberg, F. Brner, F. Redmann, Impurity gettering by vacancy-type defects in high-energy ion-implanted silicon at $R_p/2$, Appl. Phys. Lett. 77 (2000) 3932.

[145] R. Krause-Rehberg, F. Brner, F. Redmann, J. Gebauer, R. Kögler, R. Kliemann, W. Skorupa, W. Egger, G. Kgel, W. Triftshuser, Identification of getter defects in high-energy self-implanted silicon at $R_p/2$, Physica B 308 (2001) 442.

[146] A. Peeva, P. F. P. Fichtner, D. L. D. Silva, M. Behar, R. Kögler, W. Skorupa, Gettering of copper in silicon at half of the projected ion range induced by helium implantation, J. Appl. Phys. 91 (2002) 69.

[147] A. Peeva, R. Kögler, W. Skorupa, Visualization of vacancy type defects in the $R_p/2$ region of ion implanted and annealed silicon, Nucl. Instrum. Methods Phys. Res. B 206 (2003) 71.

[148] A. Peeva, R. Kögler, W. Skorupa, J. S. Christensen, A. Y. Kuznetsov, Spatial distribution of cavities in silicon formed by ion implantation generated excess vacancies, J. Appl. Phys. 95 (2004) 4738.

[149] L. C. Kimerling, J. L. Benton, Electronically controlled reactions of interstitial iron in silicon, Physica B+C 116 (1983) 297.

[150] P. A. Stolk, J. L. Benton, D. J. Eaglesham, D. C. Jacobson, J.-H. Cheng, J. M. Poate, S. M. Myers, T. E. Haynes, The mechanism of iron gettering in boron-doped silicon, Appl. Phys. Lett. 68 (1996) 51.

[151] U. Wahl, Emission channeling studies of Li in semiconductors, Phys. Rep. 280 (1997) 145.

[152] A. Ourmazd, W. Schröter, Phosphorus gettering and intrinsic gettering of nickel in silicon, Appl. Phys. Lett. 45 (1984) 781.

[153] M. Syre, S. Karazhanov, B. R. Olaisen, A. Holt, B. G. Svensson, Evaluation of possible mechanisms behind p gettering of iron, J. Appl. Phys. 110 (2011) 024912.

[154] E. Spiecker, M. Seibt, W. Schröter, Phosphorous-diffusion gettering in the presence of a nonequilibrium concentration of silicon interstitials: A quantitative model, Phys. Rev. B 55 (1997) 9577.

[155] A. Bentzen, A. Holt, R. Kopecek, G. Stokkan, J. S. Christensen, B. G. Svensson, Gettering of transition metal impurities during phosphorus emitter diffusion in multicrystalline silicon solar cell processing, J. Appl. Phys. 99 (2006) 093509.

[156] H. Talvitie, V. Vhnissi, A. Haarahiltunen, M. Yli-Koski, H. Savin, Phosphorus and boron diffusion gettering of iron in monocrystalline silicon, J. Appl. Phys. 109 (2011) 093505.

[157] D. P. Fenning, A. S. Zuschlag, M. I. Bertoni, B. Lai, G. Hahn, T. Buonassisi, Improved iron gettering of contaminated multicrystalline silicon by high-temperature phosphorus diffusion, J. Appl. Phys. 113 (2013) 214504.

[158] S. P. Phang, D. MacDonald, Direct comparison of boron, phosphorus, and aluminum gettering of iron in crystalline silicon, J. Appl. Phys. 109 (2011) 073521.

[159] W. Schröter, R. Khnapfel, Model describing phosphorus diffusion gettering of transition elements in silicon, Appl. Phys. Lett. 56 (1990) 2207.

[160] A. G. Shaikh, W. Schröter, W. Bergholz, Mechanism of phosphorus diffusion gettering of cobalt in silicon studied by Mössbauer spectroscopy, J. Appl. Phys. 58 (1985) 2519.

[161] M. Bolduc, C. Awo-Affouda, A. Stollenwerk, M. B. Huang, F. G. Ramos, G. Agnello, V. P. LaBella, Above room temperature ferromagnetism in Mn-ion implanted Si, Phys. Rev. B 71 (2005) 033302.

[162] M. Bolduc, C. Awo-Affouda, F. Ramos, V. P. LaBella, Annealing temperature effects on the structure of ferromagnetic Mn-implanted Si, J. Vac. Sci. Technol. A 24 (2006) 1648.

[163] M. Bolduc, C. Awo-Affouda, A. Stollenwerk, M. B. Huang, F. Ramos, V. P. Labella, Investigation of the structural properties of ferromagnetic Mn-implanted Si, Nucl. Instrum. Methods Phys. Res. B 242 (2006) 367.

[164] C. Awo-Affouda, M. Bolduc, M. B. Huang, F. Ramos, K. A. Dunn, B. Thiel, G. Agnello, V. P. LaBella, Observation of crystallite formation in ferromagnetic Mn-implanted Si, J. Vac. Sci. Technol. A 24 (2006) 1644.

[165] C. Awo-Affouda, M. Bolduc, V. P. Labella, Implantation damage study in ferromagnetic Mn-implanted Si, J. Vac. Sci. Technol. A 25 (2007) 976.

[166] A. F. Orlov, A. B. Granovsky, L. A. Balagurov, I. V. Kulemanov, Y. N. Parkhomenko, N. S. Perov, E. A. Gan'Shina, V. T. Bublik, K. D. Shcherbachev, A. V. Kartavykh, V. I. Vdovin, A. Sapelkin, V. V. Saraikin, Y. A. Agafonov, V. I. Zinenko, A. Rogalev, A. Smekhova, Structure, electrical and magnetic properties, and the origin of the room temperature ferromagnetism in Mn-implanted Si, J. Exp. Theor. Phys. 109 (2009) 602.

[167] A. Wolska, K. Lawniczak-Jablonska, M. Klepka, M. S. Walczak, A. Misiuk, Local structure around Mn atoms in Si crystals implanted with Mn^+ studied using X-ray absorption spectroscopy techniques, Phys. Rev. B 75 (2007) 113201.

[168] P. Romanowski, J. Bak-Misiuk, K. Sobczak, P. Dziawa, E. Dynowska, A. Szczepanska, A. A. Misiuk, Mn_4Si_7 nanoinclusions in Mn-implanted Si, Radiat. Phys. Chem. 93 (2013) 67.

[169] A. Wolska, K. Lawniczak-Jablonska, S. Kret, P. Duzewski, A. Szczepaska, M. Klepka, M. S. Walczak, Y. Lefrais, M. J. Htch, A. Misiuk, Atomic order in magnetic Mn inclusions in Si crystals: XAS and TEM studies, J. Non-Cryst. Solids 354 (2008) 4189.

[170] A. F. Orlov, V. T. Bublik, V. I. Vdovin, Y. A. Agafonov, L. A. Balagurov, V. I. Zinenko, I. V. Kulemanov, K. D. Shcherbachev, On the state of Mn impurity implanted in Si, Crystallogr. Rep. 54 (2009) 555.

[171] P. R. Bandaru, J. Park, J. S. Lee, Y. J. Tang, L.-H. Chen, S. Jin, A. B. Song, J. R. O'Brien, Enhanced room temperature ferromagnetism in Co- and Mn-ion-implanted silicon, Appl. Phys. Lett. 89 (2006) 112502.

[172] R. Yilgin, M. K. Yurtisigi, A. Parabas, M. Turksoy, M. Ozdemir, B. Aktas, A. Kolitsch, Ferromagnetic behavior of Fe^{+} implanted Si(100) semiconductor, J. Supercond. Nov. Magn. 25 (2012) 2731.

[173] U. Wahl, J. G. Correia, A. Vantomme, Lattice location of implanted Ag in Si, Nucl. Instrum. Methods. Phys. Res. B 190 (2002) 543.

Chapter 3

Emission channeling

This chapter describes the experimental technique emission channeling, outlining first the principle of the technique for the particular case of Si single crystals, as well as the way the desired radioactive probes are introduced. The several elements of the experimental setup are then listed. Finally, the data analysis is described in 3 subsections: the *manybeam* simulation process used to model the obtained two-dimensional experimental electron yield patterns, the respective fitting procedure and the background corrections.

3.1 Principle

Looking at possible orientations of a single crystal, it is straightforward that the respective projection shows a highly open structure if the line of sight is aligned with a crystal axis, or a crystal plane, and a densely packed structure if seen from orientations well off major crystallographic directions [1]. This simple fact has considerable consequences to the motion of charged particles that move under small angles with respect to major crystallographic directions. The steering of charged particles under these conditions is known as channeling. The opposite effect is known as blocking [2]. If the charge of steering particles is positive the channeling effect is promoted along the open structure (away from positively charged nuclei). The steering of negatively charged particles occurs along rows of nuclei. Because channeling effects are highly sensitive to the atomic arrangement of crystals, they can be used in order to extract information about the lattice. Depending on the source of charged particles, channeling techniques can be categorized into (a) channeling effects of beams entering single crystals and (b)

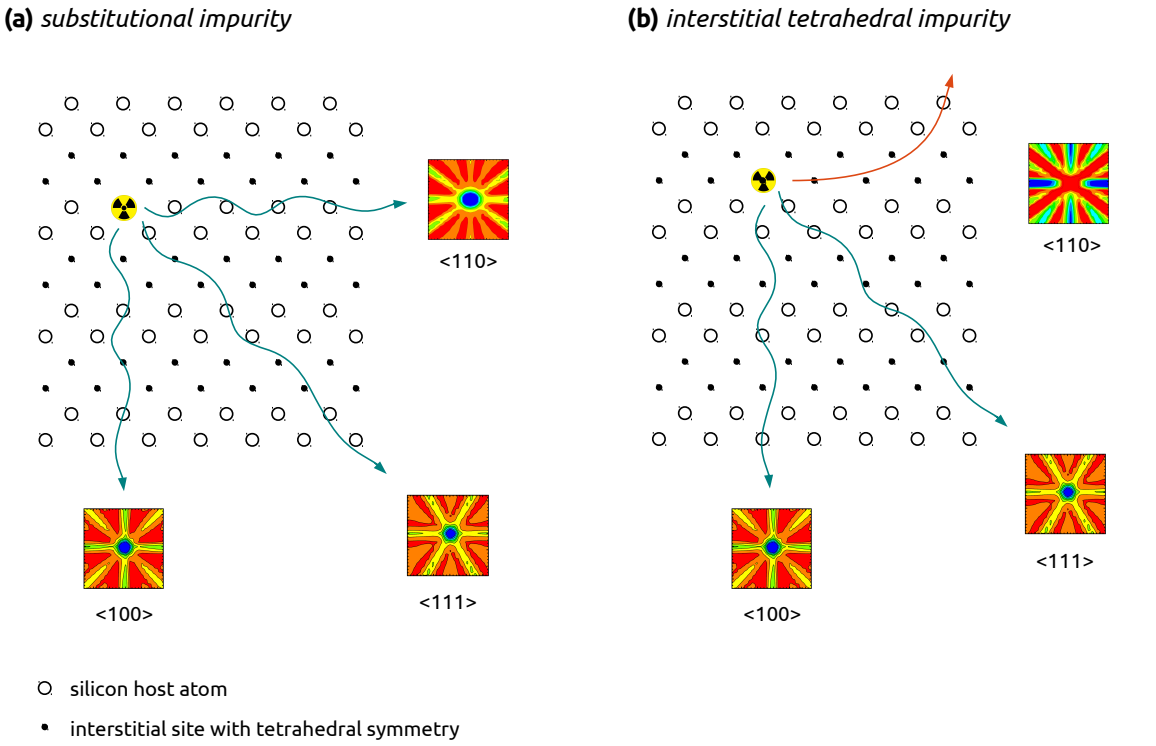

Figure 3.1: Channeling and blocking of e^- emitted from an impurity located on (a) a substitutional and (b) an interstitial tetrahedral site, along <111>, <100> and <110>. The figure illustrates the {110} plane of the Si lattice. Blue corresponds to higher electron yields.

channeling effects where the source of charged particles lies inside the crystal, by means of implanted radioactive probe isotopes. The techniques of (a) are also known as ion beam channeling (IBC) while those of (b) are known as emission channeling (EC) techniques [3]. The analysis of angle yields of these two types of channeling techniques have been shown to be equivalent. In fact, the transition probabilities for direct (charged particle coming from the outside of the crystal) and reversed processes are equal. This equivalence, known as rule of reversibility, was concluded by Lindhard on his first theoretical study on channeling effects [4].

One important feature of channeling techniques is their ability to investigate defects and impurities in single crystals [3, 5–7]. The presence of impurities in crystals can, in fact, impose restrictions to channeling depending on the abundance and location of impurities: in IBC techniques the yield of measured backscattered particles is changed depending on the location of the impurity, while in EC the implanted impurity is itself the source of emitted charged particles; EC has hence four orders of magnitude

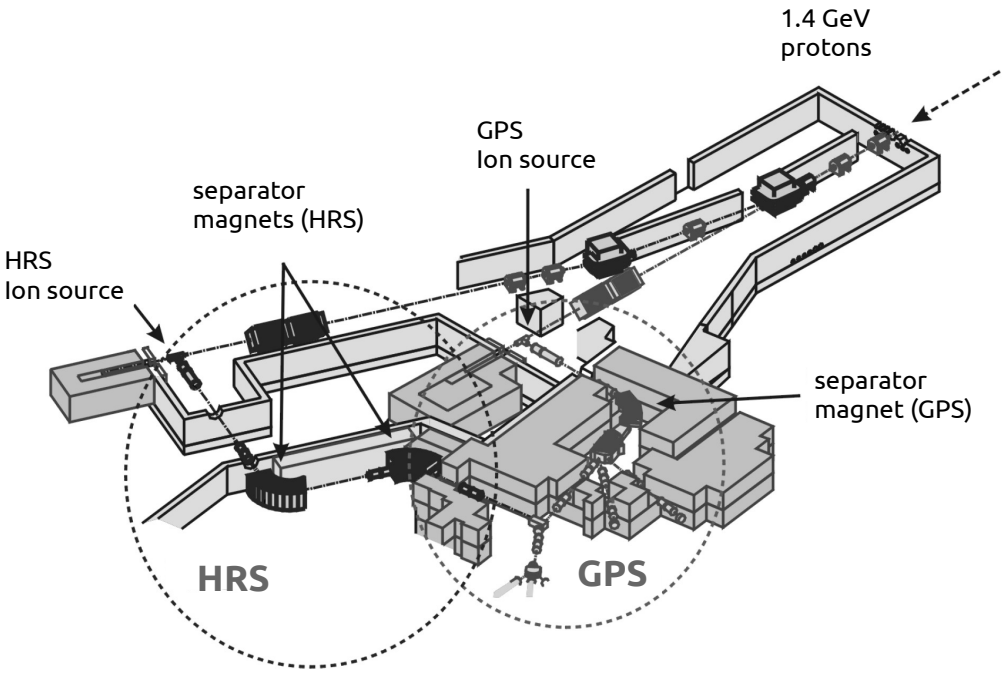

Figure 3.2: Scheme of the production process of radioactive ion beams from ISOLDE. Radioactive ion beams can be separated with the general purpose separator (GPS) or the high resolution separator (HRS) magnets.

higher efficiency on localizing impurities compared to IBC techniques, allowing one to perform detailed lattice location investigations of low solubilities of impurities [1]. Furthermore, EC is able to investigate elements lighter than host atoms.

Figure 3.1 illustrates how an EC experiment can obtain the lattice sites of probes that decay by emitting e^-. If the probe is located on substitutional sites, the emitted e^- are channeled along the three crystallographic directions <111>, <100> and <110>. Channeling peaks will hence be seen in the respective measured two-dimensional electron yield patterns. If the probe sits on interstitial sites with tetrahedral symmetry, one still observes channeling effects along <111> and <100>, but the electrons from <110> are blocked.

3.2 Radioactive implantation

The main difficulty of the EC technique is to perform the ion implantation of probes that decay by emitting positively charged particles (such as α or β^+) or e^- (from β^-

decays or conversion electrons (CE)). So far, EC investigations have been performed at the isotope separator on line device (ISOLDE) facility located at CERN in Switzerland [8, 9], where radioactive nuclides are produced via spallation, fission or fragmentation reactions in thick targets, induced by proton beams from a proton synchrotron booster (PSB) at energies and intensities up to 1.4 GeV and 2 μA, respectively, as illustrated in Fig. 3.2. The volatile nuclear reaction products are then released from the high temperature target. To accelerate them one has to ionize the desired species. Three different types of ion sources are used: (a) surface ion source (b) plasma ion source and (c) resonance ionization laser ion source. Surface ion source consists on the heating of materials in contact with the targets, such as tantalum or tungsten, with a larger work function than the atom to be ionized. In a plasma ion source, electrons are freed from the radioactive isotopes through collisions with gas ions in plasma discharges. Finally, a laser ion source applies the excitation of specific electrons from the radioactive isotopes by photons from lasers [10]; Radioactive isotope ions are then accelerated, reaching energies up to 60 keV. This unique process is coupled to powerful mass separators from which radioactive beams of high isotopic purity are produced.

Figure 3.3 indicates the elements from which radioactive isotopes have been used so far in EC experiments. They include those from α, β^- and β^+ decays and those in which some states emit CEs. One can promptly note that CE and β^- probes, involving e^-, are the most used, hence, related investigations are known to be obtained by electron emission channeling. In particular, it is common referring EC experiments with β^- probes as β^- emission channeling (β^--EC). This work used the following β^- probes:

- ^{56}Mn ($t_{1/2}$ = 2.57 h): This isotope is directly obtained from the respective radioactive beam.

- ^{59}Fe ($t_{1/2}$ = 44.6 d): To dope silicon with ^{59}Fe, the precursor isotope ^{59}Mn ($t_{1/2}$ = 4.6 s) was implanted.

- ^{61}Co ($t_{1/2}$ = 1.65 h): In this case, the precursor isotope ^{61}Mn is implanted in silicon, which follows the decay chain ^{61}Mn ($t_{1/2}$=0.61 s) $\rightarrow$ ^{61}Fe (5.98 min) $\rightarrow$ ^{61}Co.

- ^{65}Ni ($t_{1/2}$ = 2.5 h): This isotope is also obtained directly from the respective radioactive beam.

In all cases the isotopes, or precursor isotopes, are laser ionized.

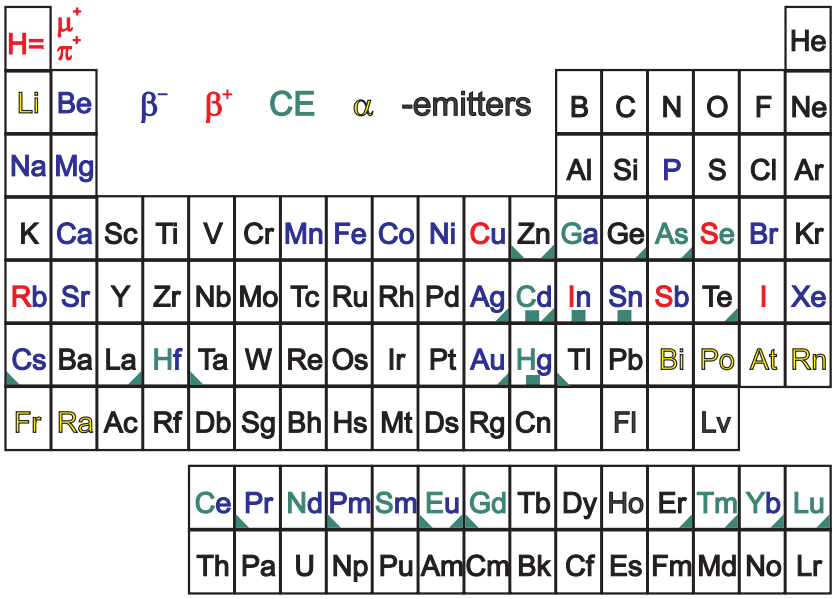

Figure 3.3: Radioactive isotopes used so far in EC experiments [11]. Parent isotopes of decays leading to neighboring daughter nuclei that emit CEs are indicated by the hollow triangles, pointing to the daughter, or hollow squares, if the daughter is the same element as the parent.

3.3 Experimental setup

Electron emission channeling experiments consist generally of: (i) ion implanting the radioactive isotope. (ii) performing the respective annealing, if any. (iii) orienting the sample and further measuring the electron yield in the vicinity of several crystallographic directions. So far, processes (i) and (ii-iii) have been performed separately. Only long lived isotopes could hence be investigated by implanting in one chamber (implantation chamber) and measuring in another one (offline chamber). The restriction to long lived isotopes, and resulting separate handling between measurement and implantation, was a consequence of the limited $\sim$ 250 Hz count rate of the available detectors. However, with a recent upgrade of the detectors to higher count rates (several kHz) an online setup was installed at the end of one of the general purpose separator (GPS) ISOLDE beam lines, allowing now both implantation and measurement taking place at the same time, i.e. processes from (i) to (iii) taking place in the same chamber [12]. This new online chamber allows currently to investigate the short lived isotopes ^{56}Mn, ^{61}Co and ^{65}Ni, listed above, being only limited by the time required for thermal treatments. Each EC setup consists of a high vacuum chamber,

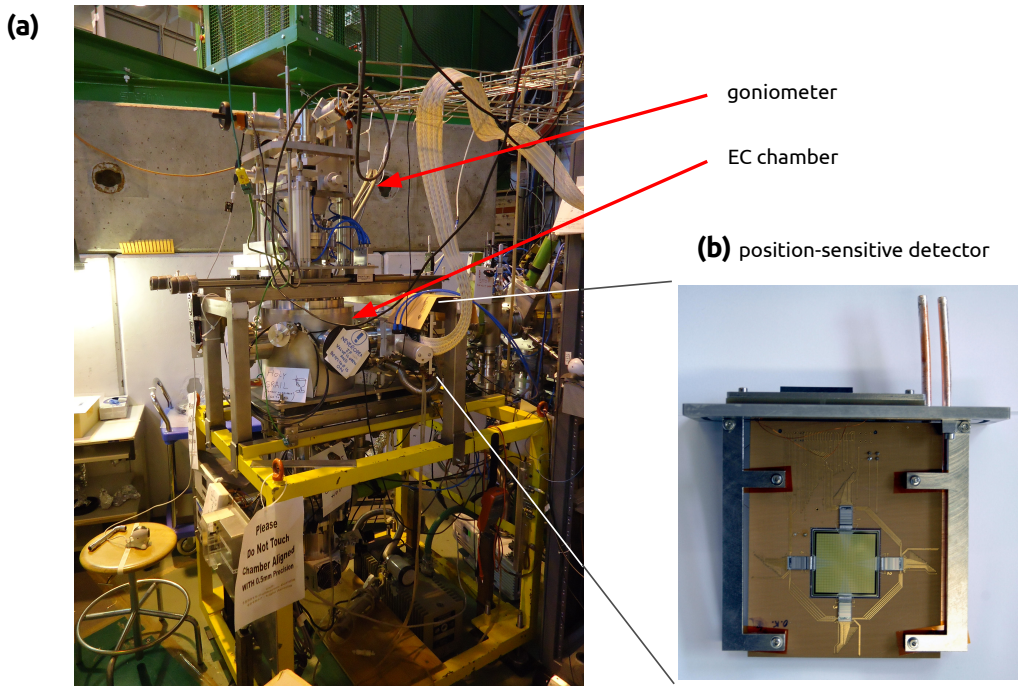

Figure 3.4: (a) Photograph of the online setup consisting of a high vacuum chamber, a goniometer and a (b) position-sensitive detector.

a goniometer and a position sensitive detector, shown in Fig. 3.4 and described briefly below:

High vacuum chamber: With a vacuum around 10^{-6} mbar, the sample is mounted inside a chamber vertically on the sample holder, in front of the detector, oriented in such a way that electrons emerging from the sample's surface parallel to the measured crystallographic axis reach the center of the position sensitive detector.

Goniometer: The goniometer allows moving the sample up and down and rotating it around two axes of rotation, with a typical angular precision around 0.05° - 0.1°. The sample holder is also equipped with a tungsten wire (resistive) heating device, which allows the *in situ* vacuum annealing of samples up to 900°C.

Position-sensitive detector: The principle of operation of these detectors is based on integrating an array of separate detector cells (pads or pixels) on a single Si chip [13]. The square-shaped sensitive area is 28.6 × 28.6 mm^2 and consists of 22 × 22 pixels (1.3 × 1.3 mm^2). The energy resolution for electrons is 5-6 keV. These detectors have undergone technical developments during the upgrade of the EC chambers from offline to online, as aforementioned.

3.4 Data analysis

To obtain a quantitative analysis that allows to access the fraction of several occupied lattice sites one has to fit the experimental two-dimensional emission yield patterns with theoretical ones calculated for emitter atoms on different lattice sites. In this section it is described briefly how theoretical patterns are obtained, with the so called *manybeam* simulations, and the related fitting procedure. Some background corrections are also outlined.

3.4.1 Manybeam calculations

The first code that calculates electron emission yields from radioactive probes was developed by Hofsäss and Lindner [2, 7, 14]. Their accurate model was based on the *manybeam* formalism, but was limited to one dimension. To overcome this issue, U. Wahl introduced modifications to this code, which resulted in a final program that obtains calculated two-dimensional angle-dependent electron yields for any lattice position of emitter impurities in the vicinity of any crystallographic direction [15]. The basic ingredient of such simulations is the crystallographic structure. For the case of silicon, the structure (diamond) and the respective lattice parameter have been well established. For the present investigations the specific emitters were considered to sit on the high symmetry sites shown in Fig. 2.2, as well as displacements along the <111>, <100>, and <110> crystallographic directions. One should note that dechanneling, which accounts for incoherent scattering events, is also taken into account. Dechanneling includes thermal vibrations of the lattice nuclei, inelastic electronic scattering and scattering by crystal defects. Each calculated two-dimensional electron emission yield pattern takes into account the following information:

(i) The emission yield of a set of e^- energies are considered from each lattice site and further weighted according to the β^- spectrum of the emitter.

(ii) The code calculates the electron flux at specific sites inside the crystal as a function of depth. The final theoretical pattern is weighted according to the depth profile of the probe atoms, which is currently obtained with the SRIM monte carlo simulation code [16, 17].

(iii) One important parameter is the angular resolution [13]. Assuming that both the position resolution of the detector and the projected beam spot distribution can be approximated by two-dimensional isotropic Gaussian distributions with standard

deviations σ_d and σ_b, respectively, the total angular resolution is then given by

$$\sigma_{ang} \approx \frac{\sqrt{\sigma_d^2 + \sigma_b^2}}{d} \tag{3.1}$$

where d is the distance between the sample and the detector, which is typically 30 cm in order to cover an angular range of $5° - 6°$. Different σ_{ang} values have also to be considered, especially due to the used beam spot, which is typically around 1 mm.

(iv) One also takes into account the vibration amplitudes of the probes. The one-dimensional root mean square (rms) vibration amplitude u_{imp} can be approximated with the following formula:

$$u_{imp}^2 = \frac{3\hbar T}{M k_B \Theta_{imp}^D} \left[\varphi\left(\frac{\Theta_{imp}^D}{T}\right) + \frac{\Theta_{imp}^D}{4T} \right] \tag{3.2}$$

where M is the mass of the element in question, k_B the Boltzmann constant, Θ_{imp}^D the Debye temperature of the impurity, which can be further approximated by $\Theta^D \sqrt{\frac{M}{M_{imp}}}$ with M_{imp} being the mass of the impurity, and Θ^D the Debye temperature of Si. The Debye function $\varphi(x)$ is defined as

$$\varphi(x) = \frac{1}{x} \int_0^x \frac{t dt}{e^t - 1}. \tag{3.3}$$

Within this approximation, the impurity is considered to be bound to its neighbors with the same elastic constants as the lattice host atoms.

With such extended procedure, one immediately foresees that a high computing power is required. This explains why such procedure lasted more than a decade to be fully operational [11]. The size and shape of the detector pads is taken into account by averaging over the simulated yield falling within the angular range ($0.26° \times 0.26°$) of one pixel, resulting into the two-dimensional electron yield patterns $\chi^{theo}(\theta, \phi)$ for each lattice site of a specific emitter, where θ and ϕ are the polar and azimuthal emission angle of the e^- with respect to the channeling direction.

3.4.2 Fitting procedure

To perform the fitting of the experimental patterns $\chi^{exp}(\theta, \phi)$ to linear combinations of the calculated theoretical yields $\chi^{theo}(\theta, \phi)$ a program so-called fdd, first developed by U. Wahl, has been used. The parameters varied during the fit are the axis position in the detector (x_0, y_0), the azimuthal rotation angle of the pattern with respect to

the channeling axis ϕ_0, the scaling factor S and the relative fractions f_i of emitter atoms occupying the ith site. The experimental yield is thus approximated using the formula:

$$\chi^{exp}(\theta,\phi) = S\left[f_{rand} + \sum_{i=1}^{N} f_i \chi_i^{theo}(\theta,\phi)\right], \tag{3.4}$$

where N is the number of occupied lattice sites used in the fit. The χ^2 of the difference between experiment and fit is then optimized by using non-linear least squares fitting routines [15] that vary the parameters described above. The random fraction f_{rand} accounts for emitter atoms which do not contribute to the anisotropy of the pattern, i.e. which are located on sites with very low crystal symmetry such as in heavily damaged surroundings. f_{rand} is given by

$$f_{rand} = 1 - \sum_{i=1}^{N} f_i. \tag{3.5}$$

Increasing the number of fractions N usually improves the χ^2 of fit since it increases the number of fit parameters. However, such an improvement does not necessarily mean that the real picture involves a large number of lattice sites with considerable fractions. One has to be careful with such interpretations, analyzing each case as unique. This will become clearer in chapter 4. In order for additional lattice sites to be identified, the improvement in χ^2 of fit should be significant and consistent for all crystallographic directions measured under the same conditions. One should finally mention that the fitting procedure is usually also performed choosing different values for u_{imp} and σ_{ang}. Increasing these parameters flattens the patterns since the variations of the yield within a detector pixel are reduced, which may result in better χ^2 of fit. One must hence also evaluate prudently the respective physical meaning of a reduction of χ^2 in these cases.

3.4.3 Background corrections

The position sensitive detector is sensitive not only to electrons but also to photons such as γ-rays (see Fig. 3.5 (1-2)). The number of counts will therefore be influenced also by the γ-rays emitted from the sample, sample holder, chamber walls or occasionally even from radioactive gases still present in the vacuum chamber. The detection of such γ-rays cannot be prevented as they are difficult to shield. To take into account this detected γ-rays one can isolate their detection from e^- by making use of an electron barrier, which can be achieved by, e.g., closing the detector valve that separates the EC

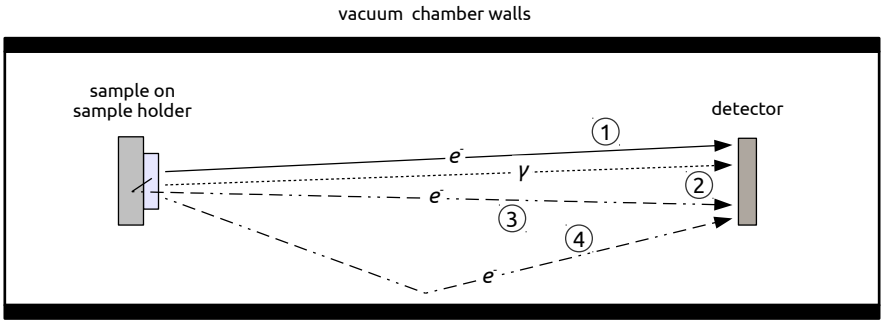

Figure 3.5: Typical particle tracks and related sources of background in electron emission channeling measurements. In (1) the detected electron is emitted from inside the sample directly towards the detector. γ-rays are also taken into account in (2). In (3) the emitted electrons from the probes are backscattered from the sample holder and in (4) from the chamber walls.

chamber from the detector: with the detector valve closed, one measures experimental patterns corresponding to the γ-rays. The respective background correction is hence performed by subtracting the γ-rays background from the measured experimental patterns with the detector valve open, taking additionally into account the measuring times.

Besides γ-rays, a second source of background are electrons emitted from the sample which are backscattered under large angles before being detected. These scattering events can occur inside the sample itself through scattering by the host atoms, or outside the sample by parts of the setup, such as by the sample holder or by the chamber walls (Fig. 3.5 (3-4)). Backscattered electrons produce an isotropic background in the experimental patterns which is not accounted for in the theoretical framework of channeling simulations. In case of conversion electron emitting isotopes, which are characterized by discrete emission energies, the amount of backscattered electrons can be quite well estimated from the inelastically scattered tails at lower energies in the energy spectrum. For β^- emitting isotopes, though, such a simple correction is not possible due to the continuous nature of the beta spectra. In this case Monte-Carlo calculations using the so-called GEANT4 code [18] are performed, which simulate a large number of electron tracks, taking into account the beta emission energies, the geometry and materials of sample, sample holder and vacuum chamber.

Bibliography

[1] U. Wahl, Emission channeling: charged particle-solid interaction, detection and lattice location methods, University of Lisbon, 2006.

[2] H. Hofsäss, G. Lindner, Emission channeling and blocking, Phys. Rep. 201 (1991) 121.

[3] G. Schatz, A. Weidinger, J. A. Gardner, Nuclear condensed matter physics, John Wiley & Sons Ltd., 1992.

[4] J. Lindhard, Influence of crystal lattice on motion of energetic charged particles, Matemat.-Fysis. Meddel. 34 (1965) 3.

[5] D. S. Gemmell, Channeling and related effects in the motion of charged particles through crystals, Rev. Mod. Phys. 46 (1974) 129–227.

[6] M. L. Swanson, The study of lattice defects by channelling, Rep. Prog. Phys. 45 (1982) 47.

[7] H. Hofsäss, U. Wahl, S. G. Jahn, Impurity lattice location and recovery of structural defects in semiconductors studied by emission channeling, Hyperfine Interact. 84 (1994) 27.

[8] E. Kugler, The ISOLDE facility, Hyperfine Interact. 129 (2000) 23.

[9] M. Deicher, G. Weyer, T. Wichert, Solid state physics at ISOLDE, Hyperfine Interact. 151 (2003) 105.

[10] V. N. Fedoseyev, G. Huber, U. Köster, J. Lettry, V. I. Mishin, H. Ravn, V. Sebastian, The ISOLDE laser ion source for exotic nuclei, Hyperfine Interact. 127 (2000) 409.

[11] U. Wahl, J. Correia, A. Costa, E. David-Bosne, L. M. C. Pereira, L. M. Amorim, V. Augustyns, K. Temst, A. Vantomme, M. R. da Silva, D. J. Silva, J. P. Araújo, P. Miranda, K. Bharuth-Ram, Emission channeling with short-lived isotopes (EC − SLI) at CERNs ISOLDE facility, Proceedings of the First International African Symposium on Exotic Nuclei (IASEN 2013).

[12] M. R. da Silva, U. Wahl, J. G. Correia, L. M. Amorim, L. M. C. Pereira, A versatile apparatus for on-line emission channeling experiments, Rev. Sci. Instrum. 84 (2013) 073506.

[13] U. Wahl, J. G. Correia, A. Czermak, S. G. Jahn, P. Jalocha, J. G. Marques, A. Rudge, F. Schopper, J. C. Soares, A. Vantomme, P. Weilhammer, Position-sensitive Si pad detectors for electron emission channeling experiments, Nucl. Instrum. Methods Phys. Res. Sect. A 524 (2004) 245.

[14] H. Hofsäss, Emission channeling, Hyperfine Interact. 97 (1996) 247.

[15] U. Wahl, Advances in electron emission channeling measurements in semiconductors, Hyperfine Interact. 129 (2000) 349.

[16] J. F. Ziegler, SRIM - 2003, Nucl. Instrum. Methods. Phys. Res. Sect. B 219 (2004) 1027.

[17] J. F. Ziegler, M. D. Ziegler, J. P. Biersack, SRIM - the stopping and range of ions in matter (2010), Nucl. Instrum. Methods Phys. Res. B 268 (11-12) (2010) 1818.

[18] S. Agostinelli, *et al.*, GEANT4 - a simulation toolkit, Nucl. Instrum. Methods Phys. Res. A 506 (2003) 250.

Chapter 4

Lattice location

This chapter compiles the manuscripts regarding the results of the lattice location of the transition metals iron, nickel, cobalt and manganese in silicon by means of emission channeling experiments. The order of the studied transition metal impurities exposed here follows the chronology of writing (or publication), which will be helpful during the discussion of each experimental work. All the used probes have been listed in chapter 3.

The six manuscripts can be summarized as follow. **Iron** has already been investigated with the emission channeling technique, however without observing any influence of the electronic doping. *Article I* describes in detail such influence on the lattice sites of Fe by investigating heavily doped silicon samples, while *article II* focuses on the method of analysis of the sites displaced from bond-centered sites found in article I. The obtained lattice sites of **nickel** by means of emission channeling experiments is for the first time described in *article III*. To explore the origin of the three types of lattice sites found for Cu, Ag, Fe and Ni in silicon, one has investigated the lattice location of the transition metal **cobalt** in lightly doped n-type silicon, described in *article IV*, and in heavily doped n^+- and p^+-type silicon, described in *article V*. Last but not least, the lattice location of **manganese**, important for the clarification of the complexes formed during the tentative incorporation of Mn into substitutional sites, is treated in *article VI*.

4.1 Contributions of the PhD candidate

The experiments carried out in this investigation were performed under the ISOLDE proposals IS368 ("Lattice location of transition metals and rare earths in semiconductors") and IS453 ("Emission channeling lattice location experiments with short-lived isotopes"), in which Dr. Ulrich Wahl is the spokesperson. While the proposal IS368 included experiments performed between 1998 and 2006, the proposal IS453 was approved in 2006 and is still running. In the following it is described in detail the contributions of the PhD candidate to the publications compiled in the next sections.

Article I: The used data was collected under proposal IS368 in 1999, thus by the co-authors before the beginning of this PhD. The analysis, which includes the fitting procedure, background corrections, and modeling of the possible complexes and related kinetics, was made by the PhD candidate. Both the writing of the paper as well as the incorporation of corrections and comments made by the co-authors into the manuscript were carried out by the PhD candidate.

Article II: As aforementioned, *article II* describes in more detail the fitting procedure of *article I*, focusing on the identification of the sites displaced from the bond-centered site and on the determination of respective fractions. Both the writing of the paper as well as the incorporation of corrections and comments made by the co-authors into the manuscript were carried out by the PhD candidate.

Article III: The investigation presented in *article III* was carried out with the short lived isotope ^{65}Ni in three silicon samples with different doping types, thus under proposal IS453. The PhD candidate participated in the experiment that took place from the 21st and 24th September of 2011, during a Ni beam time. One should note that because the beam times gained by such proposals are very short (days or some weeks at most), one must collect data continuously, day and night. Therefore, the PhD candidate participated in one of the two shifts. While proposal IS453 was approved before this PhD in 2006, the annealing steps to be performed were still to be decided. In fact, in the majority of emission channeling experiments it is hard to predict which dependence of the identified fractions will be observed. The planing of annealing treatments was hence carried out during each beam time, in which the PhD candidate also participated. The analysis, which includes the fitting procedure, background corrections, and modeling of the possible complexes and related kinetics, was made by the PhD candidate. Both the writing of the paper as well as the incorporation of corrections and comments made by the co-authors into the manuscript were carried

out by the PhD candidate.

Article IV: The study of *article IV* was performed by implanting the precursor and short lived isotope ^{61}Mn, hence under proposal IS453. The PhD candidate participated in the experiment in the same manner described in the last paragraph, but here between the 1st and 5th September 2011 during the Mn beam time. The analysis, which includes the fitting procedure, background corrections, and modeling of the possible complexes and related kinetics, was made by the PhD candidate. Both the writing of the paper as well as the incorporation of corrections and comments made by the co-authors into the manuscript were carried out by the PhD candidate.

Article V: While in the investigation described in *article IV* ^{61}Mn was implanted in a lightly doped n-type silicon sample, in *article V* ^{61}Mn was implanted in n^+- and p^+-type silicon samples, under proposal IS453, following the same procedures described above. The beam times in question were the following: for the p^+-type silicon sample, the emission channeling experiment was carried out between the 5th and 7th September 2011; for the n^+-type silicon sample, the emission channeling experiment was carried out between the 25th and 27th November 2012. The analysis, which includes the fitting procedure, background corrections, and modeling of the possible complexes and related kinetics, was made by the PhD candidate. Both the writing of the paper as well as the incorporation of corrections and comments made by the co-authors into the manuscript were carried out by the PhD candidate.

Article VI: Finally, the experiment treated in *article VI* was performed under proposal IS453 with the short lived isotope ^{57}Mn in 2009 and 2010, hence by the co-authors before the beginning of this PhD. The analysis, which includes the fitting procedure, background corrections, and modeling of the possible complexes and related kinetics, was made by the PhD candidate. Both the writing of the paper as well as the incorporation of corrections and comments made by the co-authors into the manuscript were carried out by the PhD candidate.

4.2 Article I - Influence of n^+ and p^+ doping on the lattice sites of implanted Fe in Si

D. J. Silva[1], U. Wahl[2], J. G. Correia[2], J. P. Araújo[1]
[1] IFIMUP and IN-Institute of Nanoscience and Nanotechnology, Departamento de Física e Astronomia da Faculdade de Ciências da Universidade do Porto, Rua do Campo Alegre 687, 4169-007 Porto, Portugal
[2] Instituto Superior Técnico/Instituto Tecnológico e Nuclear, Universidade de Lisboa, 2695-066 Bobadela, Portugal

Journal of Applied Physics **114**, 103503 (2013)

abstract

We report on the lattice location of implanted ^{59}Fe in n^+- and p^+-type Si by means of emission channeling. We found clear evidence that the preferred lattice location of Fe changes with the doping of the material. While in n^+-type Si Fe prefers displaced bond-centered (BC) sites for annealing temperatures up to 600°C, changing to ideal substitutional sites above 700°C, in p^+-type Si Fe prefers to be in displaced tetrahedral interstitial positions after all annealing steps. The dominant lattice sites of Fe in n^+-type Si therefore seem to be well characterized for all annealing temperatures by the incorporation of Fe into vacancy-related complexes, either into single vacancies which leads to Fe on ideal substitutional sites, or multiple vacancies, which leads to its incorporation near BC sites. In contrast, in p^+-type Si the major fraction of Fe is clearly interstitial (near-T or ideal T) for all annealing temperatures. The formation and possible lattice sites of Fe in FeB pairs in p^+-Si are discussed. We also address the relevance of our findings for the understanding of the gettering effects caused by radiation damage or P-diffusion, the latter involving n^+-doped regions.

4.2.1 Introduction

For decades, 3d transition metals in Si have been in the focus of silicon research due to their unwanted presence as contaminants [1–5]. Depending on the complexes that the transition metals (TMs) form, and thus on their lattice sites, deep levels can be created, forming recombination centers and, therefore, acting as lifetime killers

for minority carriers [2, 5]. The electric passivation of TMs is required to prevent, e.g., the malfunctioning of electronic circuits based on silicon or the efficiency degradation of solar cells. To reduce the harmful effects of such deep levels a number of gettering techniques were developed in order to either trap TMs into inactive areas or to transform them into electrically inactive forms [3, 4, 6]. Some of the gettering techniques rely on deliberately creating highly doped regions in the Si wafer, e.g. through p^+-doping with boron, or by diffusing the n-type dopant P in from the surface, others on creating vacancies through irradiation. More recently TM-doped silicon has also attracted attention as a possible magnetic semiconductor system. The magnetic properties of TMs in Si are expected to depend on whether the TMs are incorporated substitutionally or interstitially and based on first principle calculations it was proposed that the position of the Fermi level (which depends on n- or p-doping) and the availability of vacancies are of crucial importance in controlling the lattice site [7–12]. Most of the theoretical work on this subject concerned Mn in Si, but also Fe was addressed [9, 12].

Regarding the gettering processes for TM contaminants in Si, Fe remains the best-studied species. While the macroscopic behavior of Fe during gettering can now be predicted to some extent, see e.g. Ref. [13], many fundamental questions on the basic underlying microscopic mechanisms are still poorly understood, among them the detailed knowledge of Fe lattice sites in different types of silicon, or when forming complexes with other impurities, such as dopants, or implantation defects, such as vacancies. For instance, the P-diffusion gettering process, which is nowadays widely used in the fabrication of n-p-junction Si solar cells [13–20] is known to create on top of a low p-doped multi-crystalline Si wafer highly-doped n^+-regions, in which Fe is trapped. It has been recently suggested [20] that the high concentration of vacancies created during P-diffusion is a key ingredient in the gettering process; at the same time it is expected from theoretical grounds that Fe becomes less electrically active when it is trapped by Si vacancies [21]. Consequently, providing microscopic information what actually happens to Fe when it encounters Si vacancies in an n^+-type environment, as is achieved in this paper, will be crucial to understand the fundamental principles underlying this gettering process. In p^+-type Si, on the other hand, the formation of FeB pairs between the acceptor B and interstitial Fe is a well-known phenomenon studied by electrical and optical techniques [1–3, 22–24], but so far no detailed information on the lattice sites of Fe in such pairs has been available, which is why we have also devoted special attention to this subject.

Emission Channeling (EC) is a unique technique which can investigate the lattice

sites of low concentrations of impurities in single crystals. EC relies on implanting radioactive probe atoms that decay by the emission of β^- particles, which, on their way out of the crystal, experience channeling effects along some crystal directions, depending on the lattice site occupied by the probe atom.

EC has already been applied to study the lattice sites of ^{59}Fe in low and moderately doped n- and p-type Si [25, 26]. The results showed ^{59}Fe in three different positions: ideal substitutional (S), displaced substitutional (near-S) and displaced tetrahedral interstitial (near-T) sites. Iron on near-S sites was the dominating fraction for annealing temperatures below 500°C, while annealing between 500°C and 800°C moved the majority of ^{59}Fe to near-T sites, and ideal S sites dominated, along with near-T sites, the channeling patterns of 800-900°C annealed samples. Similar to other EC studies involving the transition metals Cu [27–29] and Ag [30], it was suggested that the observed sites, in particular near-S sites, could be related not only to Fe interacting with single vacancies but also to vacancy clusters, such as divacancies [31], where the TM prefers to sit between the two vacancies (bond-centered sites). Furthermore, *ab initio* calculations have recently confirmed the stability of fourfold coordinated vacancy clusters based on hexavacancy rings [32, 33]. It was theoretically predicted that interstitial Cu atoms can be trapped inside such vacancy clusters and their positions seem to be close to a displaced bond-centered site in an undisturbed crystal [34, 35].

A change of doping type can have profound implications on the preferred lattice sites of impurities by several active mechanisms. Generally speaking, if the impurity is electrically active, the formation energies and solid solubilities of its various configurations are directly coupled to the electron-hole charge equilibrium in the semiconductor. Hence, a change of the Fermi level can lead to a particular form of impurity defect becoming more or less energetically favorable. In the simplest case, a change of the Fermi level will directly change the prevailing charge state of the impurity itself. For instance, interstitial iron has a well-known deep donor level at $E_V + 0.40$ eV, i.e. close to the valence band [1, 2]. While in intrinsic and n-type Si interstitial iron is neutral, it will prevail in a +1 charge state in p-type Si, and, in principle, Fe might prefer a different interstitial site. Another example is the increase in the solubility of donors in case of counter-doping with acceptors. If, e.g., an interstitial impurity acts as a donor while the substitutional form is an acceptor, counter doping with acceptors will clearly increase the solubility of donors. A particular case is the situation when certain charge states of an impurity enable it to form pairs with other impurities. The most common such example are the formation of donor-acceptor pairs, e.g. FeB [1–3, 22, 23]. The

binding energy, which is gained when the pairs are formed, can cause the impurity within the pair to be much more stable and hence prevail over other configurations in the lattice. On the other hand, the position of the Fermi level also changes the preferred charge states and concentrations of other defects that can interact and form complexes with Fe. For instance, the single vacancy in Si has been reported to exist in various charge states, ranging from -2 in highly n-type to +1 or +2 in highly p-type Si [36]. Neutral or positively charged interstitial Fe_i^+ will obviously much easier combine with negatively charged vacancies in n-type Si than with positively charged ones in p-type Si.

In our previous EC study [25], no significant changes were observed in the ^{59}Fe lattice position when using different types of Si for resistivities above ~ 0.01 Ωcm. However, this was attributed to the possibility that the Fermi level, following implantation into low or moderately doped Si, is most likely close to the midgap position, due to the fact that the concentration of implantation defects is, by several orders of magnitude, larger than those of n- or p-type dopants. Therefore, in this work, we have applied the EC technique to study the lattice sites of ^{59}Fe implanted into highly doped n^+- and p^+-type Si. Our results confirm the presence of ^{59}Fe in three different lattice sites: displaced bond-centered (near-BC), displaced tetrahedral interstitial (near-T) and ideal substitutional (S) sites. We show that the stability of ^{59}Fe on near-BC sites changes with the doping of the material. By comparing with other experimental techniques from literature, we also show evidence of FeB pairs in p^+-type Si, with ^{59}Fe on near-T sites. Although FeB pairs dissociate easily during a low temperature annealing, they should also form again during cooling down, while defects produced during implantation tend to disappear upon annealing.

4.2.2 Experiment

Czochralski grown silicon samples were doped with the long-lived isotope ^{59}Fe ($t_{1/2}$ = 44.6 d) by implanting the precursor isotope ^{59}Mn ($t_{1/2} = 4.6$ s) at the on-line isotope mass separator facility ISOLDE at CERN, with 60 keV. Upon decay of ^{59}Mn, the ^{59}Fe atoms receive a mean recoil of 200 eV, assuring their re-implantation and thus avoiding any influence from the previous site of ^{59}Mn.

The samples used were n^+-type Si (n^+-Si) with a $< 111 >$ surface, doped with arsenic, and p^+-type Si (p^+-Si) with a $< 100 >$ surface, doped with boron. The resistivity and arsenic concentration of the n^+-Si sample were < 0.001 Ωcm and [As] $> 1.2 \times 10^{20}$

cm^{-3}, while the resistivity and boron concentration of the p^+-Si sample were < 0.002 Ωcm and [B] $> 6.5 \times 10^{19}$ cm^{-3}.

^{59}Fe was implanted in both types of Si during approximately 2 h to obtain a fluence of 6×10^{12} cm^{-2}, with each sample mounted in such a way that the surface normal was off beam by 10° to avoid channeled implantation. In our previous studies of ^{59}Fe in low-doped Si [25, 26], 14 samples were studied of which 9 were <111> and 5 <100> oriented, but no significant difference was found in the lattice location of Fe. We hence believe that the different surface type of the two Si samples will have no particular influence on the outcome of the studies presented here. The depth profile of the implanted ^{59}Fe was obtained using the SRIM code [37]. The implanted ^{59}Fe profile is approximated by a Gaussian distribution centered at 558 Å from the surface, with a straggling of 213 Å and a peak concentration of 1.1×10^{18} cm^{-3}. SRIM simulations also show that about 1000 vacancies per implanted Fe ion are generated at 0 K and that their distribution profile peaks at about half way from the surface to the maximum implanted ^{59}Fe concentration. The concentration peak of the vacancy profile was approximately 1×10^{21} cm^{-3}.

A few days after the implantation, the samples were mounted on a goniometer made of Ta and Mo and annealed *in situ* up to 900°C in steps of 100°C, during 10 min, under vacuum better than 10^{-5} mbar. During annealing, the time it took to heat up the sample was quite fast (a few minutes at most). On the other hand, the cool down was slow, lasting up to 30 min to reach room temperature for the highest annealing temperatures. After each annealing step, the β-emission yield in the energy window 50-461 keV was measured at room temperature using a position-sensitive detector. The electron intensity patterns were taken as a function of angle (+/- 2.5°) near the $< 110 >$, $< 100 >$ and $< 111 >$ axis in n^+-Si and near the $< 211 >$, $< 100 >$ and $< 111 >$ axis in p^+-Si. For each experimental EC pattern, electrons that are scattered into the detector by the chamber walls were taken into account by subtracting a flat background pattern, obtained with Monte Carlo electron scattering simulations [38], from every pattern. Each measurement took about 1-2 days depending on the necessary statistics for each orientation.

4.2.3 Results

The two-dimensional experimental data were fitted using calculated emission channeling patterns, obtained with the so-called *manybeam* approach [25]. The calculated

emission channeling patterns include the emission probability of the substitutional (S), hexagonal (H), tetrahedral (T), bond-centered (BC), anti-bonding (AB), split (SP) and the so-called Y and C sites, as well as $< 111 >$, $< 100 >$ and $< 110 >$ displacements between these positions. The location of these sites can be found in Ref. [27]. To understand the results and data analysis, one should first discuss the fitting procedure adopted in this study. First, each experimental pattern was fitted by considering one fraction only. Depending on the annealing temperature and whether it was n^+- or p^+-Si we obtained three types of sites: ideal substitutional sites (S), sites displaced from bond-centered towards substitutional sites (near-BC) and sites displaced from ideal tetrahedral interstitial towards AB sites (near-T). We then fitted each pattern again by considering these three fractions in the proportion that best decreased the χ^2 of fit. We note that the near-BC sites from this study can be interpreted as near-S sites observed in previous studies on Fe in Si [25, 26]. In fact, new simulations that include more displacements from S towards BC sites (step width 0.0588 Å vs. 0.1470 Å in Refs. [25, 26]) were here used which enabled us to conclude that these displacements are such that the sites are closer to BC than to S sites. We would like to point out that we can only assess the quality of fit for those lattice sites that we have calculated the emission yield. It thus can never be excluded with absolute certainty that there exist lattice sites which would provide a better fit but which were not calculated. However, the fact that we considered $\sim$ 250 different lattice sites displaced along the major directions <111>, <100> and <110> in the unit cell in steps of less than 0.06 Å, gives us some confidence that we probably did not miss the actual sites by a large amount. On the other hand, sites that are of very low structural symmetry as a rule lead to very small anisotropy in emission channeling patterns, and the possible fraction of emitter atoms on such sites can be estimated from the random fraction in our experiments, which amounts to the deviation of the sum of all fractions from 100%. It is also important to understand that the use of 3 fit fractions only does not necessarily mean that not more than 3 different lattice sites of Fe are present in our samples. For instance, likely candidates for additional sites of Fe would be ideal BC and ideal T sites. However, if one performs 4-site fits where these sites are allowed in addition, no significant decrease of χ^2 is found, and possible Fe fractions on these sites are small. Therefore, for instance ^{59}Fe on ideal BC sites was not further considered in the following discussion.

Figure 4.1 shows the experimental and best fit patterns of ^{59}Fe in n^+-Si, obtained after room temperature implantation (**a**) and after annealing at 600°C (**b**), in the vicinity of $< 110 >$, $< 100 >$ and $< 111 >$. After room temperature implantation ^{59}Fe prefers to

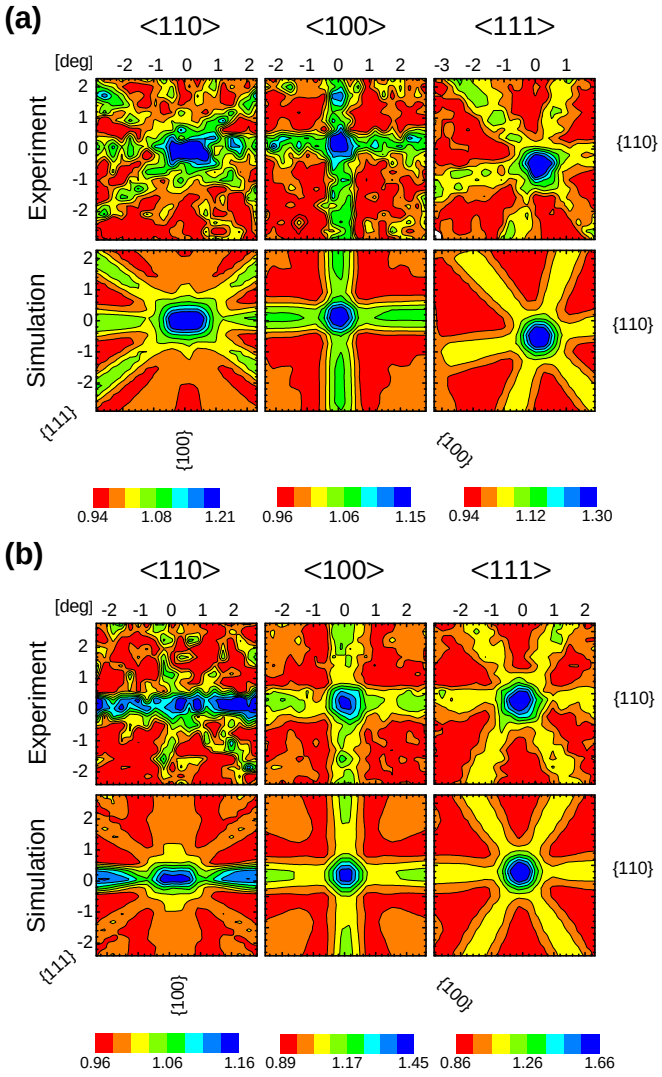

Figure 4.1: Comparison of the two-dimensional experimental and calculated emission channeling patterns from ^{59}Fe in n^+-Si in the vicinity of $< 110 >$, $< 100 >$ and $< 111 >$, following (**a**) room temperature implantation and (**b**) annealing at 600°C. The reduction of the channeling effect of the {111} planes after the 600°C anneal proves the increase of the near-T fraction. In fact, in (**a**) only 23% of ^{59}Fe is on near-T sites (21% on ideal S sites and 50% on near-BC sites), while in (**b**) 40% of ^{59}Fe is on near-T sites (16% on ideal S sites and 44% on near-BC sites).

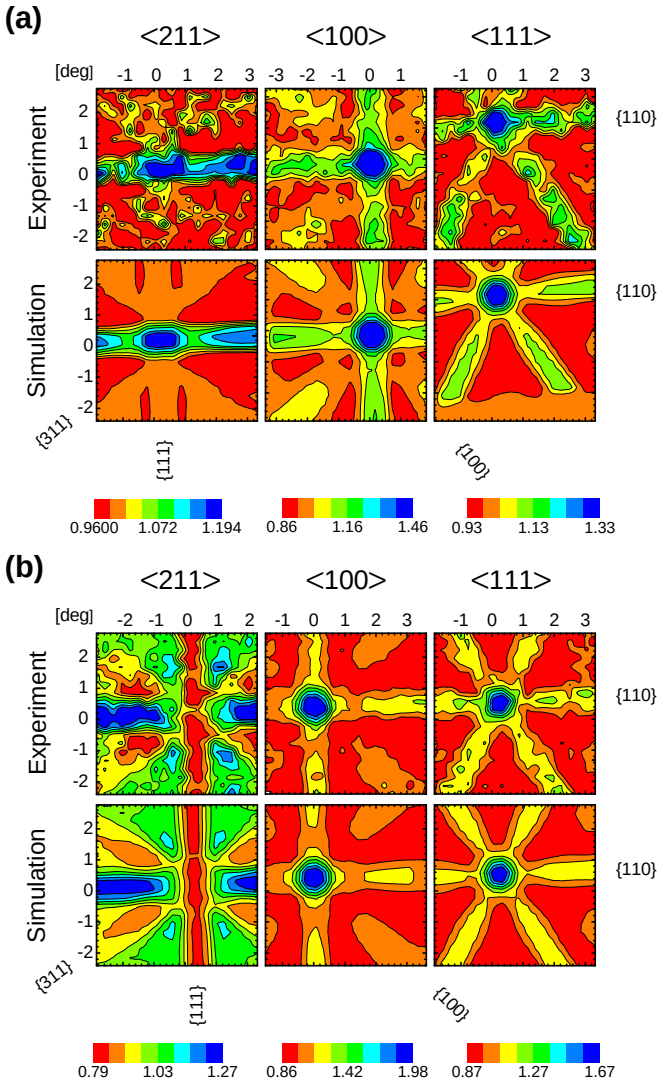

Figure 4.2: Comparison of the two-dimensional experimental and calculated emission channeling patterns from ^{59}Fe in p^+-Si in the vicinity of $< 211 >$, $< 100 >$ and $< 111 >$, following (**a**) room temperature implantation and (**b**) annealing at 400°C. With annealing temperatures up to 400°C, the channeling effect of the {111} plane in the as-implanted state is converted to a blocking effect, showing a considerable increase of the near-T fraction. In fact, in (**a**) 48% of ^{59}Fe is on near-T sites (18% on ideal S sites and 21% on near-BC sites), while in (**b**) 91% of ^{59}Fe is on near-T sites (no ideal S nor near-BC fractions were detected).

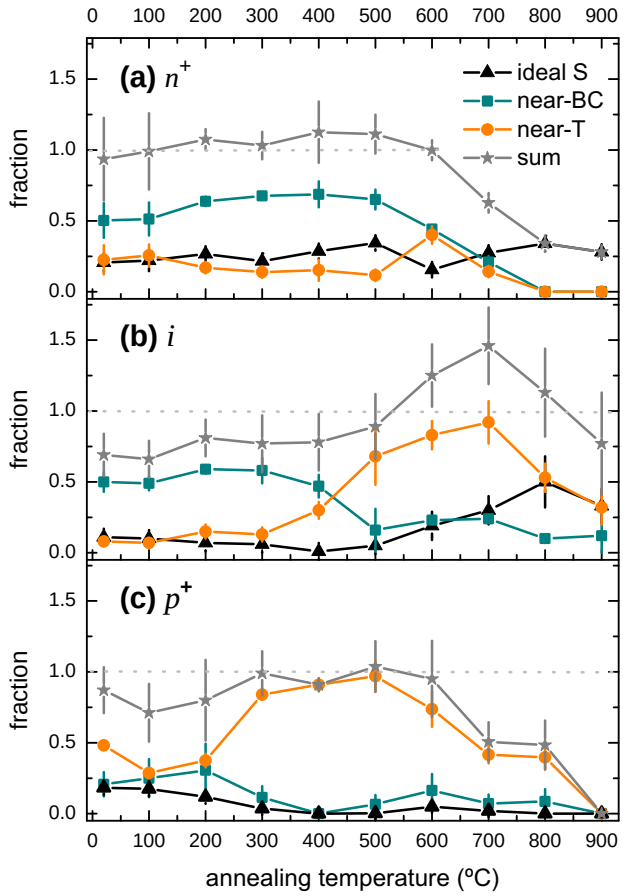

Figure 4.3: Annealing temperature dependence of the fractions of ^{59}Fe in n^+-Si (**a**) and p^+-Si (**c**), in comparison to the average results of low doped Si (i-Si) from Ref. [26] (**b**).

stay on near-BC positions, but a smaller fraction is also present on ideal S and near-T sites. These fractions do not change much while annealing up to 500°C. However, after annealing at 600°C (Fig. 4.1 (**b**)) one can observe a less pronounced channeling effect in the {111} planes of the $< 110 >$ pattern, which corresponds to an increase of the near-T fraction. Although this behavior is similar when compared to the previous study on low and moderately doped n- and p-type Si, in the present case of n^+-Si the near-T sites never became the dominant fraction and have their highest population following annealing in a narrow temperature range, around 600°C (cf. the discussion of Fig. 4.3 above). The displacements of the fitted near-BC and near-T sites in n^+-Si were both $\sim$ 0.8 Å (corresponding to 70% from S to BC and from T to AB sites,

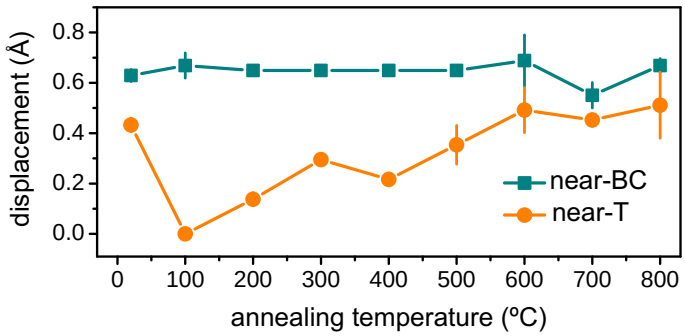

Figure 4.4: Displacements of the near-BC and near-T sites, occupied by ^{59}Fe, from S towards BC sites and from T towards AB sites, respectively, in p^+-Si.

respectively), except after annealing at 600°C where the displacement of the near-T sites was $\sim$ 0.2 Å. This means that for most annealing temperatures the interstitial fraction of Fe in n^+-Si was actually found somewhat closer to the AB than to the T site.

Emission channeling patterns from ^{59}Fe in p^+-Si are shown in Fig. 4.2, after room temperature implantation (**a**) and after annealing at 400°C (**b**). As is quite obvious from the $< 211 >$ patterns, the {111} planes present visible blocking effects after room temperature implantation [Fig. 4.2 (**a**)], which become even more intense by increasing the annealing temperature up to 400°C [Fig. 4.2 (**b**)]. This blocking effect is also a consequence of the occupation of near-T sites. From Fig. 4.3 (**c**) we can see that this near-T fraction increases by annealing up to 500°C, where it starts to reduce until ^{59}Fe diffuses through the bulk or to the surface, at the annealing temperature of 900°C. The near-BC sites in p^+-Si were displaced $\sim$ 0.6 Å from ideal S sites, for all annealing temperatures. However, in contrast to n^+-Si, different displacements for the near-T sites are here observed (Fig. 4.4), suggesting the existence of different ^{59}Fe complexes.

Note that the sum of all fitted fractions, which is also shown in Fig. 4.3, may deviate from 100%. While small deviations can be explained by statistical errors in the analysis, there are also some systematic effects: (1) After the implantation, a small fraction of ^{59}Fe is located in heavily damaged surroundings or sites of very low crystal symmetry (random sites), so that the sum of all regular and identified site fractions becomes smaller than 100%; (2) When some of the ^{59}Fe moves towards the surface compared with the assumed implantation depth profile, the intensity of the channeling effects is increased as well as the corresponding fitted fractions. This explains why

the sum may reach values above 100% at intermediate annealing temperatures [25]; if diffusing, ^{59}Fe accumulates at the surface (out-diffusion) or escapes to the bulk of the wafer (in-diffusion), channeling effects are lost, the random fraction increases, and the sum drops to values below 100% [25]. This is what supposedly happens at the highest annealing temperatures.

4.2.4 Discussion

As we have seen, the lattice site preference of Fe changes with the doping type of the Si material. The observed lattice sites of ^{59}Fe can be either related to its isolated form or complexes with other defects. Because isolated interstitial iron is a very fast diffuser, even at room temperature, it is quite unlikely that the majority of ^{59}Fe prevails in the implanted region in the form of isolated interstitial Fe. In contrast, the formation of complexes with other defects seems to be a more plausible explanation for the observed lattice sites. These complexes can be a result of aggregation of ^{59}Fe with damage defects or pairing with other impurities. A considerable fraction of ^{59}Fe in complexes with other defects can only be present if the defect concentration has at least the same order of magnitude as the implanted ^{59}Fe concentration. Therefore, observation of complexes of ^{59}Fe and C can be excluded since typical concentrations of C in Si are of the order of 10^{16} cm^{-3} that when compared to the iron peak concentration is two orders of magnitude smaller. What is not obvious to rule out is for instance the pairing of ^{59}Fe with O or H whose typical concentrations may be comparable to the implanted iron peak concentration (10^{18} cm^{-3}). However, no significant difference was observed between low doped Czochralski and Float Zone Si in the previous EC study [25, 26] and, therefore, O and ^{59}Fe seem not to have paired in considerable quantities on the reported experiments. Regarding the formation of complexes between Fe and H, deep level transient spectroscopy (DLTS) has observed the existence of new levels when H is intentionally introduced in n-type Si doped with Fe [39]. However, the levels disappeared again after annealing at 175°C. Although the lattice location of ^{59}Fe in hydrogenated Si samples has not yet been investigated by means of EC, the fact that pronounced changes in the lattice locations of Fe are absent up to an annealing temperature of 200°C, suggests that such Fe-H complexes are probably not a characteristic feature in our experiments. In order to investigate this issue, we are planning to study the lattice location of ^{59}Fe also in hydrogenated Si samples. Another possibility that cannot be ruled out is the presence of clusters of ^{59}Fe such as dimers. In fact, Fe precipitates easily in Si. Yet, previous EC experiments

which used implanted Fe fluences that varied up to a factor of 50 and hence covered a wide range of ^{59}Fe concentrations, have not given any hints that would allow to confirm the presence of such clusters [25]. Regarding possible Fe traps, from the viewpoint of concentration the most likely interaction of Fe is hence not with C, O or H, neither by forming clusters of ^{59}Fe such as dimers, but with self-interstitials, vacancies or dopants (As or B). For ionized dopants, the Coulomb interaction can act as a decisive force which drives the formation of pairs. For instance, while there are no indications that interstitial Fe, either neutral Fe^0 or positively charged Fe^+, should pair with positively charged donors such as As^+ [40], the formation of pairs between positively charged interstitial Fe_i^+ and negatively charged acceptors, e.g. B^-, is a well-known phenomenon [1–3, 22, 23, 40]. In the next subsections we discuss each type of observed lattice site that we unambiguously identified, comparing with *ab initio* calculations [21, 41, 40] and Mössbauer spectroscopy [42–45] studies from literature.

4.2.4.1 ideal S sites

Substitutional iron has already been observed in Si by means of Mössbauer spectroscopy and emission channeling techniques. A natural explanation for the formation of substitutional Fe is the presence of high concentrations of vacancies created during implantation [25, 45, 46]. In fact, as previously noted, the implanted ^{59}Fe produced a large amount of vacancies and thus the condition for the trapping of ^{59}Fe by single vacancies was probably satisfied. In particular, a fraction of Fe on ideal S sites is present in n^+-Si and i-Si following all annealing steps up to 900°C (Fig. 4.3), showing its considerable thermal stability and thus its high dissociation energy from the ideal S site, which was estimated in the previous study to be $E_d(\mathrm{Fe_S}) = \sim 2.6 - 3.5$ eV [26]. In comparison, the calculated binding energy of substitutional Fe to a vacancy, from Refs. [40] and [41], is $2.93 - 3.20$ eV, which, after adding the migration energy of interstitial Fe of ~ 0.7 eV, would result in an activation energy for dissociation around $3.6 - 3.9$ eV. In p^+-Si the stability of the ideal S sites seems to be much lower. It has been suggested that substitutional iron acts as a deep acceptor in Si, being negatively charged in n-Si, but neutral in p-Si [21]. This fact, together with the fact that positively charged interstitial Fe_i^+ should not easily combine with positively charged Si vacancies in p-Si (as was outlined in the introduction), may explain the larger fractions of ideal substitutional Fe observed in i- and n^+-Si since the solubility of substitutional Fe should be higher in n-Si (where it acts as counter-dopant to the donors). We also note that only a small fraction of substitutional ^{59}Fe is present at low annealing temperatures in both types of highly doped Si. This can be explained

by the fact that the quantity of vacancies is so large that most of the single vacancies aggregate into complexes of multivacancies.

4.2.4.2 near-BC sites

Iron on near-BC sites has also been observed previously using EC, as a near-S fraction [25, 26], being assigned to complexes of ^{59}Fe with multivacancies. From Fig. 4.3 one can see that ^{59}Fe is stable on near-BC positions up to 500°C in n^+-Si, while in p^+-Si it starts to dissociate from these sites already at 300°C. We also note that ^{59}Fe is stable in these sites up to 400°C when using low and moderately doped n- and p-type Si [26]. We can estimate values for the dissociation energy E_d of ^{59}Fe from near-BC sites, using [26, 47]:

$$E_d = k_B T \log \left[\frac{\nu_0 \Delta t}{N} \frac{1}{\log\left(\frac{f_{n-1}}{f_n}\right)} \right], \tag{4.1}$$

where ν_0 is the attempt frequency, Δt the annealing time, T the annealing temperature, f_n the fraction after annealing at T, f_{n-1} the fraction following the previous annealing step, i.e. before the anneal at T, and N the required number of steps for ^{59}Fe to go to another type of trap or to diffuse through the bulk or to the surface so that channeling is not observed. We consider two limits for N: an upper limit for the dissociation energy is obtained for $N = 1$, i.e. when one successful attempt is enough to move ^{59}Fe to a more stable type of trap or to initiate diffusion through the bulk or to the surface; the other case occurs when ^{59}Fe is freed from near-BC sites but is retrapped again by the same type of trap multiple times, until it diffuses through the bulk or to the surface [26]. For this last case, and supposing that ^{59}Fe on near-BC sites is due to vacancies, we take $N = 3\pi R^2 \phi$, where R is the capture radius of the multivacancy trap, while ϕ is the fluence of the implanted ^{59}Fe times the number of created vacancies by each ^{59}Fe. By using $R = 1$ nm and $\phi \sim 6 \times 10^{15}$ cm^{-2} one obtains

Table 4.1: Estimated activation energies E_d for dissociation of ^{59}Fe from near-BC sites (displaced $\sim 0.6 - 0.8$ Å from ideal S towards BC sites), and from near-T sites (displaced ~ 0.2 Å from ideal T).

Fe-site	p^+-Si	i-Si	n^+-Si
near-BC	$1.37 - 1.68$ eV	$1.91 - 2.37$ eV	$2.15 - 2.63$ eV
near-T	-	$2.57 - 3.20$ eV	$2.28 - 2.80$ eV

the estimate of N $\sim$ 550. Table 4.1 shows the E_d values for ^{59}Fe on near-BC sites by using T = 600°C in n^+-Si and T = 300°C in p^+-Si. It also shows estimated values in low-doped Si from Ref. [26]. From this table and from Fig. 4.3, supposing that the complex that this fraction is associated with is the same in all samples, since the displacements are in accordance with each other ($\sim 0.6 - 0.8$ Å), we can conclude that the stability of ^{59}Fe on near-BC sites increases from p^+- to n^+-Si. Also, one can deduce that if these sites would be related to impurity defects, these impurities would have to be present in both p^+- and n^+-Si, which obviously excludes the main dopants. Summarizing, our data show that the stability of the near-BC fraction clearly increases from p^+- to n^+-doped material, but rather than concluding that this effect is due to the direct interaction of Fe with the dopants in higher concentrations, it seems to be a consequence of an upward shift in the Fermi-level and, consequently, on the charge states of Fe and the multivacancy traps involved. We should now discuss the origin of the near-BC sites. From theoretical calculations it was proposed that a divacancy in Si should trap an Fe atom in a position that is centered between the two vacant Si sites, which corresponds to a BC site [41]. Based on emission channeling data and *ab initio* calculations, similar configurations were previously also proposed by us for a number of transition metals (Fe, Cu and Ag [48], Sn [49], Mn [50]) inside a divacancy in Ge. The theoretically predicted energy to completely dissociate the Fe atom from the divacancy in Si is $\sim$ 3.5 eV [41], which is $\sim$ 0.8 - 1.8 eV larger than our estimated values for ^{59}Fe dissociation from near-BC sites. What is particularly difficult to reconcile with theoretical predictions is the displacement of Fe from the ideal BC site towards S sites, which is indicated by our results. In that respect, however, it is worth while to point out the following. Based on *ab initio* calculations, so-called fourfold configurations have been proposed to be particularly stable for 3-6 vacancy clusters in Si [32, 33]. The fourfold configuration is based on a hexavacancy ring where extra Si atoms have been inserted in interstitial sites near BC positions, where they satisfy the dangling bonds of four Si atoms. Similar geometries were already proposed if a hexavacancy is filled up by Cu atoms instead of Si host atoms [34, 35] and it appears possible that this may be the case also for other transition metals such as Fe. It seems hence feasible that the near-BC fraction, which we observe in our experiments, represents a mixture of Fe not only inside double vacancies (where it should occupy ideal BC sites) but also inside more complicated multivacancies (where it should sit off the BC site). Such a mixture of sites in close vicinity would be quite impossible to resolve with the emission channeling technique and could result in the near-S or near-BC fractions that we have identified in the case of Fe [25, 26] (and this work), Cu [27–29] and Ag [30].

4.2.4.3 near-T sites

First we note that Fe on interstitial near-T sites is never dominant in n^+-Si. We attribute this to the high thermal stability of the near-BC fraction in n^+-Si, which keeps Fe gettered and prevents interstitial Fe from becoming prominent. In the case of i-Si [25, 26], we proposed the near-T fraction not to be free interstitial Fe, but probably also bound to vacancy-related defects. This point of view was considerably strengthened in the meantime by the theoretical study [41] published by Estreicher et al. in 2008. They predicted that interstitial Fe_i assumes metastable positions next to a vacancy or double vacancy, and that around 3 eV are needed for Fe to completely escape from this trap, while the positions of Fe in these Fe_i-V and Fe_i-V_2 complexes were predicted also somewhat shifted ($\sim 0.2 - 0.3$ Å) from the ideal T towards the AB sites. Both the displacements and expected activation energies for dissociation are similar to our data (cf. Tab. 4.1).

The observed near-T sites in p^+-Si deserve a more careful analysis due to the possible formation of FeB pairs, which is driven by the Coulomb interaction between positively charged interstitial Fe_i^+ and negatively charged substitutional B^- acceptors. The diffusion of Fe and the kinetics of the formation and dissociation of FeB pairs are quite well studied, cf. Refs. [1–4, 22–24]. Note that we have also discussed the mathematical formulae used in the following in more detail in Ref. [51], where they were applied to a similar case, the pairing of interstitial Li^+ with substitutional B^-. The time constant τ until a freely diffusing interstitial Fe^+ is captured at a B^- acceptor can be calculated by the well-known formula [2, 22, 23]

$$\tau = [4\pi R C_B D]^{-1}, \tag{4.2}$$

where R is the Coulomb capture radius, C_B the ionized B concentration, and D the diffusion coefficient of interstitial Fe_i^+ at temperature T. Using R = 47 Å, D = $1{\times}10^{-3}$ exp(-0.67 eV/k_BT) cm^2/s as in Refs. [2] and [22] and $C_B = 6.5{\times}10^{19}$ cm^{-3} (the acceptor concentration in our p^+ sample) we obtain for instance τ = 0.38 s at 20°C, 2 $\times 10^{-5}$ s at 200°C, $2{\times}10^{-8}$ s at 600°C, and $4{\times}10^{-9}$ s at 800°C. On the other hand, the breakup rate Λ of FeB pairs can be estimated using the formula [2, 51]

$$\Lambda = \nu_0 \exp(-E_d/k_BT), \tag{4.3}$$

where ν_0 is the attempt frequency, and the activation energy E_d for dissociation of the pairs is the sum of the binding energy E_b plus the migration energy E_m of interstitial Fe^+ in Si, $E_d = E_b + E_m$. Using an attempt frequency of the order of the lattice

vibrations [2, 51], $\nu_0 \sim 1{\times}10^{12}$ s^{-1}, and using $E_b = 0.65$ eV and $E_m = 0.67$ eV (from Refs. [2], [22] and [23]), one estimates that the average lifetime $1/\Lambda$ of a FeB pair is $5{\times}10^{10}$ s at 20°C, 120 s at 200°C, $4{\times}10^{-5}$ s at 600°C, and $2{\times}10^{-6}$ s at 800°C. Hence, for the high B concentration of $6.5{\times}10^{19}$ cm^{-3} the capture of diffusing Fe_i^+ into FeB pairs should always be faster than the average rate of breakup of the pairs for practical annealing temperatures. Considering that a typical ^{59}Fe channeling pattern takes a day or so to be measured, it is clear that, in the absence of any other traps, at room temperature we would always measure Fe in FeB pairs, since, even if no pairs were existing during annealing, they would form again at 20°C within a few seconds. The rms width of diffusion d during time t at temperature T is generally given by the well-known Einstein relation $d = [6D(T)t]^{1/2}$. As outlined in Ref. [2], the diffusion coefficient D of Fe is reduced in the presence of FeB pairs, so that

$$d = [6 f_i D(T) t]^{1/2} \tag{4.4}$$

should be used, where f_i is the fraction of free interstitial Fe (in contrast to the paired fraction). If f_i is calculated using, e.g., the formulae in Refs. [2], [22] and [23], one estimates for $t = 10$ min at 20°C $d = 0.04$ Å, but already 600 Å at 200°C, and 580000 Å at 600°C. It is hence clear that the fact that FeB pairs are easily formed does not mean that long-range diffusion of Fe is completely suppressed, it is only slowed down somewhat since at elevated temperatures pairs are dynamically formed and break up again. Fe has thus ample possibility to react with other defects in the sample, e.g. vacancy-type defects resulting from the implantation. What will thus determine in which complexes Fe is actually found in p^+-Si, is the stability of the FeB pairs vs the stability of Fe in other defect complexes, the relative concentrations of the trapping centers and, last but not least, their charge states. In that respect, Fe^+ and B^- are oppositely charged, so that Coulomb interaction certainly would allow the formation of FeB pairs already at room temperature. On the other hand, since the stability of Fe within vacancy defects is, in general, much higher than the stability of FeB pairs, already moderate annealing should break up FeB pairs and favor the trapping of Fe within vacancy-type complexes. Finally, if the concentration of vacancies is reduced during high temperature annealing, FeB pairs might be dominating again after cool down to room temperature.

The displacements of interstitial Fe from the ideal T sites as a function of annealing temperature (Fig. 4.4) show both abrupt and gradual changes. In the as-implanted state, Fe is found displaced from ideal T sites ~ 0.43 Å towards the AB position. However, annealing at 100°C already changes the position to the ideal T site, while increasing the annealing temperature further the displacement gradually reaches around

0.5 Å again, comparable to the value in the as-implanted state. Hence, if FeB pairs are present in considerable quantities in our sample, it is quite likely that the Fe atom may be displaced from T sites within the pairs. If one assumes simple electrostatic binding in the pair, the distance a between Fe^+ and B^- would be fully determined by the pair binding energy E_b according to [2, 22, 51]

$$a = q^2/(4\pi\epsilon\epsilon_0 E_b), \tag{4.5}$$

where $q = 1$ are the charges within the pair and $\epsilon = 11.9$ the dielectric constant of Si. Using $E_b = 0.65$ eV [2, 22] one arrives at $a = 1.86$ Å, which means that under these assumptions Fe^+ would be displaced 0.49 Å from the ideal T site towards the AB site within the pair. However, the microscopic structure of trigonal FeB pairs predicted by *ab initio* calculations [40] points towards Fe and B occupying ideal tetrahedral interstitial and substitutional sites, respectively, but with the four Si nearest neighbors around the B uniformly displaced inward by 0.27 Å. How such a breathing mode relaxation of the Si atoms around the B would influence the emission channeling effects from the neighboring ^{59}Fe is currently not feasible to predict quantitatively, however, it seems possible it might have a similar effect as a small displacement of the ^{59}Fe itself. Summarizing, there are good reasons that suggest that ^{59}Fe within FeB pairs might result in emission channeling patterns that exhibit a displacement from ideal T site patterns.

Finally we would like to compare the present interpretation of the emission channeling results on ^{59}Fe in p^+-Si with those of on-line Mössbauer spectroscopy [43, 45] from ^{57}Mn $\rightarrow$ ^{57}Fe. In these experiments, the radioactive probe ^{57}Mn ($t_{1/2} = 1.45$ min) is implanted, which decays into the well-known 14.4 keV excited Mössbauer state ^{57m}Fe ($t_{1/2} = 98$ ns). Note that characteristic thermally activated interactions of Fe have to happen within the short time interval of the 140 ns lifetime of the ^{57m}Fe probe, which requires considerably higher temperatures than in conventional annealing experiments. In any case, due to the very short time window of the Mössbauer state, this type of experiments may not be sensitive to interactions that take place between Fe and defects present in relatively low concentrations in the samples. In p^+-Si below 600°C the dominating fraction in the Mössbauer spectrum resulted from Fe in a quadrupole-split defect, which was interpreted as complexes of interstitial Fe with vacancies, Fe_i-V, and would correspond to Fe on near-T sites in our ^{59}Fe experiments. Around 600°C and above, this Fe_i-V related fraction started to disappear, for which an activation energy of ~ 1.1 eV was estimated. The reduction in the Fe_i-V related signal was accompanied by the appearance of a new quadrupole-split line in the Mössbauer spectrum, which was interpreted as resulting from the formation of ^{57}FeB

pairs during the 140 ns lifetime of ^{57m}Fe. Besides an isomer shift and quadrupole split that are characteristic for interstitial Fe, a major argument for the identification as ^{57}FeB pairs was the fact that the diffusion length of Fe is estimated to reach $\sim$ 16 Å during the lifetime of the Mössbauer state [43, 45], a value which is comparable to the average distance between B dopants. We can use eq. 4.3 in order to estimate, approximately, at which temperature such a transition of Fe from Fe_i-V complexes to FeB pairs should be observable in emission channeling experiments. Assuming that only one successful attempt against an activation energy of 1.1 eV is needed on an annealing time scale of 10 min, one arrives at a temperature of 102°C. This would mean that our as-implanted measurements would be characterized mainly by Fe in Fe_i-V complexes, which are broken at annealing temperatures higher than 100°C, leading to the increased formation of FeB complexes. As was discussed above and in Ref. [25], Fe_i-V complexes are most likely responsible for at least a part of the near-T fraction in ^{59}Fe emission channeling experiments, so they should be difficult to distinguish from FeB pairs, in which Fe occupies a similar lattice site. However, as is illustrated in Fig. 4.4, an abrupt change of displacement from ideal T sites is observed for an annealing temperature of 100°C, and in light of the Mössbauer results it is tempting to interpret this as a transition from Fe_i-V complexes to FeB pairs. Such an argument, though, may be misleading. Since the p^+ sample was kept at room temperature for four days before the annealing step at 100°C took place, such transition may have happened, at least partially, already before the first annealing step.

In conclusion, by taking into account all three types of arguments presented, kinetic estimates regarding the formation and stability of FeB pairs, their likely geometrical structure, and the comparison to Mössbauer results in similar samples, one states that it is difficult to arrive at a coherent picture of the nature of the near-T sites observed in the p^+-Si EC and Mössbauer experiments. While there are quite strong arguments that both FeB pairs and other interstitial Fe-related complexes, e.g. Fe_i-V, contribute to the measured patterns in varying fractions at all annealing temperatures, we tend to favor the view that FeB pairs may be particularly important in the as-implanted state and following the highest annealing temperatures, i.e. when the near-T sites are characterized by the relatively large displacements up to $\sim$ 0.5 Å. This interpretation, however, would require a very efficient mechanism that favors pairing of Fe and B over the formation of Fe_i-V complexes already in the as-implanted state. It seems possible that Coulomb attraction might be such a powerful driving force, for instance if directly following the implantation in p^+-Si Fe^+ would preferentially interact with B^- and, to some extent, with neutral vacancies, but it would be repelled from positively charged

vacancies.

4.2.5 Conclusion

We have given for the first time clear and direct evidence that the predominant lattice location of Fe in Si changes with the doping of the material. While in analogy to previous experiments, in low-doped Si, the same three types of lattice sites (ideal S, near-BC, and near-T) were identified with varying fractions depending on the annealing temperature, the near-T sites were clearly dominant in p^+-Si, and near-BC or ideal S sites in n^+-Si. We show evidence that the near-BC sites are due to the same type of complex after all annealing steps as a result of the similar displacement from BC towards S sites, independently of the type of silicon used. However, their thermal stability increases when the doping is changed from p^+ to i and further to n^+. The dominant lattice sites of Fe in n^+-Si seem to be well characterized for all annealing temperatures (except maybe T_A=600°C) by the incorporation of Fe into vacancy-related complexes, either into single vacancies which leads to Fe on ideal substitutional sites, or multiple vacancies, which leads to its incorporation near BC sites. We point out that this strong interaction between Fe and vacancy-type defects in n^+-Si and the high thermal stability of the formed complexes can provide an explanation for the P-diffusion gettering effect, where Fe is gettered in a less electrically active form in the n^+-doped surface region created during the in-diffusion of phosphorus.

In contrast, in p^+-Si the major fraction of Fe is clearly interstitial (near-T or ideal T) for all annealing temperatures. The microscopic nature of the interstitial sites in p^+-Si as function of annealing temperature is not clear at the moment, although the formation of FeB pairs is obviously expected to play a major role. Arguments have been presented that point towards the possibility that the lattice site of Fe within FeB pairs is considerably displaced (up to 0.5 Å) from the ideal T site towards the AB site. While this would be quite well in accordance with the lattice site estimated from the measured pair binding energy found in the literature, it is not obvious to reconcile it with the structure of the FeB pair predicted by *ab initio* calculations, which consists of Fe on an ideal T site with only a breathing mode relaxation (0.27 Å inward) of the four Si atoms surrounding the B atom. In any case, a considerable displacement of Fe in FeB pairs would mean that its site is difficult to distinguish from the displaced T sites found in low-doped or n^+-Si, which were attributed to interstitial Fe next to vacancy-type defects.

Bibliography

[1] E. R. Weber, Transition metals in silicon, Appl. Phys. A 30 (1983) 1.

[2] A. A. Istratov, H. Hieslmair, E. R. Weber, Iron and its complexes in silicon, Appl. Phys. A 69 (1999) 13.

[3] A. A. Istratov, H. Hieslmair, E. R. Weber, Iron contamination in silicon technology, Appl. Phys. A 70 (2000) 489.

[4] S. M. Myers, M. Seibt, W. Schröter, Mechanisms of transition-metal gettering in silicon, J. Appl. Phys. 88 (2000) 3795.

[5] A. A. Istratov, T. Buonassisi, M. D. Pickett, M. Heuer, E. R. Weber, Control of metal impurities in "dirty" multicrystalline silicon for solar cells, Mater. Sci. Eng. B 134 (2006) 282.

[6] R. A. Brown, O. Kononchuk, G. A. Rozgonyi, S. Koveshnikov, A. P. Knights, P. Simpson, F. Gonzalez, Impurity gettering to secondary defects created by MeV ion implantation in silicon, J. Appl. Phys. 84 (1998) 2459.

[7] G. M. Dalpian, A. J. R. D. Silva, A. Fazzio, Theoretical investigation of a possible Mn_xSi_{1-x} ferromagnetic semiconductor, Phys. Rev. B 68 (2003) 1133101.

[8] F. Bernardini, S. Picozzi, A. Continenza, Energetic stability and magnetic properties of Mn dimers in silicon, Appl. Phys. Lett. 84 (2004) 2289.

[9] Z. Z. Zhang, B. Partoens, K. Chang, F. M. Peeters, First-principles study of transition metal impurities in Si, Phys. Rev. B 77 (2008) 155201.

[10] W. Zhu, Z. Zhang, E. Kaxiras, Dopant-assisted concentration enhancement of substitutional Mn in Si and Ge, Phys. Rev. Lett. 100 (2008) 027205.

[11] H. Chen, W. Zhu, E. Kaxiras, Z. Zhang, Optimization of Mn doping in group-IV-based dilute magnetic semiconductors by electronic codopants, Phys. Rev. B 79 (2009) 235202.

[12] F. Kwen, R. Leitsmann, F. Bechstedt, Mn and Fe doping of bulk Si: Concentration influence on electronic and magnetic properties, Phys. Rev. B 80 (2009) 045203.

[13] D. F. Fenning, J. Hofstetter, M. I. Bertoni, G. Coletti, B. Lai, C. D. C. nizo, T. Buonassisi, Precipitated iron: A limit on gettering efficacy in multicrystalline silicon, J. Appl. Phys. 113 (2013) 044521.

[14] S. M. Myers, G. A. Petersen, C. H. Seager, Binding of cobalt and iron to cavities in silicon, J. Appl. Phys. 80 (1996) 3717.

[15] G. Coletti, P. C. P. Bronsveld, G. Hahn, W. Warta, D. Macdonald, B. Ceccaroli, K. Wambach, N. L. Quang, J. M. Fernandez, Impact of metal contamination in silicon solar cells, Adv. Funct. Mater. 21 (2011) 879.

[16] A. Bentzen, A. Holt, Overview of phosphorus diffusion and gettering in multicrystalline silicon, Mater. Sci. Eng. B 159 (2009) 228.

[17] S. Dubois, N. Enjalbert, F. Warchol, S. Martinuzzi, Is impurity gettering or passivation by hydrogen the improvement key of mc-Si solar cells during processing steps?, Mater. Sci. Eng. B 159 (2009) 239.

[18] I. Prichaud, S. Martinuzzi, J. Degoulange, C. Trassy, Limiting factors of gettering treatments in mc-Si wafers from the metallurgical route, Mater. Sci. Eng. B 159 (2009) 256.

[19] S. P. Phang, D. MacDonald, Direct comparison of boron, phosphorus, and aluminum gettering of iron in crystalline silicon, J. Appl. Phys. 109 (2011) 073521.

[20] M. Syre, S. Karazhanov, B. R. Olaisen, A. Holt, B. G. Svensson, Evaluation of possible mechanisms behind P gettering of iron, J. Appl. Phys. 110 (2011) 024912.

[21] D. J. Backlund, S. K. Estreicher, Ti, Fe, and Ni in Si and their interactions with the vacancy and the a center: A theoretical study, Phys. Rev. B 81 (2010) 235213.

[22] L. C. Kimerling, J. L. Benton, Electronically controlled reactions of interstitial iron in silicon, Physica B 116 (1983) 297.

[23] G. Zoth, W. Bergholz, A fast, preparation-free method to detect iron in silicon, J. Appl. Phys. 67 (1990) 6764.

[24] J. L. Benton, P. A. Stolk, D. J. Eaglesham, D. C. Jacobson, J.-Y. Cheng, J. M. Poate, N. T. Ha, T. E. Haynes, S. M. Myers, Iron gettering mechanisms in silicon, J. Appl. Phys. 80 (1996) 3275.

[25] U. Wahl, J. G. Correia, E. Rita, J. P. Araújo, J. C. Soares, Lattice sites of implanted Fe in Si, Phys. Rev. B 72 (2005) 014115.

[26] U. Wahl, J. G. Correia, E. Rita, J. P. Araújo, J. C. Soares, Fe and Cu in Si: Lattice sites and trapping at implantation-related defects, Nucl. Instrum. Methods Phys. Res. B 253 (2006) 167.

[27] U. Wahl, J. G. Correia, A. Vantomme, G. Langouche, Lattice location of implanted Cu in Si, Physica B 273 (1999) 367.

[28] U. Wahl, A. Vantomme, G. Langouche, J. P. Araújo, L. Peralta, J. G. Correia, Lattice location of implanted Cu in highly doped Si, Appl. Phys. Lett. 77 (2000) 2142.

[29] U. Wahl, A. Vantomme, G. Langouche, J. G. Correia, Lattice location and stability of ion implanted Cu in Si, Phys. Rev. Lett. 84 (2000) 1495.

[30] U. Wahl, J. G. Correia, A. Vantomme, Lattice location of implanted Ag in Si, Nucl. Instrum. Methods Phys. Res. B 190 (2002) 543.

[31] C. K. Tang, L. Vines, V. P. Markevich, B. G. Svensson, E. V. Monakhov, Divacancy-iron complexes in silicon, J. Appl. Phys. 113 (2013) 044503.

[32] D. V. Makhov, L. J. Lewis, Stable fourfold configurations for small vacancy clusters in silicon from *ab initio* calculations, Phys. Rev. Lett. 92 (2004) 255504.

[33] S. Lee, G. S. Hwang, Theoretical determination of stable fourfold coordinated vacancy clusters in silicon, Phys. Rev. B 78 (2008) 125310.

[34] S. K. Estreicher, Rich chemistry of copper in crystalline silicon, Phys. Rev. B 60 (1999) 5375.

[35] S. K. Estreicher, Structure and dynamics of point defects in crystalline silicon, Phys. Status Solidi B Basic Res. 217 (2000) 513.

[36] G. D. Watkins, Deep Centers in Semiconductors, Gordon and Breach, New York, 1986.

[37] J. F. Ziegler, SRIM-2003, Nucl. Instrum. Methods Phys. Res. B 219 (2004) 1027.

[38] S. Agostinelli, *et al.*, GEANT4 - a simulation toolkit, Nucl. Instrum. Methods Phys. Res. A 506 (2003) 250.

[39] T. Sadoh, K. Tsukamoto, A. Baba, D. Bai, A. Kenjo, T. Tsurushima, H. Mori, H. Nakashima, Deep level of iron-hydrogen complex in silicon, J. Appl. Phys. 82 (1997) 3828.

[40] M. Sanati, N. G. Szwacki, S. K. Estreicher, Interstitial Fe in Si and its interactions with hydrogen and shallow dopants, Phys. Rev. B 76 (2007) 125204.

[41] S. K. Estreicher, M. Sanati, N. G. Szwacki, Iron in silicon: Interactions with radiation defects, carbon, and oxygen, Phys. Rev. B 77 (2008) 125214.

[42] H. P. Gunnlaugsson, G. Weyer, N. E. Christensen, M. Dietrich, M. Fanciulli, K. Bharuth-Ram, R. Sielemann, A. Svane, On the kinetics of the formation of interstitial Fe-vacancy pairs in silicon at high temperatures, Physica B 340 (2003) 532.

[43] H. P. Gunnlaugsson, K. Bharuth-Ram, M. Dietrich, M. Fanciulli, H. O. U. Fynbo, G. Weyer, Formation of $Fe_i - B$ pairs in silicon at high temperatures, Hyperfine Interact. 169 (2006) 1315.

[44] G. Weyer, A. Burchard, M. Fanciulli, V. N. Fedoseyev, H. P. Gunnlaugsson, V. I. Mishin, R. Sielemann, The electronic configuration of substitutional Fe in silicon, Physica B 273 (1999) 363.

[45] G. Weyer, Defects in semiconductors - results from Mössbauer spectroscopy, Hyperfine Interact. 177 (2007) 1.

[46] H. P. Gunnlaugsson, G. Weyer, M. Dietrich, M. Fanciulli, K. Bharuth-Ram, R. Sielemann, Charge state dependence of the diffusivity of interstitial Fe in silicon detected by Mössbauer spectroscopy, Appl. Phys. Lett. 80 (2002) 2657.

[47] L. M. Pereira, U. Wahl, S. Decoster, J. G. Correia, M. R. D. Silva, A. Vantomme, J. P. Araújo, Direct identification of interstitial Mn in heavily p-type doped GaAs and evidence of its high thermal stability, Appl. Phys. Lett. 98 (2011) 201905.

[48] S. Decoster, S. Cottenier, B. D. Vries, H. Emmerich, U. Wahl, J. G. Correia, A. Vantomme, Transition metal impurities on the bond-centered site in germanium, Phys. Rev. Lett. 102 (2009) 065502.

[49] S. Decoster, S. Cottenier, U. Wahl, J. G. Correia, A. Vantomme, Lattice location study of ion implanted Sn and Sn-related defects in Ge, Phys. Rev. B 81 (2010) 155204.

[50] S. Decoster, S. Cottenier, U. Wahl, J. G. Correia, L. M. C. Pereira, C. Lacasta, M. R. D. Silva, A. Vantomme, Diluted manganese on the bond-centered site in germanium, Appl. Phys. Lett. 97 (2010) 151914.

[51] U. Wahl, the ISOLDE collaboration, Emission channeling studies of Li in semiconductors, Phys. Rep. 280 (1997) 145.

4.3 Article II - Influence of the doping on the lattice sites of Fe in Si

D. J. Silva[1], U. Wahl[2], J. G. Correia[2], J. P. Araújo[1]
[1] IFIMUP and IN-Institute of Nanoscience and Nanotechnology, Departamento de Física e Astronomia da Faculdade de Ciências da Universidade do Porto, Rua do Campo Alegre 687, 4169-007 Porto, Portugal
[2] Instituto Superior Técnico/Instituto Tecnológico e Nuclear, Universidade de Lisboa, 2695-066 Bobadela, Portugal

AIP Conference Proceedings **1583**, 24 (2014)

abstract

We report on the lattice location and thermal stability of Fe in n^+- and p^+-type silicon. By means of emission channeling we have observed Fe on ideal substitutional sites, sites located in between bond-centered (BC) and substitutional sites, and sites displaced from tetrahedral towards anti-bonding sites. Here, we focus our analysis on the identification of Fe displaced $0.4 - 0.6$ Å from BC sites and the influence of the doping on the stability of these sites. Fe on near-BC sites is found to be more thermally stable in n^+-type Si than in low doped or p^+-type Si, and seems to be related to multiple vacancy defects. We suggest that the complexes which trap Fe near BC sites, as well as the formation of substitutional Fe, may play a crucial role in P-diffusion gettering.

4.3.1 Introduction

The structural and electrical properties of transition metal impurities (TMs) have been an important subject in the manufacturing of Si-based devices. In fact, depending on the complexes that TMs form, deep levels are introduced within the silicon bandgap, which are unwanted in most applications, e.g. microelectronics or photovoltaics [1, 2]. One of the most harmful TMs is Fe due to its presence in comparatively high concentrations during Si production, e.g. iron is present in silica. Gettering has therefore been pointed out as the most effective solution to reduce its malicious effect [3]. Although many gettering procedures have been developed, in particular in solar cell processing P-diffusion (involving n^+ regions) has gained eminence over the past

years. The microscopic nature of this gettering mechanism is still not completely clear. It has been suggested, however, that the interaction of Fe with native defects, in particular related to vacancies, might play a role during P-diffusion gettering [4–6].

One way to explore the microscopic nature of the interaction of Fe with vacancy-related defects is to study the influence of the doping on the lattice sites of implanted Fe in silicon. A unique technique to investigate the sites of impurities is electron emission channeling (EC) which relies on implanting single crystals with radioactive probe atoms that decay by the emission of β^- particles. The β^- particles experience channeling effects along crystallographic directions depending on the lattice site occupied by the probe atom. EC was previously used to investigate the lattice location of the ^{59}Fe probe atom in different lightly doped Si samples (with resistivities above ~ 0.01 Ωcm) [7, 8]. Three lattice sites were observed: ideal substitutional sites (S), displaced from bond-centered towards substitutional sites (near-BC) and displaced from tetrahedral towards anti-bonding sites (near-T). It seemed, however, that in lightly doped Si the doping was not influencing the preferred lattice sites of implanted Fe, presumably since the defect production during Fe implantation shifts the Fermi level towards midgap, thus compensating the effect of doping.

In this work, we present results on the lattice location of Fe in heavily doped n^+- and p^+-type silicon, with a special focus on the identification and stability of Fe on near-BC sites. A correlation of our findings between the high thermal stability of Fe on near-BC and ideal S sites in n^+-type Si and P-diffusion gettering is given. A more complete description of the experimental results and their comprehensive discussion is about to be published elsewhere [9].

4.3.2 Experiment

The long-lived isotope ^{59}Fe ($t_{1/2} = 44.6$ d) was introduced in n^+-type (n^+-Si; resistivity of < 0.001 Ωcm) and p^+-type (p^+-Si; < 0.002 Ωcm) Cz silicon samples by implanting the precursor isotope ^{59}Mn ($t_{1/2} = 4.6$ s), at the on-line isotope mass separator facility ISOLDE at CERN, with 60 keV. The fluence was 6×10^{12} cm^{-2}. The depth profiles of the implanted ^{59}Fe and created vacancies were estimated using the SRIM code [10]. The implanted ^{59}Fe profile is approximately a Gaussian distribution centered at 558 Å with a straggling of 213 Å and a peak concentration of 1.1×10^{18} cm^{-3}. At 0 K, each implanted ^{59}Fe creates 900 vacancies along its path, producing a peak concentration of $\sim 5 \times 10^{21}$ cm^{-3}. The dopants of the n^+- and p^+-Si samples were, respectively,

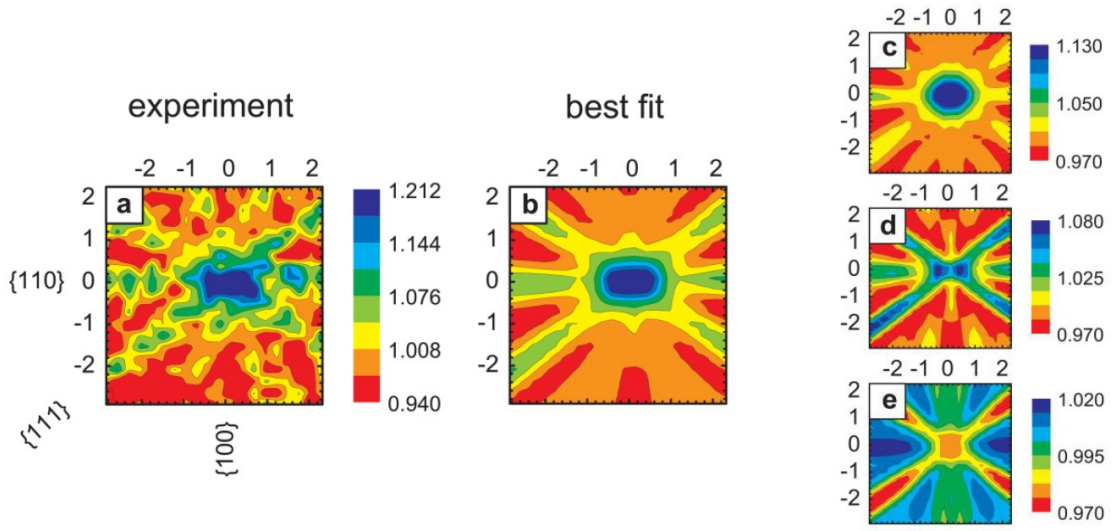

Figure 4.5: Comparison of the (**a**) two-dimensional experimental and (**b**) best fit of theoretical emission channeling patterns from ^{59}Fe in n^+-Si in the vicinity of <110> in the as-implanted state. Panels (**c**), (**d**) and (**e**) represent the contributions to the EC patterns of the ideal S site (21%), near-BC site (50%) and near-T site (23%) patterns, respectively.

phosphorus and boron. Starting a few days after the implantation, the samples were mounted on a goniometer made of Ta and Mo and annealed *in situ* up to 900°C in steps of 100°C, during 10 min. After each annealing step, the β^--emission yield was measured at room temperature using a position and energy-sensitive detector in the vicinity of <110>, <100> and <111> for the n^+-Si and <211>, <100> and <111> for the p^+-Si samples.

4.3.3 Results

The two-dimensional experimental channeling patterns were fitted by using calculated beta emission yields, obtained with the so-called *manybeam* formalism for electron channeling in single crystals, in order to quantitatively characterize the occupied lattice sites of ^{59}Fe. The emission probability of the substitutional (S), hexagonal (H), tetrahedral (T), bond-center (BC), anti-bonding (AB), split (SP) and the so-called DS, DT, Y and C sites, as well as <111>, <100> and <110> displacements between these positions were considered in the fitted patterns [11].

In analogy to the previous experiments in low-doped Si [7, 8], the same three types of

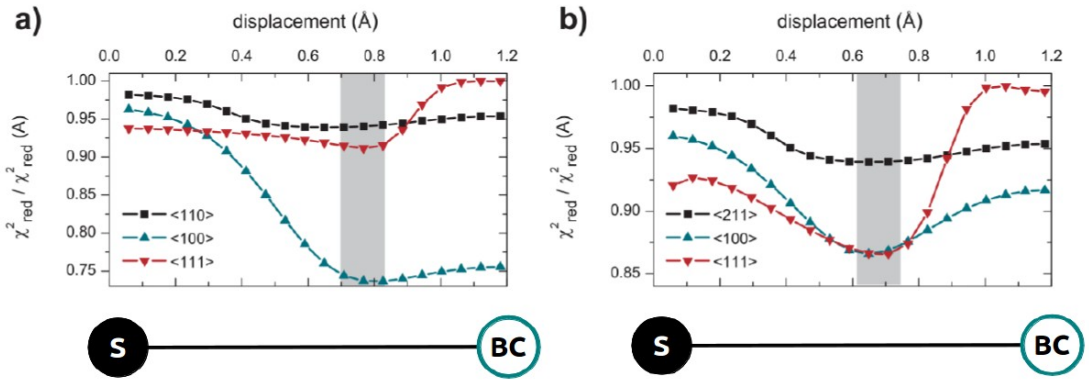

Figure 4.6: Reduced χ^2 of the fits to the experimental emission yields as a function of displacement from ideal S to ideal BC sites following room temperature implantation (**a**) in n^+-Si, for <110>, <100>, and <111>, and (**b**) in p^+-Si for <211>, <100>, and <111>. The reduced chi square $\chi^2_{red}/\chi^2_{red}$(A) is normalized to single- or double-site fits, where for the <100> and <111> data A represents sites ideally aligned with the axis, i.e. ideal S or ideal T, while for the <110> and <211> data A represents a combination of ideal S + near-T sites.

lattice sites (ideal S, near-BC and near-T sites) were necessary to obtain the best fits. As an example, Fig. 4.5 shows the two-dimensional experimental emission channeling patterns around the <110> direction from as-implanted ^{59}Fe in n^+-Si. Also shown are the calculated emission yields from ideal S, near-BC and near-T sites. Note that the comparatively strong {111} planar channeling in the experimental pattern is a characteristic of the presence of near-BC sites. Also the fact that the axial <110> channeling peak appears spread along the {110} plane indicates that it consists of a superposition of the single peak of ideal S sites and the double peak characteristic for near-BC sites.

To illustrate in more detail how the occupied lattice sites are identified, we use the determination of the most likely position of Fe in between S and BC sites as an example. In Fig. 4.6 we plotted for the as-implanted state the reduced χ^2 for multi-site fits as a function of <111> displacements from the ideal positions. In case of the <111> and <100> patterns, the reduced χ^2 is plotted for 2-site fits, where the first site is kept ideally aligned with the <111> or <100> rows (i.e. S or T sites), while the position of the second site is moved along all equivalent <111> directions from the ideally aligned position. One concludes that the position of the second site is roughly around 0.6-0.8 Å from the axis. Note however, that for <111> and <100> patterns

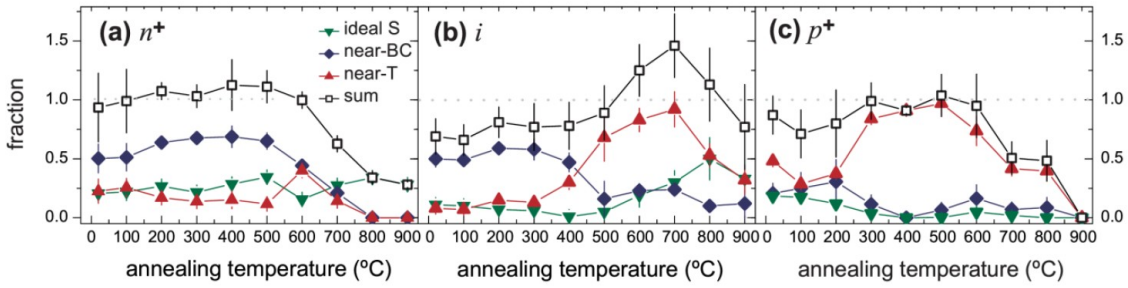

Figure 4.7: Annealing temperature dependence of the ideal S, near-BC and near-T fractions in n^+-Si, p^+-Si, and low doped silicon (i-Si). Data for i-Si are from Refs. [7, 8].

the <111> displacements S→BC, S→AB, T→AB, T→H are completely equivalent, so that these patterns do not allow to independently determine whether the displacement is with respect to S or T sites. In order to distinguish between S or T sites, <110> or <211> patterns are needed (as illustrated already in Fig. 4.5). In case of the <110> or <211> data in Fig. 4.6, the reduced χ^2 is plotted for 3-site fits, where the first site is kept fixed at the ideal S position, the second site is kept fixed at a position 0.45 Å from T sites towards AB sites, while the position of the third site is shifted from ideal S towards the BC position as indicated. Note that the exact choice of the interstitial site in this case, e.g. ideal T vs a shift from T to AB, is not very critical, since the <110> or <211> patterns vary relatively little when the position of the interstitial fraction is varied. Overall, one arrives at the result that the most likely displacement in between S and BC sites is as indicated by the grey shaded area. It is clear from this analysis, that for instance major fractions of ^{59}Fe on ideal BC sites can be ruled out, since the χ^2 of fit becomes significantly worse for the <111> patterns, and to lesser extent also for <100> patterns. On the other hand, the possibility of minor fractions on ideal BC sites in addition to a major displaced fraction exists. To quantitatively assess this possibility it would require performing 3- or 4-site fits. However, in this case the fit results become increasingly ambiguous.

Figure 4.7 shows the annealing temperature dependence of the fractions of ^{59}Fe on the identified lattice sites in n^+- and p^+-Si, in comparison to the average results of low doped Si from Refs. [7, 8]. While the same three types of lattice sites were identified in analogy to the previous experiments in low-doped Si, the preferred sites of Fe change clearly with the doping of the material. While near-T interstitial sites were dominant in p^+-Si ($\sim$ 91% after annealing at 400°C), the majority of Fe occupied near-BC sites in n^+-Si ($\sim$ 65% after annealing at 500°C).

4.3.4 Discussion and Conclusion

Comparing these EC experiments with theoretical predictions, one concludes that the ideal S and near-BC sites result from the interaction of iron with vacancy-type defects. In fact, *ab initio* calculations have shown that Fe prefers ideal S sites when trapped by single vacancies, while divacancies should trap iron on ideal BC sites [12]. What cannot be explained so far by theory is the displacement of Fe from the ideal BC site towards S sites suggested by our data. It seems, however, feasible that the near-BC fraction represents a mixture of Fe not only inside divacancies but also inside more complicated multivacancies where it may sit somewhat off the ideal BC site, e.g. inside multivacancies with fourfold configurations based on hexavacancy rings [13, 14].

As is discussed in detail in Ref. [9], the microscopic nature of the near-T sites in p^+-Si is not totally clear at the moment, although the positive charge state of interstitial Fe_i^+ in p^+-Si and the formation of Fe^+B^- pairs are obviously expected to play a major role. In that respect it seems that the sites of Fe within Fe^+B^- pairs are substantially displaced (up to 0.5 Å) from the ideal T site towards the AB site. While this would agree with the lattice site estimated from the measured pair binding energy of 0.65 eV found in the literature, assuming a simple Coulomb interaction between Fe^+ and Fe^+B^-, it is not obvious to reconcile it with the structure of the Fe^+B^- pair predicted by *ab initio* calculations, consisting of Fe on an ideal T site with a breathing mode relaxation (0.27 Å inward) of the four Si atoms surrounding the B atom [15].

To conclude, we have studied the influence of n^+ and p^+ doping on the lattice sites of implanted iron in silicon. While near-T interstitial sites are prominent in p^+-type silicon, Fe clearly prefers near-BC sites in n^+-type silicon. Arguments have been given to support that near-BC sites result from the trapping of Fe into multivacancy defects produced during implantation. We have shown that the thermal stability of near-BC Fe is higher in n^+- than in low doped or p^+-Si. Remarkably, following annealing at 500°C more than 90% of Fe in n^+-Si remains trapped in vacancy-related complexes, i.e. in near-BC or ideal S-sites. We hence propose that the strong interaction with vacancy-type defects and the thermally stable binding of Fe to them, both of which are characteristic for n^+-Si, play a crucial role in the P-diffusion gettering process, where Fe is gettered in the n^+-doped surface region created during the in-diffusion of phosphorus.

Bibliography

[1] E. R. Weber, Transition metals in silicon, Appl. Phys. A 30 (1983) 1.

[2] A. A. Istratov, H. Hieslmair, E. R. Weber, Iron and its complexes in silicon, Appl. Phys. A 69 (1999) 13.

[3] S. M. Myers, M. Seibt, W. Schröter, Mechanisms of transition-metal gettering in silicon, J. Appl. Phys. 88 (2000) 3795.

[4] A. Bentzen, A. Holt, Overview of phosphorus diffusion and gettering in multicrystalline silicon, Mater. Sci. Eng. B 159 (2009) 228.

[5] S. P. Phang, D. MacDonald, Direct comparison of boron, phosphorus, and aluminum gettering of iron in crystalline silicon, J. Appl. Phys. 109 (2011) 073521.

[6] M. Syre, S. Karazhanov, B. R. Olaisen, A. Holt, B. G. Svensson, Evaluation of possible mechanisms behind P gettering of iron, J. Appl. Phys. 110 (2011) 024912.

[7] U. Wahl, J. G. Correia, E. Rita, J. P. Araújo, J. C. Soares, Lattice sites of implanted Fe in Si, Phys. Rev. B 72 (2005) 014115.

[8] U. Wahl, J. G. Correia, E. Rita, J. P. Araújo, J. C. Soares, Fe and Cu in Si: Lattice sites and trapping at implantation-related defects, Nucl. Instrum. Methods Phys. Res. B 253 (2006) 167.

[9] *Article I.* D. J. Silva, U. Wahl, J. G. Correia, J. P. Arajo, Influence of n^+ and p^+ doping on the lattice sites of implanted Fe in Si, J. Appl. Phys. 114 (2013) 103503.

[10] J. F. Ziegler, SRIM-2003, Nucl. Instrum. Methods Phys. Res. B 219 (2004) 1027.

[11] U. Wahl, J. G. Correia, A. Vantomme, G. Langouche, Lattice location of implanted Cu in Si, Physica B 273 (1999) 367.

[12] S. K. Estreicher, M. Sanati, N. G. Szwacki, Iron in silicon: Interactions with radiation defects, carbon, and oxygen, Phys. Rev. B 77 (2008) 125214.

[13] D. V. Makhov, L. J. Lewis, Stable fourfold configurations for small vacancy clusters in silicon from *ab initio* calculations, Phys. Rev. Lett. 92 (2004) 255504.

[14] S. K. Estreicher, Rich chemistry of copper in crystalline silicon, Phys. Rev. B 60 (1999) 5375.

[15] M. Sanati, N. G. Szwacki, S. K. Estreicher, Interstitial Fe in Si and its interactions with hydrogen and shallow dopants, Phys. Rev. B 76 (2007) 125204.

4.4 Article III - Lattice location and thermal stability of implanted nickel in silicon studied by on-line emission channeling

D. J. Silva[1], U. Wahl[2], J. G. Correia[2], L. M. C. Pereira[3], L. M. Amorim[3], M. R. da Silva[3], E. Bosne[2,5], J. P. Araújo[1]

[1] IFIMUP and IN-Institute of Nanoscience and Nanotechnology, Departamento de Física e Astronomia da Faculdade de Ciências da Universidade do Porto, Rua do Campo Alegre 687, 4169-007 Porto, Portugal

[2] Centro de Ciências e Tecnologias Nucleares, Instituto Superior Técnico, Universidade de Lisboa, 2686-953 Sacavém, Portugal

[3] Instituut voor Kern- en Stralingsfysica, KU Leuven, 3001 Leuven, Belgium

[4] Centro de Física Nuclear da Universidade de Lisboa, 1649-003 Lisboa, Portugal

[5] Departamento de Física da Universidade de Aveiro, 3810-193 Aveiro, Portugal

Journal of Applied Physics **115**, 023504 (2014)

abstract

We have studied the lattice location of implanted nickel in silicon, for different doping types (n, n^+ and p^+). By means of on-line emission channeling, ^{65}Ni was identified on three different sites of the diamond lattice: ideal substitutional sites, displaced bond-center towards substitutional sites (near-BC) and displaced tetrahedral interstitial towards anti-bonding sites (near-T). We suggest that the large majority of the observed lattice sites are not related to the isolated form of Ni but rather to its trapping into vacancy-related defects produced during the implantation. While near-BC sites are prominent after annealing up to 300-500°C, near-T sites are preferred after $500-600$°C anneals. Long-range diffusion starts at $600-700$°C. We show evidence of Ni diffusion towards the surface and its further trapping on near-T sites at the "$R_p/2$" region, providing a clear picture of the microscopic mechanism of Ni gettering by vacancy-type defects. The high thermal stability of near-BC sites in n^+-type Si, and its importance for the understanding of P-diffusion gettering are also discussed.

4.4.1 Introduction

The search for more reliable silicon-based technologies has been hampered by the presence of transition metals (TMs) as contaminants. Because TMs act as recombination centers, due to the introduction of deep levels in the silicon bandgap, the reduction of minority carrier lifetime hinders, e.g., the efficiency of silicon solar cells, even when TMs are present at low concentrations [1–4]. Together with copper, nickel is an ultrafast diffuser in Si, with an often quoted activation energy for migration of E_m = 0.47 eV [5], which has recently been proposed to be as low as 0.15 eV [6]. Although being one of the less studied, Ni is one of the most harmful TMs. Efforts have been made to both passivate its malicious electrical effect with, e.g., hydrogenation [7], or by moving the Ni impurity away from the active area of the device with the so called gettering procedures, such as by trapping Ni into defects [8, 9] or the use of P-diffusion to getter Ni into n^+ rich regions [10, 11].

First principle theoretical studies have concluded that interstitial tetrahedral Ni does not have energy levels in the Si bandgap [5, 6]. The reason for its harmful effect comes from the fact that the solubility of the harmless and fast diffusing interstitial nickel is so small [12] that it is normally trapped into defects, forming, in particular, electrically active silicides when agglomeration of Ni takes place [1, 11, 13]. The introduction of deep levels by nickel contamination will thus depend on its ability to form complexes with other defects. Although the information is scarce, a way to distinguish different complexes is by observing the different lattice sites of Ni. For instance, single vacancies will in principle trap Ni atoms on substitutional sites [5, 6] while divacancies might trap Ni on other sites, e.g. bond-centered sites. Moreover, the microscopic picture of Ni gettering by defects and the mechanism of P-diffusion gettering are still not yet well understood. The knowledge of the lattice sites of Ni might thus provide crucial information for the clarification of such complex mechanisms.

Beta emission channeling (EC) is a unique technique to investigate the preferred lattice sites of low concentrations of impurities following implanting single crystals with radioactive probe atoms which decay by emitting β^- particles. On their way out of the crystal, β^- particles experience channeling effects along low-index crystallographic directions, depending on the lattice site occupied by the probe atom. EC has been used to study the lattice sites of long-lived TM isotopes in Si, such as ^{67}Cu ($t_{1/2}$ = 2 d) [14–17], ^{59}Fe (45 d) [17–19] and ^{111}Ag (7.45 d) [20], by means of off-line experiments. Studies of other TMs, in particular Ni, Co and Mn, were not feasible since the only suitable isotopes were too short-lived in order to be used off-line. However, this

situation has recently changed with the installation of an on-line EC setup at the isotope mass separator facility ISOLDE at CERN [21]. This online setup has allowed to study the lattice location of: ^{56}Mn ($t_{1/2}$ = 2.56 h) in Ge [22], GaAs [23, 24], GaN [25], and ZnO [26]; ^{61}Co (1.6 h) in ZnO [26]; and ^{65}Ni (2.5 h) in ZnO [27].

Since Ni is a very fast diffuser, only the interaction with defects, such as other impurities, other Ni atoms, self-interstitials or vacancy-type defects, can immobilize Ni atoms even at room temperature. Anyhow, the properties of Ni as a fast diffuser might influence which traps are preferred. For instance, isolated interstitial nickel prevails in the neutral charge state, which makes its interaction with immobile charged dopants unlikely. In fact, the formation of pairs driven by Coulomb interactions, e.g. NiB, have not been experimentally reported. On the contrary, while pairing with Si interstitials is also not expected [6], neutral Ni can be effectively trapped by vacancies. Indeed, clusters of vacancies are one of the most effective gettering centers [9, 28]. In that respect, defects in irradiated silicon have been reported to getter Ni in two different regions: around the peak concentration of the implanted impurity, known as the "R_p" region, and midway between the peak concentration and the surface, known as the "$R_p/2$" region [8, 29, 30]. It was suggested by positron annihilation spectroscopy that the latter region might correspond to the vacancy peak concentration produced by the implanted Si [31, 32].

Changing the doping type may also influence the preferred sites of Ni since the stability of its various configurations are directly coupled to the electron-hole charge equilibrium. Although isolated tetrahedral interstitial nickel has no acceptor neither donor levels in the silicon bandgap, other configurations have the possibility to be electrically active. For instance, substitutional nickel has two acceptor levels close to the conduction band, $E_C - 0.09$ eV and $E_C - 0.43$ eV, and one donor level close to the valence band, $E_V + 0.17$ eV [5, 33]. Depending on the Fermi level, the different charge states will have, in principle, different activation energies for their formation and dissociation. The consequence will thus be the observation of different temperatures for which the corresponding complexes are annealed.

Here, we present detailed results on the lattice location of the transition metal Ni in different types of Si, which were obtained from on-line EC experiments using the short-lived isotope ^{65}Ni ($t_{1/2}$ = 2.5 h).

4.4.2 Experiment

Three Czochralski grown silicon samples were studied: (**i**) lightly doped n-type Si (n-Si) with a resistivity of $7.3 - 12$ Ωcm, doped with $2{\times}10^{15}$ cm^{-3} phosphorus; (**ii**) n^+-type Si (n^+-Si) with a resistivity of $(4.5 - 5.7){\times}10^{-3}$ Ωcm, doped with $2.5{\times}10^{19}$ cm^{-3} arsenic; (**iii**) p^+-type Si (p^+-Si) with a resistivity of $(1 - 5){\times}10^{-3}$ Ωcm, doped with $6{\times}10^{19}$ cm^{-3} boron. All samples had $< 111 >$ surfaces.

^{65}Ni was implanted at the on-line isotope separator facility ISOLDE at CERN. ISOLDE provides mass-separated beams of radioactive Ni isotopes, produced by nuclear fission of uranium carbide UC_2 targets induced by 1.4 GeV proton beams. A laser ion source was used for chemically selective ionization of the desired element. Unlike typical EC experiments using long-lived TM isotopes, e.g. ^{59}Fe, ^{67}Cu and ^{111}Ag, where the samples are implanted and measured in different setups, the ^{65}Ni experiments were carried out using an on-line setup where both implantation and measurement took place [21]. Since the half-life of ^{65}Ni is relatively short ($t_{1/2}$ = 2.5 h), carrying out the measurements on-line is indispensable. Therefore, for each experiment, the sample was mounted on a goniometer inside the on-line setup, at the end of one of the ISOLDE general purpose separator beam lines. ^{65}Ni was implanted before each annealing treatment, into the three samples with an energy of 50 keV, under an angle of 17° from the surface normal in order to avoid channeling implantation. The accumulated fluences were 3.2×10^{13} cm^{-2} in n^+- and p^+-Si and 2.4×10^{13} cm^{-2} in n-Si. The anneals were performed *in situ* up to 700°C in steps of 100°C, during 10 min, under vacuum better than 10^{-5} mbar. The warm-up times were relatively short (under 5 minutes, even for the highest annealing temperatures). The time required to cool the sample down to room temperature (before starting the measurements) was significantly longer, up to 30 minutes for the highest annealing temperatures.

Angular-dependent emission yields of the β^- particles emitted during radioactive decay were measured at room temperature, in the vicinity of the $< 110 >$, $< 211 >$, $< 100 >$ and $< 111 >$ directions. These patterns were recorded using a position- and energy-sensitive detection system similar to that described in Ref. [34]. As mentioned above, given the relatively short half-life of ^{65}Ni, this system was installed on-line and upgraded with self-triggering readout chips for the Si pad detectors, enabling measurements during and/or immediately after implantation with count rates of up to several kHz [21]. The electrons that are backscattered into the detector by the chamber walls were accounted for by subtracting an isotropic background, estimated using the Monte Carlo electron scattering simulation code GEANT4 [35].

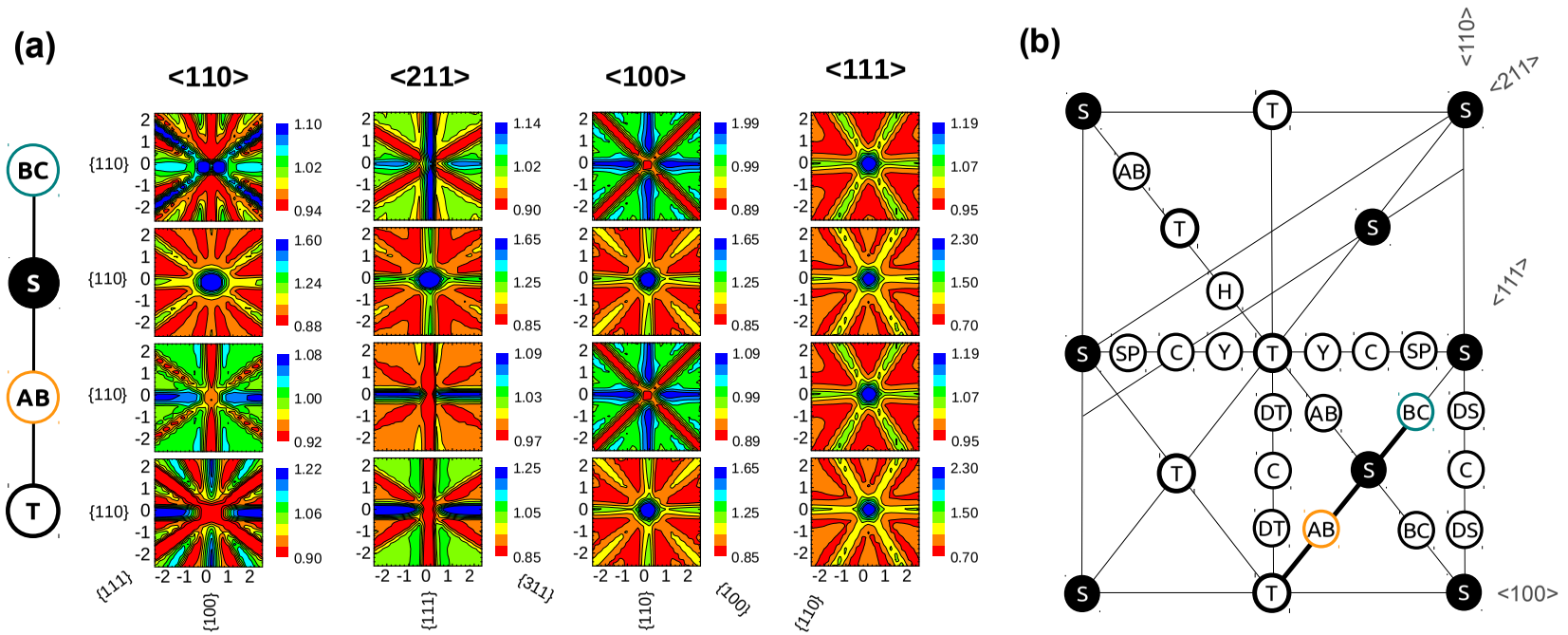

Figure 4.8: (**a**) Theoretical β^- emission yield patterns for the sequence of sites along the <111> direction, BC → S → AB → T, around <110>, <211>, <100> and <111>. The patterns of S sites are characterized by channeling peaks from all the four orientations shown. On the contrary, the channeling peaks from <211> and <100> are absent in the patterns of BC sites. While exhibiting channeling effects along {111} planes, the β^- emission yields of BC sites show blocking effects along {100} and {311}. Moreover, BC sites are characterized by a double peak along <110>. Both the patterns of T and AB sites present blocking effects of the {111} planes, but while the patterns of T sites show channeling effects from <100> and {100}, patterns of AB sites show blocking effects along these axis and planes. (**b**) Positions of the major sites in the silicon lattice, shown in the {110} plane.

The depth profile of the implanted ^{65}Ni and created vacancies were estimated using the SRIM code [36]. The implanted ^{65}Ni profile is approximately a Gaussian distribution centered at 453 Å with a straggling of 172 Å and a peak concentration of 5×10^{18} cm^{-3}. At 0 K, each implanted ^{65}Ni creates $\sim$ 900 vacancies along its path, producing a vacancy depth profile centered approximately half way from the surface to the peak of the implanted ^{65}Ni concentration. The concentration peak of the vacancy profile is $\sim 5\times10^{21}$ cm^{-3}.

4.4.3 Method of analysis

In order to obtain the occupied lattice sites of ^{65}Ni, the two-dimensional experimental patterns were fitted by using calculated β^- emission yields, obtained with the so-called *manybeam* formalism for electron channeling in single crystals [37]. In the following it is given a detailed description of the used lattice sites in the analysis, as well as the fitting procedure adopted in this work.

4.4.3.1 Lattice sites

Theoretical patterns were calculated for ^{65}Ni emitters in all the relevant high symmetry sites in Si: substitutional (S), hexagonal (H), tetrahedral (T), bond-center (BC), anti-bonding (AB), split (SP) and the so-called DS, DT, Y and C sites. Lower-symmetry sites were also considered, corresponding to displacements between the higher-symmetry ones along the $<111>$, $<100>$ and $<110>$ directions. As examples, which will be useful for the understanding of the experimental patterns below, Fig. 4.8 (**a**) shows the theoretical emission yield for the S, BC, AB and T sites in the vicinity of the four measured directions. The position of all the mentioned high-symmetry sites in the Si lattice is depicted in Fig. 4.8 (**b**). We note that the emission channeling technique does not provide information about the immediate neighbourhood of the radioactive ^{65}Ni probes but rather on their geometrical position with respect to the perfect diamond lattice. The microscopic origin of the observed sites can therefore not be directly inferred from our measurements. In that respect, our use of the term bond-centered (BC) does not imply a position of Ni where it perturbs SiSi covalent bonds, as occurring for the case of hydrogen [38] (Si-H_{BC}-Si bond) or oxygen [39] (slightly puckered Si-O_{BC}-Si bond), but rather to its geometrical position in the lattice. This position would be the same for instance for Ni atoms disturbing covalent Si-Si bonds in an ideal BC position, or for Ni atoms located in the center of

a divacancy.

4.4.3.2 Fitting procedure

The analysis was started by fitting with one fraction only for each experimental pattern, and only then we added more fractions to the analysis if justified. Therefore, depending on the annealing temperature, two sites gave consistently the lowest value for the χ^2 of fit in the studied three types of silicon: sites in the vicinity of BC sites and sites in the vicinity of T sites. A two fraction fit was then carried out with these two types of sites. The small displacements from S and T sites were adjusted by minimizing the χ^2 of fit as function of these parameters. Since the occupation of ideal S sites by ^{65}Ni is often mentioned in literature, a three fraction fit was also evaluated by allowing for an extra ideal S fraction to the two fractions mentioned above. The inclusion of the ideal S fraction resulted in a significant decrease of χ^2 , although ideal S sites were not the dominant fraction in any of the fitted patterns. A further adjustment of the near-BC and near-T displacements was then allowed. At this point additional fractions seemed not to reduce the χ^2 of fit considerably. In particular, ideal BC sites were included in a four fraction fit but without a significant χ^2 reduction. Therefore, the fits were confined to the three lattice sites: ideal S sites; sites displaced from BC towards S sites (near-BC) and sites displaced from T towards AB sites (near-T).

In addition to the high-symmetry sites mentioned so far, which contribute with an anisotropic emission yield, other sites may also be occupied which contribute with a virtually isotropic component, i.e. the *random* fraction (R). R is given by 100% minus the fractions of all regular sites included in the fits. Generally, R is largest in the as-implanted state and decreases with annealing temperature. Note that R will become negative if the sum of all fractions on regular sites grows above 100%. This behavior occurs when the actual ^{65}Ni profile moves towards the surface compared to the assumed ^{65}Ni profile, since the β^- channeling is more pronounced when the emission occurs closer to the surface.

4.4.4 Results

The two-dimensional experimental channeling patterns from ^{65}Ni in low doped n-Si, n^+-Si and p^+-Si for various annealing temperatures are shown in Figs. 4.9, 4.10 and 4.11, while the fractions on the three fitted sites as a function of annealing temperature are shown in Fig. 4.12.

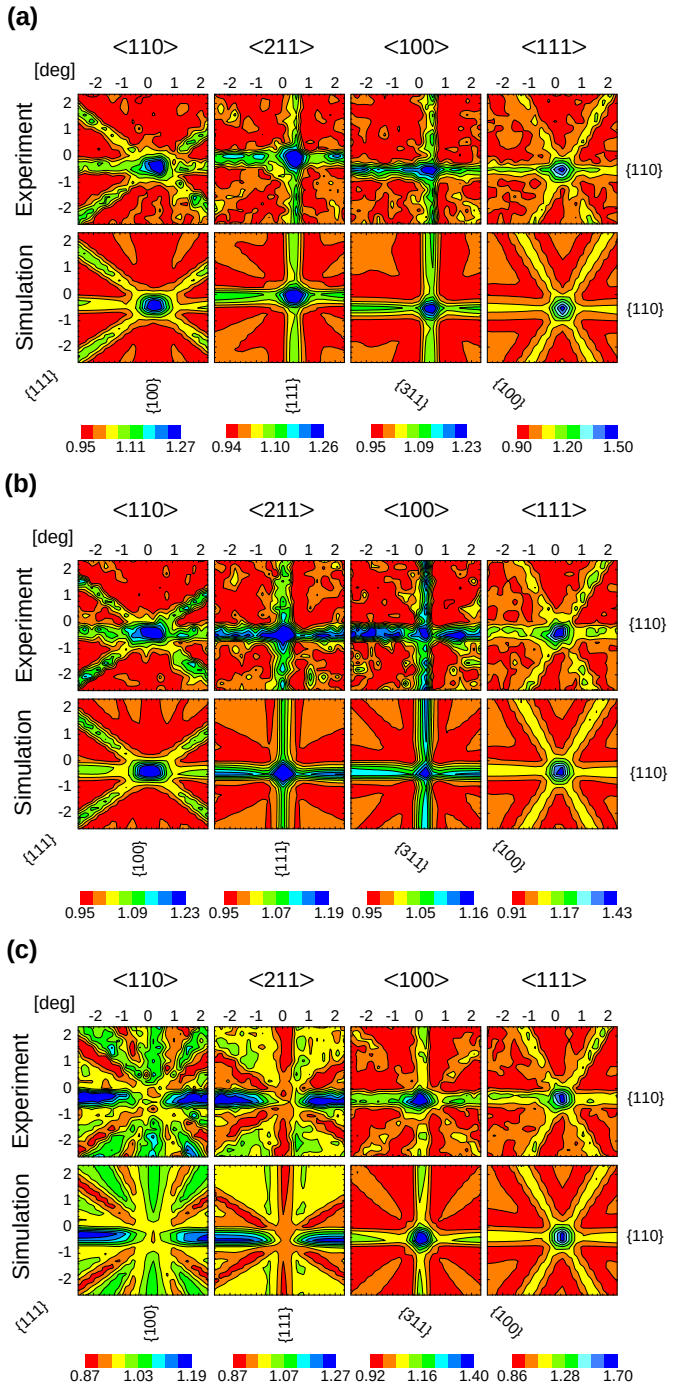

Figure 4.9: Comparison of the two-dimensional experimental and calculated emission channeling patterns from ^{65}Ni in n-Si. The β^- emission yield is represented in the vicinity of $< 110 >$, $< 211 >$, $< 100 >$ and $< 111 >$ following (**a**) implantation at room temperature, (**b**) annealing at 400°C and (**c**) 500°C.

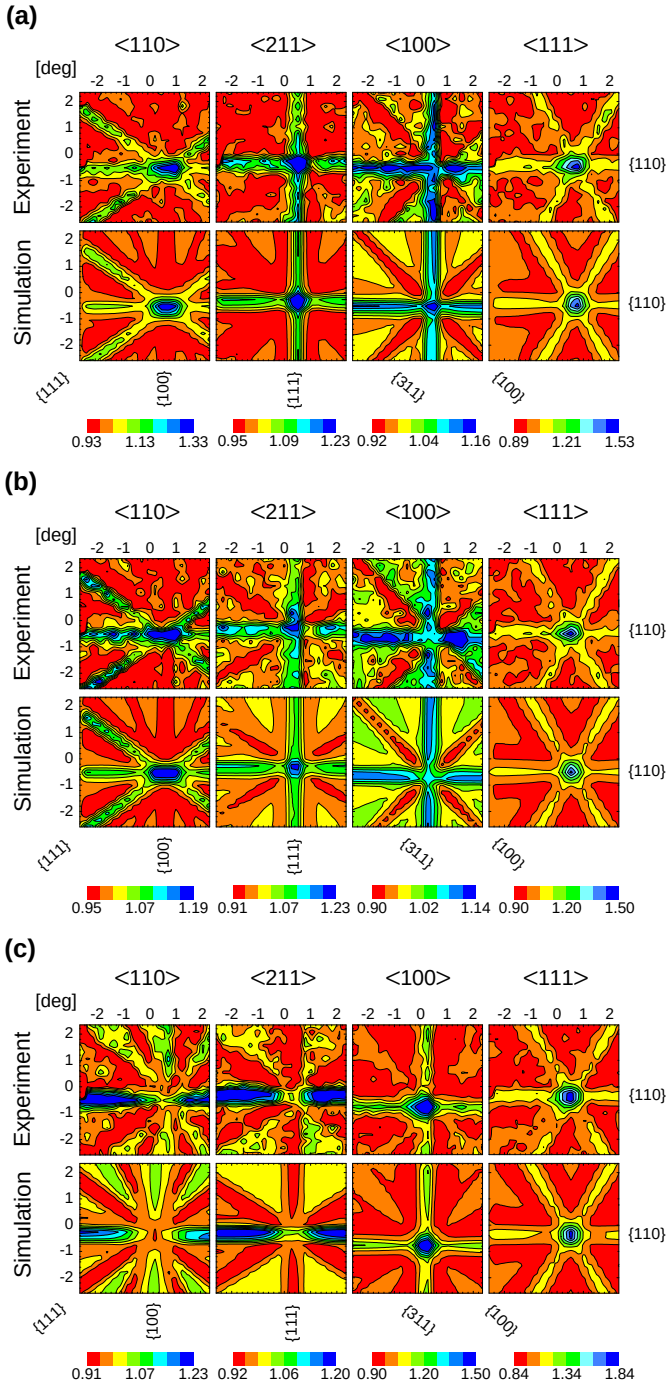

Figure 4.10: Comparison of the two-dimensional experimental and calculated emission channeling patterns from ^{65}Ni in n^+-Si, following (**a**) annealing at 400°C, (**b**) 500°C and (**c**) 600°C.

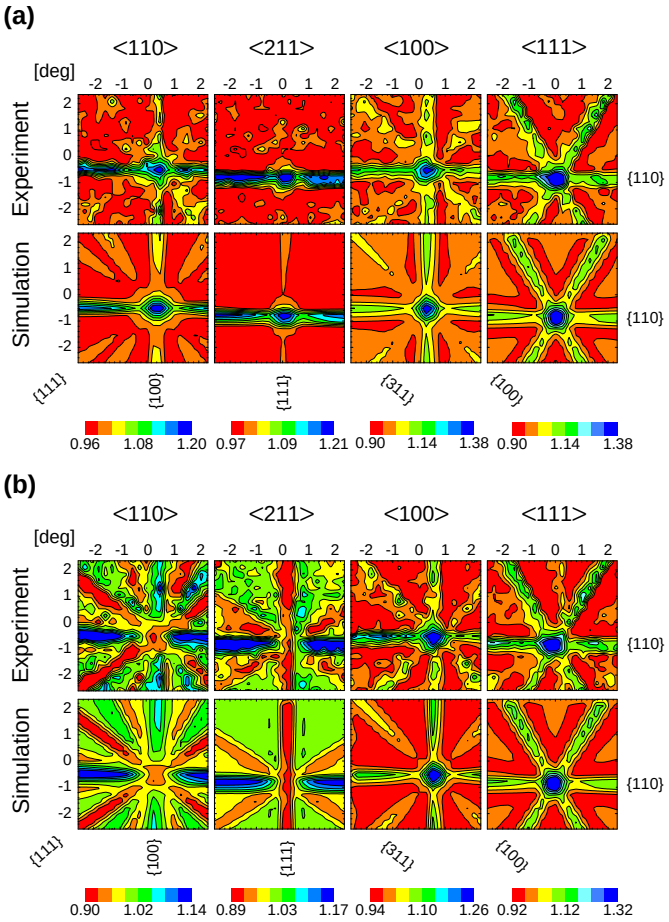

Figure 4.11: Comparison of the two-dimensional experimental and calculated emission channeling patterns from ^{65}Ni in p^+-Si, following (**a**) annealing at 400°C and (**b**) 500°C.

4.4.4.1 *n*-type Si

In the as-implanted state, the best fits show that 21% of Ni occupies ideal S sites, 22% near-BC sites and 27% near-T sites [Fig. 4.9 (**a**)]. Note that the patterns show the presence of channeling peaks along all four orientations, characteristic for S sites, and a significant absence of channeling {100} planes, characteristic for the AB and BC sites. Following annealing up to 400°C, only small changes are to be seen in the patterns: {311} and {100} planes in the vicinity of the $< 211 >$ and $< 100 >$ directions become completely blocked, from Fig. 4.9 (**a**) to (**b**). Furthermore, {111} channeling planes are still present, at least with the same intensity. These two observations suggest an increase of a near-BC fraction, cf. the β^- emission yield of BC sites from Fig. 4.8 (**a**). However, by annealing the sample at 500°C, the vanishing of the channeling peaks of

the $< 110 >$ and $< 211 >$ directions [from Figs. 4.9 (**b**) to (**c**)] clearly shows a site change of ^{65}Ni to near-T sites. In fact, by fitting the two-dimensional experimental β^- emission yield of ^{65}Ni with the calculated emission yield from the three types of sites, ideal S, near-BC and near-T, one can conclude that after annealing at 400°C the majority of Ni ($\sim$ 43%) sits on near-BC sites, while after annealing at 500°C Ni prefers near-T sites ($\sim$ 54%). After annealing at 600°C, the channeling effects are no longer observed, suggesting long-range diffusion of ^{65}Ni. The displacements, given by the best fits, from the ideal BC and T sites are plotted in Fig. 4.13 as a function of annealing temperature. Both near-BC and near-T displacements seem to be stable against annealing, around 0.25 Å for near-BC sites and 1.18 Å for near-T sites. These strongly displaced near-T sites are, in fact, very close to the ideal AB site. Only for the 500°C annealing step, the near-T sites are clearly off the AB site. In fact, at this annealing temperature we can observe a pronounced peak along the $< 100 >$ direction [Fig. 4.9 (**c**)], characteristic of the ideal T rather than AB sites [Fig. 4.8 (**a**)].

4.4.4.2 n^+-type Si

Figure 4.10 shows the two-dimensional experimental patterns from ^{65}Ni in n^+-Si following annealing at 400°C, 500°C and 600°C. The fraction dependence on the annealing temperature is plotted in Fig. 4.12 (**a**). A similar behavior of the patterns compared to those from low-doped n-Si is exhibited, in particular with similar fractions for the three lattice sites occupied by ^{65}Ni after room temperature implantation. Nevertheless, the site change of ^{65}Ni from near-BC to near-T sites occurs here at 600°C. Also, after annealing the silicon sample at 500°C [Fig. 4.10 (**b**)] one can observe more intense blocking effects of the {311} and {100} planes and a significant decrease of the channeling peak from the $< 100 >$ direction, suggesting a larger near-BC fraction compared to that of n-Si. After the 600°C anneal [Fig. 4.10 (**c**)] the channeling peaks from the $< 110 >$ and $< 211 >$ directions disappear while that from $< 100 >$ becomes more intense, showing evidence of an increase of the near-T fraction: the best fit results show that after the 500°C anneal ^{65}Ni prefers near-BC sites ($\sim$ 64%), while after the 600°C anneal the majority of ^{65}Ni ($\sim$ 76%) sits on near-T sites. From Fig. 4.13 one can also observe a similar dependence of the displacements from BC and T sites on the annealing temperature compared to those from n-Si. While near-BC sites are very close to the ideal BC site in the whole range of the annealing temperature, near-T sites are located close to AB sites up to 500°C, changing to sites closer to the ideal T site at 600°C. Finally, channeling effects disappear at 700°C, which suggests ^{65}Ni long-range diffusion.

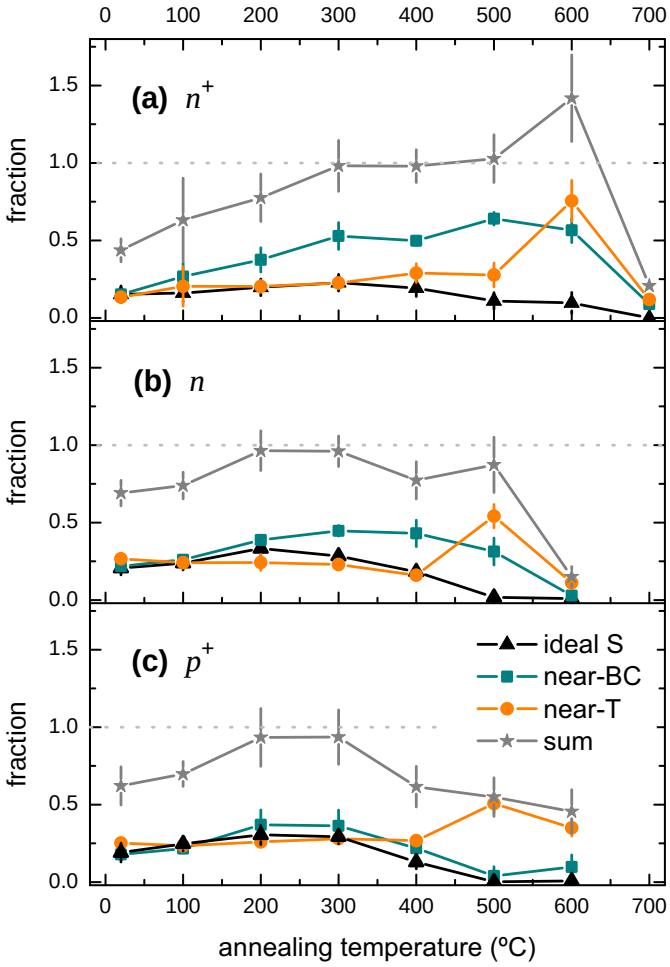

Figure 4.12: Fractions of ^{65}Ni on the ideal S, near-BC and near-T sites as a function of annealing temperature, in (**a**) n^+-, (**b**) n- and (**c**) p^+-Si.

4.4.4.3 p^+-type Si

The experimental EC patterns from ^{65}Ni in p^+-Si are shown in Fig. 4.11 after annealing at 400°C and 500°C. Once more, a similar behavior with the annealing temperature is observed as for the other doping types. Nevertheless, after the 400°C anneal, the experimental patterns exhibit a less pronounced channeling effect of the {111} plane in the vicinity of the $< 110 >$ and $< 211 >$ directions. This fact indicates a higher near-T fraction already at 400°C in comparison to the other two samples, with $\sim$ 27% of the ^{65}Ni atoms on near-T sites. Similarly to the n-Si experiment, the near-T fraction reaches its maximum value after annealing at 500°C [Fig. 4.11 (**b**)], where the fraction of ^{65}Ni on near-T sites increases to $\sim$ 51%. However, the near-T fraction

does not drop to a value close to zero after the 600°C anneal. Instead, it decreases to $\sim$ 35%. The annealing temperature required for long-range diffusion of Ni was therefore probably not reached in this type of sample. The displacement from the BC sites is again stable with the annealing temperature, ^{65}Ni sitting close to BC sites in the whole temperature range. A more complex dependence is, however, observed for the near-T sites. In fact, from Fig. 4.13, one can see that near-T sites are close to AB sites, but an anneal of 200°C pushes the near-T sites towards the ideal T position, where they remain up to the annealing temperature of 600°C.

4.4.5 Discussion

Using similar arguments as outlined for the case of ^{59}Fe in Si in Ref. [19], it appears that only vacancies, self-interstitials and the formation of ^{65}Ni clusters might be responsible for the confinement of ^{65}Ni at the channeling region. As was suggested by a recent theoretical study [6] vacancies are very stable traps for Ni, while interactions with Si interstitials, C and O impurities or other Ni atoms seem to play only a minor role. In the following subsections we discuss the origin of the lattice sites of ^{65}Ni as well as the evidence of ^{65}Ni trapping into defects at the "$R_p/2$" region and the influence of the doping on their thermal stability. Finally, a comparison to other EC studies involving transition metals is given.

4.4.5.1 Lattice location

Ideal S sites

Although some energy levels from DLTS studies have been assigned to substitutional Ni [5, 13, 40], an unambiguous proof for its existence could never be established. Here, we can show that substitutional Ni is indeed stable. One should note, however, that this substitutional fraction is likely to result from the high concentration of single vacancies that is introduced during Ni implantation.

Near-BC sites

The origin of the near-BC sites seems to be related to the ^{65}Ni interaction with multivacancies. For clusters constituted by only two vacancies, ideal BC sites might be preferred over other positions [41, 42]. On the other hand, for vacancy clusters constituted by more than two vacancies, e.g. $3-6$ vacancy clusters, the structural

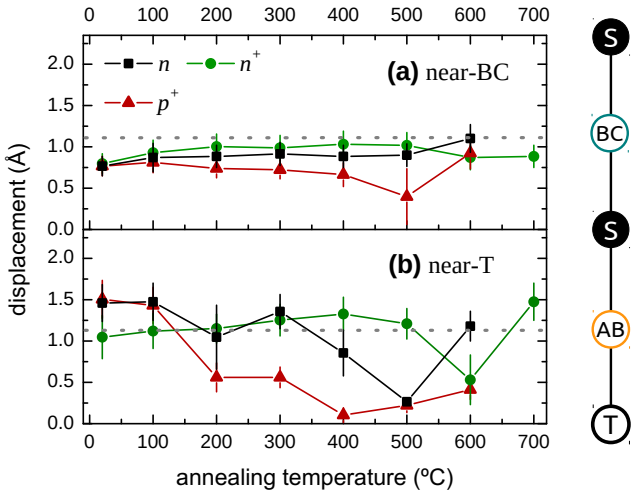

Figure 4.13: Displacement of (**a**) near-BC and (**b**) near-T sites along the <111> direction as a function of annealing temperature, in n-, n^+- and p^+-Si.

rearrangement after their formation can, for instance, result in a fourfold configuration based on hexavacancy rings where extra Si atoms are incorporated near BC positions to satisfy dangling bonds [43]. Similar geometries were also proposed when hexavacancies are filled up by Cu atoms [44]. It should thus be feasible that other transition metals such as Ni might be incorporated, perhaps along with self-interstitials from the "R_p" region, into multivacancies based on hexavacancy rings, and be stable on near-BC sites. The final result would hence be a near-BC fraction constituted by a mixture of ^{65}Ni inside divacancies, occupying ideal BC sites, and ^{65}Ni inside more complex multivacancies, occupying off-BC sites. Note that because the displacements from the BC sites are small, it is hard to distinguish these two complexes during the fitting procedure. Moreover, as pointed out, the effect on χ^2 of adding an additional fraction to the other three would be very small, and therefore inconclusive.

Near-T sites

The trapping mechanism of ^{65}Ni atoms on near-T sites is more complex than that on ideal S or near-BC sites. This fact is evident from Fig. 4.13 (**b**) showing the dependence of the displacement from ideal T towards AB sites with the annealing temperature, which suggests the existence of different complex structures with ^{65}Ni sitting on near-T sites. Though in n^+- and n-Si the position differs considerably with annealing temperature, we can classify the related complexes into two classes of ^{65}Ni displacements from the ideal T site:

(**i**) ^{65}Ni on ideal AB sites,
(**ii**) ^{65}Ni close to ideal T sites.
In p^+-Si, ^{65}Ni behaves in a different way and therefore cannot be described in terms of these two classes. In fact, although decreasing from the ideal AB site to the ideal T site with the annealing temperature, as in n^+ and n-Si, the ^{65}Ni displacement changes more gradually rather than abruptly. It seems, however, feasible that the intermediate displacements, at the annealing temperatures of 200°C and 300°C, could result from a mixture of ^{65}Ni atoms trapped by the two discussed classes of complexes. The origin of these sites might be again related to ^{65}Ni interactions with vacancy-type defects. As an example, it is known that although ideal S and BC sites are the preferred positions when Fe is trapped into single and double vacancies in silicon, respectively, near-T sites also present some stability [18, 41]. Ni may thus behave in a similar way. While the participation of self-interstitials as well as the formation of ^{65}Ni clusters cannot be ruled out, both have recently been suggested to be not very effective from an energetic point of view [6]. Because of the reasons pointed out above we conclude that a complete picture of the structure of the complexes in which Ni occupies near-T sites is difficult to obtain. We can nevertheless present some of their characteristics as well as their thermal stability, which will be discussed in more detail in the next two subsections.

4.4.5.2 ^{65}Ni profile

Eventual changes in the ^{65}Ni depth profile upon thermal annealing can be inferred from changes in intensity of the channeling effects, i.e. from changes in the sum of the three fitted fractions. If the ^{65}Ni profile starts to change, e.g. due to dissociation of the complexes in the "R_p" region, the intensity of the channeling effects will in principle also change. If the profile moves to the bulk, channeling effects are reduced and thus the sum fraction decreases. On the other hand, if the ^{65}Ni profile moves towards the surface, the channeling effects are enhanced and the sum fraction can increase to values above 100%. This is what probably happened in n^+-Si [Fig. 4.12 **(a)**]. A fraction of ^{65}Ni might have started to diffuse from the "R_p" region, after dissociating from the observed lattice sites, towards the surface, and be trapped into other defects. This explanation is consistent with the so called "$R_p/2$ effect" in which Ni is gettered into defects at the "$R_p/2$" region of the wafer, rich in vacancy-type defects resulting from implantation [31, 32]. This behavior seems to be also present in n-Si and p^+-Si after annealing at 500°C, but to a lesser extent since the fraction sum never attains values above 100%.

An important information that we can extract from our emission channeling experiments is the lattice sites where ^{65}Ni sits at the "$R_p/2$" region. In that respect, we can observe a prevailing near-T fraction when the sum increases in n- and n^+-Si or decreases at a lower rate in p^+-Si, at the annealing temperatures of 500-600°C. Moreover, during the relocation of ^{65}Ni, the displacement of the near-T sites seems to change from the ideal AB site to sites closer to the ideal T site in n- and n^+-Si. The same change of displacement is again observed in p^+-Si but more gradually. Within this scenario such a change might be explained either by a different channeling effect of the relocated ^{65}Ni profile, that is not considered in our simulated patterns, or by the presence of a different trap structure at $R_p/2$ compared to those of the "R_p" region.

Summarizing, although we do not have access to the complete structure of the traps, it appears that a fraction of ^{65}Ni atoms, that is dissociated from the sites at the "R_p" region, is retrapped on near-T sites at $R_p/2$. This retrapping occurs in the narrow window of 100°C after annealing at $500-600$°C. The observed change of displacement of the near-T sites might be a consequence of this transition.

4.4.5.3 Influence of the doping on the thermal stability

From Fig. 4.12 one can observe different lattice sites prevailing at different annealing temperatures, as a result of their distinct thermal stabilities. By using an Arrhenius model described in, e.g., Refs. [17, 23, 19], one can estimate the activation energies E_d for the ^{65}Ni dissociation from each of the three observed lattice sites with the formula:

$$E_d = k_B T \log \left[\frac{\nu_0 \Delta t}{N} \frac{1}{\log\left(\frac{f_{n-1}}{f_n}\right)} \right], \tag{4.6}$$

where ν_0 is the attempt frequency, Δt the annealing time, T the annealing temperature, f_n the fraction after annealing at T, f_{n-1} the fraction before the anneal at T, and N the required number of steps for ^{65}Ni to go to another type of trap or to escape from the channeling region. Table 4.2 shows the values obtained for the three observed lattice sites. We could not find, however, a reliable value for E_d of ^{65}Ni on ideal S sites in n^+-Si, due to the difficulty in identifying at which temperature the fraction starts to decrease [see Fig. 4.12 (**a**)]. Note also that, although it is not possible to conclude accurately on the thermal stability of near-T sites at the "R_p" region, we can estimate activation energies for ^{65}Ni dissociation from the "$R_p/2$" region.

It is clear from Table 4.2 that the activation energy for dissociation of ^{65}Ni from near-BC sites changes with the doping, increasing from p^+-Si to n-Si and further to n^+-Si.

The values in Table 4.2 show also that the thermal stability of near-T sites at the "$R_p/2$" region does not change much with the doping. Furthermore, by comparing the near-T sites to the behavior of Ni at $R_p/2$ from Ref. [8], one can conclude that a lower concentration of vacancies leads to a smaller gettering efficiency. In fact, when using fluences of implanted Si of $\sim 1 \times 10^{15}$ cm^{-2}, Ni shows thermal stability at $R_p/2$ up to the temperature of 900°C, while in our case ^{65}Ni, implanted with fluences of $\sim 1 \times 10^{13}$ cm^{-2}, dissociates already at 600°C from near-T sites. Finally, the estimated activation energies for dissociation of ^{65}Ni from ideal S sites seem not to change from p^+- to n-Si, showing a value ranging from 1.6 eV to 2.0 eV. These values are smaller than the estimate $\sim$ 3 eV from first principle calculations [5].

4.4.5.4 Comparison to other transition metals

In this subsection we discuss the similarities and differences between the present emission channeling work on ^{65}Ni with those on ^{59}Fe [17–19], ^{67}Cu [14–16] and ^{111}Ag [20]. While both ^{67}Cu and ^{59}Fe were investigated in lightly and heavily doped n- and p-type silicon, ^{111}Ag was only studied in two light doping types. ^{59}Fe was the only transition metal that was identified on the same three types of lattice sites observed in this work. ^{67}Cu was identified on near-S and ideal S sites, and ^{111}Ag on near-S and near-T sites.

Near-S and near-BC sites can be considered as being part of the same type of sites since they only differ in their distances from the S or BC sites, along the <111> direction [see Fig. 4.8 (**b**)]: near-BC sites are closer to BC while near-S sites are closer to S. It is evident that the three transition metals Ni, Fe and Cu start their dissociation in n^+-Si from near-BC or near-S sites in the same range of temperatures (500-600°C). Furthermore, they show a change of thermal stability with the doping when sitting on near-S or near-BC sites, increasing from p^+- to n- and further to n^+-Si. We can therefore conclude that the nature of the transition metal does not play a major role

Table 4.2: Estimated activation energies for dissociation of ^{65}Ni from near-BC, near-T and ideal S sites, in the three types of silicon.

Defect	p^+-type Si	n-type Si	n^+-type Si
ideal S	$1.8 - 2.0$ eV	$1.6 - 1.8$ eV	-
near-T	$2.4 - 2.6$ eV	$2.3 - 2.5$ eV	$2.5 - 2.8$ eV
near-BC	$1.8 - 2.0$ eV	$2.1 - 2.3$ eV	$2.5 - 2.7$ eV

on the trapping mechanism into near-S and near-BC sites. This might be relevant for the understanding of the microscopic mechanism of P-diffusion gettering, which is used for a *wide* number of transition metals and in which vacancy-related defects have been suggested to play a role [11, 45].

The evidence of ^{65}Ni trapping on near-T sites at $R_p/2$ has similarities with the ^{59}Fe behavior on near-T sites in lightly doped Si. In fact, the increase of the near-T fraction is also accompanied with a sum of all the fractions to values above 100%. Although the dependence of the displacement from the ideal T site was not studied at that time, since simulations were only available for a small number of displacements, it was clear that a reshaping of the ^{59}Fe profile was taking place at high temperatures. A particular feature of the near-T sites of ^{59}Fe in p^+-Si was its prevalence over the other two fractions in the whole annealing temperature range. It was suggested that the mobile ^{59}Fe, predominantly positively charged in p^+-Si, might be trapped by immobile B^- acceptors, on near-T sites. This observation contrasts with that of Ni. Indeed, Ni prevails in the neutral charge state when diffusing interstitially, which makes such interactions between interstitial Ni^0 and B^- unlikely. This might explain why Ni does not prevail in p^+-Si on near-T sites in the whole annealing temperature range, as observed for ^{59}Fe.

Finally, we should note that although also detected in ^{59}Fe and ^{67}Cu studies, ideal S sites seem to have different thermal stabilities. While an activation energy of 3.5 eV for dissociation of ^{59}Fe from ideal S sites was obtained in Ref. [17], compared to the 3.0 eV from the theoretical grounds of Ref. [5], ^{67}Cu seemed to need 2.9 eV to dissociate [17], compared to the first principle calculated value of 2.8 eV from Ref. [42]. The experimental value for ^{65}Ni dissociation from ideal S sites (Table 4.2) is thus the lowest among the three discussed transition metals.

4.4.6 Conclusion

We have experimentally identified ^{65}Ni on three different lattice sites: ideal S, near-BC and near-T sites. Arguments have been presented to assign the trapping of ^{65}Ni into implantation defects to the majority of the three observed lattice sites. This study shows an appreciable thermal stability of Ni on ideal S sites in silicon, for which the activation energy for Ni dissociation 1.6-2.0 eV was obtained. A significant fraction of ^{65}Ni seems to be also trapped into multivacancies on near-BC sites, such as into divacancies and fourfold coordinated vacancy clusters based on hexavacancy rings.

Because the thermal stability of near-BC sites is similar to those of ^{59}Fe, ^{67}Cu and ^{111}Ag, we show that the nature of the transition metal does not play a major role on the related trapping mechanism. In particular, the thermal stability of near-BC sites seems to change with the doping, increasing from p^+- to n- and further to n^+-Si. The high thermal stability of near-BC sites in n^+-Si shall hence have an important role not only on the P-diffusion gettering of Fe but also on that of Ni. Although the three lattice sites were found to coexist at R_p, we identified ^{65}Ni at the vacancy rich region "$R_p/2$" on near-T sites. Finally, unlike Fe that is confined at the channeling region even at 900°C, long-range diffusion of ^{65}Ni was observed already at 600-700°C. Vacancy-related defects seem therefore to be less thermally stable in gettering Ni than Fe.

Bibliography

[1] E. R. Weber, Transition metals in silicon, Appl. Phys. A 30 (1983) 1.

[2] D. MacDonald, Impact of nickel contamination on carrier recombination in n- and p-type crystalline silicon wafers, Appl. Phys. A 81 (2005) 1619.

[3] A. A. Istratov, T. Buonassisi, R. J. McDonald, A. Smith, R. Schindler, J. A. Rand, J. P. Kalejs, E. R. Weber, Metal content of multicrystalline silicon for solar cells and its impact on minority carrier diffusion length, J. Appl. Phys. 94 (2003) 6552.

[4] S. Pizzini, Towards solar grade silicon: Challenges and benefits for low cost photovoltaics, Sol. Energy Mater. Sol. Cells 94 (2010) 1528.

[5] D. J. Backlund, S. K. Estreicher, Ti, Fe, and Ni in Si and their interactions with the vacancy andvthe A center: A theoretical study, Phys. Rev. B 81 (2010) 235213.

[6] J. Lindroos, D. P. Fenning, D. J. Backlund, E. Verlage, A. Gorgulla, S. K. Estreicher, H. Savin, T. Buonassisi, Nickel: A very fast diffuser in silicon, J. Appl. Phys. 113 (2013) 204906.

[7] D. J. Backlund, S. K. Estreicher, Structural, electrical, and vibrational properties of Ti − H and Ni − H complexes in Si, Phys. Rev. B 82 (2010) 155208.

[8] R. A. Brown, O. Kononchuk, G. A. Rozgonyi, S. Koveshnikov, A. P. Knights, P. Simpson, F. Gonzlez, Impurity gettering to secondary defects created by MeV ion implantation in silicon, J. Appl. Phys. 84 (1998) 2459.

[9] S. M. Myers, D. M. Follstaedt, D. M. Bishop, Binding of copper and nickel to cavities in silicon formed by helium ion implantation, Materials Research Society Symposium Proceedings 316 (1994) 33–38.

[10] A. Ourmazd, W. Schröter, Phosphorus gettering and intrinsic gettering of nickel in silicon, Appl. Phys. Lett. 45 (1984) 781.

[11] S. M. Myers, M. Seibt, W. Schröter, Mechanisms of transition-metal gettering in silicon, J. Appl. Phys. 88 (2000) 3795.

[12] A. A. Istratov, P. Zhang, R. J. McDonald, A. R. Smith, M. S. J. Moreland, J. Shen, R. Wahlich, E. R. Weber, Nickel solubility in intrinsic and doped silicon, J. Appl. Phys. 97 (2005) 023505.

[13] A. A. Istratov, E. R. Weber, Electrical properties and recombination activity of copper, nickel and cobalt in silicon, Appl. Phys. A 66 (1998) 123.

[14] U. Wahl, J. G. Correia, A. Vantomme, G. Langouche, Lattice location of implanted Cu in Si, Physica B 273 (1999) 367.

[15] U. Wahl, A. Vantomme, G. Langouche, J. P. Araújo, L. Peralta, J. G. Correia, Lattice location of implanted Cu in highly doped Si, Appl. Phys. Lett. 77 (2000) 2142.

[16] U. Wahl, A. Vantomme, G. Langouche, J. G. Correia, Lattice location and stability of ion implanted Cu in Si, Phys. Rev. Lett. 84 (2000) 1495.

[17] U. Wahl, J. G. Correia, E. Rita, J. P. Araújo, J. C. Soares, Fe and Cu in Si: Lattice sites and trapping at implantation-related defects, Nucl. Instrum. Methods. Phys. Res. Sect. B 253 (2006) 167.

[18] U. Wahl, J. G. Correia, E. Rita, J. P. Araújo, J. C. Soares, Lattice sites of implanted Fe in Si, Phys. Rev. B 72 (2005) 1.

[19] *Article I.* D. J. Silva, U. Wahl, J. G. Correia, J. P. Araújo, Influence of n^+ and p^+ doping on the lattice sites of implanted Fe in Si, J. Appl. Phys. 114 (2013) 103503.

[20] U. Wahl, J. G. Correia, A. Vantomme, Lattice location of implanted Ag in Si, Nucl. Instrum. Methods. Phys. Res. B 190 (2002) 543.

[21] M. R. da Silva, U. Wahl, J. G. Correia, L. M. Amorim, L. M. C. Pereira, A versatile apparatus for on-line emission channeling experiments, Rev. Sci. Instrum. 84 (2013) 073506.

[22] S. Decoster, S. Cottenier, U. Wahl, J. G. Correia, L. M. C. Pereira, C. Lacasta, M. R. D. Silva, A. Vantomme, Diluted manganese on the bond-centered site in germanium, Appl. Phys. Lett. 97 (2010) 151914.

[23] L. M. Pereira, U. Wahl, S. Decoster, J. G. Correia, M. R. da Silva, A. Vantomme, J. P. Araújo, Direct identification of interstitial Mn in heavily p-type doped GaAs and evidence of its high thermal stability, Appl. Phys. Lett. 98 (2011) 201905.

[24] L. M. C. Pereira, U. Wahl, S. Decoster, J. G. Correia, L. M. Amorim, M. R. D. Silva, J. P. Araújo, A. Vantomme, Stability and diffusion of interstitial and substitutional Mn in GaAs of different doping types, Phys. Rev. B 86 (2012) 125206.

[25] L. M. C. Pereira, U. Wahl, J. G. Correia, S. Decoster, L. M. Amorim, M. R. D. Silva, J. P. Araújo, A. Vantomme, Evidence of N substitution by Mn in GaN, Phys. Rev. B 86 (2012) 195202.

[26] L. M. C. Pereira, U. Wahl, S. Decoster, J. G. Correia, L. M. Amorim, M. R. D. Silva, J. P. Araújo, A. Vantomme, Mixed Zn and O substitution of Co and Mn in ZnO, Phys. Rev. B 84 (2011) 125204.

[27] L. M. C. Pereira, U. Wahl, J. G. Correia, L. M. Amorim, D. J. Silva, E. Bosne, S. Decoster, M. R. da Silva, K. Temst, A. Vantomme, Minority anion substitution by Ni in ZnO, Appl. Phys. Lett. 103 (2013) 091905.

[28] B. Mohadjeri, J. S. Williams, J. Wong-Leung, Gettering of nickel to cavities in silicon introduced by hydrogen implantation, Appl. Phys. Lett. 66 (1995) 1889.

[29] S. Koveshnikov, O. Kononchuk, Gettering of Cu and Ni in mega-electron-volt ion-implanted epitaxial silicon, Appl. Phys. Lett. 73 (1998) 2340.

[30] A. Peeva, R. Koegler, W. Skorupa, Visualization of vacancy type defects in the $R_p/2$ region of ion implanted and annealed silicon, Nucl. Instrum. Methods. Phys. Res. B 206 (2003) 71.

[31] J. S. Williams, M. J. Conway, B. C. Williams, J. Wong-Leung, Direct observation of voids in the vacancy excess region of ion bombarded silicon, Appl. Phys. Lett. 78 (2001) 2867.

[32] A. Peeva, R. Kögler, W. Skorupa, J. S. Christensen, A. Y. Kuznetsov, Spatial distribution of cavities in silicon formed by ion implantation generated excess vacancies, J. Appl. Phys. 95 (2004) 4738.

[33] H. Kitagawa, S. Tanaka, H. Nakashima, M. Yoshida, Electrical properties of nickel in silicon, J. Electron. Mater. 20 (1991) 441.

[34] U. Wahl, J. G. Correia, A. Czermak, S. G. Jahn, P. Jalocha, J. G. Marques, A. Rudge, F. Schopper, J. C. Soares, A. Vantomme, P. Weilhammer, Position-sensitive Si pad detectors for electron emission channeling experiments, Nucl. Instrum. Methods Phys. Res. A 524 (2004) 245.

[35] S. Agostinelli, *et al.*, GEANT4 - a simulation toolkit, Nucl. Instrum. Methods Phys. Res. A 506 (2003) 250.

[36] J. F. Ziegler, SRIM-2003, Nucl. Instrum. Methods Phys. Res. B 219 (2004) 1027.

[37] U. Wahl, J. G. Correia, S. Cardoso, J. G. Marques, A. Vantomme, G. Langouche, Electron emission channeling with position-sensitive detectors, Nucl. Instrum. Methods. Phys. Res. Sect. B 136 (1998) 744.

[38] T. L. Estle, S. Estreicher, D. S. Marynick, Bond-centered hydrogen or muonium in diamond: The explanation for anomalous muonium and an example of metastability, Phys. Rev. Lett. 58 (1987) 1547.

[39] J. W. Corbett, R. S. McDonald, G. D. Watkins, The configuration and diffusion of isolated oxygen in silicon and germanium, J. Phys. Chem. Solids 25 (1964) 873.

[40] M. Shiraishi, J. Sachse, H. Lemke, J. Weber, DLTS analysis of nickel-hydrogen complex defects in silicon, Mater. Sci. Eng. B 58 (1999) 130.

[41] S. K. Estreicher, M. Sanati, N. G. Szwacki, Iron in silicon: Interactions with radiation defects, carbon, and oxygen, Phys. Rev. B 77 (2008) 125214.

[42] S. K. Estreicher, First-principles theory of copper in silicon, Mater. Sci. Semicond. Process. 7 (2004) 101.

[43] D. V. Makhov, L. J. Lewis, Stable fourfold configurations for small vacancy clusters in silicon from *ab initio* calculations, Phys. Rev. Lett. 92 (2004) 255504.

[44] S. K. Estreicher, Rich chemistry of copper in crystalline silicon, Phys. Rev. B 60 (1999) 5375.

[45] M. Syre, S. Karazhanov, B. R. Olaisen, A. Holt, B. G. Svensson, Evaluation of possible mechanisms behind P gettering of iron, J. Appl. Phys. 110 (2011) 024912.

4.5 Article IV - Origin of the lattice sites occupied by implanted Co in Si

D. J. Silva[1], U. Wahl[2], J. G. Correia[2], L. M. C. Pereira[3], L. M. Amorim[3], M. R. da Silva[4], J. P. Araújo[1]

[1] IFIMUP and IN-Institute of Nanoscience and Nanotechnology, Departamento de Física e Astronomia da Faculdade de Ciências da Universidade do Porto, Rua do Campo Alegre 687, 4169-007 Porto, Portugal

[2] Centro de Ciências e Tecnologias Nucleares, Instituto Superior Técnico, Universidade de Lisboa, 2686-953 Sacavém, Portugal

[3] Instituut voor Kern- en Stralingsfysica, KU Leuven, 3001 Leuven, Belgium

[4] Centro de Física Nuclear da Universidade de Lisboa, 1649-003 Lisboa, Portugal

Semiconductor Science and Technology **29**, 125006 (2014)

abstract

We have investigated the lattice location of implanted ^{61}Co in silicon. By means of emission channeling, three different lattice sites have been identified: ideal substitutional sites, displaced bond-centered sites and displaced tetrahedral interstitial sites. To assess the origin of the observed lattice sites we have compared our results to emission channeling studies on ^{59}Fe and ^{65}Ni and to Mössbauer spectroscopy experiments on ^{57}Co, present in literature. The possible interpretation of several ^{57}Co Mössbauer lines is discussed in the light of our new results on the ^{61}Co lattice location. The conclusions are relevant for the microscopic understanding of some gettering techniques.

4.5.1 Introduction

Together with other Transition Metals (TMs), Co introduces deep levels in the silicon bandgap. These deep levels depend on the complexes that Co forms [1], and are unwanted in most applications, e.g. causing efficiency degradation of solar cells. To avoid such harmful effects, gettering procedures, relying on moving the unwanted impurity away from the active area of devices, have been used, e.g., by introducing gettering centers through irradiation or by diffusing phosphorus [2]. Although a quantitative description of the macroscopic behavior of gettering procedures is now quite

well established, the involved microscopic complexes are far from being understood and subject of ongoing discussions. Studies of the lattice location of the ion implanted radioactive 3d TM probes ^{67}Cu [3, 4], ^{59}Fe [5, 6] and ^{65}Ni [7] with the Emission Channeling (EC) technique have been previously exploring such complexes, and here we provide results on ^{61}Co. We note that the various types of lattice sites identified are also likely to be of relevance if the TMs are introduced by other processes than implantation, although quite likely with different abundancies. A certain shortcoming of the EC technique is its lack of sensitivity to the immediate local environment of the probe atoms, which complicates the identification of the complexes responsible for the observed lattice sites. In that respect, ^{57}Co $\rightarrow$ ^{57}Fe Mössbauer Spectroscopy (MS) is a complimentary technique, since it gives information on the charge distribution in the local environment of the probe atom via the hyperfine interaction. The comparison of ^{61}Co lattice location (via EC of emitted electrons) and ^{57}Co hyperfine interaction (via MS of emitted gamma particles) hence offers the opportunity to provide a more detailed understanding. We will therefore also critically assess the interpretation of MS results for implanted ^{57}Co in Si in the literature [8–10].

In this work, we have investigated experimentally the lattice location of ^{61}Co ($t_{1/2}$ = 1.65 h) in monocrystalline silicon by means of EC with Short-Lived Isotopes (EC-SLI). ^{61}Co was produced, introduced in the silicon sample and measured at CERN's ISOLDE facility. In EC-SLI experiments, the preferred lattice sites can be derived from the strong dependence of the channeling effects of the emitted β^- particles on the sites occupied by the short lived probe atoms [7, 4, 11–13]. We compare our results to EC studies on ^{59}Fe [5, 6] and ^{65}Ni [7], and to MS experiments from Refs. [8–10].

4.5.2 Experiment and method of analysis

The sample used was n-type Si with a resistivity of 7.3 − 12 Ωcm and a <111> surface. In order to dope the silicon sample with ^{61}Co, the precursor isotope ^{61}Mn was implanted with an energy of 50 keV under a tilt angle of 17°. ^{61}Mn was converted into ^{61}Co as a result of the decay chain ^{61}Mn ($t_{1/2}$ = 0.61 s) $\rightarrow$ ^{61}Fe (5.98 min) $\rightarrow$ ^{61}Co (1.65 h). Since the recoil energy of the ^{61}Fe decay (103 eV [12]) is well above the average threshold displacement energy in silicon (36 eV [14]), the resulting ^{61}Co was re-implanted, avoiding therefore the influence of the sites occupied by ^{61}Fe. The annealing treatment and emission channeling measurements took place only $\sim$ 30 min after each implantation stop, to be sure that ^{61}Fe was not present in significant quantities. Hence, if despite of the 103 eV recoil any of the ^{61}Co probes should have survived on the same

lattice sites as ^{61}Fe, the interaction with their surroundings during thermal treatment happened when the chemical nature of the probe was Co and should hence characterize the behaviour of this element. Due to the short half-life of ^{61}Co and its continuous decay into ^{65}Ni, the amount of ^{61}Co left in the sample at the end of each measurement is negligible. However, at the beginning of the last measurement of the experiment more than ten times as much stable ^{61}Ni than radioactive ^{61}Co has accumulated. Therefore, while each measured two dimensional pattern was not influenced by the previous observed lattice sites of ^{61}Co, the accumulated ^{61}Ni content, though very small, might have played a role to some extent, e.g. in interacting with ^{61}Co. Also, in the course of the experiment, radiation damage will increase in the sample according to the detailed implantation and annealing history.

^{61}Mn was implanted in 9 steps of $\sim 1.5\times10^{12}$ cm^{-2}. While after the first implantation step the sample was measured as-implanted at room temperature (RT), each successive implantation step was followed by annealing *in situ* during 10 min at a given temperature, applying 150°C, 300°C, 400°C, 475°C, 550°C, 650°C, 750°C and 850°C. The two-dimensional EC patterns were measured at room temperature after each anneal in the vicinity of <110>, <211>, <100> and <111>, by using a position and energy sensitive detector. The electrons that reach the detector after being backscattered inside the sample or from the wall of the vacuum chamber were considered by subtracting an isotropic background, obtained with the Monte Carlo electron scattering simulation code GEANT4 [15]. The whole experiment was performed inside an on-line chamber [16].

The depth profile of the implanted ^{61}Mn was obtained using the SRIM code [17]. It can be approximated by a Gaussian centered at 463 Å from the surface with a straggling of 180 Å and a peak of 3.8×10^{17} cm^{-3} (for each of the implantation steps). Each implanted ^{61}Mn ion produces approximately 700 vacancies. The depth profile of produced vacancies is centered approximately half way from the surface to the peak concentration of ^{61}Mn (so-called "$R_p/2$" region). The vacancy peak concentration is $\sim 3\times10^{20}$ cm^{-3}, also for each implantation steps.

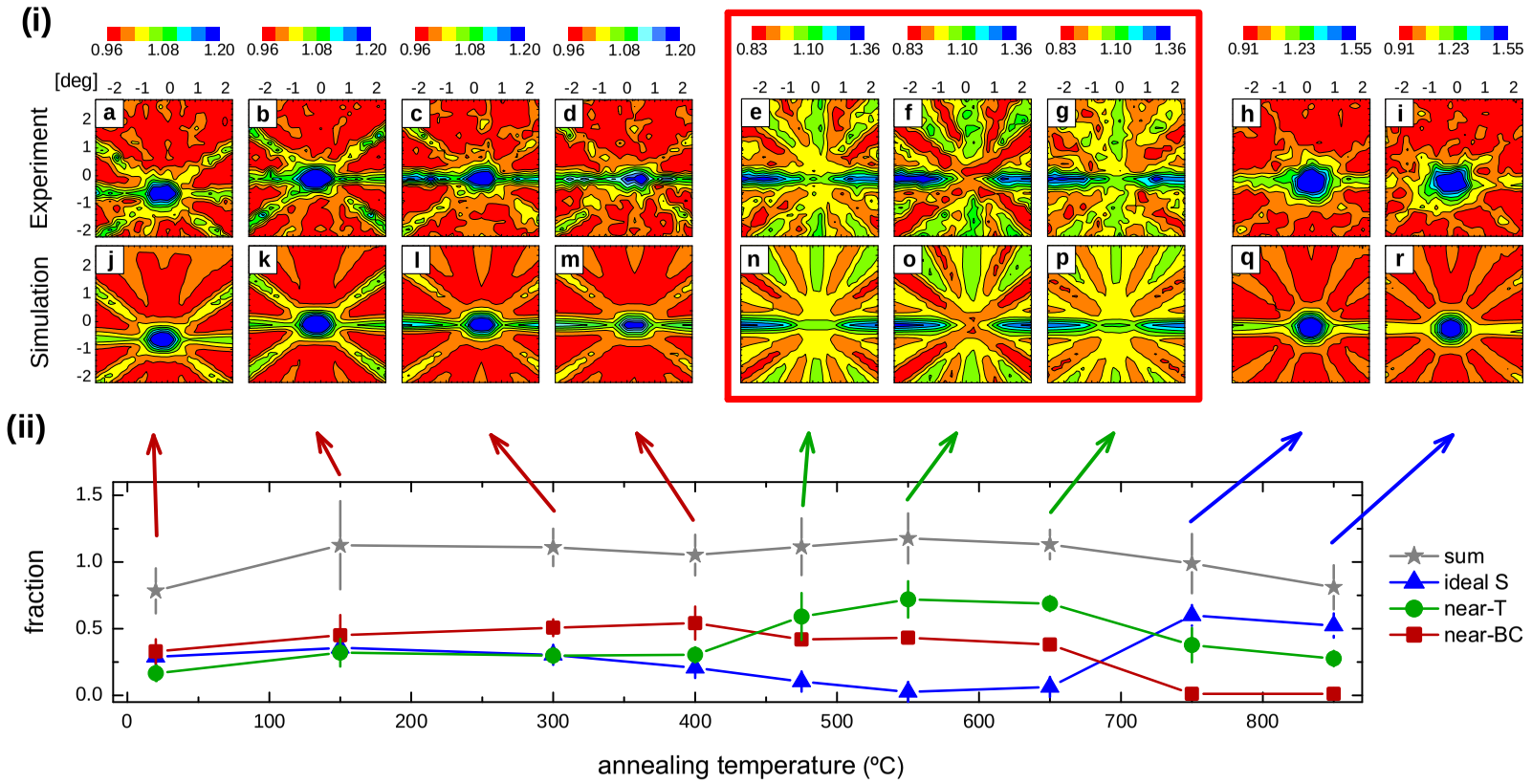

Figure 4.14: (**i**) Comparison of the two-dimensional experimental and best fit of simulated emission channeling patterns from ^{61}Co in n-type Si in the vicinity of $< 110 >$, after room temperature implantation (**a**,**j**) and after annealing at 150°C (**b**,**k**), 300°C (**c**,**l**), 400°C (**d**,**m**), 475°C (**e**,**n**), 550°C (**f**,**o**), 650°C (**g**,**p**), 750°C (**h**,**q**) and 850°C (**i**,**r**). (**ii**) Fractions of the three observed lattice sites ideal S, near-T sites and near-BC sites as a function of annealing temperature.

In order to obtain the occupied lattice sites of ^{61}Co, the two-dimensional experimental patterns were fitted using calculated beta emission yields, obtained with the *manybeam* formalism for electron channeling in single crystals [18]. The emission probability of the substitutional (S), hexagonal (H), tetrahedral (T), bond-centered (BC), anti-bonding (AB), split $< 100 >$ (SP), $< 110 >$ displaced substitutional (DS), $< 110 >$ displaced tetrahedral (DT), ytterbium (Y) and carbon (C) sites, as well as $< 111 >$, $< 100 >$ and $< 110 >$ displacements between these positions, were included in the fitted patterns. The detailed location of these sites within the Si lattice has been described in Fig. 1 of Ref. [7]. When fitting with only one fraction three types of sites resulted in the best fits, depending on the annealing temperature. For low annealing temperatures the best fits were obtained considering sites displaced from BC towards ideal S sites (near-BC sites), while for high annealing temperatures the best fits resulted from ideal S sites. At intermediate annealing temperatures, sites displaced from T towards AB sites (near-T sites) resulted in the lowest χ^2 of fit. A second fitting procedure was therefore performed by considering these three lattice sites at the same time.

4.5.3 Results and discussion

Figure 4.14 shows the two-dimensional experimental and best fit EC patterns in the vicinity of <110> for all the studied annealing temperatures, and the corresponding dependence of the site fractions on the annealing temperature. Figure 4.15 also shows the emission channeling patterns for the remaining three orientations <100>, <211> and <111>, after the 550°C anneal. While near-BC and near-T sites were present in a continuous range of annealing temperatures, the ideal S fraction was considerably reduced at intermediate annealing temperatures. It seems thus possible that the complex structure with Co sitting on ideal substitutional sites may be different for low and high annealing temperatures.

At this point it is worthwhile mentioning that the overall trend of the ^{61}Co lattice location as a function of annealing temperature shows considerable similarities to our previous results on ^{59}Fe [5, 6] and ^{65}Ni [7] in Si samples of similar doping type, i.e. neither highly n- nor highly p-type Si. For all three elements at low annealing temperatures near-BC sites were quite prominent, followed by an intermediate annealing temperature regime, starting around $400 - 500$°C, where interstitial sites near the T position were dominating. However, while for ^{61}Co and ^{59}Fe at the highest annealing temperatures ideal substitutional sites were increasingly contributing, in the case of

^{65}Ni the emission channeling effects already nearly disappeared after annealing at 600°C. The fact that near-BC sites and near-T sites were found in all three cases and with a relatively similar dependence on annealing temperature, suggests that the underlying defects are formed via a mechanism that may be common to all three of these transition metals. Our interpretation in the case of ^{59}Fe and ^{65}Ni had been that the near-BC sites are associated with transition metals that are located in the center of a divacancy or within more extended vacancy-type complexes, such as fourfold hexavacancy clusters [6, 7, 19]. We also suggest this interpretation here for ^{61}Co. The nature of the near-T sites was far less clear. Regarding the near-T sites, we had tentatively suggested that they may result from ^{59}Fe and ^{65}Ni on metastable positions next to a vacancy or divacancy. While in the case of ^{59}Fe in low-doped Si the prominent occupation of near-T sites was apparently accompanied by Fe diffusing into the damage-rich "$R_p/2$" region, such diffusion was not obvious for ^{65}Ni or ^{61}Co.

To compare the observed emission channeling sites in this work with the Mössbauer lines from Refs. [8–10, 20] it is imperative to discuss first the differences and similarities of the experimental conditions. The probe investigated by MS was ^{57}Co ($t_{1/2}$ = 270 d) which decays by capturing an electron from the inner shell and by gamma emission into the well-known ^{57m}Fe ($t_{1/2}$ = 98 ns) state. The Mössbauer effect measurement takes place subsequently when the ^{57m}Fe state de-excites to the ground state, hence on a Fe impurity. While the ^{57}Co electron capture decay transfers only a small recoil energy of 4.6 eV to its ^{57*}Fe daughter nucleus, which is probably not enough to displace it from its lattice site, the transfer of kinetic energy might certainly result in structural configurations of the Fe defect that are different from the Co precursor. Also, since initially its innermost electron is missing, the electronic shell of ^{57}Fe subsequently undergoes a complete restructuring by means of X-ray and Auger electron emission, at the end of which the Fe impurity may be left in a charge state that does not correspond to thermal equilibrium for a Fe impurity either. However, the 98 ns half-life of ^{57m}Fe is much smaller than the time taken by the fast interstitial diffuser Fe to make one diffusion step at room temperature ($\sim$ 300 ms). Summarizing, the Mössbauer effect from ^{57}Co measures on a Fe impurity whose structural properties, however, are probably still influenced by those of the ^{57}Co precursor. On the other hand, in β^- emission channeling experiments, the emitted β^- particles characterize the lattice location of the ^{61}Co impurity in thermal equilibrium. Another important parameter for comparing both experiments is the fluence. For the case of MS the fluence ranged from 2.5×10^{12} to 1×10^{13} cm^{-2} and was applied in a single implantation, corresponding to peak concentrations between 1×10^{17} and 1×10^{18} cm^{-3}. We note, however, that the

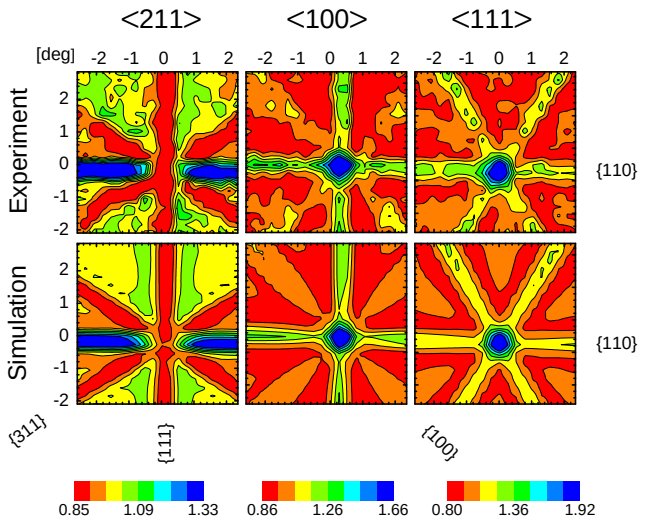

Figure 4.15: Two-dimensional experimental and calculated emission channeling patterns from ^{61}Co in n-type Si, in the vicinity of <211>, <100> and <111> following annealing at 550°C.

presence of the Mössbauer lines that will be compared with the EC lattice sites inferred from this work appeared for the lower fluence case.

For low annealing temperatures (≤400°C) MS only observes the singlet line assigned to ideal substitutional sites and the amorphous doublet [8, 9, 20]. While one would expect that the amorphous doublet in MS directly corresponds to the random sites in EC, the related fractions do not match: in the RT as-implanted state and in the $10^{11} - 10^{12}$ cm^{-2} fluence range, the amorphous doublet accounts for ∼ 80% of the spectral intensity (with the remaining ∼ 20% being substitutional singlet) [9], while the random fraction in our EC experiment, under similar conditions, is only ∼ 20% (with ∼ 27% identified on ideal S, ∼ 30% on near-BC and ∼ 15% on near-T). On the other hand, one would expect that MS probes on any type of near-BC site are subject to an electrical field gradient since their environment is not of cubic symmetry. It hence seems as if the amorphous doublet is actually a combination of several sites that are characterized by similar electric field gradients, most likely including the random as well as the near-BC sites identified by EC.

For annealing temperatures of 475−650°C [Fig. 4.14 (**ii**)], the dominating ^{61}Co fraction in emission channeling are the near-T sites, with maximum fractions around 70%. They become prominent in a similar temperature range where a second Mössbauer quadrupole doublet line appears (400 − 450°C) with maximum fractions around 40%

[8, 9, 20]. The range of annealing temperatures up to which the near-T fraction and this second quadrupole doublet prevail is not exactly the same, $\sim 475-500$°C in the MS experiments and 475−650°C in EC. However, this can possibly be explained by the fact that the annealing treatments of Ref. [8] lasted 1 h (under Ar atmosphere), which could have broken up the complexes associated with this Mössbauer line already at 500°C, while in the EC experiments 10 min annealing was used. Also, the much longer measuring times in MS may have played a role and caused the premature annealing of the doublet line. It should also be noted that the resistivities of the samples in the investigation of Ref. [8] were both n- and p-type Si FZ of $0.06-0.13$ Ωcm, while in this work we studied only n-type Si CZ with $7.3-12$ Ωcm, i.e. a sample that is more intrinsic than the two types of Si samples used in the MS studies. As mentioned in Refs. [8, 9] the quadrupole doublet lines were visible both in n- and p-type Si, although being much more prominent in n-type material. Hence there is good reason to expect them, although less prominent, in the type of sample used in our study. Remarkably, this second Mössbauer quadrupole doublet was suggested to be due to the formation of dimers of two Co atoms [8, 9, 20]. However, as we will outline in the following, this interpretation poses quite some inconsistencies and we hence consider it doubtful. First of all, the MS quadrupole doublet was identified as Co dimers despite of the fact that its relative intensity compared to the total spectrum area was found to be inversely proportional to the Co concentration: it dominated the Mössbauer spectrum at 2.5×10^{12} cm^{-2} but was barely visible at fluences above 10^{14} cm^{-2}. While one would expect that a defect containing two Co atoms would have a higher probability of being formed when the Co concentration is increased, it was proposed in Refs. [8, 9] that already in the low 10^{12} cm^{-2} range one is in a regime where the formation of higher order Co clusters dominates over the formation of dimers above 500°C. Consequently, irrespective of fluence, any ^{57}Co MS signal in Si observed after annealing above 500°C was attributed to even higher-order Co clusters, Co silicides, or segregation of Co to the surface. We note that it is easy to estimate that, if Co dimers would be formed in, e.g., 2.5×10^{12} cm^{-2} implanted samples, there should be a mechanism that very efficiently pairs two Co atoms even if their initial separation would be more than 200 Å and despite of a considerable number of implantation-related defects that survive 500°C annealing and may trap them. Moreover, in the MS experiments there was only one quadrupole doublet found. If this would result from Co dimers, it clearly means that the two Co atoms occupy equivalent sites since otherwise the defect would give rise to two different quadrupole doublets, as was also pointed out in Ref. [20]. The only structural model proposed so far for a Co-dimer with two Co atoms on equivalent sites is a pair of substitutional Co atoms that are in a complex with a Si interstitial

[20], requiring actually three constituents. This model, however, is clearly not backed by the emission channeling results, which find an increase in the near-T fraction at 475°C, suggesting that if Co dimers would be formed at this temperature they would involve at least one interstitial Co atom, or consist of two interstitial Co atoms that are both displaced from the ideal T site. It is also not backed by Ref. [21], which suggests the most stable configuration of Co dimers being a substitutional Co atom paired with a Co interstitial. Summarizing, while the formation of Co dimers cannot be ruled out with certainty, there exists currently no microscopic model for such dimers that could consistently explain both the Mössbauer and emission channeling results.

Finally, annealing above 750°C caused the majority of ^{61}Co to occupy ideal substitutional sites. In ^{57}Co MS single lines and doublets observed in Si at such high annealing temperatures were generally associated with Co silicides [9]. In that respect, one may consider the question whether the observation of S sites at high annealing temperatures is due to the formation of epitaxial silicide precipitates [22]. Since the characteristic of substitutional Si sites, as observed by our emission channeling experiments, is that the ^{61}Co probe atoms are perfectly aligned with each crystallographic direction of the Si matrix, this puts considerable constraints on the possible structure of the silicide precipitate. For instance, $CoSi_2$ exhibits the calcium fluoride structure which can be obtained from the diamond structure of Si by replacing one fcc sublattice of Si with Co atoms and, in addition to the second fcc lattice of Si, filling also the interstitital T sites of the Co sublattice with additional Si atoms. ^{61}Co probes in such a structure would in fact produce S-like emission channeling patterns but only if the precipitate expands within the surrounding Si matrix so that the 1.2% lattice mismatch of relaxed $CoSi_2$ with Si is completely removed by strain. In that respect it should be pointed out that the Mössbauer single lines identified as substitutional ^{57}Co [23] and ^{57}Co in $CoSi_2$ [9] have very similar isomer shift, so that they are in any case difficult to distinguish. We should also note the fact that due to the short half-life of ^{61}Co and its continuous decay into ^{61}Ni, the actual amount of ^{61}Co in our sample at any given time was very small, usually less than 10^{12} cm^{-2}, while at the end of the experiment more than ten times as much stable ^{61}Ni has accumulated. Summarizing, our interpretation is that in low-fluence implanted samples, even after annealing at 850°C the substitutional Co fraction does not represent silicide precipitates but still single Co atoms, or at most aggregates of a small number of Co atoms that still allow all of them to occupy substitutional Si sites.

4.5.4 Conclusion

The comparison of the identified lattice sites (ideal S, near-BC and near-T) with the Mössbauer lines reported in literature allowed to obtain a more differentiated picture of the complexes formed by implanted Co in Si. In particular, we propose that the Co visible on near-BC sites in emission channeling experiments, where the related structure have recently been suggested to be involved on P-diffusion gettering of Fe and Ni [6, 7], forms a part of the amorphous doublet line seen in ^{57}Co Mössbauer spectroscopy. This point of view fits well with our previous interpretations of similar near-BC sites for ^{59}Fe and ^{65}Ni, which we attributed to the transition metals being located inside double and multiple vacancies. The local atomic structure around the transition metal would be characterized by somewhat varying bond lengths and angles which may result in Mössbauer parameters quite similar to an amorphous matrix. In addition, we showed that ^{61}Co atoms occupy sites displaced from tetrahedral interstitial towards anti-bonding sites in about the same annealing temperature range where ^{57}Co MS observes a distinctive quadrupole doublet that was previously suggested to result from the formation of Co dimers. We have presented arguments why we consider the interpretation as Co dimers doubtful. Finally, the ideal S sites observed by emission channeling at the highest annealing temperatures represent most likely still single Co atoms or clusters of few substitutional Co atoms involved in the first stages of precipitation. If ^{61}Co should be found within silicide precipitates, our data are only compatible with transition metal precipitates where the ^{61}Co atoms would be perfectly aligned with the surrounding Si matrix.

Bibliography

[1] E. R. Weber, Transition metals in silicon, Appl. Phys. A: Solids Surf. 30 (1983) 1.

[2] S. M. Myers, M. Seibt, W. Schröter, Mechanisms of transition-metal gettering in silicon, J. Appl. Phys. 88 (2000) 3795.

[3] U. Wahl, A. Vantomme, G. Langouche, J. G. Correia, Lattice location and stability of ion implanted Cu in Si, Phys. Rev. Lett. 84 (2000) 1495.

[4] U. Wahl, A. Vantomme, G. Langouche, J. P. Araújo, L. Peralta, J. G. Correia, Lattice location of implanted Cu in highly doped Si, Appl. Phys. Lett. 77 (2000) 2142.

[5] U. Wahl, J. G. Correia, E. Rita, J. P. Araújo, J. C. Soares, Lattice sites of implanted Fe in Si, Phys. Rev. B 72 (2005) 014115.

[6] *Article I.* D. J. Silva, U. Wahl, J. G. Correia, J. P. Araújo, Influence of n^+ and p^+ doping on the lattice sites of Fe in Si, J. Appl. Phys. 114 (2013) 103503.

[7] *Article III.* D. J. Silva, U. Wahl, J. G. Correia, L. M. C. Pereira, L. M. Amorim, E. Bosne, M. R. da Silva, J. P. Araújo, Lattice location and thermal stability of implanted nickel in silicon studied by on-line emission channeling, J. Appl. Phys. 115 (2014) 023504.

[8] G. Langouche, M. D. Potter, D. Schroyen, Observation of Co-dimer formation during thermal annealing of Co-implanted Si, Phys. Rev. Lett. 53 (1984) 1364.

[9] G. Langouche, M. D. Potter, I. Dézsi, M. F. Wu, A. Vantomme, Mössbauer spectroscopy study of the thermal annealing behavior of very low and very high dose Co-implanted Si, Nucl. Instrum. Methods Phys. Res. B 37 (1989) 438.

[10] D. Gilles, W. Schröter, W. Bergholz, Impact of the electronic structure on the solubility and diffusion of 3d transition elements in silicon, Phys. Rev. B 41 (1990) 5770.

[11] L. M. Pereira, U. Wahl, S. Decoster, J. G. Correia, M. R. D. Silva, A. Vantomme, J. P. Araújo, Direct identification of interstitial Mn in heavily p-type doped GaAs and evidence of its high thermal stability, Appl. Phys. Lett. 98 (2011) 201905.

[12] L. M. C. Pereira, U. Wahl, S. Decoster, J. G. Correia, L. M. Amorim, M. R. D. Silva, J. P. Araújo, A. Vantomme, Mixed Zn and O substitution of Co and Mn in ZnO, Phys. Rev. B 84 (2011) 125204.

[13] L. M. C. Pereira, U. Wahl, J. G. Correia, L. M. Amorim, D. J. Silva, E. Bosne, S. Decoster, M. R. da Silva, K. Temst, A. Vantomme, Minority anion substitution by Ni in ZnO, Appl. Phys. Lett. 103 (2013) 091905.

[14] E. Holmström, A. Kuronen, K. Nordlund, Threshold defect production in silicon determined by density functional theory molecular dynamics simulations, Phys. Rev. B 78 (2008) 045202.

[15] S. Agostinelli, *et al.*, GEANT4 - a simulation toolkit, Nucl. Instrum. Methods Phys. Res. A 506 (2003) 250.

[16] M. R. da Silva, U. Wahl, J. G. Correia, L. M. Amorim, L. M. C. Pereira, A versatile apparatus for on-line emission channeling experiments, Rev. Sci. Instrum. 84 (2013) 073506.

[17] J. F. Ziegler, M. D. Ziegler, J. P. Biersack, SRIM - the stopping and range of ions in matter (2010), Nucl. Instrum. Methods Phys. Res. B 268 (2010) 1818.

[18] U. Wahl, J. G. Correia, S. Cardoso, J. G. Marques, A. Vantomme, G. Langouche, Electron emission channeling with position-sensitive detectors, Nucl. Instrum. Methods Phys. Res. B 136 (1998) 744.

[19] D. V. Makhov, L. J. Lewis, Stable fourfold configurations for small vacancy clusters in silicon from *ab initio* calculations, Phys. Rev. Lett. 92 (2004) 255504.

[20] A.-M. V. Bavel, G. Langouche, H. Overhof, The atomic structure of Co dimers in silicon, Semicond. Sci. Technol. 13 (1998) 108.

[21] Z. Z. Zhang, B. Partoens, K. Chang, F. M. Peeters, First-principles study of transition metal impurities in Si, Phys. Rev. B 77 (2008) 155201.

[22] A. A. Istratov, E. R. Weber, Electrical properties and recombination activity of copper, nickel and cobalt in silicon, Appl. Phys. A 66 (1998) 123.

[23] G. Langouche, M. D. Potter, Identification of substitutional and interstitial Co implanted in Si, Nucl. Instrum. Methods Phys. Res. B 19 (1987) 322.

4.6 Article V - Lattice sites of implanted Co in heavily doped Si

D. J. Silva[1], U. Wahl[2], J. G. Correia[2], L. M. C. Pereira[3], L. M. Amorim[3], M. R. da Silva[4], J. P. Araújo[1]

[1] IFIMUP and IN-Institute of Nanoscience and Nanotechnology, Departamento de Física e Astronomia da Faculdade de Ciências da Universidade do Porto, Rua do Campo Alegre 687, 4169-007 Porto, Portugal

[2] Centro de Ciências e Tecnologias Nucleares, Instituto Superior Técnico, Universidade de Lisboa, 2686-953 Sacavém, Portugal

[3] Instituut voor Kern- en Stralingsfysica, KU Leuven, 3001 Leuven, Belgium

[4] Centro de Física Nuclear da Universidade de Lisboa, 1649-003 Lisboa, Portugal

in preparation for *Semiconductor Science and Technology*

abstract

We have studied the influence of electronic doping on the preferred lattice sites of implanted ^{61}Co, and related thermal stabilities, in silicon. By using the β^- emission channeling technique we have identified Co on ideal substitutional (ideal S) sites, sites displaced from bond-centered towards substitutional (near-BC) sites and sites displaced from tetrahedral interstitial towards anti-bonding (near-T) sites. We show clearly that the fractions of Co on these lattice sites change with doping. While near-BC sites prevail in n^+-type Si, near-T sites are preferred in p^+-type Si. Less than $\sim$ 35% of Co occupies ideal S sites in both types of heavily doped silicon, showing that the majority of implanted Co forms complex defect structures. Implantation-induced defects seem to getter more efficiently Co in lightly doped n-type than in heavily doped n^+- or p^+-type silicon. The formation of CoB pairs may also play a role on the observed near-T sites in p^+-type silicon.

4.6.1 Introduction

The unintentional introduction of deep levels in the bandgap during silicon growth and device processing has been pointed out as one of the main source of malfunctioning of devices [1]. One such example occurs in the photovoltaic (PV) industry where even small concentrations of transition metal (TM) impurities limit a satisfactory

performance of solar cells [2]. Although rarely mentioned, one important contaminant is Co [3]. Since the introduction of deep levels depends on the position of the contaminant in the crystal lattice, the manipulation of the occupied lattice sites could lead to an increase of device efficiency. However, the two common symmetric lattice sites of Co, substitutional and tetrahedral interstitial sites, have been shown to introduce deep levels within the silicon bandgap. In fact, three deep levels have consistently been identified experimentally, $E_C - 0.19$ eV and $E_V + 0.53$ eV when Co occupies tetrahedral interstitial sites [4] and $E_C - 0.39$ eV when Co occupies substitutional sites [5], where E_C and E_V are the energies of the conduction and valence band edges respectively. Furthermore, like all 3d TMs, the preference of Co for tetrahedral interstitial sites makes it a very fast diffuser (activation energy for diffusion of ~ 0.40 eV) [6], precipitating easily and thus forming very effective traps for minority carriers with the introduction of other deep levels [1]. Attention has hence been directed to their mitigation, e.g. by introducing gettering centers such as implantation-induced defects or negatively charged substitutional boron dopants, B_S^-. In that respect, only the complexes formed by Co and implantation-induced defects have been addressed so far by studying the lattice sites of Co by means of a β^- emission channeling experiment [7]. Three different lattice sites were identified depending on the annealing temperature: ideal substitutional sites, sites displaced from bond-centered sites and sites displaced from tetrahedral interstitial sites [7]. The influence of electronic doping on the occupied lattice sites of implanted Co was, however, not considered.

Another important feature of Co in Si is its none zero magnetic moment when occupying substitutional sites [8]. This fact brought attention into the dilute magnetic semiconductor (DMS) research community. The challenge has been to find a mechanism that leads to the formation of substitutional Co without forming secondary phases or other complexes that could destroy possible dilute magnetism. One way to incorporate Co on substitutional sites is by ion implantation. However, it has been shown that no more than $\sim 60\%$ of implanted Co occupies substitutional sites in n-type Si (with resistivities of $7.3 - 12$ Ωcm and Co fluence of $\sim 1.5{\times}10^{12}$ cm^{-2}) [7]. The remaining Co forms other complexes with agglomerations of vacancies.

These two important features of Co illustrate firmly why the understanding of the microscopic formation mechanisms of the formed complexes is important. Some questions have, however, still to be answered. In particular, if electronic doping could lead to different occupied lattice sites or different thermal stabilities of the lattice sites identified in Ref. [7]. Here, we address these questions by applying the β^- emission

channeling technique in two different heavily doped silicon samples (p^+-type and n^+-type). The thermal stability of each identified lattice site was inferred from studying the dependence of the related fraction with annealing temperature.

4.6.2 Experiment

The introduction of the radioactive isotope ^{61}Co in two heavily doped silicon samples was obtained by implanting the precursor isotope ^{61}Mn at the on-line isotope separator ISOLDE facility at CERN. ISOLDE provides pure beams of ^{61}Mn, which is obtained by nuclear fission of UC_2 targets induced by a 1.4 GeV proton beam. The chemical selection of Co species was achieved by a laser ion source [9]. ^{61}Mn was further mass separated before being implanted.

The conversion of ^{61}Mn into ^{61}Co takes place along the decay chain ^{61}Mn ($t_{1/2}$ = 0.61 s) $\rightarrow$ ^{61}Fe (5.98 min) $\rightarrow$ ^{61}Co (1.65 h) [7]. To obtain the lattice location of ^{61}Co we have used the β^- emission channeling (EC) technique. With this experimental method the occupied lattice sites of the radioactive probes are deduced from the channeling (or blocking) effects of the emitted β^- particles along major crystallographic directions [10]. The measurements were performed under a vacuum better than 10^{-5} mbar with an energy- and position-sensitive detector placed along the crystallographic directions <110>, <211>, <100> and <111>. References. [10] and [11] can be consulted for more detailed information about both the technique and the apparatus. One should note finally that the recoil energy of the ^{61}Fe decay was 103 eV, which re-implanted ^{61}Co and hence removed any influence of the ^{61}Fe position on the observed lattice sites.

The two single crystal samples used were Czochralski grown with <111> surfaces: boron-doped p^+-type silicon (p^+-Si) with a resistivity of $(4.6 - 5.9)\times10^{-3}$ Ωcm, corresponding to a boron concentration of [B] $\sim 3\times10^{19}$ cm^{-3}, and arsenic-doped n^+-type silicon (n^+-Si) of $(1.0 - 5.0)\times10^{-3}$ Ωcm, corresponding to [As] $\sim 3\times10^{19}$ cm^{-3}. Both samples were implanted at room temperature, followed by measuring the emission channeling effects in the as-implanted state. After the decay of the previous implanted activity, the samples were re-implanted, annealed for 10 min and then measured again at room temperature. This procedure was repeated with increasing annealing temperatures, using 150°C, 300°C, 450°C, 600°C, 675°C and 850°C for the p^+-Si sample and 400°C, 500°C, 600°C, 700°C and 800°C for the n^+-Si sample. While the heating of the samples was quite fast, the cool down lasted up to 30 min for the

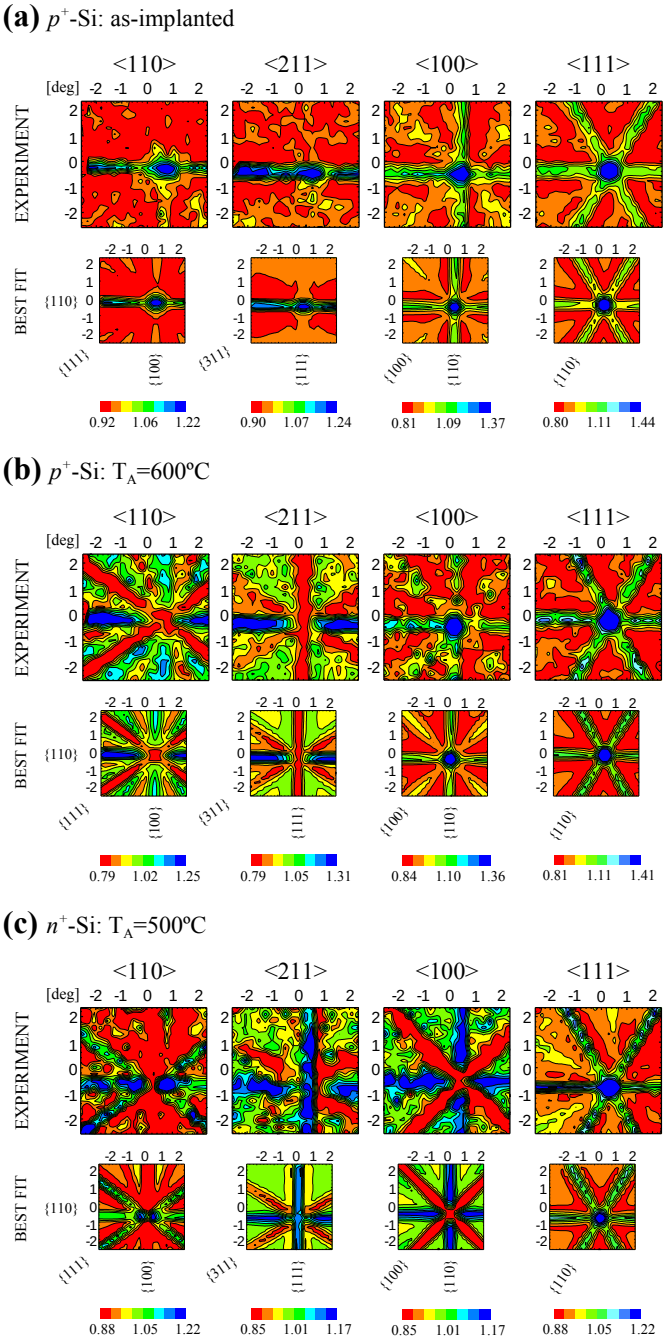

Figure 4.16: Two dimensional experimental patterns and corresponding best fits from ^{61}Co, in the vicinity of <110>, <211>, <100> and <111> after (**a**) implanting at room temperature in p^+-Si, (**b**) annealing at 600°C in p^+-Si and (**c**) annealing at 500°C in n^+-Si.

higher annealing temperatures. The fluence for each implantation step was 1.4×10^{12} cm^{-2} for the p^+-Si sample using 50 keV, and 1.9×10^{12} cm^{-2} for the n^+-Si at 40 keV, with the accumulated fluences at the end of the experiments being $\sim 10^{13}$ cm^{-2} in both cases. An estimate for the number of produced vacancies by ^{61}Mn was obtained with the SRIM code. While each 50 keV implanted ^{61}Mn ion produces approximately 850 vacancies, each 40 keV implanted ^{61}Mn results in approximately 700 vacancies. The depth profiles of the implanted ^{61}Mn were also estimated with SRIM, being approximated by Gaussians centered at $R_p = 460$ Å for 50 keV and $R_p = 370$ Å for 40 keV. The estimated straggling is 180 Å and 150 Å, respectively. The estimated peak concentrations of ^{61}Mn are therefore 4.2×10^{17} cm^{-3} for 50 keV and 4.6×10^{17} cm^{-3} for 40 keV. Note that although ^{61}Co receives a nuclear recoil of ~ 103 eV, this does not significantly alter its depth profile. For both cases, the peak of the vacancy profile is located midway from the surface to the peak concentration of the implanted ^{61}Mn (at $R_p/2$). In addition to the detected β^- particles that comes directly from the probes, also β^- particles which are backscattered inside the sample or the walls of the setup, as well as a small contribution from detected γ particles contribute to the count rate in the position-sensitive detector used in these experiments. These events produce a nearly isotropic background which has to be removed or corrected during the analysis. The backscattered β^- particles were considered by subtracting an isotropic background from the channeling patterns, i.e. angle-independent emission yield which was estimated with the Monte Carlo simulation code GEANT4 [12]. The contribution from γ particles was taken into account by subtracting a background pattern, which was measured when a shutter was closed in front of the detector, from the channeling patterns.

4.6.3 Results

The two dimensional experimental emission yields in the vicinity of the four crystallographic directions were fitted by considering theoretical patterns obtained with the *manybeam* formalism. The identification of the occupied lattice sites followed the approach which was already described in detail in Ref. [7], considering as possible sites the substitutional and major interstitial sites, as well as displacements between them along <111>, <100> and <110> directions. While, as in Ref. [7], the lattice sites identified were also ideal substitutional (S), sites displaced along <111> from bond-centered towards substitutional (near-BC), and sites displaced along <111> from tetrahedral interstitial towards anti-bonding (near-T), clear changes in the distribution

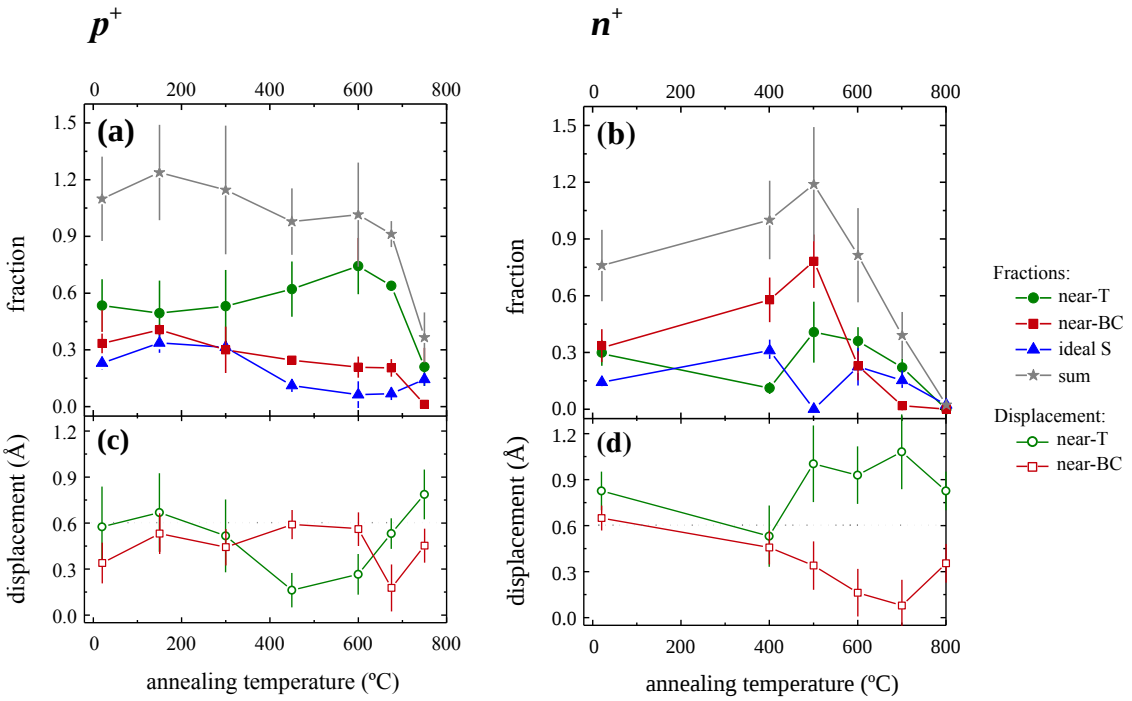

Figure 4.17: Dependence of the fractions, and related sum, of the three identified lattice sites with annealing temperature for (**a**) the p^+-Si and (**b**) the n^+-Si sample. The displacement of the near-BC and near-T sites from the ideal BC site towards the ideal S site and from the ideal T site towards the ideal AB site, respectively, is shown in (**c**) for the p^+-Si sample and (**d**) for the n^+-Si sample.

of Co among those sites were observed as a function of doping type. This is illustrated by the experimental and best fit patterns in Fig. 4.16, and the fractions of Co on the three different lattice sites as a function of annealing temperature, as well as the displacements from the ideal BC and T sites (Fig. 4.17) for the different doping types.

The electron emission patterns from the as-implanted state of the p^+-Si sample [Fig. 4.16 (**a**)] are characterized by maxima of the emission yield along all major axial directions, which shows that significant fractions of emitter atoms are located close to substitutional sites. However, at the same time the planar {111} channeling effects of these patterns are practically absent, which can be explained by the fact that the {111} channeling effects from substitutional Co are completely compensated by a large fraction of Co emitter atoms close to the interstitial T sites, which are characterized by blocking effects along {111} planes. The best fit results completely confirm this first visual analysis, showing that in the as-implanted state in p^+-Si $\sim$ 53% of ^{61}Co occupy near-T sites, $\sim$ 23% ideal S sites, and $\sim$ 33% near-BC sites. With increasing

annealing temperature in the same material one observes a gradual change in the patterns which are characterized by an increasing intensity of blocking effects along the {111} and {311} planes and <110> and <211> axial directions. As is illustrated in Fig. 4.16 (**b**), the <110> and <211> axial as well as the {111} and {311} planar blocking effects in p^+-Si become more intense following annealing at $T_A = 600°C$, resulting in electron emission patterns that show all characteristics of emitter atoms on interstitial sites close to the ideal T position. At this annealing temperature, $\sim$ 74% of ^{61}Co occupies near-T sites, $\sim$ 6% ideal S sites and $\sim$ 11% near-BC sites. The fractions of the three lattice sites in p^+-Si can be seen in Fig. 4.17 (**a**), which shows the prevailing of near-T sites over the whole range of annealing temperatures. The increase in the intensity of blocking effects with annealing temperature, up to $T_A = 600°C$, is accompanied by a pronounced channeling peak along <100>, showing that near-T sites approach the ideal T site with T_A as illustrated in Fig. 4.17 (**c**). Near-BC sites show consistently displacements of $\sim$ 0.6 Å from ideal BC sites, except for $T_A = 675°C$. Long-range diffusion seems to be attained near 800°C.

In contrast, in the n^+-Si experiment the near-T fraction is much less significant for all annealing temperatures. In the as-implanted state, $\sim$ 14% of ^{61}Co occupies S sites and $\sim$ 32% near-BC sites, while only $\sim$ 29% of ^{61}Co are found on near-T sites. Although no measurements were made for intermediate annealing temperatures, after a 400°C annealing near-BC sites have become more significant [Fig. 4.17 (**b**)], and they dominate the electron emission patterns following $T_A = 500°C$ [Fig. 4.16 (**c**)]: in particular the double channeling peak in the electron emission yield along the <110> axis and the clear blocking effects of the {100} planes and <100> axial direction are all characteristics of emitter atoms close to ideal BC sites. Annealing above 500°C makes the sum of all fractions to decrease, along with the near-BC and near-T fractions. Long-range diffusion of ^{61}Co in n^+-Si starts at 800°C.

4.6.4 Discussion

As has been discussed in more detail in previous publications [13–15],[1] the concentration of implantation-induced defects is about two orders of magnitude higher in the samples than the concentration of ^{61}Co and its decay product ^{61}Ni. The only other impurities present in comparable amounts (approximately two orders of magnitude

[1] In order to keep both manuscripts on Co together, the chronological order of writing of the manuscripts is here broken. Article VI was written before Article V, explaining why article VI (Ref. [15]) is here cited.

above the peak concentration of ^{61}Co) are the electrical dopants B for the p^+ and As for the n^+ sample, while other common impurities in Si, e.g. C or O, are much less abundant. It seems hence reasonable to assume that the observed lattice site preferences of Co are a consequence of its direct interaction with vacancies, self-interstitials and electric dopants, taking into account that these processes are of course also influenced by the position of the Fermi level caused by the presence of the electric dopants and the radiation damage. Clustering of ^{61}Co or of ^{61}Co and ^{61}Ni atoms (or other TMs unintentionally present in the sample) is a possibility which cannot be ruled out, but it would need a very efficient mechanism in order for clustering to be dominant.

Several mechanisms can lead to distinct lattice sites of ^{61}Co for different doping types of silicon. For instance, while the majority of interstitial ^{61}Co is neutral or negatively charged in n^+-Si, due to the deep acceptor level $E_C - 0.19$ eV, most of interstitial ^{61}Co is positively charged in p^+-Si due to the deep donor level $E_V + 0.53$ eV. Therefore, if the electrostatic interaction drives the pairing of ^{61}Co with different defects, the change of its charge state, when using distinct doping types of silicon, will result in different complexes and thus in different observed lattice sites. Another influence of the doping comes from the well-known counter-doping phenomenon driven by the electron-hole equilibrium. If ^{61}Co in a particular lattice site exhibits dopant characteristics opposite to those of the major electric dopants (usually meaning that the Co defect will be oppositely charged to B^- or As^+) its thermal stability may be increased. One way to infer if this mechanism is playing a role is by observing different annealing temperatures, for which the fraction of a particular lattice site starts to reduce, when using different doping types of the semiconductor material. This has been observed for the near-BC (or near-S) sites of Cu [16], Fe [13], Ni [14] and Mn [15] in Si. In the following, we discuss in detail the obtained results for the p^+-Si and n^+-Si samples.

4.6.4.1 p^+-type silicon

Despite the fact that the same three lattice sites are observed as in the low-doped n-Si sample of Ref. [7], they show quite different fractions in p^+-Si as a function of annealing temperature. First of all, in p^+-Si the ideal S sites are only prominent for low annealing temperatures and disappear to a large extent during annealing at 450°C. In that respect, by using the formula of Refs. [13] and [14] of the activation energy for dissociation from the respective defects [13, 14], one obtains $E_d = (1.8 - 2.0)$ eV for the experiment of Ref. [7] (in n-type Si) and $E_d = (1.8 - 2.0)$ eV for the p^+-Si

sample. Hence, there is no noticeable influence of the doping on the thermal stability of S sites that appear after annealing at low temperatures. In fact, the fraction of those S sites never exceeds $\sim$ 35%, as observed in n-type Si for the low annealing temperature regime [7].

As described in previous emission channeling investigations, near-BC sites may result from the trapping of transition metals into multivacancies produced during implantation, such as divacancies and fourfold coordinated vacancy clusters [7, 13–15]. Co, in addition to Mn, Fe and Ni, may also behave in the same manner.

The use of a heavily doped p-type silicon sample seems to convert part of the near-BC sites, observed in n-type Si of Ref. [7], to near-T sites seen in this work. Near-T sites are, in fact, the prevailing fraction over the whole range of annealing temperatures. In addition to the multivacancies, which might be present in high concentrations, boron may also be involved in the observed near-T sites by forming Co_iB_S pairs [1, 17]. The pair formation of implanted Fe, in which the behavior of the three identified fractions with annealing temperature follows the same trend as for the present case of Co, with boron dopants has recently been discussed [13]. In a similar analysis, one can deduce that while Co dissociates easily from the pairs at relatively low temperatures, since the binding energy is small (E_b = 0.6 eV) [4], they are in principle reformed again when returning to room temperature. It has been shown for the case of Fe that while FeB pairs are dynamically formed and dissociated, long-range diffusion is not suppressed but only slowed down [13]. The fact that in this investigation long-range diffusion or substantial reduction of the near-T fraction only occurs for high annealing temperatures ($\sim$ 750°C) makes it difficult to draw conclusions on the mechanisms of formation and dissociation of CoB pairs. We can nevertheless compare the distance between boron and cobalt ions, where the electrostatic interaction energy corresponds to the binding energy of the pair, to the Co displacements observed from ideal T sites in this work. By using the formula $d = q^2/(4\pi\epsilon\epsilon_0 E_b)$, in which q is the charge of the electron, ϵ the dielectric constant of Si, ϵ_0 the dielectric constant of vacuum and E_b the binding energy of the pair one obtains d = 2.01 Å, which corresponds to a displacement of 0.34 Å from the ideal T site towards the AB site. This means that for Co within CoB pairs the value of the expected Co displacement from ideal T sites is quite similar to the displacements found following annealing at $450 - 600$°C. One should, however, note that such displacements are also observed in the n-Si sample of Ref. [7], where such pairs are not likely to be found due to the absence of acceptor dopants. This fact complicates the distinction between ^{61}Co in CoB pairs and the near-T ^{61}Co not involving such pairs.

4.6.4.2 n^+-type silicon

In the as-implanted state of the highly-doped n^+-Si sample, the three identified lattice sites of Co show similar fractions as in the low-doped n-Si sample from Ref. [7]. In that respect, one should note that only one acceptor level very close to the conduction band is present in the bandgap when Co is in its interstitial form. The charge state of Co may hence be preserved when changing the electronic doping from intrinsic, or n-type, to n^+-type Si (with the condition that the Fermi level does not overcome the deep acceptor level). Therefore, the interaction between Co and other defects that also keep their charge state may, in principle, be the same in n and n^+-Si. From the annealing temperature of 400°C to 500°C, the fraction of near-BC sites increases significantly along with that of near-T sites. On the contrary, the ideal S fraction decreases. This behavior contrasts with that in n-type Si [7], but follows the trend of more prominent near-BC sites observed for Fe, Cu and Ni in n^+-type Si [16, 13, 14]. One important feature of this particular annealing temperature is that the sum fraction attains values above 100%. This might be explained by the diffusion of Co towards $R_p/2$. What seems, however, inconclusive is whether near-BC or near-T sites are involved in such traps. In that respect, it is worthwhile to point out that for all TMs observed so far by emission channeling experiments in Si, such changes of the sum are followed by an increase of near-T sites. Ideal S sites disappear at the annealing temperature of 500°C, but reappear at 600°C. This behavior seems to follow the trend of the ideal S fraction in n-type Si, however to a minor extent. There is also the possibility that the channeling effects from $R_p/2$, that are not considered in the simulated patterns, provoke an unwanted effect in the analysis, such as by reducing some fractions of the observed lattice sites at $T_A = 500$°C. One should finally discuss the possible formation of CoAs pairs in n^+-type Si. It has been suggested that Co prefers substitutional sites when forming CoP pairs [17]. The same behavior could be found for CoAs. Such formation cannot, however, be inferred in this investigation. Ideal S sites seem to follow a similar trend as in n-type Si.

4.6.5 Conclusion

We identified implanted Co on ideal substitutional sites, sites displaced from bond-centered sites and sites displaced from tetrahedral interstitial sites. We proved unambiguously that the related fractions are influenced by the doping type of the silicon material. In both doping types, n^+ and p^+, the substitutional fraction never exceeds $\sim$

35%, in contrast to the substitutional fraction of Co in lightly doped n-type Si where $\sim$ 60% of Co can be incorporated on substitutional sites. The use of heavily doped Si hence reduces the substitutional fraction of Co, important feature to understand the Co-doped Si system as a possible dilute magnetic semiconductor. Long-range diffusion occurs already at $T_A \sim 800$°C in both n^+ and p^+, while in lightly doped n-Si the observed lattice sites were even still present after annealing at 850°C. Hence, the immobilization of Co by implantation-induced defects is less effective in n^+ and p^+ than in n regions. This may have some implications, e.g. by using irradiated lightly doped n regions to getter Co more efficiently. We also showed that CoB pairs may exist, and that Co may prefer sites near the tetrahedral interstitial position within the pair.

Bibliography

[1] S. M. Myers, M. Seibt, W. Schröter, Mechanisms of transition-metal gettering in silicon, J. Appl. Phys. 88 (2000) 3795.

[2] S. Pizzini, Towards solar grade silicon: Challenges and benefits for low cost photovoltaics, Sol. Energy Mater. Sol. Cells 94 (2010) 1528.

[3] E. R. Weber, Transition metals in silicon, Appl. Phys. A 30 (1983) 1.

[4] H. Lemke, K. Irmscher, Proof of interstitial cobalt defects in silicon float zone crystals doped during crystal growth, ECS Trans. 3 (2006) 299.

[5] L. Scheffler, V. Kolkovsky, J. Weber, Isolated substitutional cobalt and Co-related complexes in silicon, J. Appl. Phys. 113.

[6] K. Matsukawa, K. Shirai, H. Yamaguchi, H. Katayama-Yoshida, Diffusion of transition-metal impurities in silicon, Phys. B Condens. Matter 401 (2007) 151.

[7] *Article IV.* D. J. Silva, U. Wahl, J. G. Correia, L. M. C. Pereira, L. M. Amorim, M. R. da Silva, J. P. Araújo, Origin of the lattice sites occupied by implanted Co in Si, submitted to Semicond. Sci. Tech.

[8] Z. Z. Zhang, B. Partoens, K. Chang, F. M. Peeters, First-principles study of transition metal impurities in Si, Phys. Rev. B 77.

[9] V. N. Fedosseev, L.-E. Berg, N. Lebas, O. J. Launila, M. Lindroos, R. Losito, B. A. Marsh, F. K. Österdahl, T. Pauchard, G. Tranströmer, J. Vannesjö, ISOLDE

RILIS: New beams, new facilities, Nucl. Instrum. Methods Phys. Res. B 266 (19) (2008) 4378.

[10] U. Wahl, J. G. Correia, S. Cardoso, J. G. Marques, A. Vantomme, G. Langouche, Electron emission channeling with position-sensitive detectors, Nucl. Instrum. Methods. Phys. Res. Sect. B 136 (1998) 744.

[11] M. R. da Silva, U. Wahl, J. G. Correia, L. M. Amorim, L. M. C. Pereira, A versatile apparatus for on-line emission channeling experiments, Rev. Sci. Instrum. 84 (2013) 073506.

[12] S. Agostinelli, *et al.*, GEANT4 - a simulation toolkit, Nucl. Instrum. Methods Phys. Res. A 506 (2003) 250.

[13] *Article I.* D. J. Silva, U. Wahl, J. G. Correia, J. P. Araújo, Influence of n^+ and p^+ doping on the lattice sites of Fe in Si, J. Appl. Phys. 114 (2013) 103503.

[14] *Article III.* D. J. Silva, U. Wahl, J. G. Correia, L. M. C. Pereira, L. M. Amorim, E. Bosne, M. R. da Silva, J. P. Araújo, Lattice location and thermal stability of implanted nickel in silicon studied by on-line emission channeling, J. Appl. Phys. 115 (2014) 023504.

[15] *Article VI.* D. J. Silva, U. Wahl, J. G. Correia, L. M. C. Pereira, L. M. Amorim, S. Decoster, M. R. da Silva, J. P. Araújo, Direct observation of the lattice sites of implanted manganese in silicon, to be submitted to Phys. Rev. B.

[16] U. Wahl, A. Vantomme, G. Langouche, J. P. Araújo, L. Peralta, J. G. Correia, Lattice location of implanted Cu in highly doped Si, Appl. Phys. Lett. 77 (2000) 2142.

[17] D. Gilles, W. Schröter, W. Bergholz, Impact of the electronic structure on the solubility and diffusion of 3d transition elements in silicon, Phys. Rev. B 41 (1990) 5770.

4.7 Article VI - Direct observation of the lattice sites of implanted manganese in silicon

D. J. Silva[1], U. Wahl[2], J. G. Correia[2], L. M. C. Pereira[3], L. M. Amorim[3], S. Decoster[3], M. R. da Silva[4], J. P. Araújo[1]

[1] IFIMUP and IN-Institute of Nanoscience and Nanotechnology, Departamento de Física e Astronomia da Faculdade de Ciências da Universidade do Porto, Rua do Campo Alegre 687, 4169-007 Porto, Portugal

[2] Centro de Ciências e Tecnologias Nucleares, Instituto Superior Técnico, Universidade de Lisboa, 2686-953 Sacavém, Portugal

[3] Instituut voor Kern- en Stralingsfysica, KU Leuven, 3001 Leuven, Belgium

[4] Centro de Física Nuclear da Universidade de Lisboa, 1649-003 Lisboa, Portugal

in preparation for *Physical Review B*

abstract

We have investigated the lattice location of implanted Mn in silicon of different doping types in the highly dilute regime. Three different lattice sites were identified by means of emission channeling experiments: ideal substitutional sites; sites displaced from bond-centered towards substitutional sites and sites displaced from anti-bonding towards tetrahedral interstitial sites. For all three doping types, the substitutional fraction remained below $\sim 30\%$. We discuss the origin of the observed lattice sites as well as the implications of such structures on the understanding of Mn-doped Si as a dilute magnetic semiconductor.

4.7.1 Introduction

While Mn-doped III-V semiconductors, such as GaMnAs or InMnAs, have become model host materials for dilute magnetic semiconductors (DMS) [1], group IV semiconductors (Si, Ge) are regarded as advantageous for tackling some of the challenges currently facing DMS research [2]. For Mn-doped Si/Ge DMS systems, however, the lattice location and thermal stability of the Mn dopants is far from established, although the issues of occupation of substitutional versus interstitial sites and dilution versus segregation have already been investigated (e.g. Ref. [3]). In that respect, it has been suggested from first principle calculations that Mn incorporates a consid-

erable magnetic moment when substituting Si host atoms [4]. However, the ease of precipitation, due to its high interstitial diffusivity (the activation energy for diffusion of Mn is ~ 0.72 eV [5]) and excessively low solubility [6], prevents the immobilization of Mn atoms in either interstitial or substitutional sites. An example of secondary phase segregation is the formation of $MnSi_{1.7}$ silicides [7, 8]. One way to promote the incorporation of Mn on substitutional sites is the creation of single vacancies, e.g., by using ion implantation as doping method. Advancing the understanding of Mn-doped Si will require a detailed study of the lattice sites occupied by implanted Mn in the phase-pure regime (dilute, randomly distributed Mn) and their thermal stability. Here, we address these questions by applying the electron emission channeling (EC) technique to identify the lattice sites occupied by the implanted β^- probes ^{56}Mn in different doping types of Si single crystals. The lattice sites of ^{56}Mn were hence inferred from the dependence of the channeling directions and planes of emitted β^- particles [9–12].

4.7.2 Experiment

^{56}Mn was implanted in: n-type Si (n-Si), at an energy of (**i**) 30 keV and (**ii**) 60 keV; (**iii**) n^+-type Si (n^+-Si), at an energy of 30 keV; and (**iv**) p^+-type Si (p^+-Si), at an energy of 30 keV. All samples had <111> oriented surfaces. The implantation took place at the on-line isotope separator facility ISOLDE at CERN, which provides mass separated beams of radioactive isotopes of Mn produced by inducing nuclear fission of uranium carbide targets with a 1.4 GeV proton beam. ^{56}Mn implantations were carried out under a vacuum $< 1\times10^{-5}$ mbar, and under an angle of 17° from the surface normal to avoid channeling implantation. Specifications about the used samples and implantation parameters can be seen in table 4.3. The ^{56}Mn profile as well as the number of vacancies were estimated using the SRIM code [13]. For the 60 keV implantation, the profile can be approximated by a Gaussian centered at 544 Å with a straggling of 212 Å. Each implanted Mn creates ~ 1000 vacancies. For the 30 keV implantation, the profile is centered at 302 Å with a straggling of 123 Å. At this implantation energy, each ^{56}Mn produces ~ 500 vacancies (half those at 60 keV). For both implantation energies, the vacancy concentration peak is located midway from the peak concentration of ^{56}Mn to the surface.

Table 4.3: Sample and implantation details of the four experiments carried out in the present investigation.

experiment	**doping type**	**dopant**	**dopant concentration**	**resistivity**	**implantation energy**	**accumulated ^{56}Mn fluence**
(i)	n	phosphorus	$\sim 1\times10^{15}$ cm^{-3}	$3-12$ Ωcm	30 keV	2.4×10^{13} cm^{-2}
(ii)	n	phosphorus	$\sim 1\times10^{15}$ cm^{-3}	$3-12$ Ωcm	60 keV	1.5×10^{13} cm^{-2}
(iii)	n^+	arsenic	$\sim 3\times10^{19}$ cm^{-3}	$(1-5)\times10^{-3}$ Ωcm	30 keV	2.5×10^{13} cm^{-2}
(iv)	p^+	boron	$\sim 2\times10^{19}$ cm^{-3}	$(4.8-5.8)\times10^{-3}$ Ωcm	30 keV	3.6×10^{13} cm^{-2}

After implanting ^{56}Mn, the samples were annealed *in situ* at several temperatures for 10 min and further measured at room temperature. The electron yield was measured in the vicinity of the <110>, <211>, <100> and <111> crystallographic directions using a position- and energy- sensitive detector [14]. The resulting two-dimensional experimental patterns were further corrected due to the background from γ particles and backscattered β^- particles. While the γ contribution was measured by blocking the β^- particles by means of closing a valve in front of the detector, the contribution of backscattered β^- particles was estimated with the Monte Carlo GEANT4 code [15].

4.7.3 Results

The two-dimensional experimental patterns were fitted by theoretical β^- emission yields for ^{56}Mn emitters, calculated with the *manybeam* formalism for electron channeling [14]. A range of lattice sites were considered in the theoretical patterns covering the following relevant high symmetry sites: substitutional (S), hexagonal (H), tetrahedral (T), bond-centered (BC), anti-bonding (AB), split (SP), $< 110 >$ displaced substitutional (DS), $< 110 >$ displaced tetrahedral (DT), ytterbium (Y) and carbon (C) sites. Sites displaced from these high symmetry sites along <111>, <100> and <110> were also considered. The minimum step of displacement was ~ 0.03 Å. The lattice sites are discussed in detail in Ref. [16].

The fitting procedure was started with the use of one fraction only. The minimization of the χ^2 of fit resulted consistently, over the whole range of annealing temperatures, on sites displaced from BC towards S sites (near-BC sites), for the n- and n^+-Si samples. For p^+-Si, sites displaced from AB towards T sites (near-AB sites)[2] presented the best χ^2 of fit. The introduction of a second fraction, near-AB in the n- and n^+-Si experiments and near-BC in the p^+-Si experiment, led to an additional considerable decrease of the χ^2 of fit. Since substitutional sites are recurrently mentioned in literature we tested the ideal S site as a third fraction. It gave a further significant reduction of the χ^2 of fit for all the annealing temperatures. The addition of a fourth lattice site did not result in a significant change in the χ^2 of fit. Figure 4.18 shows the two-dimensional experimental patterns for ^{56}Mn emitters from the n-Si sample after implanting at 60 keV and from the n-, n^+- and p^+-Si samples after implanting at 30 keV. The dependence of the fraction of each identified lattice site as well as

[2]In the abstract and conclusion of the present PhD thesis, near-AB sites are considered equivalent to near-T sites. In fact, they can be interpreted as being the same type of lattice sites, sites between tetrahedral interstitial and anti-bonding sites.

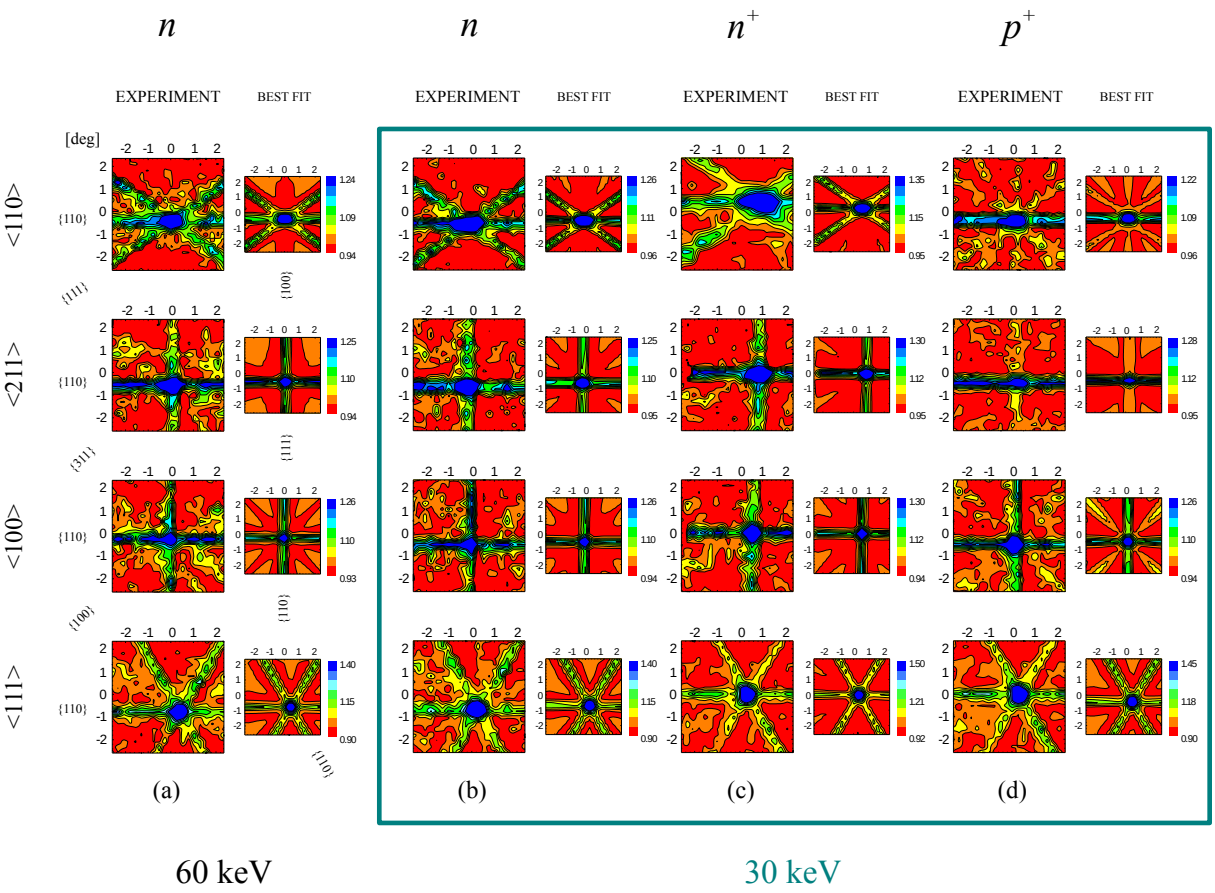

Figure 4.18: Two-dimensional experimental and calculated emission channeling patterns from ^{56}Mn in (**a,b**) n-type, (**c**) n^+-type and (**d**) p^+-type Si, after implanting at room temperature. While in (**a**) ^{56}Mn was implanted at 60 keV, in (**b-d**) the implantation energy was 30 keV.

the respective sum for all the four experiments are plotted in Fig. 4.19. Finally, the dependence of the displacement of near-BC and near-AB sites with annealing temperature is shown in Fig. 4.20. In the following, we describe in detail the obtained results for each of the four experiments.

4.7.3.1 n-type

30 keV

After implanting at 30 keV, the fractions of the identified three lattice sites of ^{56}Mn are quite similar (30% of ^{56}Mn occupies near-BC sites, 20% ideal S sites and 27% near-AB sites). This fact can be easily observed with the prominent channeling {111} planes

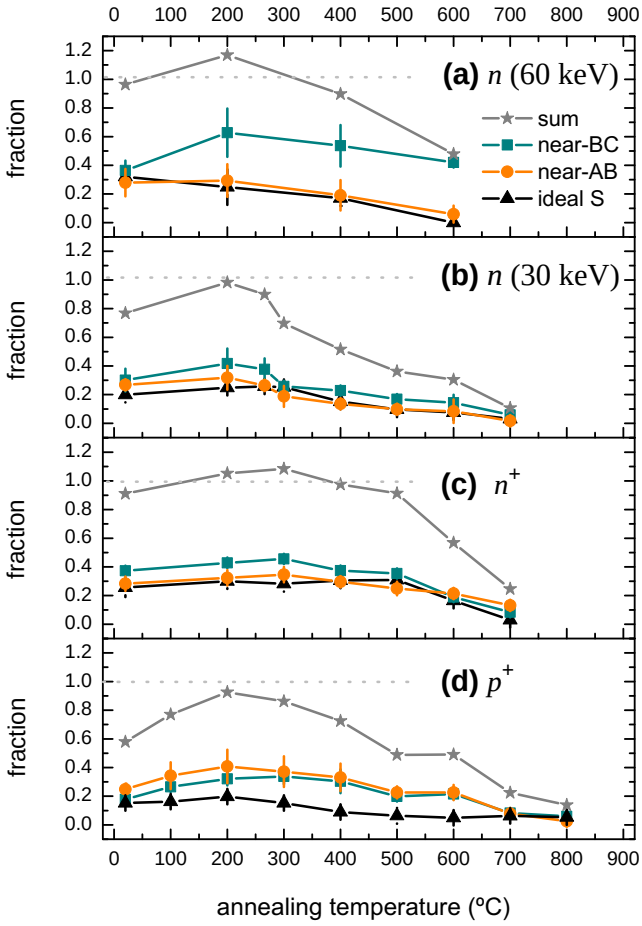

Figure 4.19: Fractions of the three identified lattice sites as a function of annealing temperature for (**a**) n-type Si after implanting at 60 keV, and (**b**) n-type, (**c**) n^+-type and (**d**) p^+-type Si, after implanting at 30 keV.

indicative of the presence of sites near the BC position, prominent channeling {110} planes characteristic of sites near T or AB positions and presence of the channeling peak along the <211> direction originated by ideal S sites. The fitting results agree with this scenario for all annealing steps. In particular, after the 200°C anneal, 42% of ^{56}Mn occupies near-BC sites, 25% ideal S sites and 32% near-AB sites.

The sum of all fractions varies with the annealing temperature. While a maximum is obtained at $T_A = 200$°C, a reduction of the sum is prominent up to the annealing temperature where long-range diffusion takes place (700°C).

The displacements of near-BC and near-AB sites are also similar for the different

annealing temperatures. While near-BC sites are displaced ~ 0.3 Å from the ideal BC site, near-AB sites show a displacement of ~ 0.3 Å from the ideal AB site.

60 keV

The best fit results showed that near-BC sites unambiguously prevail for all the annealing steps. In particular, after annealing at 200°C, 25% of ^{56}Mn occupies ideal S sites, 29% near-AB sites and 63% near-BC sites.

The average displacement of the near-BC and near-AB sites from the ideal BC site and the ideal AB site, respectively, are both ~ 0.4 Å.

4.7.3.2 n^+-type

For n^+-Si, we obtained similar two-dimensional experimental patterns as in the case of n-Si (from Fig. 4.18 (**b**) to (**c**)). Two differences are, however, observed in the evolution of the fractions and displacements with annealing temperature. First, from Fig. 4.19 (**c**) one can notice that the sum of all the fractions only starts to decrease significantly after the 600°C anneal, while in n-Si the sum already reduces at ~ 300°C. There is, therefore, an higher thermal stability of the three observed lattice sites in n^+-Si. Secondly, Fig. 4.20 shows that, compared to n-Si, near-AB sites are closer to the ideal AB site (average displacement of ~ 0.1 Å from the ideal AB site), while near-BC sites are closer to the ideal BC site (average displacement of ~ 0.2 Å from the ideal BC site).

4.7.3.3 p^+-type

In experiment (**iv**), similar fractions for the three identified lattice sites of ^{56}Mn are again observed at room temperature. However, once the annealing temperature increases one notices that both near-BC and near-AB fractions differ from those of ideal S sites, with a small, but consistent, prevailing of the near-AB sites.

Both near-BC and near-AB sites show the highest displacements compared to n- and n^+-Si, as observed in Fig. 4.20: near-AB and near-BC sites are displaced ~ 0.5 Å from the ideal AB site and ideal BC site, respectively.

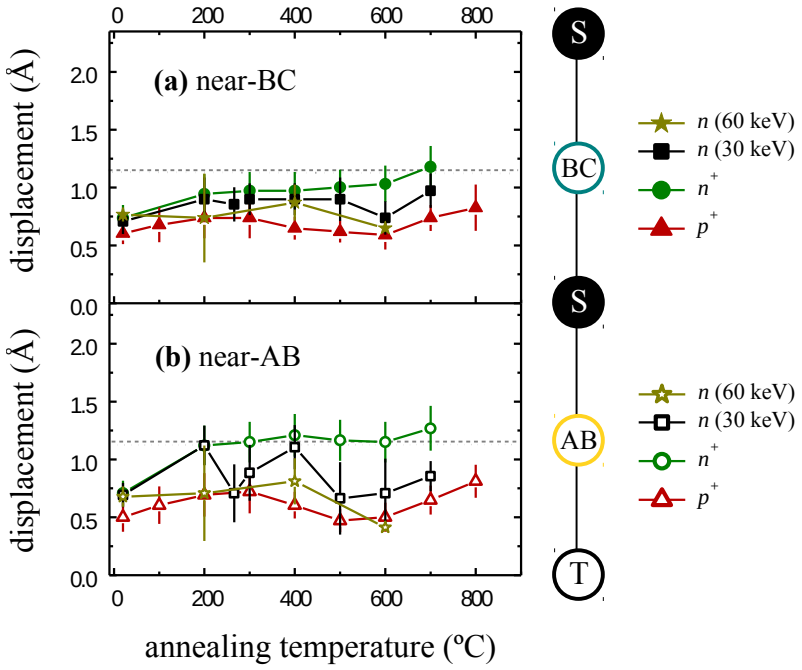

Figure 4.20: Displacements of the (**a**) near-BC and (**b**) near-AB sites from S towards BC sites and from T towards AB sites, respectively, as a function of annealing temperature, for all the three types of Si and two different implantation energies.

4.7.4 Discussion

The observation of the non regular sites near-BC and near-T sites suggests the involvement of complex structures. Moreover, isolated interstitial Mn_i may not take part in the majority of observed lattice sites, since its fast diffusing behavior would lead to long-range diffusion already at room temperature. It is possible that ^{56}Mn interacts with contaminant impurities, e.g. O, H or C. However, using similar arguments as given for EC studies on other 3d TMs in Si [9, 16–22], such as the influence of different silicon materials (Czochralski or float zone silicon) and comparison of both the TM and contaminant impurity concentrations, one can conclude that such interactions, if present, only affect a small fraction of ^{56}Mn. Hence, the most plausible origin for the observed lattice sites may come from the interaction of Mn with self-interstitials, vacancies and electric dopants. While the trapping of Mn into defective regions of the silicon material (involving vacancies and self-interstitials) may result from local changes in the lattice potential caused by open volumes or strain, the pairing of Mn

with electric dopants is mostly driven by the Coulomb interaction, e.g. immobile B_S^- will attract Mn_i^+. The charge state of the fast interstitial Mn_i will hence determine the ease of Mn-dopant pair formation. In that respect, it is known that Mn_i presents three deep levels ($E_C - 0.12$ eV, $E_C - 0.41$ eV, $E_V + 0.32$ eV [5]), which represents charge transitions between Mn_i^-, Mn_i^0, Mn_i^+ and Mn_i^{++}. While in n^+-type Si, Mn is neutral or negatively charged, in p^+-type Si, Mn is mostly positively charged (1+ or 2+). Last but not least, aggregation of Mn may also occur. However, clustering has been shown to play a minor role in an EC study on Fe [20], where different fluences of Fe (between 10^{12} and 10^{14} cm^{-2}) showed essentially the same behavior. Additionally, a careful assessment of the possibility of Co forming dimers in Si showed that only a very efficient pairing mechanism could promote clustering in highly dilute regimes and in regions plenty of defects [22]. There is no reason to expect Mn to behave differently. In the following, it is discussed in detail possible origins for the observed three lattice sites as well as their thermal stabilities.

4.7.4.1 Ideal S sites

The incorporation of Mn on ideal S sites most likely results from its trapping into the single vacancies produced during implantation. The incorporation of Mn on ideal S sites seems hence to be hampered by the existence of more effective traps. This is likely to be more problematic when creating more defects, allowing their aggregation, e.g. by increasing the fluence. For Mn-doped silicon at fluences around 10^{16} cm^{-2}, the fraction of substitutional Mn might hence represent a value below 30%. By comparing to Co, which is also a potential magnetic dopant in Si, one can observe that the substitutional fraction of Co can reach twice that of the present case of Mn, for particular annealing treatments [22]. Co is thus more efficiently incorporated into S sites. One should, however, note that for the case of Co other origins, other than the related formation of its substitutional form, might have played a role in the observed ideal S sites, especially for high annealing temperatures. One crucial observation for the understanding of the microscopic nature of the magnetism of Mn is the fact that the fraction of the ideal S sites is less than $\sim 30\%$ in all the studied samples. With $\lesssim 30\%$ of Mn on ideal S sites, the risk of having part of the remaining $\gtrsim 70\%$ forming other complexes that can destroy the ferromagnetic order of dilute substitutional Mn, is very high. How this can affect the ferromagnetism is not known and, therefore, needs further theoretical investigation that includes structures where Mn occupies near-BC and near-AB sites, discussed in the next two subsections. Finally, one should discuss the fact that the observed ideal S sites are more thermally stable in n^+-Si, as observed in Fig. 4.19 (**c**).

Such fact may be related to some extent to the existence of the deep donor level of the substitutional form of Mn at $E_C - 0.51$ eV [5]. The change of the Fermi level towards the conduction band, from n- to n^+-type Si, may allow Mn to change its charge state from + to 0, reducing the number of conduction electrons of the silicon material. A consequence of this might hence be the increase of the ideal S fraction in n^+-Si to rebalance the electron-hole equilibrium. This phenomenon is similar to the so-called counter-doping, well known for Fe [21].

4.7.4.2 near-BC sites

Near-BC sites have been identified as one of the most frequently occupied lattice sites of other 3d TMs in Si [16, 19, 21]. Several origins have been proposed, however all involving the trapping of the TM into multivacancy defects. One suggested mechanism was the trapping of the TMs into the middle of double vacancies. The resulting lattice site of the TM would be, however, a perfect BC site. This has been suggested, e.g., for several TMs in Ge [23, 24]. Because this ideal configuration is not observed for 3d TMs in Si, it has been proposed that other multivacancy complexes could be involved. In particular, the TM may occupy displaced BC sites inside hexavacancy rings to satisfy the fourfold coordination of neighbor Si host atoms. From Fig. 4.20, one can observe that the displacement decreases from p^+ to n- and further to n^+-type Si. A possible explanation could be the more relaxed multivacancy-related structure in p^+ than in n^+-Si. One intriguing observation that can be made from Figs. 4.19 (a) to (b) is the increase of the near-BC fraction from the 30 keV to the 60 keV experiments. In that respect, it is tempting to relate this increase to the generation of more vacancies during implantation. In fact, SRIM calculations estimate that the number of produced vacancies per implanted Mn atom increases from $\sim$ 500 at 30 keV to $\sim$ 1000 at 60 keV. Nevertheless, the vacancy profile of the 60 keV experiment seems to be spread over twice the depth profile of vacancies of the 30 keV experiment. The aggregation of vacancies, which depends first on its concentration, may be the same in both experiments. What can also play a role is the fact that dechanneling becomes more prominent for deeper impurity profiles and hence higher implantation energies. Since dechanneling is only implemented by means of perturbation theory in the *manybeam* simulations, an unexpected and systematic change of the near-BC fraction, such as occurred during the fitting procedure for different implantation energies, can indicate problems in the implementation of dechanneling. Establishing the exact cause would hence require more systematic studies where implanted Mn fluence and depth profiles are systematically varied. Finally, one should discuss the dependence of the thermal

stability of near-BC sites with the doping. The trend is far less clear compared to previous works on Cu [17], Fe [9, 21] and Ni [16]. Nevertheless, an increase from n to n^+ for the 30 keV experiments seems plausible since in n-Si the near-BC fraction starts to decrease significantly already at $T_A = 300$°C, while in n^+-Si such decrease begins after annealing at 600°C.

4.7.4.3 near-AB sites

Before discussing the possible complexes involved in the observed near-AB sites one should first examine the similarities and differences of the mathematical position in the diamond lattice between the near-AB sites found in this work and the near-T sites found in the Fe, Ni and Co emission channeling experiments from Refs. [21], [16] and [22], respectively. The displacement from the ideal T site varied considerably across the annealing steps and for different doping types for the near-T sites of Fe, Ni and Co. For instance, Ni showed that the displacement was closer to the ideal AB site at low annealing temperatures, but also closer to the ideal T site at high annealing temperatures. In those studies, the presence of sites closer to the ideal T site was followed by an increase of the sum fraction. A plausible explanation was associated with the increase of intensity of channeling effects, suggesting that Mn on such near-T sites was present at midway from the peak of the depth profile to the surface (at $R_p/2$). On the other hand, the sites closer to the ideal AB site seemed to be immobile around the peak concentration of the implanted TMs (at R_p). In the present work, the large majority of Mn seems, therefore, to be located at R_p in n- and n^+-Si samples, since no increase of the sum was observed after the recrystallization at $T_A \sim 200$°C. Not much is known in the literature about possible complexes involving near-AB (or near-T) sites, except that Fe shows metastability on displaced T sites within single and double vacancies [25]. Because this explanation involves metastable complexes, we believe that more complicated structures, other than single or double vacancies, are involved. For the p^+-Si experiment, a different scenario has to be considered, since [Mn] $\sim$ [B]. In fact, as already seen, the pairing of the fast interstitial diffuser Mn_i with immobile B_s^- dopants is driven by Coulomb interactions [26]. If Mn_i is positive, the pairing will likely occur. Because p^+ doping shifts the Fermi level towards the valence band, the charge state of Mn will change from 0 to +, and perhaps further to ++ (see the three deep levels pointed out above). The large majority of Mn_i will have, therefore, a positive charge state, which satisfies an imperative condition for $Mn_i^+B_S^-$ pairing. It was suggested that Mn occupies T sites while boron keeps its substitutional position within the pair [26]. In fact, taking into account that such

pairing is driven by electrostatic attraction, one can estimate the distance d that would have to result between Mn and B: $d = q^2/(4\pi\epsilon\epsilon_0 E_b)$, in which q is the charge of the electron, ϵ the dielectric constant of Si, ϵ_0 the dielectric constant of vacuum and E_b the binding energy of the pair. Assuming $E_b = 0.5$ eV [27], one obtains $d \sim$ 2.4 Å, which corresponds to a displacement of 0.05 Å from T towards the ideal H site (almost ideal T site), if considering that B is on the ideal S site. The closest observed sites from T positions are near-AB sites. However, the large displacement from T positions seems to contradict such assignment. It is hence likely the involvement of several complexes in the observed near-AB sites in p^+-Si, in which MnB pairs are one of them. One argument in favor of this model is related to the higher displacements towards the ideal T site of near-AB sites from n- to p^+-Si, as shown in Fig. 4.20. One should finally remark that these pairs do not, however, take part in significant quantities when using higher fluences, since [Mn] becomes much larger than [B].

4.7.5 Conclusions

Although it is becoming increasingly accepted that the ferromagnetism observed in Mn-doped Si emerges from the formation of Mn-silicide precipitates, the presence and magnetic behavior of the remaining Mn in the substitutional or interstitial forms remain paradigmatic facts. Here, we investigated the lattice sites occupied by implanted Mn in Si, in the highly dilute regime. We found less than $\sim$ 30% of Mn on ideal S sites. More than $\sim$ 70% of Mn was found to form complex structures with implantation defects, such as with multivacancies. In particular, we found substantial fractions of Mn occupying sites near the bond-centered site and sites near the anti-bonding site. In p^+-type Si, the positively charged fast interstitial form of manganese Mn_i may also pair to B_S^- on sites very close to tetrahedral interstitial positions. We attribute the increase of the observed displaced anti-bonding sites to this pairing phenomenon. These findings illustrate the complex defect physics of transition-metal doped Si and related dilute magnetic semiconductors, which must be carefully taken into account when investigating their electric and magnetic properties.

Bibliography

[1] T. Dietl, H. Ohno, Dilute ferromagnetic semiconductors: Physics and spintronic structures, Rev. Mod. Phys. 86 (2014) 187.

[2] S. Zhou, H. Schmidt, Mn-doped Ge and Si: A review of the experimental status, Materials 3 (2010) 5054.

[3] V. Ko, K. L. Teo, T. Liew, T. C. Chong, M. MacKenzie, I. MacLaren, J. N. Chapman, Origins of ferromagnetism in transition-metal doped Si, J. Appl. Phys. 104 (2008) 033912.

[4] Z. Z. Zhang, B. Partoens, K. Chang, F. M. Peeters, First-principles study of transition metal impurities in Si, Phys. Rev. B 77 (2008) 155201.

[5] H. Nakashima, K. Hashimoto, Deep impurity levels and diffusion coefficient of manganese in silicon, J. Appl. Phys. 69 (1991) 1440.

[6] E. R. Weber, Transition metals in silicon, Appl. Phys. A 30 (1983) 1.

[7] S. Zhou, K. Potzger, G. Zhang, A. Mücklich, F. Eichhorn, N. Schell, R. Grötzschel, B. Schmidt, W. Skorupa, M. Helm, J. Fassbender, D. Geiger, Structural and magnetic properties of Mn-implanted Si, Phys. Rev. B 75 (2007) 085203.

[8] S. Zhou, A. Shalimov, K. Potzger, M. Helm, J. Fassbender, H. Schmidt, $MnSi_{1.7}$ nanoparticles embedded in Si: Superparamagnetism with collective behavior, Phys. Rev. B 80 (2009) 174423.

[9] U. Wahl, J. G. Correia, E. Rita, J. P. Araújo, J. C. Soares, Lattice sites of implanted Fe in Si, Phys. Rev. B 72 (2005) 014115.

[10] L. M. C. Pereira, U. Wahl, S. Decoster, J. G. Correia, L. M. Amorim, M. R. D. Silva, J. P. Araújo, A. Vantomme, Mixed Zn and O substitution of Co and Mn in ZnO, Phys. Rev. B 84 (2011) 125204.

[11] L. M. C. Pereira, U. Wahl, J. G. Correia, S. Decoster, L. M. Amorim, M. R. D. Silva, J. P. Araújo, A. Vantomme, Evidence of N substitution by Mn in GaN, Phys. Rev. B 86 (2012) 195202.

[12] L. M. C. Pereira, U. Wahl, S. Decoster, J. G. Correia, L. M. Amorim, M. R. D. Silva, J. P. Araújo, A. Vantomme, Stability and diffusion of interstitial and substitutional Mn in GaAs of different doping types, Phys. Rev. B 86 (2012) 125206.

[13] J. F. Ziegler, SRIM - 2003, Nucl. Instrum. Methods. Phys. Res. Sect. B 219 (2004) 1027.

[14] U. Wahl, J. G. Correia, S. Cardoso, J. G. Marques, A. Vantomme, G. Langouche, Electron emission channeling with position-sensitive detectors, Nucl. Instrum. Methods. Phys. Res. Sect. B 136 (1998) 744.

[15] S. Agostinelli, *et al.*, GEANT4 - a simulation toolkit, Nucl. Instrum. Methods Phys. Res. A 506 (2003) 250.

[16] *Article III.* D. J. Silva, U. Wahl, J. G. Correia, L. M. C. Pereira, L. M. Amorim, E. Bosne, M. R. da Silva, J. P. Araújo, Lattice location and thermal stability of implanted nickel in silicon studied by on-line emission channeling, J. Appl. Phys. 115 (2014) 023504.

[17] U. Wahl, J. G. Correia, A. Vantomme, G. Langouche, Lattice location of implanted Cu in Si, Physica B 273 (1999) 367.

[18] U. Wahl, A. Vantomme, G. Langouche, J. P. Araújo, L. Peralta, J. G. Correia, Lattice location of implanted Cu in highly doped Si, Appl. Phys. Lett. 77 (2000) 2142.

[19] U. Wahl, A. Vantomme, G. Langouche, J. G. Correia, Lattice location and stability of ion implanted Cu in Si, Phys. Rev. Lett. 84 (2000) 1495.

[20] U. Wahl, J. G. Correia, E. Rita, J. P. Araújo, J. C. Soares, Fe and Cu in Si: Lattice sites and trapping at implantation-related defects, Nucl. Instrum. Methods Phys. Res. B 253 (2006) 167.

[21] *Article I.* D. J. Silva, U. Wahl, J. G. Correia, J. P. Araújo, Influence of n^+ and p^+ doping on the lattice sites of implanted Fe in Si, J. Appl. Phys. 114 (2013) 103503.

[22] *Article IV.* D. J. Silva, U. Wahl, J. G. Correia, L. M. C. Pereira, L. M. Amorim, M. R. da Silva, J. P. Araújo, Origin of the lattice sites occupied by implanted Co in Si, Submitted to Semicond. Sci. Tech.

[23] S. Decoster, S. Cottenier, B. D. Vries, H. Emmerich, U. Wahl, J. G. Correia, A. Vantomme, Transition metal impurities on the bond-centered site in germanium, Phys. Rev. Lett. 102 (2009) 065502.

[24] S. Decoster, S. Cottenier, U. Wahl, J. G. Correia, L. M. C. Pereira, C. Lacasta, M. R. D. Silva, A. Vantomme, Diluted manganese on the bond-centered site in germanium, Appl. Phys. Lett. 97 (2010) 151914.

[25] S. K. Estreicher, M. Sanati, N. G. Szwacki, Iron in silicon: Interactions with radiation defects, carbon, and oxygen, Phys. Rev. B 77 (2008) 125214.

[26] D. Gilles, W. Schroter, W. Bergholz, Impact of the electronic structure on the solubility and diffusion of 3d transition elements in silicon, Phys. Rev. B 41 (1990) 5770.

[27] H. Lemke, Energy levels and binding energies of ion pairs in silicon. [energieniveaus und bindungsenergien von ionenpaaren in silizium.], Phys. Status Solidi A 76 (1983) 223.

Chapter 5

Conclusions

This thesis explored some structural properties of 3d transition metal impurities in Si by investigating the lattice location of the probes ^{56}Mn, ^{59}Fe, ^{61}Co and ^{65}Ni by means of electron emission channeling experiments. We identified three different lattice sites in all probes: ideal substitutional (S) sites, displaced bond-centered (near-BC) sites and displaced tetrahedral interstitial (near-T) sites. The existence of each lattice site and related thermal stability allowed one to include more information to the understanding of some microscopic mechanisms, which is described in the following.

Vacancy-related defects induced locally by ion implantation, e.g. of H or He, or by electron irradiation play an important role in gettering transition metals during the silicon processing. This work concluded that, when forming complexes with vacancy-related defects, 3d transition metals prefer to occupy ideal substitutional sites, most likely resulting from the trapping into single vacancies, and near-BC sites and near-T sites, most likely resulting from the trapping into multivacancies. By comparing to theoretical investigations from literature one was able to conclude that most of the observed near-BC sites may result from the trapping of the 3d transition metals into divacancies and fourfold coordinated vacancy clusters. The structure involving 3d transition metals on near-T sites is more difficult to predict. One has, however, observed that the most stable positions of 3d transition metals within complexes resulting from their trapping at $R_p/2$ correspond to near-T sites. During the relocation of the transition metals from R_p to $R_p/2$, the displacement of the near-T sites changes significantly. Such change might be the result of either a different channeling effect of the relocated transition metal profile that is not considered in the simulated patterns, or of the presence of a different trap structure at $R_p/2$ compared to those at the R_p region.

Although gettering through P-diffusion has been currently employed to mitigate the unwanted electrical effects of transition metals, it is still unknown which microscopic mechanisms are involved. In that respect it was suggested that other defects in addition to phosphorus and transition metal impurities, perhaps vacancy-related, might play a role. This work showed that 3d transition metals prefer near-BC sites, irrespective of the TM species, in environments rich in vacancy-related defects, and that the thermal stability of the related complexes increases from p^+- to n- and further to n^+-type silicon. This complex is hence more stable when the Fermi level approaches the conduction band, as occurring in the n^+ regions during P-diffusion. Why only phosphorus can getter transition metals with such a mechanism is, however, still unknown.

Another important gettering technique consists of using a p-type layer to trap some transition metals which are mostly positively charged in p-type silicon when diffusing interstitially, such as Mn, Fe and Co. Their capture into the p-type layer is most likely driven by the Coulomb attraction between the positively charged interstitial transition metals and the electric acceptors, such as B^-. The structure of such pairs has been investigated theoretically. Their most stable geometry places the 3d transition metal on one of the nearest T sites of the substitutional acceptor atom, but with a breathing mode relaxation, i.e. with a displacement with respect to the mathematical tetrahedral interstitial position. Here, we confirmed such configuration and determined a range of displacement, for Mn, Fe and Co. Ni did not prevail on near-T sites for all annealing temperatures, in agreement with its most likely neutral charge state when isolated on tetrahedral interstitial sites in p-type silicon, which might have prevented its pairing with boron.

One important microscopic phenomenon, which has been difficult to investigate, is clustering. Investigations based on Mössbauer spectroscopy have claimed to observe a particular Mössbauer quadrupole doublet with some characteristics of Co-dimers. Following similar experimental conditions it was investigated in this work the lattice location of Co. It was found that, in n-type Si, the near-T fraction increases in the annealing temperature range where this doublet component appears. A comparison to other emission channeling investigations on iron in silicon is, however, at variance with such a conclusion. This particular doublet component, and hence near-T sites, is most likely not due to clustering.

Finally, the two most likely magnetic dopant candidates in silicon are Mn and Co, if immobilized on substitutional sites. The substitutional fraction of Mn and Co in implanted samples has been, however, difficult to determine. The lattice location

of Co and Mn by means of emission channeling experiments allowed to obtain this relevant quantity. This work found that while $\sim$ 60% of Co can occupy S sites, less than $\sim$ 30% of Mn sits on S sites. Hence, although the magnetic moment of Co is smaller than that of Mn, Co is easier incorporated on S sites. The question that this work raises is whether the S sites actually originate from the substitutional form of Co. Anyhow, the remaining Co and Mn is found on near-BC and near-T sites for fluences of $\sim$ 10^{12}-10^{13} cm^{-2}, in which the related complexes may probably destroy the possible dilute ferromagnetism.

Appendix A

Table of complexes

The following tables list some physical properties of relevant complexes that either might be involved on the lattice sites observed in this work or are mentioned in the introduction, namely their geometrical structures, some of their kinetics and some energy levels that they introduce in the Si bandgap. The description of the several geometrical structures makes use of the mathematical lattice sites from Fig. 2.2. Each formula of the diffusion coefficient D is given in cm^2/s. The activation energies for migration and dissociation are represented by E_m and E_d, respectively, while E_b represents binding energies. The energy levels are given with respect to the conduction and valence band edges E_C and E_V, respectively, in eVs. Finally, one should note that some complexes are referred after the related centers measured by electron paramagnetic resonance (referred by the so-called NL resonances), by photoluminescence (referred by PL) or by Mössbauer spectroscopy (referred by "M"). The quotation marks of "M" means that the M nomenclature has not been used in the literature.

defect	**structure**	**kinetics**	**energy levels**	**bibliography**
I (self-interstitial)	Si most likely on SP sites	$D = 5 \times 10^{-3} exp(-2.45/k_B T)$		[1]
V (vacancy)		$E_m = 0.3$ eV	present in 5 charge states (from 2- to 2+)	[2, 3]
V-V (divacancy)		$E_m = 0.3$ eV $E_d = 2.05$ eV	E_c−0.23; E_c−0.41; E_v+0.20;	[4, 5]
V_6 (hexavacancy)	hexagonal ring of vacancies	$E_b \sim 2.5$ eV ($V_6 \rightarrow V_5 + V$)		[6–8]
V_5 (pentavacancy)	fourfold coordination of 1 extra Si atoms in V_6	$E_b \sim 2.5$ eV ($V_5 \rightarrow V_4 + V$)		[9]
V_4 (tetravacancy)	fourfold coordination of 2 extra Si atoms in V_6	$E_b \sim 2.5$ eV ($V_4 \rightarrow V_3 + V$)		[9]
V_3 (trivacancy)	fourfold coordination of 3 extra Si atoms in V_6	$E_b \sim 2.5$ eV ($V_3 \rightarrow V_2 + V$)		[9]
O_i	slightly puckered BC sites	$D = 0.13 exp(-2.56/k_B T)$		[10]
OV (A-center)	O displaced from S sites along <001>	$E_d = 2.13$ eV	E_c−0.17;	[11–14]
H_i	on BC sites when + on T sites when - on BC or T sites when neutral	$E_m \sim 0.3$ eV	$E_c - 0.21$; $E_v + 0.30$;	[11, 15]

Implantation-induced and light impurity-related defects

defect	**structure**	**kinetics**	**energy levels**	**bibliography**
VH	H near BC sites	$E_b \sim 3.6$ eV ($VH \rightarrow V + H$)		[16–19]
VH_2	H on both BC and AB sites	$E_b \sim 3.3$ eV ($VH_2 \rightarrow VH + H$)		[11, 16]
VH_3	H near BC sites	$E_b \sim 3.2$ eV ($VH_3 \rightarrow VH_2 + H$)		[16]
VH_4	H near BC sites	$E_b \sim 3.0$ eV ($VH_4 \rightarrow VH_3 + H$)		[16]
C_S	on ideal S sites	$D = 1.9exp(-3.04/k_BT)$	none	[11, 20]
C_i	on C sites	$D = 0.44exp(-0.87/k_BT)$	$E_c - 0.1$; $E_v + 0.28$;	[11, 21, 22]
C_iC_S	under debate			[22, 23]
P_S	on S sites		$E_c - 0.045$;	[24]
As_S	on S sites		$E_c - 0.049$;	[24]
B_S	on S sites		$E_v + 0.045$;	[24]
C_iO_i (C3-center)	both on C sites with no bonds between them	$E_b = 1.64$ eV	E_v+0.38;	[22, 23, 25]
$Si_iC_iO_i$ (C4-center)	under debate	$E_b \sim 1.50$ eV		[22]

Implantation-induced and light impurity-related defects

defect	**structure**	**kinetics**	**energy levels**	**bibliography**
H_iO_i	both H and O on puckered BC sites of			[26]
$O(R_p)$	complexes with vacancies and/or self-interstitials	stable up to 1000°C		[27]
$O(R_p/2)$	complexes with vacancies	stable up to 1000°C		[27]
As_SH_i	As on S sites H near BC sites			[26]
B_SH_i	B on S sites H near BC sites			[26]

Complexes formed by Fe

defect	**structure**	**kinetics**	**energy levels**	**bibliography**
Fe_i	on ideal T sites	$D = 1.0 \times 10^{-3} exp(-0.67\text{eV}/k_BT)$	E_v+0.4;	[12, 28, 29]
Fe_S	ideal S sites	$E_d \sim 2.93 - 3.20$ eV	E_c−0.38;	[12, 28, 30–36]
V-Fe	Fe on T sites displaced along <111>	$E_b \sim 1.50 - 1.62$ eV	E_c−0.38; E_v−0.35;	[12, 28, 31] [32, 35–38]
V-V-Fe	Fe on T sites displaced along <111>	$E_b \sim 1.57 - 1.69$ eV	E_c−0.75; E_v+0.25;	[29, 35, 36, 38]
V-Fe-V	Fe on ideal BC sites	$E_b \sim 2.5$ eV	E_c−0.55; E_c−0.73;	[39, 40]
Fe_iI	Fe near the T site	$E_b \sim 1.07$ eV	E_v+0.42;	[39]
Fe_iFe_i	both Fe on T sites	$E_b \sim 0.34$ eV	E_v+0.44;	[41]
Fe_SFe_i	one Fe on T sites and one on S sites	$E_b \sim 0.85$ eV	E_v+0.40; E_c−0.19;	[28, 41]
Fe_iB_S (a)	Fe on 1st T sites and B on S sites (trigonal <111>)	$E_b = 0.58 - 0.65$ eV	E_c−0.29;	[29, 42–49]
Fe_iB_S (b)	Fe on 2nd T sites and B on S sites (orthorhombic <100>)		E_c−0.43;	[29]
Fe_SP_S	Fe and P on S sites			[42]
Fe_SO_i	Fe on S sites, O on puckered BC sites	$E_b \sim 1.19$ eV	$E_c - 0.38$;	[12, 29]

Complexes formed by Fe

defect	**structure**	**kinetics**	**energy levels**	**bibliography**
Fe_iH_i	Fe on H sites, H on T sites	$E_b \sim 0.4 - 0.82$ eV	E_v+0.31; E_c−0.26;	[48, 50, 51]
Fe_iC_i	Fe on T sites and C on C sites	$E_b \sim 0.52 - 0.73$ eV	E_c−0.44; E_v+0.67;	[39]
$Fe(R_p)$	complexes with vacancies and/or self-interstitials			[27]
$Fe(R_p/2)$	complexes with vacancies			[27]
N19	Fe_iV (trigonal)			[52]
NL20	Fe_iFe_iV (orthorhombic)			[29, 52]
NL21	$Fe_iFe_iV_2$ (monoclinic)			[29, 52]
NL25	Fe_iFe_i(a) (orthorhombic)			[29, 52]
NL24	Fe_iFe_i(b) (monoclinic)			[29, 52]
NL22	Fe_{i4} (trigonal)			[29, 52]
NL23	Fe_iFe_iB (triclinic)			[53, 54]

Complexes formed by Fe

defect	**structure**	**kinetics**	**energy levels**	**bibliography**
"M1"	singlet (interstitial Fe)	Stable up to 400°C		[32, 33, 38, 47]
"M2"	singlet (substitutional Fe)	Stable up to 600°C		[32, 33, 38, 47]
"M3"	doublet (FeV pair)	Stable up to 550°C		[32, 33, 47]
"M4"	doublet (FeB)	Stable up to 750°C		[32, 47]

Table A.3: Complexes formed by Mn

defect	**structure**	**kinetics**	**energy levels**	**bibliography**
Mn_i	on T sites	$D = 2.4 \times 10^{-3} exp(-0.72\text{eV}/k_B T)$	$E_c - 0.12$; $E_c - 0.41$; $E_v + 0.32$;	[28, 42, 55–57]
Mn_S	on S sites		$E_c - 0.51$;	[28, 42, 57–60]
$Mn_S I$	Mn on S sites, I on T site (kick-out mechanism)		$E_v + 0.23$; $E_c - 0.85$; $E_c - 0.35$;	[61]
$Mn_i Mn_i$	both Mn on T sites		$E_v + 0.1$; $E_c - 0.9$; $E_c - 0.55$;	[28, 61]
$Mn_S Mn_S$	both Mn on S sites		$Ec - 1.0$; $E_c - 0.39$; $E_c - 0.36$;	[28, 61]
$Mn_S Mn_i$	one Mn on T and one Mn on S sites		$E_c - 0.4$; $E_c - 0.3$;	[28, 61]
$Mn_S P_S$	Mn and P on S sites		$E_c - 0.55$;	[42, 62]
$Mn_i B_S$	Mn on T and B on S sites		$E_c - 50$;	[42, 57, 63, 64]

Table A.4: Complexes formed by Ni

defect	**structure**	**kinetics**	**energy levels**	**bibliography**
Ni_i	on T sites	$D = 1.69 \times 10^{-4} exp(-0.15\text{eV}/k_B T)$	none	[12, 28, 55] [65–67]
Ni_S	on S sites	$E_d = 2.7$ eV	$E_c - 0.09$; $E_v + 0.17$; $E_c - 0.43$;	[12, 25, 28, 68]
Ni_iNi_i	both Ni on T sites			[28]
Ni_SO_i	Ni on S sites, O on puckered BC sites	$E_b \sim 1.21$ eV	$E_c - 0.19$; $E_v + 0.04$;	[12, 25]
Ni_SH_i	Ni on S sites, H ~ 1.66Å from Ni	$E_d = 1.44$ eV	$E_c - 0.22$; $E_c - 0.34$; $E_v + 0.06$; $E_v + 0.20$;	[68]
Ni_SH_2		$E_d = 1.39$ eV	$E_c - 0.24$;	[68]
Ni(R_p)	complexes with vacancies and/or self-interstitials	$E_b \sim 0.65$ eV		[27, 69]
Ni($R_p/2$)	complexes with vacancies	$E_b \sim 1.35$ eV		[27, 69]

Complexes formed by Co

defect	structure	kinetics	energy levels	bibliography
Co_i	ideal T sites	$D = 1.0 \times 10^{-5} exp(-0.4\text{eV}/k_B T)$	E_c−0.19; E_v+0.53;	[28, 42, 55] [56, 70–72]
Co_S	on S sites		E_c−0.39;	[28, 73–75]
$Co_S Co_i$	one Co on S sites and one on T sites			[28]
$Co - I - Co$	both Co on S sites, with I on a puckered BC site			[76]
$Co_i B_S$	Co on T and B on S sites		E_c−0.08;	[42, 71, 72, 77]
$Co_S P_S$	both Co and P on S sites			[42]
"M1"	singlet (Co_S)			[42, 73, 74] [78, 79]
"M2i"	doublet attributed to Co on amorphous sites			[74, 78]
"M3i"	doublet tentatively assigned to Co-dimers	appears in the annealing temperature range $475 - 650°C$		[73, 74, 80]
"M4"	doublet tentatively assigned to adsorption of Co inside voids			[78]
"M5"	doublet tentatively assigned to adsorption of Co inside voids			[78]
"M6"	doublet (CoB)			[42, 72, 77, 81]

Complexes formed by Co

defect	**structure**	**kinetics**	**energy levels**	**bibliography**
"M7"	doublet (CoB)			[72, 77, 81]
"M8"	doublet (CoB)			[77, 81]
"M9"	doublet (CoP)			[42]

Complexes formed by Cu

defect	**structure**	**kinetics**	**energy levels**	**bibliography**
Cu_i	on T sites	$D = 4.5 \times 10^{-3} exp(-0.18\text{eV}/k_B T)$	none	[82]
Cu_S	on S sites	$E_b \sim 2.7$ eV	$E_c - 0.17$; E_v+0.41; E_v+0.20;	[25, 83–86]
Cu_iCu_S	one Cu on T sites and one Cu on S sites			[86]
V-Cu_i-V	Cu on BC sites	$E_b \sim 2.5$ eV		[86]
Cu_iV_6	Cu near BC sites within the hexavacancy	$E_b \sim 3.36$ eV		[87]
Cu_SO_i	Cu on S sites O on puckered BC sites	$E_b \sim 1.7$ eV		[25]
Cu_SH_i	Cu on S sites, H on AB sites	$E_b \sim 2.3$ eV		[88]
Cu_iB_S	Cu on T sites and B on S sites	$E_d \sim 0.69$ eV		[87]
Cu(R_p)	complexes with vacancies and/or self-interstitials			[27, 69]
Cu($R_p/2$)	complexes with vacancies			[27, 69]
PL1014	photoluminescence line attributed to Cu_iCu_S			[86]

Complexes formed by Cu

defect	**structure**	**kinetics**	**energy levels**	**bibliography**
EX1	assigned to Cu-Si at the surface of voids			[89]
EX2	assigned to Cu-Cu at the surface of voids			[89]

Bibliography

[1] B. Sahli, W. Fichtner, *Ab initio* molecular dynamics simulation of self-interstitial diffusion in silicon, Phys. Rev. B 72 (2005) 245210.

[2] G. D. Watkins, J. Phys. Soc. Jpn. 18 (1963) 22.

[3] S. K. Estreicher, Structure and dynamics of point defects in crystalline silicon, Phys. Status Solidi B Basic Res. 217 (2000) 513.

[4] G. D. Watkins, J. W. Corbett, Defects in irradiated silicon: Electron paramagnetic resonance of the divacancy, Phys. Rev. 138 (1965) 543.

[5] G. S. Hwang, W. A. Goddard, Diffusion and dissociation of neutral divacancies in crystalline silicon, Phys. Rev. B 65 (2002) 2332051.

[6] S. K. Estreicher, J. L. Hastings, P. A. Fedders, The ring-hexavacany in silicon: A stable and inactive defect, Appl. Phys. Lett. 70 (1997) 432.

[7] J. L. Hastings, S. K. Estreicher, P. A. Fedders, Vacancy aggregates in silicon, Phys. Rev. B 56 (1997) 10215.

[8] T. M. E. Staab, A. Sieck, M. Haugk, M. J. Puska, T. Frauenheim, H. S. Leipner, Stability of large vacancy clusters in silicon, Phys. Rev. B 65 (2002) 1152101.

[9] D. V. Makhov, L. J. Lewis, Stable fourfold configurations for small vacancy clusters in silicon from *ab initio* calculations, Phys. Rev. Lett. 92 (2004) 255504.

[10] J. W. Corbett, R. S. McDonald, G. D. Watkins, The configuration and diffusion of isolated oxygen in silicon and germanium, J. Phys. Chem. Solids 25 (1964) 873.

[11] R. C. Newman, Light impurities and their interactions in silicon, Mater. Sci. Eng. B 36 (1996) 1.

[12] D. J. Backlund, S. K. Estreicher, Ti, Fe, and Ni in Si and their interactions with the vacancy andvthe A center: A theoretical study, Phys. Rev. B 81 (2010) 235213.

[13] G. D. Watkins, J. W. Corbett, Defects in irradiated silicon. i. electron spin resonance of the $Si-A$ center, Phys. Rev. 121 (1961) 1001.

[14] J. W. Corbett, G. D. Watkins, R. M. Chrenko, R. S. McDonald, Defects in irradiated silicon. ii. infrared absorption of the $Si-A$ center, Phys. Rev. 121 (1961) 1015.

[15] J. W. Corbett, S. N. Sahu, T. S. Shi, L. C. Snyder, Atomic and molecular hydrogen in the Si lattice, Phys. Lett. A 93 (1983) 303.

[16] M. A. Roberson, S. K. Estreicher, Vacancy and vacancy-hydrogen complexes in silicon, Phys. Rev. B 49 (1994) 17040.

[17] S. J. Pearton, J. W. Corbett, T. S. Shi, Hydrogen in crystalline semiconductors, Appl. Phys. A 43 (1987) 153.

[18] S. K. Estreicher, J. L. Hastings, P. A. Feeders, Hydrogen-defect interactions in Si, Mater. Sci. Eng. B 58 (1999) 31.

[19] S. K. Estreicher, A. Docaj, M. B. Bebek, D. J. Backlund, M. Stavola, Hydrogen in C-rich Si and the diffusion of vacancy-H complexes, Phys. Status Solidi A 209 (2012) 1872.

[20] G. D. Watkins, K. L. Brower, EPR observation of the isolated interstitial carbon atom in silicon, Phys. Rev. Lett. 36 (1976) 1329.

[21] L. W. Song, X. D. Zhan, B. W. Benson, G. D. Watkins, Bistable interstitial-carbon substitutional-carbon pair in silicon, Phys. Rev. B 42 (1990) 5765.

[22] D. J. Backlund, S. K. Estreicher, C4 defect and its precursors in Si: First-principles theory, Phys. Rev. B 77 (2008) 205205.

[23] A. Docaj, S. K. Estreicher, Three carbon pairs in Si, Physica B 407 (2012) 2981.

[24] M. Grundmann, The Physics of Semiconductors, Springer, 2006.

[25] V. P. Markevich, A. R. Peaker, S. B. Lastovskii, L. I. Murin, J. Coutinho, V. J. B. Torres, P. R. Briddon, L. Dobaczewski, E. V. Monakhov, B. G. Svensson, Trivacancy and trivacancy-oxygen complexes in silicon: Experiments and *ab initio* modeling, Phys. Rev. B 80 (2009) 235207.

[26] S. K. Estreicher, L. Throckmorton, D. S. Marynick, Hydrogen passivation of shallow acceptors and donors in C-Si: Comparisons and trends, Phys. Rev. B 39 (1989) 13241.

[27] R. A. Brown, O. Kononchuk, G. A. Rozgonyi, S. Koveshnikov, A. P. Knights, P. Simpson, F. Gonzlez, Impurity gettering to secondary defects created by MeV ion implantation in silicon, J. Appl. Phys. 84 (1998) 2459.

[28] Z. Z. Zhang, B. Partoens, K. Chang, F. M. Peeters, First-principles study of transition metal impurities in Si, Phys. Rev. B 77 (2008) 155201.

[29] A. A. Istratov, H. Hieslmair, E. R. Weber, Iron and its complexes in silicon, Appl. Phys. A 69 (1999) 13.

[30] G. Weyer, A. Burchard, M. Fanciulli, V. N. Fedoseyev, H. P. Gunnlaugsson, V. I. Mishin, R. Sielemann, The electronic configuration of substitutional Fe in silicon, Physica B 273 (1999) 363.

[31] G. Weyer, H. P. Gunnlaugsson, M. Dietrich, M. Fanciulli, K. Bharuth-Ram, R. Sielemann, Creation and annealing of defect structures in silicon-based semiconductors during and after implantations at 77-500 K, Nucl. Instrum. Methods Phys. Res. B 206 (2003) 90.

[32] G. Weyer, Defects in semiconductors - results from Mössbauer spectroscopy, Hyperfine Interact. 177 (2007) 1.

[33] H. P. Gunnlaugsson, M. Dietrich, M. Fanciulli, K. Bharuth-Ram, R. Sielemann, G. Weyer, Detection of substitutional and interstitial Fe in silicon by Mössbauer spectrocopy, Phys. Scr. 101 (2002) 82.

[34] H. P. Gunnlaugsson, M. Fanciulli, M. Dietrich, K. Bharuth-Ram, R. Sielemann, G. Weyer, I. Collaboration, ^{57}Fe Mössbauer study of radiation damage in ion-implanted Si, SiGe and SiSn, Nucl. Instrum. Methods Phys. Res. B 186 (2002) 55.

[35] U. Wahl, J. G. Correia, E. Rita, J. P. Araújo, J. C. Soares, Lattice sites of implanted Fe in Si, Phys. Rev. B 72 (2005) 1.

[36] U. Wahl, J. G. Correia, E. Rita, J. P. Araújo, J. C. Soares, Fe and Cu in Si: Lattice sites and trapping at implantation-related defects, Nucl. Instrum. Methods Phys. Res. B 253 (2006) 167.

[37] H. P. Gunnlaugsson, M. Dietrich, M. Fanciulli, K. Bharuth-Ram, R. Sielemann, G. Weyer, Detection of diffusional jumps of interstitial Fe in silicon by Mössbauer spectroscopy, Physica B 308 (2001) 418.

[38] H. P. Gunnlaugsson, G. Weyer, N. E. Christensen, M. Dietrich, M. Fanciulli, K. Bharuth-Ram, R. Sielemann, A. Svane, On the kinetics of the formation of interstitial Fe-vacancy pairs in silicon at high temperatures, Physica B 340 (2003) 532.

[39] S. K. Estreicher, M. Sanati, N. G. Szwacki, Iron in silicon: Interactions with radiation defects, carbon, and oxygen, Phys. Rev. B 77 (2008) 125214.

[40] C. K. Tang, L. Vines, V. P. Markevich, B. G. Svensson, E. V. Monakhov, Divacancy-iron complexes in silicon, J. Appl. Phys. 113 (2013) 044503.

[41] M. Sanati, S. K. Estreicher, First-principles study of iron and iron pairs in Si, Physica B 401 (2007) 105.

[42] D. Gilles, W. Schröter, W. Bergholz, Impact of the electronic structure on the solubility and diffusion of 3d transition elements in silicon, Phys. Rev. B 41 (1990) 5770.

[43] K. Matsukawa, N. Hattori, S. Maegawa, K. Shirai, H. Katayama-Yoshida, Gettering mechanism of transition metals in silicon calculated from first principles, Physica B 376 (2006) 224.

[44] L. J. Geerligs, D. Macdonald, Dynamics of light-induced FeB pair dissociation in crystalline silicon, Appl. Phys. Lett. 85 (2004) 5227.

[45] A. A. Istratov, H. Hieslmair, E. R. Weber, What do we know about iron in silicon after 45 yr of research, Physica B 273 (1999) 412.

[46] G. Zoth, W. Bergholz, A fast, preparation-free method to detect iron in silicon, J. Appl. Phys. 67 (1990) 6764.

[47] H. P. Gunnlaugsson, K. Bharuth-Ram, M. Dietrich, M. Fanciulli, H. O. U. Fynbo, G. Weyer, Formation of $Fe_i - B$ pairs in silicon at high temperatures, Hyperfine Interact. 169 (2006) 1315.

[48] M. Sanati, N. G. Szwacki, S. K. Estreicher, Interstitial Fe in Si and its interactions with hydrogen and shallow dopants, Phys. Rev. B 76 (2007) 125204.

[49] C. B. Collins, R. O. Carlson, Properties of silicon doped with iron or copper, Phys. Rev. 108 (1957) 1409.

[50] N. G. Szwacki, S. K. Estreicher, First-principles investigations of $Fe - H$ interactions in silicon, Physica B 401 (2007) 171.

[51] N. G. Szwacki, M. Sanati, S. K. Estreicher, Two FeH pairs in n-type Si and their implications: A theoretical study, Phys. Rev. B 78 (2008) 113202.

[52] S. H. Muller, G. M. Tuynman, E. G. Sieverts, C. A. J. Ammerlaan, Electron paramagnetic resonance on iron-related centers in silicon, Phys. Rev. B 25 (1982) 25.

[53] W. Gehlhoff, K. Irmscher, U. Rehse, Electronic characterization of defects in iron-doped p-type silicon, Mater. Sci. Forum 38 (1989) 373.

[54] W. Gehlhoff, U. Rehse, Formation and defect structure of fe-b-fe complexes in silicon, Solid state phenom. 6 (1989) 257.

[55] E. R. Weber, Transition metals in silicon, Appl. Phys. A 30 (1983) 1.

[56] K. Matsukawa, K. Shirai, H. Yamaguchi, H. Katayama-Yoshida, Diffusion of transition-metal impurities in silicon, Physica B 401 (2007) 151.

[57] H. Nakashima, K. Hashimoto, Deep impurity levels and diffusion coefficient of manganese in silicon, J. Appl. Phys. 69 (1991) 1440.

[58] K. P. Abdurakhmanov, S. B. Utamuradova, K. S. Daliev, S. G. Tadjy-Aglaeva, R. M. Érgashev, Defect-formation processes in silicon doped with manganese and germanium, Semiconductors 32 (1998) 606.

[59] M. Haider, H. Sitter, R. Czaputa, H. Feichtinger, J. Oswald, Experimental identification of the energy level of substitutional manganese in silicon, J. Appl. Phys. 62 (1987) 3785.

[60] H. H. Woodbury, G. W. Ludwig, Spin resonance of transition metals in silicon, Phys. Rev. 117 (1960) 102.

[61] F. Bernardini, S. Picozzi, A. Continenza, Energetic stability and magnetic properties of Mn dimers in silicon, Appl. Phys. Lett. 84 (2004) 2289.

[62] G. A. Adegboyega, O. Osasona, E. Susi, Intrinsic gettering of manganese impurity in silicon substrate, Physica Status Solidi (A) Applied Research 161 (1997) 231–235.

[63] H. Lemke, Energy levels and binding energies of ion pairs in silicon. [energieniveaus und bindungsenergien von ionenpaaren in silizium.], Phys. Status Solidi A 76 (1983) 223.

[64] T. Roth, P. Rosenits, S. Diez, S. W. Glunz, D. MacDonald, S. Beljakowa, G. Pensl, Electronic properties and dopant pairing behavior of manganese in boron-doped silicon, J. Appl. Phys. 102 (2007) 103716.

[65] A. A. Istratov, P. Zhang, R. J. McDonald, A. R. Smith, M. S. J. Moreland, J. Shen, R. Wahlich, E. R. Weber, Nickel solubility in intrinsic and doped silicon, J. Appl. Phys. 97 (2005) 023505.

[66] F. H. M. Spit, D. Gupta, K. N. Tu, Diffusivity and solubility of Ni (^{63}Ni) in monocrystalline Si, Phys. Rev. B 39 (1989) 1255.

[67] J. Lindroos, D. P. Fenning, D. J. Backlund, E. Verlage, A. Gorgulla, S. K. Estreicher, H. Savin, T. Buonassisi, Nickel: A very fast diffuser in silicon, J. Appl. Phys. 113 (2013) 204906.

[68] D. J. Backlund, S. K. Estreicher, Structural, electrical, and vibrational properties of Ti − H and Ni − H complexes in Si, Phys. Rev. B 82 (2010) 155208.

[69] S. V. Koveshnikov, G. A. Rozgonyi, Mechanism of iron gettering in MeV Si ion implanted epitaxial silicon, J. Appl. Phys. 84 (1998) 3078.

[70] F. Beeler, O. K. Andersen, M. Scheffler, Electronic and magnetic structure of 3d transition-metal point defects in silicon calculated from first principles, Phys. Rev. B 41 (1990) 1603.

[71] H. Lemke, K. Irmscher, Proof of interstitial cobalt defects in silicon float zone crystals doped during crystal growth, ECS Trans. 3 (2006) 299.

[72] A.-M. V. Bavel, M. Bennebroek, D. Neerinck, G. Langouche, Mössbauer search for Co-acceptor pairs in Si, Nucl. Instrum. Methods Phys. Res. B 76 (1993) 434.

[73] G. Langouche, M. D. Potter, Identification of substitutional and interstitial Co implanted in Si, Nucl. Instrum. Methods Phys. Res. B 19 (1987) 322.

[74] G. Langouche, M. D. Potter, I. Dézsi, M. F. Wu, A. Vantomme, Mössbauer spectroscopy study of the thermal annealing behavior of very low and very high dose Co-implanted Si, Nucl. Instrum. Methods Phys. Res. B 37 (1989) 438.

[75] L. Scheffler, V. Kolkovsky, J. Weber, Isolated substitutional cobalt and Co-related complexes in silicon, J. Appl. Phys. 113 (2013) 183714.

[76] A.-M. V. Bavel, G. Langouche, H. Overhof, The atomic structure of Co dimers in silicon, Semicond. Sci. Technol. 13 (1998) 108.

[77] W. Bergholz, Pairing reactions of interstitial cobalt and shallow acceptors in silicon observed in Mössbauer spectroscopy, Physica B+C 116 (1983) 312.

[78] W. Deweerd, T. Barancira, S. Bukshpan, S. Demuynck, G. Langouche, K. Milants, R. Moons, J. Verheyden, H. Pattyn, Mössbauer study of the proximity gettering of cobalt atoms to He-induced nanosized voids in C-si, Phys. Rev. B 53 (1996) 16637.

[79] W. Bergholz, On the diffusion of co in si and its applicability to the si intrinsic defect problem, J. Phys. D : Appl. Phys. 14 (1981) 1099.

[80] G. Langouche, M. D. Potter, D. Schroyen, Observation of Co-dimer formation during thermal annealing of Co-implanted Si, Phys. Rev. Lett. 53 (1984) 1364.

[81] J. Utzig, Properties of cobalt in FZ and CZ silicon studied by Mössbauer spectroscopy, J. Appl. Phys. 64 (1988) 3629.

[82] A. A. Istratov, C. Flink, H. Hieslmair, E. R. Weber, T. Heiser, Intrinsic diffusion coefficient of interstitial copper in silicon, Phys. Rev. Lett. 81 (1998) 1243.

[83] U. Wahl, J. G. Correia, A. Vantomme, G. Langouche, Lattice location of implanted Cu in Si, Physica B 273 (1999) 367.

[84] U. Wahl, A. Vantomme, G. Langouche, J. P. Araújo, L. Peralta, J. G. Correia, Lattice location of implanted Cu in highly doped Si, Appl. Phys. Lett. 77 (2000) 2142.

[85] U. Wahl, A. Vantomme, G. Langouche, J. G. Correia, Lattice location and stability of ion implanted Cu in Si, Phys. Rev. Lett. 84 (2000) 1495.

[86] S. K. Estreicher, First-principles theory of copper in silicon, Mater. Sci. Semicond. Process 7 (2004) 101.

[87] S. K. Estreicher, Rich chemistry of copper in crystalline silicon, Phys. Rev. B 60 (1999) 5375.

[88] D. West, S. K. Estreicher, S. Knack, J. Weber, Copper interactions with H, O, and the self-interstitial in silicon, Phys. Rev. B 68 (2003) 352101.

[89] G. D. M. Azevedo, M. C. Ridgway, J. Betlehem, K. M. Yu, C. J. Glover, G. J. Foran, EXAFS measurements of metal-decorated nanocavities in Si, Nucl. Instrum. Methods Phys. Res. B 199 (2003) 179.

List of publications, communications and awards

The investigation carried out during this PhD program included the publications, oral and poster communications, and award listed below.

Publications

- **Influence of n^+- and p^+ doping on the lattice sites of implanted Fe in silicon**

  D. J. Silva, U. Wahl, J. G. Correia and J. P. Araújo.

  Journal of Applied Physics **114**, 103503 (2013)

- **Influence of the doping on the lattice sites of Fe in Si**

  D. J. Silva, U. Wahl, J. G. Correia and J. P. Araújo.

  AIP Conference Proceedings **1583**, 24 (2014)

- **Lattice location and thermal stability of implanted nickel in silicon studied by on-line Emission Channeling**

  D. J. Silva, U. Wahl, J. G. Correia, L. M. C. Pereira, L. M. Amorim, E. Bosne, M. R. da Silva and J. P. Araújo.

  Journal of Applied Physics **115**, 023504 (2014)

- **Origin of the lattice sites occupied by implanted Co in Si**

  D. J. Silva, U. Wahl, J. G. Correia, L. M. C. Pereira, L. M. Amorim, M. R. da Silva and J. P. Araújo.

  Semiconductor Science and Technology **29**, 125006 (2014)

Oral presentations

- **Lattice location of the transition metals Co and Ni in Si**

  D. J. Silva, U. Wahl, J. G. Correia, L. M. C. Pereira, L. M. Amorim, E. Bosne, M. R. da Silva and J. P. Araújo.

  ISOLDE Workshop and Users meeting 2011, Geneva, Switzerland (**2011**)

- **"Localização de metais de transição em silício através da técnica emission channeling"**

  D. J. Silva, U. Wahl, J. G. Correia and J. P. Araújo.

  18ª conferência nacional de física, Aveiro, Portugal (**2012**)

- **Influence of the doping on the preferred sites of Fe and Ni in silicon**

  D. J. Silva, U. Wahl, J.G. Correia, L.M.C. Pereira, L. Amorim, M. Ribeiro da Silva and J.P. Araújo.

  Jornadas do MAP-fis 2013, Aveiro, Portugal (**2013**)

- **Influence of the doping on the preferred sites of Fe and Ni in silicon**

  D. J. Silva, U. Wahl, J.G. Correia, L.M.C. Pereira, L. Amorim, M. Ribeiro da Silva and J.P. Araújo.

  Intensive Program "Physics and materials science of nanostructures probed by nuclear methods and intense particle beams", Leuven, Belgium (**2013**)

- **Lattice location and thermal stability of the transition metals Fe, Co and Ni in silicon by emission channeling**

  D. J. Silva, U. Wahl, J.G. Correia, L.M.C. Pereira, L. Amorim, E. Bosne, M. Ribeiro da Silva, S. Decoster and J.P. Araújo.

  Gettering and Defect Engineering in Semiconductor Technology (GADEST) 2013, Oxford, UK (**2013**)

- **Lattice location and thermal stability of the implanted transition metals Fe, Co and Ni in silicon of different doping types**

  D. J. Silva, U. Wahl, J.G. Correia, L.M.C. Pereira, L. Amorim, V. Augustyns, A. Costa, E. Bosne, M. Ribeiro da Silva and J.P. Araújo.

  ISOLDE Workshop and Users meeting 2013, Geneva, Switzerland (**2013**)

Poster presentations

- **Lattice location of the transition metals Mn, Co and Ni in Si**

  D. J. Silva, U. Wahl, J. G. Correia, L. M. C. Pereira, L. M. Amorim, E. Bosne, M. R. da Silva, S. Decoster and J. P. Araújo.

  Jornadas do MAP-fis 2012, Braga, Portugal (**2012**)

- **Lattice location of Ni in Si by means of on-line emission channeling**

  D. J. Silva, U. Wahl, J. G. Correia, L. M. C. Pereira, L. M. Amorim, E. Bosne, M. M. Ribeiro da Silva, S. Decoster and J. P. Araújo.

  E-MRS 2012 Spring Meeting, Strasbourg, France (**2012**)

- **Lattice location of the transition metals Fe and Ni in Si by means of emission channeling from implanted radioactive isotopes**

  D. J. Silva, U. Wahl, J. G. Correia, L. M. C. Pereira, L. M. Amorim, E. Bosne, M. M. Ribeiro da Silva, S. Decoster and J. P. Araújo.

  Eurisol meeting 2012, Lisbon, Portugal (**2012**)

- **Influence of the doping on the lattice sites of Fe in Si**

  D. J. Silva, U. Wahl, J. G. Correia, L. M. C. Pereira, L. M. Amorim, E. Bosne, M. M. Ribeiro da Silva, S. Decoster and J. P. Araújo.

  International conference on defects in semiconductors (ICDS) 2013, Bologna, Italy (**2013**)

- **Lattice sites of implanted Co measured by on-line Emission Channeling**

  D. J. Silva, U. Wahl, J. G. Correia, L. M. C. Pereira, L. M. Amorim, M. R. da Silva and J. P. Araújo.

  Intermag 2014, Dresden, Germany (**2014**)

Awards

- **Corbett award 2013**

  Attributed in recognition to one outstanding young researcher at the international conference on defects in semiconductors 2013, held in Bologna, Italy.

List of acronyms and abbreviations

E_d	activation energy for dissociation
E_m	activation energy for migration
T_A	annealing temperature
AB	anti-bonding
E_b	binding energy
BC	bond-centered
E_C	conduction band edge
CZ	Czochralski
DLTS	deep level transient spectroscopy
U	electrostatic potential energy
EC-SLI	emission channeling with short-lived isotopes
EPR	electron paramagnetic resonance
EG	electronic grade
EuO	europium chalcogenides
EXAFS	extended X-ray absorption fine structure
FZ	floating zone
GaAs	gallium arsenide
GPS	general purpose separator

HRS high resolution separator

IBC ion beam channeling

IS infrared spectroscopy

ISOLDE isotope separator online device

MOS metal oxide semiconductor

MG metallurgical grade

MS Mössbauer spectroscopy

NAA neutron activation analysis

PSG phosphorus-silicate glass

PV photovoltaic

R_p projected range

PSB proton synchrotron booster

RBS Rutherford backscattering spectrometry

RS Raman spectrometry

SIMS secondary ion mass spectroscopy

SoG solar grade

S substitutional

SQUID superconducting quantum interference device

SRIM stopping and range of ions in matter

T tetrahedral

TEM transmission electron microscopy

TM transition metal

E_V valence band edge

XANES X-ray absorption near edge structure

H hexagonal

List of Tables

List of Figures